Modelling of Fuel Droplet Heating in Diesel Engines

Walid Abdel Aziz Ibrahim Abdelghaffar

PhD **2005**

Modelling of Fuel Droplet Heating in Diesel Engines

Walid Abdel Aziz Ibrahim Abdelghaffar

A thesis submitted in partial fulfilment of the requirement of the University of Brighton for the degree of Doctor of Philosophy

June 2005

School of Engineering
University of Brighton
UK

ABSTRACT

This work focuses on the modelling of diesel fuel heating process taking into account temperature distribution inside droplets, and their semitransparency with a view to potential application to diesel engines. Suggested approaches to numerical modeling of droplet heating are based on new analytical solutions of the heat conduction equation inside a spherical droplet. They are obtained for constant, almost constant and arbitrary convection heat transfer coefficients (h) in the presence of thermal radiation. To take into account the semitransparency of diesel fuel droplets, the absorption spectra of four types of diesel fuel are studied experimentally in the range between 0.2 μm and 6 μm. It is shown that the solution based on the assumption of constant heat transfer coefficient is the most computer efficient for implementation into numerical codes. This approach is shown to be more effective than the approach based on the numerical solution of the discretised heat conduction equation inside the droplet, and more accurate than the solution based on the parabolic temperature profile model. Droplet evaporation and the effects of time dependent gas temperature and convection heat transfer coefficient are taken in the limit of slow evaporation. The relatively small contribution of thermal radiation to droplet heating and evaporation allows us to adopt a simplified model, which does not consider the variation of radiation absorption inside droplets. The suggested models for temperature gradient inside semitransparent droplets are applied to the investigation of the effects on droplet evaporation, break-up and the ignition of fuel vapour/ air mixture based on a zero-dimensional code. This code takes into account the heat and mass exchange between liquid and gas phases and describes the autoignition process based on the Shell model. Even in the absence of break-up the effect of temperature gradient inside droplets leads to a noticeable decrease of the total ignition delay. In the presence of the break-up process the temperature gradient inside droplets can lead to substantial decrease of the droplet evaporation time and ignition delay. The numerical algorithm based on the analytical solution of the heat conduction equation inside droplets for constant h is implemented into KIVA2 CFD code. The predictions of the new model were validated against available experimental data. It is recommended that both the effects of temperature gradient inside droplets and their semitransparency are taken into account in computational fluid dynamics codes not only in diesel sprays but also in a wide range of spray applications.

CONTENTS

		Page
ABSTRACT		ii
TABLE OF CONTENTS		iii
LIST OF FIGURES		viii
LIST OF TABLES		xix
ACKNOWLEDGEMENT		xxi
DECLARATION		xxii
NOMENCLATURE		xxiii
CHAPTER 1	INTRODUCTION	1
	1.1 Statement of the problem	1
	1.2 Background	1
	1.3 Objectives of the research project	3
	1.4 Layout of the Thesis	4
CHAPTER 2	REVIEW OF LITERATURE	7
	2.1 Heat transfer in diesel engines	7
	2.2 Heating of diesel fuel droplets	10
	2.2.1 Convection and conduction	10
	2.2.1.1 Classification of the models	10
	2.2.1.2 Approximations for Nusselt and Sherwood numbers	16
	2.2.1.3 Experimental observations	19
	2.2.2 Radiation	23
	2.3 Modelling of the processes in diesel engines	32
	2.4 Conclusions of Chapter 2	40
CHAPTER 3	RADIATIVE HEATING OF SEMI-TRANSPARENT DIESEL FUEL DROPLETS	42
	3.1 Introduction	42
	3.2 Optical properties of fuel	43
	3.2.1 Measurements of index of absorption	43
	3.2.2 Analytical presentation on index of absorption	45

3.3 Absorption efficiency factor of droplets 47
3.4 Heating and evaporation of droplets 55
3.5 Conclusions of Chapter 3 59

CHAPTER 4 TRANSIENT HEATING OF DIESEL FUEL DROPLETS: MATHEMATICAL MODELS 61
4.1 Introduction 61
4.2 Basic equations and approximations 62
4.3 Analytical solutions 64
4.3.1 Case h (t) = const 64
4.3.2 Case h (t) ≠ const (general case) 68
4.3.3 Case of almost constant h (t) 70
4.4 Applications 71
4.5 Conclusions of Chapter 4 78

CHAPTER 5 TRANSIENT HEATING AND EVAPORATION OF DIESEL FUEL DROPLETS: NUMERICAL ALGORITHMS 80
5.1 Introduction 80
5.2 Conventional algorithm ($k_l = \infty$) 82
5.3 Numerical algorithms ($k_l \neq \infty$) 84
5.3.1 Numerical solution of the discretised heat conduction equation (NSDE) 84
5.3.2 Numerical algorithm using the solution for h (t) = const 85
5.3.3 Numerical algorithm using the solution for almost constant h (t) 86
5.3.4 Numerical algorithm for arbitrary h (t) 87
5.3.5 Numerical algorithm for the parabolic temperature profile model 87
5.4 Performance of numerical algorithms 88
5.4.1 Numerical solution of the discretised heat conduction equation 90

5.4.2 New approaches for the solution of the heat conduction equation inside droplets without thermal radiation 92
5.4.3 New approaches for the solution of the heat conduction equation inside droplets with thermal radiation 95
5.4.4 Numerical algorithm for parabolic temperature profile model 98
5.5 Comparison of numerical algorithms without thermal radiation 99
5.5.1 Heating of diesel fuel droplets 99
5.5.2 Heating and evaporation of a diesel fuel droplet 101
5.6 Comparison of numerical algorithms with thermal radiation 104
5.7 Conclusions of Chapter 5 111

CHAPTER 6 TRANSIENT HEATING, EVAPORATION AND IGNITION OF DIESEL FUEL DROPLETS: COUPLED SOLUTIONS 113
6.1 Dynamics of droplets 114
6.2 Effects of internal circulation inside the droplets 116
6.3 Gas phase heat and mass exchange with diesel fuel droplets 116
6.4 Droplets' break-up model 119
6.5 The Shell autoignition model 121
6.6 Zero dimensional code: implementation of the coupled algorithms 122
6.7 Validation of the numerical algorithm 128
6.8 Application to a monodisperse spray 134
6.8.1 The effects of thermal radiation, gas temperature, and gas pressure on evaporation time without break-up 138
6.8.2 The effects of thermal radiation, gas temperature, 147

	and gas pressure on total ignition delay time without break-up	
	6.8.3 The effects of gas temperature on evaporation time and total ignition delay time with break-up	153
	6.9 Conclusions of chapter 6	157
CHAPTER 7	IMPLEMENTATION OF THE ETC MODEL INTO KIVA CFD CODE	159
	7.1 Introduction to KIVA2 CFD code	160
	7.2 Spray Modelling in KIVA2	163
	7.2.1 Droplet heating model	163
	7.2.2 Droplet evaporation model	164
	7.2.3 Droplet break-up model	164
	7.3 Implementation of the ETC model into KIVA2	166
	7.4 Results and discussions	168
	7.4.1 The effects of the temperature gradient inside droplets on the spray behaviour without combustion	168
	7.4.2 The effects of temperature gradient inside droplets on combustion performance and exhaust emissions	173
	7.5 Conclusions of Chapter 7	180
CHAPTER 8	CONCLUSIONS	181
	Recommendations for further work	184
APPENDICES		185
Appendix 1	Estimate of $G(t, r)$ at $t \rightarrow 0$	185
Appendix 2	Numerical solution of Equation (4.3.2.9)	186
Appendix 3	Investigation of the convergence of series (4.3.3.1)	189
Appendix 4	Numerical solution of the discretised heat conduction equation	191
Appendix 5	Calculation of $\overline{T}$, q_n and p_n	194
Appendix 6	The Shell autoignition model	195
Appendix 7	Physical properties of fuels under consideration	201

A7.1 Physical properties of tetradecane 201
A7.2 Physical properties of n-heptane 201
A7.3 Physical properties of n-dodecane 202
A7.4 Physical properties of diesel fuel 203

REFERENCES 205
Papers published by the author 224

LIST OF FIGURES

CHAPTER 3 **Page**

Fig.3.1 Indices of absorption of four types of diesel fuel versus wavelength λ. White corresponds to low sulphur ESSO AF1313 diesel fuel used in cars; red corresponds to BP Ford reference diesel fuel used in off road equipment. Ranges A and C were taken from Dombrovsky et al (2001) and range B was measured experimentally. 45

Fig.3.2 Index of absorption of low sulphur ESSO AF1313 diesel fuel versus wavelength λ based on the measured values and the analytical approximation (3.2.2.1). 47

Fig.3.3 $\overline{Q}_{ai}$ versus R_d (black) and Λ_0 versus R_d (gray) for $1000 \le T_{ext} \le 3000$ K (indicated near the curves) for white unboiled diesel fuel. Coefficients a and b are defined by Equation (3.3.9). Plots shown in Fig.3.2a are based on the values of coefficients found for external temperatures in the range $1000 \le T_{ext} \le 3000$ K and droplet radii in the range $2 \le R_d \le 50$ μm. Plots shown in Fig.3.2b are based on the values of coefficients found for external gas temperatures in the range $1000 \le T_{ext} \le 3000$ K and droplet radii in the range $5 \le R_d \le 100$ μm. 52

Fig.3.4 The same as in Figure (3.2) but for the range $500 \text{ K} \le T_{ext} \le 3000$ K, when the coefficients a and b are defined by Equation (3.3.10). 54

Fig.3.5 Droplet temperatures and droplet radii versus time as calculated by a stand-alone code with Runge-Kutta (R-K) and LLNL solvers for a stationary droplet. The cases are: A) the effects of thermal radiation have been ignored, B) they are taken into account based on Equations (3.3.7) and (2.2.2.10) (semi-transparent droplets), C) they are taken into account based on Equation (3.3.7) with $\overline{Q}_{ai} = 1$ (black opaque droplets). $T_{s0} = 300$ K and $p_g = 6$ MPa. $R_{d0} = 10$ μm, $T_g =$ 57

1000 K and T_{ext} = 2000 K.

Fig.3.6 The same results as in Figure 3.4 but calculated with Runge-Kutta solver for different droplet radii, gas temperature and external temperature. Results shown in (a) are based on R_{d0}= 10 μm, T_g = 1000 K and T_{ext} = 1000 K. Results shown in (b) are based on R_{d0} = 25 μm, T_g = 1000 K and T_{ext} = 2000 K. Results shown in (c) are based on R_{d0} = 10 μm, T_g = 1000 K and T_{ext} = 3000 K. Results shown in (d) are based on R_{d0} = 10 μm, T_g = 700 K and T_{ext} = 2000K. 59

CHAPTER 4

Fig.4.1 Plots of thermal radiation power density absorbed by diesel fuel droplets normalized by the product $c_l\rho_l$ versus normalised radius. The curves are presented for unboiled low sulphur ESSO AF1313 diesel fuel used in cars. 73

Fig.4.2 Plots of droplet temperature versus normalized radius r for various times (indicated near the curves). Droplet radius is taken equal 50 μm. Gas and external temperatures are taken equal 2000 K. Curves for the cases when thermal radiation was ignored (dashed) and taken into account (solid) are presented 73

Fig.4.3 Plots of droplet surface temperature versus time for the case when T_{eff} = const (zeroth iteration) and T_{eff} = T_{eff} (t) (first iteration). Curves for the cases when thermal radiation was ignored (dashed) and taken into account (solid) are presented. 74

Fig.4.4 Plots of droplet radius versus time for the case when the initial droplet radius and gas and external temperatures are equal 50 μm and 2000 K respectively. Effects of thermal radiation are taken into account. 74

Fig.4.5 Plots of droplet temperature versus normalized radius r for t =1 ms. The plots refer to the case when 1, 2, 3 and 25 terms in the series are taken. The contribution of thermal radiation is taken into account. 75

CHAPTER 5

Fig.5.1 Plots of droplet surface temperature T_s versus time. The calculation have been performed using the numerical algorithm based on NSDE (1), the numerical algorithms based on the analytical solution for constant h (2), almost constant h (3) and an arbitrary h (4) without thermal radiation effects with timestep Δt = 10 μs, number of nodes along the radius $r/\Delta r$ =1000, T_g =1000 K and R_{d0} = 10 μm. 89

Fig.5.2 The same as in Figure (5.2) using the numerical algorithm based on the analytical solution for constant h (1), NSDE based on fully implicit method (2), Crank-Nicolson method (3) and explicit method (4). 90

Fig 5.3 Fig 5.4 Plots of errors and CPU times of droplet surface temperature versus time step (a) and number of nodes ($r/\Delta r$) (b); the calculations have been performed based on NSDE for $r/\Delta r$ = 1000 (a) and versus $r/\Delta r$ for Δt = 10 μs (b). 91

Fig.5.4 Plots of errors and CPU times of droplet surface temperature versus number of terms used in series (4.3.1.19) for the numerical algorithm based on the analytical solution for constant h (a) and versus number of terms used in series (4.3.2.8) for the numerical algorithm based on the analytical solution for almost constant h and based on the solution for an arbitrary h (b) without thermal radiation effects. The plots of errors are presented using the numerical algorithms based on the analytical solution for almost constant h (1) and the solution for an arbitrary h (2). CPU times required by these numerical algorithms based on the analytical solution for almost constant h (3) and the solution for an arbitrary h (4). Δt = 1 μs, T_g = 1000 K and R_{d0} = 10 μm. Plots 1 and 2 are undistinguishable in this figure 93

Fig.5.5 Plots of errors and CPU times of calculation of droplet surface temperature versus time step. The errors were calculated relative to the result given by the numerical 95

algorithm based on the analytical solution for h = const with Δt = 10 μs and $r/\Delta r$ = 1000. The plots for errors are presented for the numerical algorithms based on the analytical solution for h = const (1), the analytical solution for almost constant h (2) and the solution for an arbitrary h (3). Plots 2 and 3 are undistinguishable in this figure. CPU times required by the numerical algorithms based on the analytical solution for h = const (4), the analytical solution for almost constant h (5) and the solution for an arbitrary h (6). Gas temperature is taken as T_g =1000 K, and initial droplet radius is taken as R_{d0} = 10 μm.

Fig.5.6 The same as in Figure (5.5) with thermal radiation effects. 96

Fig 5.7 The same as in Figure (5.6) with thermal radiation effects. 97

Fig.5.8 Plots of droplet surface temperature T_s versus time for T_g =1000 K and R_d = 10 μm. The calculations have been performed using the numerical algorithm based on the analytical solution for constant h (1), the numerical algorithm based on the parabolic temperature profile model (2) and the numerical algorithm based on the assumption of no temperature gradient inside the droplet (3). 99

Fig.5.9 Plots of errors and CPU times of calculation of evaporation time versus time step. The errors were calculated relative to the numerical algorithm based on NSDE with Δt = 10 μs and $r/\Delta r$ = 50. The plots for errors are presented using the numerical algorithm based on the analytical solution for h = const (1) and the numerical algorithm based on NSDE (2). CPU times required by the numerical algorithm based on the analytical solution for h = const (3) and the numerical algorithm based on NSDE (4). T_g =1000 K and R_{d0} = 10 μm. 100

Fig 5.10 Plots of droplet surface temperature T_s and radius R_d versus time for T_g = 1000 K, without taking into account the effect of thermal radiation. The calculation have been performed using the numerical algorithms based on the analytical solution for h = const (1), NSDE (2), the numerical solution 102

based on the parabolic temperature profile model (3) and the numerical solution based on the assumption that there is no temperature gradient inside the droplet (4).

Fig 5.11 Plots of errors and CPU times of calculation of evaporation time versus time step for the calculations presented in Figure (5.11). The errors were calculated relative to the prediction of NSDE with Δt = 10 μs and $r/\Delta r$ = 50. The plots of errors are presented for numerical algorithm based on the analytical solution for h = const (1) and NSDE (2). Plots of CPU times are presented for the numerical algorithm based on the analytical solution for h = const (3) and NSDE (4). The calculations for the parabolic temperature profile model and the numerical solution based on the assumption that there is no temperature gradient inside the droplet were performed using the adaptive time step. The errors of these calculations relative to the prediction of NSDE were 1.53 % and 3.85 % respectively. The CPU times required by these algorithms were 0.03 sec and 0.02 sec respectively. 103

Fig.5.12 Plots of droplet surface temperature T_s and radius R_d versus time taking into account the effects of thermal radiation. The letters near the curves correspond to the numerical algorithms used as indicated in the text. T_g = 700 K and T_{ext} = 2500 K. 107

Fig.5.13 The same as Fig 5.13 but for numerical algorithms 'a' – 'c' and 'e' –'f'. 107

Fig 5.14 Plots of errors of calculation of evaporation time versus time step for the curves 'c', 'e' and 'f' presented in Figure (5.14). These errors were calculated relative to the prediction of NSDE with Δt = 1 μs and $r/\Delta r$ = 1000. The letters correspond to the numerical algorithms used as indicated in the text. 108

Fig.5.15 Plots of CPU time versus time step for the curves 'c' – 'f' presented in Figure (5.14). The letters correspond to the numerical algorithms used as indicated in the text. 109

Fig.5.16 Plots of droplet surface temperature T_s and radius R_d versus 111

time, without taking into account the effect of thermal radiation (a and b) and with taking into account the effect of thermal radiation (c and d). T_g = 1000 K, T_{ext} = 2000 K. The calculation have been performed using the numerical algorithms based on the analytical solution for h = const with k_l = 10 W.m^{-2}.K^{-1} and the numerical solution based on the assumption that there is no temperature gradient inside the droplet. Initial droplet radius is indicated near the plots. Figures (b, d) are zoomed for Figures (a, c), respectively.

CHAPTER 6

Fig.6.1 Zero-dimensional code flow chart. 126

Fig.6.2 The values of $(R_d / R_{d0})^2$ for evaporating tetradecane droplets versus time, as measured by Belardini et al (1992), and the results of calculations based the ETC (effective thermal conductivity) and the ITC (infinite thermal conductivity) models implemented into the zero dimensional code. The values of the initial gas temperature 473 K and 673 K are indicated near the plots. 129

Fig.6.3 The values of $(R_d / R_{d0})^2$ for evaporating n-heptane droplets versus time for the initial pressure 0.1 MPa, as measured by Nomura et al (1996), and the results of calculations based on the ETC and the ITC models implemented into the zero dimensional code. The values of initial gas temperature 471 K, 555 K, 647 K and 741 K are indicated near the plots. 130

Fig.6.4 The plots of T_s versus time for the same values of parameters as in Figure (6.3), calculated using the ETC and the ITC models implemented into the zero dimensional code. 131

Fig.6.5 The same as in Figure (6.3) but for the initial gas pressure 0.5 MPa. 131

Fig.6.6 The same as in Figure (6.3) but for the initial gas pressure 1 MPa. 132

Fig.6.7 The values of the total ignition delay time for evaporating n-heptane droplets versus initial gas temperature, as measured 134

by Tanabe et al (1995), and the results of calculations based on the ETC and the ITC models implemented into the zero dimensional code. The version of the Shell autoignition model described in Sazhina et al (1999) and Sazhina et al (2000) was used with the coefficient $A_{f4} = 3 \times 10^6$. The ratio of the volumes of air and liquid droplet was taken equal to $19.1^3 = 6967.871$ to provide the equivalence ratio 0.5 for T_{g0} = 600 K.

Fig.6.8 The values of the equivalence ratio versus gas temperature for various gas pressures (a), and the values of the equivalence ratio versus gas pressure for various gas temperatures (b). 1 mm^3 of liquid *n*-dodecane injected into 883 mm^3. 136

Fig. 6.9 Plots of $|U_d - Ug| / |U_{d0}|$ (U_{d0} is the initial droplet velocity) versus time for $|U_{d0}|$ = 10 m/s, 50 m/s, 100 m/s and 200 m/s (a), and plots of the droplet surface temperature T_s versus time for $|U_{d0}|$ = 0, 10 m/s, 50 m/s and 100 m/s (b). In all cases U_{g0} = 0. The initial gas temperature is equal to 880 K, initial gas pressure is equal to 3 MPa, and n-dodecane droplet with initial temperature and radius equal to 300 K and 10 μm respectively are taken. The ETC model is used and the effect of thermal radiation is ignored. 137

Fig.6.10 The values of the evaporation time for *n*-dodecane droplets versus external temperature calculated based on the ETC and ITC models implemented into the zero dimensional code. The initial gas pressure and temperature are taken equal to 3 MPa and 880 K respectively. The initial droplet diameters are taken equal to 5 μm (a), 20 μm (b) and 50 μm (c). The initial droplet velocities are indicated near the curves (0 (black), 10 m/s (red), 50 m/s (blue) and 100 m/s (green)). 139

Fig 6.11 Plots of percentage reduction of evaporation time due to thermal radiation versus external temperature calculated based on the ETC and ITC models implemented into the zero dimensional code, relative to the case without thermal 140

	radiation. Initial gas pressure and temperature are taken equal to 3 MPa and 880 K respectively. The initial droplet diameter is taken 50 μm. The initial droplet velocities are indicated near the curves (0 (black), 10 m/s (red), 50 m/s (blue) and 100 m/s (green)).	
Fig.6.12	The same as in Figure (6.9c) but for diesel fuel.	141
Fig.6.13	The values of the evaporation time for *n*-dodecane droplets versus initial gas temperature calculated based on the ETC and ITC models implemented into the zero dimensional code. Initial gas pressure is taken equal to 3 MPa. The initial droplet diameters are taken 5 μm (a), 20 μm (b) and 50 μm (c). The initial droplet velocities are indicated near the curves (0 (black), 10 m/s (red), 50 m/s (blue) and 100 m/s (green)).	143
Fig.6.14	Plots of $\lvert U_d - U_g \rvert$ versus time for $\lvert U_{d0} \rvert$ = 10 m/s, 50 m/s, 100 m/s, 150 m/s and 200 m/s. $U_{g0} = 0$. The initial gas pressure is equal 3 MPa, initial gas temperature is equal 880 K, *n*-dodecane droplet with initial temperature and radius equal to 300 K and 25 μm respectively are taken. The ETC model is used and the effect of thermal radiation is ignored. The results shown in Figure (a) up to 0.25 ms are zoomed in Figure (b).	144
Fig.6.15	The same as in Figure (6.12c) but for diesel fuel.	145
Fig.6.16	The values of the evaporation time for *n*-dodecane droplets versus initial gas pressure calculated based on the ETC and ITC models implemented into the zero dimensional code. Initial gas temperature is taken equal to 880 K. The initial droplet diameters are taken 5 μm (a), 20 μm (b) and 50 μm (c). The initial droplet velocities are indicated near the curves (0 (black), 10 m/s (red), 50 m/s (blue) and 100 m/s (green)).	146
Fig.6.17	The same as in Figure (6.15c) but for diesel fuel.	147
Fig.6.18	The values of the total ignition delay time for *n*-dodecane droplets versus external temperature calculated based on the ETC and ITC models implemented into the zero dimensional code. Initial gas temperature and pressure are taken equal to	148

880 K and 3 MPa, respectively. The initial droplet diameters are taken 20 μm (a) and 50 μm (b). Figures (c, d) show a magnified view of initial part of Figures (a, b), respectively. The initial droplet velocities are indicated near the curves (0 (black), 10 m/s (red), 50 m/s (blue) and 100 m/s (green)).

Fig.6.19 The values of the total ignition delay time for *n*-dodecane droplets versus initial gas temperature calculated based on the ETC and ITC models implemented into the zero dimensional code. Initial gas pressure is taken equal to 3 MPa. The initial droplet diameters are taken 5 μm (a), 20 μm (b) and 50 μm (c). The initial droplet velocities are indicated near the curves (0 (black), 10 m/s (red), 50 m/s (blue) and 100 m/s (green)). Radiation model is disabled. 150

Fig 6.20 Plots of gas temperature and the corresponding equivalence ratio at the start of ignition for *n*-dodecane versus initial gas temperature calculated based on the ETC and ITC models implemented into the zero dimensional code. The initial droplet diameter, velocity and pressure are taken equal to 50 μm, 50 m/s and 3 MPa respectively. 151

Fig.6.21 The values of the total ignition delay time for *n*-dodecane droplets versus initial gas pressure calculated based on the ETC and ITC models implemented into the zero dimensional code. Initial gas temperature is taken equal to 880 K. The initial droplet diameters are taken 5 μm (a), 20 μm (b) and 50 μm (c). The initial droplet velocities are indicated near the curves (0 (black), 10 m/s (red), 50 m/s (blue) and 100 m/s (green)). 152

Fig.6.22 The values of the evaporation time for *n*-dodecane versus initial gas temperature calculated based on the ETC and ITC models implemented into the zero dimensional code. Bag and stripping droplet break-up were taken into account. The initial droplet diameter and velocity are taken equal to 50 μm and 50 m/s respectively. Symbols indicate the values of the initial 154

	gas temperature for which the computations were times were calculated.	
Fig.6.23	Values of $\tilde{R}_{db} \equiv R_{db}(T_s)/R_{db}(T_s = 300K)$, $\tilde{R}_{ds} \equiv R_{ds}(T_s)/R_{ds}(T_s = 300K)$ (a), $\tilde{t}_b \equiv t_b(T_s)/t_b(T_s = 300K)$ and $\tilde{t}_s \equiv t_s(T_s)/t_s(T_s = 300K)$ (b) versus droplet surface temperature.	155
Fig.6.24	The plots of the total ignition delay versus T_{g0} in the presence of the break-up for the same droplets as used in Figure (6.22), when calculated based on the ETC and the ITC models implemented into the zero dimensional code. Symbols indicate the values of the initial gas temperature for which the ignition delay times were calculated.	156
CHAPTER 7		
Fig.7.1	Block diagram for the subroutine related to spray modelling in KIVA2 CFD code.	162
Fig.7.2	Block diagram for the modified part of the KIVA2 CFD code.	167
Fig.7.3	The values of fuel vapour mass versus crank angle for diesel fuel calculated by KIVA2 CFD code without combustion based on the Spalding and the ETC models.	170
Fig.7.4	The values of Sauter mean diameter (SMD) versus crank angle for diesel fuel calculated by KIVA2 CFD code without combustion based on the Spalding and the ETC models. The initial part of Figure (a) is magnified in Figure (b) for SMD upto 10 μm.	171
Fig.7.5	The values of the liquid spray tip penetration versus crank angle for diesel fuel as measured by Beatrice et al (1995) and the results of calculations obtained by KIVA2 CFD code without combustion based on the Spalding and the ETC models.	172
Fig.7.6	Fuel vapour distribution for the Spalding model (a) and the ETC model (b) for diesel fuel without combustion. Meridional section (plane $j = 4$).	173

Fig.7.7	Plots of the in-cylinder pressure versus crank angle for tetradecane fuel as measured by Belardini et al (1996) and the calculations obtained by KIVA2 CFD code based on the Spalding and the ETC models.	175
Fig.7.8	The values of fuel vapour mass versus crank angle for tetradecane fuel calculated by KIVA2 CFD code based on the Spalding and the ETC models (both with combustion).	176
Fig.7.9	The values of O_2 mass versus crank angle for tetradecane fuel calculated by KIVA2 CFD code based on the Spalding and the ETC models (both with combustion).	177
Fig 7.10	The values of CO_2 mass versus crank angle for tetradecane fuel calculated by KIVA2 CFD code based on the Spalding and the ETC models (both with combustion).	177
Fig.7.11	The values of CO mass versus crank angle for tetradecane fuel calculated by KIVA2 CFD code based on the Spalding and the ETC models (both with combustion).	178
Fig 7.12	The values of NO mass versus crank angle for tetradecane fuel calculated by KIVA2 CFD code based on the Spalding and the ETC models (both with combustion).	178
Fig.7.13	Temperature distribution at TDC inside the combustion chamber for the Spalding model (a) and the ETC model (b) for tetradecane fuel with combustion. Meridional section (plane $j = 4$).	179

APPENDICES

APPENDIX 5

Fig.A4.1	The grid used for NSDE	191

LIST OF TABLES

CHAPTER 3		Page
Table 3.1	Computational time and error for the radiation term calculation using analytical approximations and based on measured values of the index of absorption.	47
Table 3.2	Constants in Equation (3.3.9)	51
Table 3.3	Constants in Equation (3.3.10)	53
CHAPTER 4		
Table 4.1	Number of terms and the predicted average error from series (4.3.1.19). $T_{eff} = T_g = 2000$ K.	76
Table 4.2	Number of terms and the predicted average error from series (4.3.1.19). $T_{eff} = T_g = 2000$ K, $R_d = 10$ μm, 5 μm.	76
Table 4.3	Number of terms and the predicted average error from series (4.3.1.19). $T_{eff} = T_g = 2000$ K, $R_d = 50$ μm, 25 μm. The initial distribution of droplet temperature at $t = 1$ ms.	77
Table 4.4	The upper time limit (t_{up}) for the approximation T_{eff} = const and R_d = const	78
CHAPTER 5		
Table 5.1	Errors and CPU times of calculation of evaporation time at various gas temperatures without thermal radiation. The errors were calculated relative to the prediction of NSDE with $\Delta t = 10^{-6}$ sec using 1000 grid nodes along droplet radius. The errors and CPU times are presented for the numerical algorithm based on the analytical solution for h = const (A) and NSDE (N) using 100 nodes along droplet radius.	104
Table 5.2	Errors and CPU times of calculation of evaporation time at various external temperatures. Thermal radiation effects are taken into account. The errors were calculated relative to the prediction of NSDE with $\Delta t = 10^{-6}$ sec using	110

1000 nodes along droplet radius. The errors and CPU times are presented for the numerical algorithm based on the analytical solution for h = const (A) and NSDE (N) using 100 nodes along droplet radius, T_g = 700 K.

CHAPTER 7

Table 7.1 The engine characteristics for the case without combustion 169

Table 7.2 The engine characteristics for the case with combustion 174

APPENDICES

Table A7.1 Thermal conductivity of *n*-dodecane and diesel fuel. 204

ACKNOWLEDGEMENT

I would like to express my deep gratitude to my supervisors Dr E. M. Sazhina, Professor S. S. Sazhin, and Professor M. R. Heikal for their valuable guidance, thoughtful criticism and informative and continuous observations throughout this work.

I thank Professor P. A. Krutitskii, Professor S. V. Mikhalovsky and Mr S. T. Meikle for their expertise and collaboration.

I am grateful to Mrs S. Kennaird, Dr D. Kennaird and all my colleagues in Internal Combustion Engine Group (ICEG) at School of Engineering, University of Brighton for their support of my work.

I am thankful to all at School of Engineering, University of Brighton for their kind help and support, especially Dr A. Bruce, Dr M. Jones and Dr D. Koshal.

Financial support by EPSRC (Grant GR/R82920/01) is gratefully acknowledged.

I would like to take this opportunity to thank my family for their constant affection and support.

DECLARATION

I hereby certify that this thesis is my own work except where otherwise indicated. I have identified my sources of information, and in particular have put in quotation marks any passages that have been quoted word for word and identified their origins.

Signed: Date:

NOMENCLATURE

English Symbols

a	absorption coefficient [m^{-1}] or coefficient defined in Equation (2.2.2.10)
a_v	coefficient defined in Clausius-Clapeyron Equation (3.4.4)
a_λ	spectral absorption coefficient [m^{-1}]
$a_{\lambda(ext)}$	spectral extinction coefficient [m^{-1}]
$\overline{a}$	average absorption coefficient [m^{-1}]
$\overline{a}_{tr}$	average transport extinction coefficient [m^{-1}]
a_0, a_1, a_2, a_3 and a_4	coefficients defined in Equation (3.3.10)
A	= $1-\kappa^{0.13}$ or surface area [m^2] or the amplitude of the undamped oscillation of droplets [m]
A_{f1}, A_{f2}, A_{f3}, and A_{f4}	pre-exponential factors in Arrhenius form in Equations (A6.15)-(A6.18)
b	coefficient defined in Equation (2.2.2.10)
b_v	coefficient defined in Clausius-Clapeyron Equation (3.4.4)
b_0, b_1, b_2, b_3 and b_4	Coefficients defined in Equation (3.3.10)
B	Branching agent in the Shell autoignition model
B_M	Spalding mass transfer number
B_T	Spalding heat transfer number
B_λ	Planck function defined in Equation (2.2.2.2)
B_0	drop size constant
B_1	break up time constant
c	specific heat capacity for constant pressure [J kg^{-1} K^{-1}]
c_v	specific heat capacity for fuel vapour for constant pressure [J kg^{-1} K^{-1}]
c_0	constant defined in Equation (A1.2)
$c_n(t)$	formula defined in Equation (4.3.1.16)
$\tilde{c}$	constant defined in Equation (A1.4)
C	coefficient defined in Equation (2.3.2) or coefficient defined in Equation (2.2.2.13)
C_b	dimensionless constant equal ½ in TAB break-up model

C_d	drag coefficient without evaporation effect
C_{df}	drag coefficient with evaporation effect
C_{d0}	orifice discharge coefficient
C_D, C_F, C_K	constants for TAB break-up model defined in Equation (7.2.3.1)
Cv	specific heat capacity for constant volume [J kg^{-1} K^{-1}]
C_1	coefficient defined in Equation (2.2.2.2) [W □m^4 m^{-2}]
C_2	coefficient defined in Equation (2.2.2.2) [□m K]
D_d	droplet diameter [m]
D_{12}	binary liquid diffusivity [m^2 sec^{-1}]
E	turbulence kinetic energy [J]
E_{f1}, E_{f2}, E_{f3}, and E_{f4}	activation energies in Equations (A6.15)-(A6.18) [J]
f_i	scattering phase function of the ith droplet or rate term defined in Equations (A6.9)-(A6.11)
f_n	coefficient defined in formula (4.3.1.12)
f_v	volume fraction of droplets in Equation (3.3.1)
f_1, f_2, f_3 and f_4	the rate constants in Equations (A6.9)-(A6.13) defined by Equations (A6.15)-(A6.18)
$f(r)$	function defined in formula (4.3.1.12)
$f(\mathrm{Re}_d)$	function defined in Equation (6.3.4)
F_M	heat film thickness correction factor defined in Equation (2.2.1.2.12)
F_T	mass film thickness correction factor defined in Equation (2.2.1.2.11)
$F(R_d)$	normalised distribution function of droplets by radii
Fo	Fourier number
$G(t, r)$	kernel defined by formula (4.3.2.6)
$\tilde{G}(t)$	function defined in Equation (A1.4)
h	convection heat transfer coefficient [W m^{-2} K^{-1}]
$\tilde{h}$	convection heat transfer coefficient with the effect of fuel vapour superheating [W m^{-2} K^{-1}]
h_{in}	heat transfer coefficient at the start of fuel injection [W m^{-2} K^{-1}]
h_f	heat transfer coefficient when the fuel droplet stops [W m^{-2} K^{-1}]
h_0	$= hT_gR_d / k_l$

h_1	parameter defined in formula (4.3.2.1) [W m^{-2} K^{-1}]
$H(t)$	$\frac{h(t)R_d}{k_l}-1$
$I(\bar{t})$	auxiliary integral introduced in Appendix 2
I_λ	spectral intensity of radiation in unit solid angle [W m^{-2} sr^{-1}]
$I_{\lambda b}$	spectral intensity of radiation in unit solid angle for a blackbody [W m^{-2} sr^{-1}]
$I_\lambda^0(R)$	$= \int I_\lambda(R,\Omega)d\Omega$
k	thermal conductivity [W m^{-1} K^{-1}]
k_b	rate coefficient of branching reaction in Shell autoignition model
k_p	rate coefficient of propagation reaction in Shell autoignition model
k_q	rate coefficient of initiation reaction in Shell autoignition model
k_t	rate coefficient of termination reaction in Shell autoignition model
k_{eff}	effective thermal conductivity [W m^{-1} K^{-1}]
K	$= k_l/(c_l\rho_l R_d^2)$
L	specific heat of evaporation [J Kg^{-1}]
Le	Lewis number
L_{eff}	coefficient defined in Equation (6.3.5)
m_d	droplet mass [kg]
$\dot{m}$	rate of droplet evaporation [kg sec^{-1}]
M	fuel component molecular mass [kg $kmol^{-1}$]
$[M]$	molar concentration of species M [kmol m^{-3}]
$M(t)$	$= h(t)T_{eff}(t)R_d/k_l$ [K]
M_a	molar mass of air [kg $kmol^{-1}$]
M_f	molar mass of fuel vapour [kg $kmol^{-1}$]
n	index of refraction or number of droplets or number of the current time step
Nu	Nusselt number
p	pressure [Pa]
p_{inj}	injection pressure [Pa]
p_{cyl}	in-cylinder pressure [Pa]

p_{Fs}	saturated fuel vapour pressure near the droplet surface [Pa]
p_n	coefficient defined in Equation (4.3.1.12)
P	product species in fuel combustion equation
$P(r)$	thermal radiation power density [$P_1(rR_d)/(c_l\rho_l)$] [K s^{-1}]
Pe	Peclet number
Pr	Prandtl number
$P_1(R)$	radiation power absorbed per unit volume inside the droplet [W m^{-3}]
$\tilde{P}(r)$	$= r\,P(R)$
q	coefficient defined in Equation (2.2.2.7) or stoichiometric coefficient of product P or exothermicity in the Shell autoignition model
q_n	the normal component of the radiation heat flux at the boundary [W m^{-2}] or coefficient defined in Equation (4.3.1.12)
Q	intermediate agent in the Shell autoignition model
Q_a	absorption efficiency factor
Q_H	heat consumed by droplet heating [W]
Q_K	the total heat release rate defined in Equation (A6.21) [W]
Q_l	heat conduction to the droplet surface per unit area defined in Equation (7.2.1.2) [W m^{-2}]
Q_L	heat used to heat up the liquid droplet [W] defined in Equation (6.3.2) or the heat loss through the boundary walls defined by Equation (A6.22) [W]
Q_S	heat carried back to the surrounding gas with diffusing vapour in the form of superheat defined in Equation (6.3.2.) [W]
Q_s^{tr}	transport scattering efficiency factor
Q_V	heat arriving to the droplet surface defined in Equation (6.3.2.) [W]
Q_λ	heat consumed by droplet evaporation defined in Equation (6.3.2) [W]
r	normalised radius (R/R_d)
R	distance from the centre of sphere [m] or universal gas constant [J kg^{-1} K^{-1}]
R_d	droplet radius [m]
R_{da}	parent droplet radius [m]

Re	Reynolds number
R_{ij}	coefficient defined in Equation (3.3.2)
R^*	$= R_d/n$ [m] or radical species in the Shell autoignition model
$\tilde{R}_{db(s)}$	$\equiv R_{db(s)}(T_s)/R_{db(s)}(T_s = 300\,\mathrm{K})$
S	radiation source term (Equation (A4.1)) [W m^{-3}] or the stoichiometric oxygen-fuel ratio by mass (Equation (A6.32))
Sh	Sherwood number
SMD	Sauter mean diameter [m]
t	time [sec]
t_b	the lifetime of an unstable droplet based on bag break-up model [sec]
t_{bu}	the lifetime of an unstable droplet based on TAB break-up model [sec]
t_s	the lifetime of an unstable droplet based on stripping break-up model [sec]
$\tilde{t}_{b(s)}$	$\equiv t_{b(s)}(T_s)/t_{b(s)}(T_s = 300\,\mathrm{K})$
T	temperature [K]
T_c	temperature at droplet centre [K]
T_{eff}	effective temperature [K]
T_{ext}	external temperature [K]
T_{ref}	$= (T_g + 2T_s)/3$ [K]
T_0	initial temperature [K]
$\tilde{T}_0(r)$	$= r\,T_0(r)$ [K]
u	$= T\,r$ (Equation (4.2.5)) [K]
u_c	$= \sqrt{1-(1/n)^2}$ (Equation (2.2.2.18))
u_*	$= \sqrt{1-\left(\frac{1}{nr}\right)^2}$ (Equation (2.2.2.18))
$U(r, t)$	function defined in formula (4.3.2.4)
U	velocity [m sec^{-1}]
V	volume [m^3]
w	normalized absorption spectral power of radiation per unit volume

W	function defined in Equation (4.3.1.17)
We	Weber number
x	diffraction parameter of droplet or the displacement of the drop equator from its equilibrium position in TAB breakup model [m]
Y_f	mass fraction of fuel vapour
z	$= \dot{m}_v c_v / hA_d$

Greek Symbols

α	shape parameter defined in Equation (2.2.1.1.7) or parameter defined in Equation (6.1.4)
β	shape parameter defined in Equation (2.2.1.1.7)
β_n	coefficient defined in Equation (A6.1)
χ	k_{eff} / k_l
δ	parameter defined in Equation (2.2.2.11)
δ_M	thickness of mass boundary layer [m]
δ_{nm}	0 if $n \neq m$, 1 if $n = m$
δ_T	thickness of heat boundary layer [m]
δm_{RBQ}	total change in mass of R^*, B and Q over a time step [kg sec^{-1}]
Δt	time step [sec]
ε	small parameter defined in Equation (4.3.3.1)
ε_d	emissivity of fuel droplet
ϕ_z	crank angle (Equation (2.3.1)) [degree]
γ	= 1.4 – exp (-80 κ) in Equation (2.2.2.13) or coefficient defined in Equation (2.2.1.1.7)
$\bar{\gamma}$	$= (1.5/\tau_0^2) - (0.6/n^2)$,
$\eta(t)$	$h_1(t) / \varepsilon$
κ	index of absorption ($a_\lambda \lambda / 4\pi$)
κ_c	thermal diffusivity [m^2 sec^{-1}]
φ	$= 1 + 0.2\xi$ in Equation (5.3.5.1)
φ_n	coefficient defined in Equation (A5.3)

λ	wavelength [□m]
λ_n	eigenvalues
μ	cos θ or dynamic viscosity [Pa sec]
μ_c	parameter introduced in Equation (2.2.2.18)
$\mu_{g0}(t)$	$=h_1(t)\,u+\mu_0(t)$
μ_i	$\frac{1}{4\pi}\int(\Omega\Omega')f_i(\Omega\Omega')d\Omega'$ in Equation (2.2.2.3)
μ_0	$\Omega\Omega'$ in Equation (2.2.2.3)
$\mu_0(t)$	$= hT_{eff}(t)R_d / k_l$
μ_*	parameter introduced in Equation (2.2.2.18)
$\nu_j(t)$	function defined in Equation (4.3.3.5)
θ	azimuthal angle [rad] or weighting parameter
θ_R	radiation temperature [K]
θ_s	$= (T_s - T_0)/(T_g - T_0)$
$\bar{\theta}$	$=1-\exp(-3\xi Fo)$ for isothermal model and $=1-\exp(-3\xi Fo/(1+0.2\xi))$ for parabolic model
ρ	density [kg m^{-3}]
σ	Stefan- Boltzmann constant [W m^{-2} K^{-4}]
σ_s	droplet surface tension [N m^{-1}] or scattering coefficient [m^{-1}]
$\sigma_{s\lambda}$	spectral scattering coefficient [m^{-1}]
τ	optical thickness or the argument in the integrands
τ_z	delay period time (Equation (2.3.1)) [sec]
τ_0	$a_\lambda R_d$
$\upsilon_n(r)$	the full set of non-trivial solutions of Equation (4.3.1.6)
$\|\upsilon_n(r)\|$	parameter defined in Equation (4.3.1.11)
ω	droplet oscillation frequency [rad sec^{-1}]
ξ	Nu $k_g/(2\ k_l)$ or coefficient defined in Equation (2.2.2.13) or coefficient defined in Equation (2.2.2.19)
Λ	coefficient defined in Equation (2.2.2.9)
Λ_0	aR_d^b , R_d is in □m, Equation (2.2.2.10)
Ω	solid angle [sr]

$\psi(t)$	function defined in formula (A2.1)
ζ	coefficient defined in Equation (5.3.6.1)
ς	coefficient defined in Equation (2.2.1.2.20)
ϑ	wave growth rate [m sec^{-1}]

Subscripts

air	air
b	bag break-up or boiling
cr	critical
d	droplet
ev	evaporation
f	fuel
l	liquid
max	maximum
min	minimum
g	gas
n	new
o	old
p	particle
R	radical
s	droplet surface or stripping break-up
v	vapour
w	wall or boundary
0	initial or non evaporating
∞	far from the droplet surface

Superscripts

—	average
~	normalized

1. INTRODUCTION

1.1 Statement of the problem

Heating of droplets by a hot surrounding gas in diesel engines is driven by convective and radiative heat transfer. In the case of convective heating, there is an initial increase of temperature at the surface of the droplets, from where the heat is transferred to their main body by conduction. In the case of radiative heating of realistic semi-transparent droplets, the thermal radiation is absorbed inside the droplets (Dombrovsky et al, 2001). If the droplet is moving the circulation inside the droplet becomes significant and convective heat transfer inside the droplet should be taken into account (Sirignano, 1999).

A considerable progress has been achieved in developing models of droplet convective and radiative heating (Abramzon and Sirignano, 1989; Lage and Rangel, 1993a; Griffiths and Barnard, 1996; Aggarwal, 1998; Sirignano, 1999; Dombrovsky, 2000; Sazhina et al, 2000; Sazhin et al 2001a, 2004a, b, c; Dombrovsky, 2002b; Dombrovsky and Sazhin, 2003b, 2004). At the same time the application of these models in computational fluid dynamics (CFD) codes, used in engineering applications, is still limited (see Bertoli and Migliaccio, 1999; Sazhin et al, 2002). This leads to the need to develop the models of these processes to describe the essential features of the phenomena while keeping them simple enough for implementation into CFD codes. These models, which take into account radiative heating of realistic semi-transparent droplets, temperature gradient and the effects of recirculation inside droplets, shall be implemented into a CFD code to provide more accurate modelling of fluid dynamics, heat transfer and combustion processes in diesel engines.

1.2 Background

Bertoli and Migliaccio (1999) were perhaps the first who drew attention to the fact that the accuracy of CFD computations of heating, evaporation and combustion of diesel fuel sprays could be substantially increased if the finite thermal conductivity of the liquid is taken into account. They suggested that the numerical solution of the heat conduction equation inside the droplet is added to the solution of the other governing equations in any CFD code. The authors performed some numerical tests for a combustion bomb to analyse the influence of the modified model on droplet heating, evaporation rate and droplet lifetime. The results showed that this approach increased the accuracy of CFD predictions. However, the additional computational cost of this approach might be too

high for practical applications. Also the authors did not take into account the thermal radiation effects.

Sazhin and Krutitskii (2003) derived the solution of the heat conduction equation inside droplets using simplified assumptions. They assumed constant heat transfer coefficient and constant initial temperature distribution inside droplets. The authors also neglected the thermal radiation term. In the limiting case of infinitely large thermal conductivity, this solution is reduced to that predicted in the 'rapid mixing limit'.

An alternative approach to taking into accounts the effect of finite thermal conductivity and recirculation inside droplets has been suggested by Dombrovsky and Sazhin (2003a). This model is based on the parabolic approximation of the temperature profile inside droplets. This approximation does not satisfy the heat conduction equation with appropriate boundary conditions, but satisfies the equation of thermal balance at the droplet surface. Comparison with numerical solutions of the transient problem for moving droplets showed the applicability of this approximation to modelling the heating and evaporation processes of fuel droplets in diesel engines. The simplicity of the model makes it practically convenient for implementation into multidimensional CFD codes. This model was implemented into a research version of the CFD code VECTIS of Ricardo Consulting Engineers and preliminary results were published by Sazhin et al (2002). This model can be used in CFD codes if the high accuracy of calculations is not essential. The predicted error for the evaporation time from this model has not been investigated.

The model suggested by Dombrovsky et al (2001) took into account the semi-transparency of fuel droplets but assumed that the radiation is absorbed uniformly inside the droplets. Detailed Mie calculations were replaced by the approximation of the absorption efficiency factor for droplets with an analytical formula aR_d^b, where R_d is the droplet radius, a and b are quadratic functions of gas temperature (the authors implicitly assumed that the external gas temperature, responsible for radiative heating of droplets is equal to the ambient gas temperature, responsible for their convective heating). The coefficients of these functions were found based on the comparison with rigorous calculations for a realistic diesel fuel, for droplet radii and gas temperatures in the ranges 5 - 50 μm and 1000 - 3000 K respectively. This model allowed the authors to attain a reasonable compromise between accuracy and computational efficiency. This is particularly important for the implementation of a thermal radiation model into a multidimensional CFD code designed to model combustion processes in diesel engines.

The coefficients a and b were obtained based on values of index of absorption in the wavelength ranges: 0.2-1 μm and 2- 6 μm.

Dombrovsky and Sazhin (2003b) developed a simple analytical approximation for normalised absorbed radiation power assuming that the geometrical optics approximation is valid. The authors used the simplified MDP_0 approximation (Dombrovsky, 2000; 2002b). It was shown that the radiation power absorbed in the droplet core is rather large and almost homogeneous. Also, the absorbed power is large in the vicinity of the droplet surface, but is minimal in the intermediate region. It is worth pointing out that these results were obtained based on the limited data of diesel fuel index of absorption reported in Dombrovsky et al (2001). Although this approximation is more accurate than that based on the assumption of uniform thermal radiation absorption inside the droplet the additional computational cost might be too high for practical applications.

1.3 Objectives of the research project

There are two main objectives of the present research project. The first objective is to develop accurate and computer efficient physical models for convective and radiative droplet heating and the method of their implementation into CFD codes. The second is to investigate the applicability of the models to realistic conditions in diesel engines and their usefulness.

These objectives are expected to be achieved based on the following investigations:

1) Extending the applicability of the model suggested by Dombrovsky et al (2001) for a wider range of droplet radii, external and ambient gas temperatures and for various types of diesel fuel. This will be based on the experimental measurements of the index of absorption in the whole range of wavelength (0.2 – 6 μm) for various types of diesel fuel.
2) The applicability of the absorbed radiation power model by Dombrovsky and Sazhin (2003b) for diesel fuels will be investigated based on a wider range of measured data for the index of absorption for different types of diesel fuel. Also the comparison of this model with that based on the assumption of uniform radiation distribution inside the droplet (Dombrovsky et al, 2001) will be performed.
3) The parabolic temperature profile model suggested by Dombrovsky and Sazhin (2003a) will be investigated in details taking into account the effect of

evaporation on the droplet surface temperature calculations. The accuracy of this approach will be discussed based on the solution of the heat conduction equation inside the droplets.

4) The analytical solution of the heat conduction equation inside the droplets for constant h, almost constant h and an arbitrary h will be developed taking into account the thermal radiation effects on heating and evaporation of diesel fuel droplets. This will allow us to take into account the temperature variation inside the droplet more accurately and computer efficiently than in the case of the direct numerical solution of the heat conduction equation.
5) The numerical algorithms based on the analytical solution of the heat conduction equation inside the droplet for constant h, almost constant h and an arbitrary h will be developed and compared with the numerical algorithm based on:
   a) The numerical solution of the discretised heat conduction equation inside the droplet.
   b) The numerical algorithm based on the parabolic temperature profile model (Dombrovsky and Sazhin, 2003a).
   c) The numerical algorithm based on the assumption of no temperature gradient inside the droplet.
6) The zero-dimensional algorithm taking into account radiative heating of droplets, temperature gradient inside droplets, droplet evaporation, coupling with surrounding gas will be developed and tested. Effects of droplet motion and break-up will be taken into account. Also the ignition of the fuel vapour / air mixture will be taken into account based on the Shell autoignition model using the mathematical formulation developed by Sazhina et al (1999, 2000).
7) The numerical algorithms based on the analytical solution of the heat conduction equation inside the droplet for constant h will be implemented into KIVA2 CFD code and tested for the realistic diesel engine condition.

Recommendations on the applicability of the new models for numerical modelling of fluid dynamics heat transfer and combustion processes in internal combustion engines will be made.

1.4 Layout of the Thesis

The following chapters present the methodology and the results of the work. The review of literature is discussed in Chapter 2. This literature review is divided into three

main parts. The first is focused on the global heat transfer processes in diesel engines (Section 2.1). The second is focused on the heating of diesel fuel droplet (Section 2.2) and the third is focused on modelling the processes in diesel engines (Section 2.3). The results of measurements of spectral index of absorption of diesel fuels, the approximation of the absorption efficiency factor in various ranges of droplet radii and external gas temperature and the implementation of the results into a stand-alone code, which assumed that there is no temperature variation inside the droplet, are presented and discussed in Chapter 3. The solutions of the heat conduction equation inside a fuel droplet are presented and discussed in Chapter 4. Three approximations for the convection heat transfer coefficient are considered. Firstly, the coefficient is assumed constant and an explicit formula for the time dependent distribution of temperature inside droplets is derived (Section 4.3.1). Secondly, the general case of time dependent convection heat transfer coefficient is considered. In this case the solution of the original differential equation is reduced to the solution of the Volterra integral equation of the second kind (Section 4.3.2). A numerical scheme for the solution of this equation is suggested. Thirdly, the case of almost constant convection heat transfer coefficient is considered. In this case the problem has been solved using the perturbation theory. A set of solutions corresponding to ascending approximations is obtained (Section 4.3.3). In Chapter 5 the numerical algorithms based on direct numerical solution of heat conduction equation inside the droplet, the analytical solution of this equation for constant h and almost constant h, the solution for an arbitrary h, the parabolic temperature profile model and the assumption of no temperature variation inside the droplet are developed. The performances of these numerical algorithms and their comparisons with and without the effect of thermal radiation are discussed. The investigation of the radiation term is performed by comparing two codes, when the distribution of radiation power inside the droplet is neglected and when it is taken into account. In Chapter 6 further development of the numerical algorithm based on the analytical solution of the heat conduction equation inside a droplet described in Chapters 3-5 is discussed. This will take into account coupling between droplets and gas and the autoignition process in the frame work of a zero-dimensional code. Results of its testing and application to modelling the processes of heating, evaporation, ignition, and break-up of diesel fuel droplets are presented. The effects of droplets' velocities, heating and evaporation on the surrounding gas are shown to lead to acceleration of gas by moving droplets. Cooling of gas, accompanying heating and evaporation of droplets, diffusion of

fuel vapour through the gas and, finally to the ignition of fuel vapour/ air mixture are taken into account. All values of gas parameters (velocity, temperature, fuel vapour concentration etc) are assumed to be spatially homogeneous. Parameters typical for a diesel engine combustion chamber are used. This code is tested against sets of several available experimental data. Results of sensitivity studies of the effects of temperature gradient inside droplets and radiation on droplet evaporation time, ignition delay and the break-up process are discussed. The results of implementation of the new model in KIVA2 CFD code is described in Chapter 7. The main results of the Thesis are summarized in Chapter 8.

2. REVIEW OF LITERATURE

This literature review includes three main parts. The first part is focused on the global heat transfer in diesel engine combustion chamber (Section 2.1). The second part is focused on the heating of diesel fuel droplet by surrounding gas (Section 2.2). The third part is focused on modelling of the processes in diesel engine (Section 2.3). The main conclusions of this chapter are summarized in Section 2.4

2.1 Heat transfer in diesel engines

The heat transfer from the combustion chamber to the cooling medium in diesel engines has been studied by various investigators (Lichty, 1967; Woschni, 1967; Taylor, 1979; Xu et al, 1984; Crook et al, 1985; Assanis and Heywood, 1986; Alkidas, 1987; Borman and Nishiwaki, 1987; Woschni, 1988; Heywood, 1988; Assanis and Badillo, 1989; Saeed, 1989; Shyler and May, 1993; Lingen et al, 1996; Rakopoulos Mavropoulos, 1998; Abdelghaffar et al, 2002). The instantaneous heat flux inside the diesel engine combustion chamber was studied by Baker and Assanis (1994), Han and Reitz (1997), Uchimi et al (2000), Yamada et al (2002) and Reichelt et al (2002). The details of these studies are beyond the scope of this research.

The radiation is particularly important during the combustion period of the cycle. It is estimated that up to 40 % of heat is transferred to combustion chamber walls by radiation (Chapman et al, 1983). Its share depends on the engine type, speed and load. The main sources of radiation are soot particles formed in the areas of locally rich fuel-air mixture (Chapman et al, 1983). The radiation heat transfer process has been studied by a number of authors. Flynn et al (1972) studied the radiation heat transfer in an operating diesel engine under a wide range of operating conditions. The result of this work indicates that the radiation temperature during the heat release event is much higher than the average bulk gas temperature and is much closer to the flame temperature. Annand and Ma (1972) developed an approximate relation to compute the instantaneous radiative heat flux from the flame to the wall in a diesel engine combustion chamber. Kunitomo and Matsuoka (1975) studied the instantaneous radiative heat flux from the flame to the wall in a diesel engine combustion chamber. Chapman et al (1983) developed a three-dimensional spatial model to determine the instantaneous radiation heat transfer in direct injection diesel engines, based on the assumption that the primary source of radiation is the soot formed on the fuel-rich side

of the combusting spray plumes. The radiation from the soot was assumed to be that of a grey body. Their study indicated that there are significant spatial and temporal variations in the incident radiation in various regions of the diesel engine combustion chamber. Chang and Rhee (1983) developed a radiation heat transfer model of diesel combustion. They indicated that the radiation absorption and emission by gaseous combustion products could be neglected when compared with that of soot. They also indicated that in the very beginning of the combustion process, the thermal radiation is insignificant due to the low gas-soot temperature even though the soot concentration is potentially high at the time. Mengüc et al (1985) used the P-1 and P-3 approximations (approximations for the radiative transfer equation for optically thick medium (see Sazhina et al (2000b)) to calculate the radiative heat loss to the combustion chamber surfaces at different times during the combustion events. The results showed that the P-3 approximation is more accurate than P-1 approximation in predicting the radiative transfer for the conditions in diesel engines. Based on the balance between the accuracy and computer efficiency, they indicated that the P-1 approximation is acceptable for modelling heat transfer in diesel engines due to the presence of soot. This approximation is valid for optically thick media. Cheung et al (1994) indicated that the gas radiation in diesel engines is negligible when compared with soot radiation, and gave the dependence of the absorption coefficient on crank angle for a direct injection diesel engine. The value of the absorption coefficient could reach 40 m^{-1}, and it increased with engine load. Furmanski et al (1997) presented a mathematical and numerical model of radiation in an internal combustion engine chamber to get a local distribution of the radiative flux on the piston crown as a function of a crank angle. The results showed that uneven distribution of radiative heat flux might lead to considerable increase of the maximum temperature of the piston crown. The contribution of thermal radiation heat transfer was taken into account via the absorption coefficient or emissivity of multiphase medium, the value of which was *a priori* specified depending on soot concentration (Kunitomo et al, 1975; Chang and Rhee, 1983; Chapman et al, 1983; Mengüc et al, 1985; Viskanta and Mengüc, 1987; Wahiduzzaman et al, 1987; Cheung et al, 1994; Abraham and Magi, 1997; Furmanski et al, 1999).

Abraham and Magi (1997) solved the radiative heat transfer equation using a discrete ordinates method and applied the solution to the study of the radiant heat loss characteristics in a diesel engine (bore = 13.97 cm, stroke = 15.24 cm). The results of this study showed that the ratio of radiant heat loss to total heat loss is about 12% at

equivalence ratios of 0.3 and 0.4 and rpm of 1500 and 1900. However, it reaches 15.5% for an equivalence ratio of 0.5. It was also shown that as speed is increased from 1500 to1900 rpm both the radiant and the total heat loss increased but the ratio of radiant to total heat loss remained about the same.

From the above analysis we can conclude that a number of thermal radiation models have been discussed in review papers and monographs (e.g. Viskanta and Mengüc, 1987; Siegel and Howell, 1992; Modest, 1993; Dombrovsky, 1996a, b, c). There is no universally accepted radiation transfer model that could be applied to all industrial problems, and the choice of the model is often based on engineers' experience and intuition. The radiation model, which seems to be most widely used in mathematical modelling of combustion processes in diesel engines, is the so-called P-1-model (Sazhin et al, 1996; Dombrovsky et al, 2001). This model uses indirect discretisation in different directions based on the expansion of the radiation intensity in an orthogonal series of spherical harmonics (Siegel and Howell, 1992; Sazhin et al, 1996). In this model the radiation temperature θ_R can be obtained as (Sazhin et al, 1996):

$$\frac{1}{3a}\nabla\frac{1}{a+\sigma_s}\nabla\theta_R^4-\theta_R^4+T_g^4=0. \tag{2.1.1}$$

where a and σ_s are the absorption and scattering coefficients T_g is the gas temperature, subject to appropriate boundary conditions. These conditions are usually formulated in the form suggested by Marshak (Siegel and Howell, 1992):

$$q_n=\frac{\sigma(T_w^4-\theta_R^4)}{\frac{1}{\varepsilon_w}-\frac{1}{2}} \tag{2.1.2}$$

where q_n is the normal component of the radiation heat flux at the boundary, T_w is the boundary temperature, ε_w is the emissivity of the boundary.

Once the distribution of θ_R in a given domain has been found from Equation (2.1.1) the thermal radiation flux can be estimated as (Sazhin et al, 1996):

$$q=-\frac{4\sigma}{3(a+\sigma_s)}\nabla\theta_R^4 \tag{2.1.3}$$

Equation (2.1.1) has the same structure as most of transport equations used in CFD codes. This means that the P-1 model is particularly appropriate for implementation into these codes. The main disadvantage of the P-1 approximation is its poor accuracy in the case of concentrated sources or sinks of radiation (Sazhin et al, 1996). This means that the reliability of this approximation for modelling of realistic thermal radiation processes

can in general be established mainly by trial and error rather than rigorous analysis (Sazhin et al, 1996).

2.2 Heating of diesel fuel droplets

Evaporation of fuel droplets and ignition of fuel/air mixture is preceded by droplet heating. The heating of droplets is driven by convective and radiative heat transfer from the surrounding medium. In the case of convective heating, there is an initial increase of temperature at the surface of the droplets, from where the heat is transferred to their main body (Dombrovsky et al, 2001). In the case of radiative heating of realistic semi-transparent droplets, the thermal radiation is absorbed mainly inside the droplets (Dombrovsky, 2000; Dombrovsky et al, 2001). Radiative heat transfer may be significant whenever (1) the temperature difference between the radiative heat source and the droplets is large; (2) the emissivity of the heat source is large, and the absorptivity of the droplets is appreciable at the most intensely radiated wavelength; (3) the turbulence level in the system is low, and the importance of convective transfer is thereby reduced; and (4) the droplets are large (Friedman and Churchill, 1965). During combustion, there is radiative interchange between the fuel droplets, the flame, the combustion walls, and the products of combustion (Friedman and Churchill, 1965).

Heating of diesel fuel droplets by convection and conduction heat transfer are discussed in Section 2.2.1, while the role of the radiation heat transfer is outlined in Section 2.2.2.

2.2.1 Convection and conduction

2.2.1.1 Classification of the models

Sirignano (1999) considered the following classification of models for heat transfer inside droplets in order of increasing complexity: 1) constant droplet temperature; 2) infinite liquid thermal conductivity; 3) conduction-limit; 4) effective conductivity; 5) vortex model of droplet heating; 6) Navier-Stokes solution.

Model 2 is perhaps the most widely used in multidimensional commercial CFD codes (e.g. Aggarwal, 1998; Sazhin et al, 2001; Sazhina et al, 2000; Utyuzhinikov, 2002) and analytical studies (e.g. Gorelov et al, 1999; Dombrovsky et al, 2001; Bykov et al, 2002). The main attractive feature of this model is its simplicity. However, model 3 can give a noticeable improvement in the prediction of diesel spray evaporation processes when compared with model 2 (Bertoli and Migliaccio, 1999). It is known that model 3 may

not lead to an improvement in the accuracy of computations in the case when the contribution of recirculation inside droplets is significant (Sirignano, 1999; Levich, 1962; Abramzon and Sirignano, 1989). In this case, models 4 - 6 would have to be applied. Direct application of models 5 and 6, however, would require considerable computational resources to take into account 3D effects (Abramzon and Sirignano, 1989). Model 4, where the effect of convective heat transfer inside droplets is accounted for by replacing the actual thermal conductivity of liquid k_l by the so-called effective thermal conductivity k_{eff}, seems to be a reasonable compromise between accuracy and computational efficiency. In this model it is assumed that $k_{eff} = \chi k_l$, where the coefficient χ varies from about 1 (at droplet Peclet number $Pe_d = Re_{dl} Pr_d < 10$) to 2.72 (at $Pe_d >$ 500) and can be approximated as (Abramzon and Sirignano, 1989):

$$\chi = 1.86+0.86 \tanh [2.225 \log_{10} (Pe_d/30)], \qquad (2.2.1.1.1)$$

where the values of the liquid-phase Peclet number can be obtained as (Incropera and DeWitt, 2002; Hohmann and Renz, 2003):

$$Pe_d = Re_{dl} Pr_l, \qquad Re_{dl} = \frac{2\rho_l |U_d - U_g| R_d}{\mu_l}, \qquad Pr_l = \frac{c_l \mu_l}{k_l},$$

μ_l is the liquid viscosity, U_d and U_g are the droplet and gas velocities respectively, Re_{dl} and Pr_l are liquid Reynolds and Prandtl numbers respectively, c_l is the liquid specific heat capacity and ρ_l is its density. This factor χ describes the heat transfer enhancement due to internal circulation as an increase in the effective liquid thermal conductivity (Lage and Range, 1993). This model can predict the droplet average surface temperature, but not the distribution of temperature inside droplets. In our case, however, we are primarily interested in the accurate prediction of the former temperature, which controls droplet evaporation. Hence, the applicability of this model can be justified. The aforementioned classification of the models was suggested based on the assumption that droplet heating is driven by convection. However, it can be equally applied to the case when the contribution of radiation is to be taken into account. The contribution of radiation is particularly important in the case when fresh droplets are injected after the onset of combustion in diesel engines. The temperature of gas in this case can approach 2500 K (Mengüç et al, 1985; Flynn et al, 1999; Kavtaradze, 2001). So far the modelling of droplet convective and radiative heating, taking into account its finite effective thermal conductivity, has been performed based on the numerical simulation of the underlying equations.

Based on model 2 (infinite liquid thermal conductivity) Chin and Lefebvre (1985) studied analytically the factors governing the duration of the heat-up period in fuel droplet evaporation for *n*-heptane, JP4, JP5 and DF2. The heat-up period was defined by the duration from starting of heating until dT_s/dt becomes zero. It was calculated for droplets of different size and fuel composition under different ambient conditions of temperature, pressure and velocity. The results showed that increasing the initial temperature of fuel affects only the heat-up period and has no influence on the subsequent evaporation processes. However, increasing ambient temperature reduces both the heat-up and evaporation periods. The heat-up period increases with increasing gas pressure and is proportional to the square of fuel droplet diameter. The proportion of droplet lifetime occupied by heat-up period increases with increasing fuel droplet size. It also increases markedly with increasing velocity because of enhancing evaporation rates and thereby reduces evaporation time, while the heat-up period remains almost constant. Haywood and Renksizbulut (1986) and Renksizbulut and Haywood (1988) considered the case of droplet fuel evaporation in air at 800 K and 1 bar of pressure, and the problem of droplet fuel evaporation in fuel-vapour environment at moderate elevated pressure (p = 10 bar) using model 4. They considered the temperature dependence of liquid fuel and fuel vapour properties. Their model was extended by Chiang et al (1992) to high-temperature and high-pressure environment. They also considered the temperature dependence of multicomponent gaseous mixture properties. The authors showed that the constant property calculations could overpredict drag coefficient by as much as 20%.

For model (3) the problem of heating of droplets without external sources (radiation) reduces to the solution of equation:

$$\frac{\partial T}{\partial t} = \kappa_c \left(\frac{\partial^2 T}{\partial R^2} + \frac{2}{R}\frac{\partial T}{\partial R}\right) \qquad (2.2.1.1.2)$$

where $\kappa_c = k_l/(c_l \rho_l)$ is thermal diffusivity. $T = T(R, t)$ is the droplet temperature, R is the distance from the centre of the sphere and t is time. Equation (2.2.1.1.2) was derived under the assumption that k_l, c_l and ρ_l are constants that do not depend on time and R. It can be solved analytically subject to the initial condition $T(R, t) = T_0$ = const and the boundary condition at the droplet surface:

$$4\pi R_d^2 h(T_g - T_s) = \dot{m} L + 4\pi R_d^2 k_l \frac{\partial T}{\partial R}, \qquad (2.2.1.1.3)$$

where h is convection heat transfer coefficient, R_d is the droplet's radius, T_g is the gas temperature at large distance from the droplet's surface, $\dot{m} \geq 0$ is the rate of droplet evaporation, L is the specific heat of evaporation. Ignoring the contribution of $\dot{m}L$ during the initial heat-up of the droplet and assuming that Nusselt number (Nu) = 2 and $h = k_g/R_d$ = const (droplet is considered stationary or almost stationary), the analytical solution of Equation (2.2.1.1.2) can be presented in the form (Luikov, 1968):

$$T = T_g + \frac{T_{so} - T_g}{R/R_d}\frac{k_g}{k_d}\sum_{n=1}^{\infty}\frac{\sin\lambda_n \sin(\lambda_n R/R_d)}{\lambda_n^2\|V_n\|^2}\exp(-K\lambda_n^2 t), \qquad (2.2.1.1.4)$$

where T_{s0} is the droplet initial surface temperature, k_g is gas thermal conductivity, $K = k_l/(c_l\rho_l R_d^2)$ and $\|V_n\|^2 = 0.5(1 - \sin 2\lambda_n / 2\lambda_n)$. The values of λ_n are found from the solution of the equation $\lambda \cos\lambda + h_0 \sin\lambda = 0$; $h_0 = hT_gR_d/k_l$. It has been shown that the droplet surface temperature increases from 300 K to 400 K about 30% faster when the realistic thermal conductivity of diesel fuel droplets is taken into account when compared with the case when this conductivity is assumed to be infinitely large for R_d = 50 μm and T_g = 880 K (Sazhin and Krutitskii, 2002).

For model 5 and 6, Chiang et al (1992) studied the transient droplet heating and vaporization by solving the unsteady Navier-Stokes equations governing droplet vaporization in the intermediate Reynolds number flow. They took into account the internal circulation inside the droplet and the droplet deceleration but neglected the thermal radiation effects. The results showed that the drag coefficient depends not only on the Reynolds number but also on the Spalding number (see Equation (2.2.1.2.18)). The rapid mixing droplet model (infinite liquid thermal conductivity model) can over-estimate the drag coefficient due to the inaccurate consideration of the rate of droplet heating. The temperature gradient inside the droplet is significant near the droplet surface at the very early time of heating and the energy transfer mode within the droplet is dominated by conduction. As the internal circulation inside the droplet increases, convection gradually tends to dominate. The results also showed that the droplet with higher initial temperature uses most of the available heat energy on the evaporation process, while the droplet with lower initial temperature uses most of the available energy to heat itself first, with the remaining energy used for vaporization.

Dombrovsky and Sazhin (2003a) suggested a simplified model for convective heating of the droplets called parabolic temperature profile model. This model is based on the parabolic approximation of the temperature profile inside droplets:

$$T(r,t) = T_c(t) + [T_s(t) - T_c(t)]r^2, \qquad (2.2.1.1.5)$$

where T_c, T_s are the temperatures in the centre and on the surface of the droplet respectively and $r = R/R_d$ is the normalized radius. T defined by Equation (2.2.1.1.5) does not satisfy Equation (2.2.1.1.2) but it can satisfy the energy balance equation for droplets for appropriate values of T_s and T_c. Although Equation (2.2.1.1.5) can predict accurate results for large times it can be poor for small times. Introducing the dimensionless temperatures $\theta_s = (T_s - T_0) / (T_g - T_0)$ it was found that θ_s presented in the form (Dombrovsky and Sazhin, 2003a):

$$\theta_s = \frac{\bar{\theta} + 0.2\xi}{1 + 0.2\xi}[1 - \exp(-\xi Fo)] \qquad (2.2.1.1.6)$$

where $\bar{\theta} = 1 - \exp(-3\xi Fo/(1 + 0.2\xi))$, Fo = $\kappa_c t / R_d^2$ (Fourier number), ξ = Nu $k_g/(2k_l)$. Equation (2.2.1.1.6) describes the so-called 'corrected' parabolic model. In the limit of large times it reduces to conventional parabolic model (Equation (2.2.1.1.5)). In the limit $t \to 0$ it predicts $\theta_s = 0$ or $T_s = T_0$ which agrees with the result of the rigorous solution of the heat conduction equation. For isothermal model $(T_c = T_s = \bar{T})$ $\bar{\theta} = 1 - \exp(-3\xi Fo)$, $\bar{T}$ is the average droplet temperature. When predictions of Equation (2.2.1.1.6) were compared with the rigorous numerical analysis of the transient heat conduction equation inside a spherically symmetrical droplet and predictions of the isothermal model, it was shown that the 'corrected' parabolic model is noticeably more accurate than the isothermal model.

Lorenzo et al (2003) studied the vaporization behaviour of xenon submicron droplets in nitrogen under subcritical and supercritical conditions using a molecular dynamics method which involves identifying each molecule and following their motion in time through the basic laws of classical mechanics. The authors showed that the rate of droplet evaporation increases with increasing ambient temperature and initial droplet temperature. The submicron droplet maintains the spherical shape during its lifetime, under subcritical condition. Also for subcritical case, an initially elliptical droplet attains the spherical shape rather early in its lifetime and its temperature increases during heating stage, when the vaporization rate is relatively low, followed by nearly constant liquid-temperature evaporation. For supercritical case, the initially elliptical droplet never returns to the spherical configuration and its temperature increases continuously during the vaporization process.

Kim and Sung (2003) studied the effect of ambient pressure on the evaporation of a single droplet and a spray of *n*-heptane injected into gaseous nitrogen. The temperature distribution inside the droplet is ignored in the evaporation model. The results showed that the droplet's lifetime is increased with increasing ambient pressure (40 bar) when the ambient temperature is low (<600 K) and decreased with increasing ambient pressure when the ambient temperature is high (>800 K). This is because the droplet's temperature rose at the final stages of evaporation at high pressure. In the final stages of evaporation, the factor determining the phase equilibrium was switched from the ambient pressure to the droplet's temperature at high ambient temperature. The latent heat of evaporation was reduced by increasing the droplet temperature. These effects are amplified at the high ambient temperature due to the higher increase in the droplet temperature. These results are in accord with the results in Chin and Lefebvre (1985). The results also showed that the evaporation of a spray was enhanced at higher ambient pressure. This effect was significant at a higher ambient temperature, because both atomisation and evaporation of a single droplet Ire increased. At a low ambient temperature, the effect of ambient pressure on the evaporation of a spray was reduced, because the droplets evaporated slowly.

As the diesel fuels consist of hundreds of different hydrocarbons, Pagel et al (2002) developed a multicomponent fuel evaporation model for sprays using the principles of the continuous thermodynamics. Fuel mixture properties are described by using the Gamma distribution function in the transport equations:

$$f(M) = \frac{(M-\gamma)^{\alpha-1}}{\beta^{\alpha}\Gamma(\alpha)}\exp[-(\frac{M-\gamma}{\beta})] \qquad (2.2.1.1.7)$$

where M is the fuel component molecular weight, α and β are shape parameters and γ determines the origin. The evaporation model was applied to single component single droplet, multicomponent single droplet, and diesel fuel spray under engine condition. They showed that for the diesel fuel the lighter fuel component evaporates much quicker than the heavier fuel component.

From the above analysis it can be noticed that, based on the classifications of models for heat transfer inside droplets (Sirignano, 1999), model 4 has the advantages of relative simplicity when compared with models 5 and 6 and high accuracy when compared with models 1, 2 and 3. In this model temperature gradient inside the droplets and the effects of internal recirculation are taken into account. It can also be implemented into CFD

codes to provide more accurate modelling of fluid dynamics, heat transfer and combustion processes in diesel engines.

2.2.1.2 Approximations for Nusselt and Sherwood numbers

A number of correlations for Nusselt number (Nu) and Sherwood number (Sh) of moving and evaporating droplets have been suggested. The one for non-evaporating droplets, which is most widely used, can be obtained by the correlation (Ranz and Marshall, 1952; Incropera and DeWitt, 2002; Bird et al, 2002):

$$\mathrm{Nu}_0 = 2 + 0.6\,\mathrm{Re}_d^{1/2}\mathrm{Pr}_d^{1/3} \tag{2.2.1.2.1}$$

$$\mathrm{Sh}_0 = 2 + 0.6\,\mathrm{Re}_d^{1/2}\mathrm{Sc}_d^{1/3}, \tag{2.2.1.2.2}$$

where $\mathrm{Re}_d = \dfrac{2\rho_g |U_d - U_g| R_d}{\overline{\mu_g}}$ is Reynolds number, $\mathrm{Pr}_d = \dfrac{\overline{c_g}\,\overline{\mu_g}}{\overline{k_g}}$ is Prandtl number, $Sc_d = \dfrac{\overline{\mu_g}}{\rho_g D_{12}}$ is Schmidt number, ρ_g, $\overline{\mu_g}$ and $\overline{c_g}$ are gas density, average viscosity and average specific heat capacity at constant pressure, respectively. Sometimes the coefficient 0.6 in Equations (2.2.1.2.1), (2.2.1.2.2) is replaced by 0.552 (Abramzon and Sirignano, 1989).

An alternative correlation for Nu_0 and Sh_0 Ire suggested in the form (Clift et al, 1978; Abramzon and Sirignano, 1989):

$$\mathrm{Nu}_0 = 1 + (1 + \mathrm{Re}_d\,\mathrm{Pr}_d)^{1/3} f(\mathrm{Re}_d), \tag{2.2.1.2.3}$$

$$\mathrm{Sh}_0 = 1 + (1 + \mathrm{Re}_d\,\mathrm{Sc}_d)^{1/3} f(\mathrm{Re}_d), \tag{2.2.1.2.4}$$

where

$$f(\mathrm{Re}_d) = \begin{cases} 1 & \text{when } \mathrm{Re}_d \le 1 \\ \mathrm{Re}_d^{0.077} & \text{when } 1 < \mathrm{Re}_d \le 400 \end{cases}$$

Equations (2.2.1.2.3) and (2.2.1.2.4) approximated the numerical results by different authors in the range of $0.25 < (\mathrm{Pr}_d, \mathrm{Sc}_d) < 100$ with an error less than 3 % (Abramzon and Sirignano, 1989).

The effect of evaporation on Nu and Sh can be taken into account by modifying Nu_0 and Sh_0 to (Abramzon and Sirignano, 1989):

$$\mathrm{Nu} = \mathrm{Nu}_0 \frac{\ln(1 + B_T)}{B_T} \tag{2.2.1.2.5}$$

$$\mathrm{Sh} = \mathrm{Sh}_0 \frac{\ln(1+B_M)}{B_M} \qquad (2.2.1.2.6)$$

where B_T and B_M are Spalding heat transfer and mass transfer numbers.

These expressions Ire originally obtained assuming that the thickness of the boundary layers around droplets is infinitely large (e.g. $T\ (R = \infty) = T_{g0}$).

Further development of the model (Abramzon and Sirignano, 1989) led to considering the finite thickness of these boundary layers (film thickness). For the thermal boundary layer this thickness δ_T was introduced via assuming that the resistance to heat exchange between a non-evaporating droplet surface and a gas, as calculated from a molecular transport theory and the Newton's law are the same. This leads to the equation (Incropera and DeWitt, 2002):

$$\frac{k_g(T_g - T_d)}{R_d - \dfrac{R_d^2}{R_d + \delta_{T0}}} = h(T_g - T_d) \qquad (2.2.1.2.7)$$

Hence (Abramzon and Sirignano, 1989):

$$\delta_{T0} = \frac{2R_d}{\mathrm{Nu}_0 - 2} \qquad (2.2.1.2.8)$$

Similarly I can introduce thickness of mass boundary layer δ_M as (Abramzon and Sirignano, 1989):

$$\delta_{M0} = \frac{2R_d}{\mathrm{Sh}_0 - 2} \qquad (2.2.1.2.9)$$

The effects of evaporation modify the values of these thicknesses to:

$$\frac{\delta_T}{\delta_{T0}} = F_T\,;\ \frac{\delta_M}{\delta_{M0}} = F_M\,. \qquad (2.2.1.2.10)$$

Model calculations led to the following correlations for F_T and F_M:

$$F_T = (1+B_T)^{0.7} \frac{\ln(1+B_T)}{B_T} \qquad (2.2.1.2.11)$$

$$F_M = (1+B_M)^{0.7} \frac{\ln(1+B_M)}{B_M} \qquad (2.2.1.2.12)$$

Introducing Nu^* and Sh^* via the film thickness we can write (Abramzon and Sirignano, 1989):

$$\left.\begin{aligned}\delta_T &= \frac{2R_d}{\mathrm{Nu}^* - 2}\\ \delta_M &= \frac{2R_d}{\mathrm{Sh}^* - 2}\end{aligned}\right\} \qquad (2.2.1.2.13)$$

From (2.2.1.2.8), (2.2.1.2.9), (2.2.1.2.10) and (2.2.1.2.13) we obtain (Abramzon and Sirignano, 1989):

$$\mathrm{Nu}^* = 2 + \frac{\mathrm{Nu}_0 - 2}{F_T} \qquad (2.2.1.2.14)$$

$$\mathrm{Sh}^* = 2 + \frac{\mathrm{Sh}_0 - 2}{F_T} \qquad (2.2.1.2.15)$$

Note that for stationary non-evaporating droplet we have $\mathrm{Nu}^* = \mathrm{Nu}_0 = \mathrm{Sh}^* = \mathrm{Sh}_0 = 2$ and $\delta_T \to \infty, \delta_M \to \infty$.

In the case of moving droplets, factors F_T and F_M lead to modification of Nu_0 and Sh_0 to (Abramzon and Sirignano, 1989):

$$\mathrm{Nu} = \frac{2\ln(1+B_T)}{B_T}\left[1 + 0.3\frac{\mathrm{Re}_d^{1/3}\,\mathrm{Pr}_d^{1/3}}{F_T}\right] \qquad (2.2.1.2.16)$$

$$\mathrm{Sh} = \frac{2\ln(1+B_M)}{B_M}\left[1 + 0.3\frac{\mathrm{Re}_d^{1/3}\,\mathrm{Sc}_d^{1/2}}{F_M}\right] \qquad (2.2.1.2.17)$$

B_T and B_M are calculated as (Abramzon and Sirignano, 1989):

$$B_T = \frac{c_v(T_g - T_s)}{L_{eff}}, \qquad (2.2.1.2.18)$$

$$B_M = \frac{Y_{fs} - Y_{f\infty}}{1 - Y_{fs}}, \qquad (2.2.1.2.19)$$

$L_{eff} = L + Q_H / \dot{m}_d$, Q_H is the heat spent on droplet heating and c_v is the specific heat capacity of fuel vapour, Y_f is the fuel mass fraction; subscripts 's' and '∞' refer to the conditions at droplet surface and external gas flow, respectively. It can be noticed that (Abramzon and Sirignano, 1989):

$$B_T = (1 + B_M)^{\varsigma} - 1 \qquad (2.2.1.2.20)$$

where

$$\varsigma = \left(\frac{c_v}{c_g}\right)\left(\frac{\mathrm{Sh}^*}{\mathrm{Nu}^*}\right)\frac{1}{\mathrm{Le}}, \qquad \mathrm{Le} = k_g / (\rho_g D_{12} c_g),$$

D_{12} is the binary liquid diffusivity. In the case of weak evaporation we can assumed that $B_T \ll 1$ and Equations (2.2.1.2.5), (2.2.1.2.6) are simplified to $\mathrm{Nu} = \mathrm{Nu}_0$, $\mathrm{Sh} = \mathrm{Sh}_0$.

An alternative correlation for Nu and Sh, to take into account the effect of finite film thickness for a motionless droplet in an infinite and stagnant gas, were suggested in the form (Yao et al, 2003):

$$\mathrm{Nu} = 2\left(1+\frac{R_d}{\delta_T}\right)\frac{\ln(1+B_T)}{B_T} \qquad (2.2.1.2.21)$$

$$\mathrm{Sh} = 2\left(1+\frac{R_d}{\delta_M}\right)\frac{\ln(1+B_M)}{B_M} \qquad (2.2.1.2.22)$$

where δ_T and δ_M are the thermal and mass film thickness based on the numerical values of Nu and Sh, as obtained from the rigorous numerical analysis of heat and mass transfer during the droplet evaporation process (e.g. see Haywood et al, 1989). Equations (2.2.1.2.8) and (2.2.1.2.9) were used in which $\mathrm{Nu_0}$ and $\mathrm{Sh_0}$ were replaced by the values of Nu and Sh obtained from numerical calculations.

In some earlier models, evaporation and heating of fuel droplets was accounted for by modifying Nu and Sh to (see Feath, 1977; Lefebvre, 1989):

$$\mathrm{Nu} = \frac{2\ln(1+B_M)}{B_M}(1+0.3\,\mathrm{Re_d^{1/2}Pr_d^{1/3}}) \qquad (2.2.1.2.23)$$

$$\mathrm{Sh} = \frac{2\ln(1+B_M)}{B_M}(1+0.3\,\mathrm{Re_d^{1/2}Sc_d^{1/3}}) \qquad (2.2.1.2.24)$$

The difference between B_T and B_M is not large in most cases and the analysis of this thesis will be based on Equations (2.2.1.2.23) and (2.2.1.2.24) following Lefebvre (1989).

2.2.1.3 Experimental observations

There exists very little experimental data that droplet vaporization models can be validated against. This is mainly due to the inherent difficulties encountered in investigations employing realistic liquid-fired combustion devices (insufficient instrumentation access, obscuration due to the presence of combustion generated particulates, high temperatures, turbulence, etc.) (Megaridis, 1993). Relevant experiments have produced an array of data on the variation of global droplet parameters, but have produced very limited quantitative information on the character of temperature field. A recent experimental study by Wong and Lin (1992) produced internal temperature distributions of large, hydrocarbon droplets that vaporize after being exposed to a 1000 K gaseous stream at atmospheric pressure. The droplets studied by Wong and Lin (1992) were of initial diameter 2 mm, and were suspended by a thin

shell-shaped probe specially designed to minimize interface to the internal liquid motion. The experimental conditions investigated corresponded to Reynolds numbers between 17 and 100. In this study individual droplets of diameter 2000 ± 50 μm were suspended on a ceramic shell suspender, which was attached to a 100 μm diameter glass filament. The temperature distributions within the droplet interior were measured by using fine thermocouples (25 μm diameter, 70 μm bead diameter) that were introduced and maintained in the bulk of the suspended droplets at either one or three fixed locations; the droplet centre and two mutually symmetric locations with respect to the vertical axis. The droplets were heated by a hot (1000 K) free stream produced by a flat-flame burner or an electrical heater. Three test conditions were investigated corresponding to Reynolds numbers 17, 60 and 100. Two pure fuels were tested by Wong and Lin (1992): n-decane and JP-10. The results showed that for n-decane, the temperatures at the droplet centre are lower than the temperatures in the vicinity of the droplet surface. For this large droplet, the temperature distribution inside the droplet showed that the minimum temperatures occur around R_d/R_{d0} = 0.6 - 0.7. These results were qualitatively validated numerically by Megaridis (1993).

In the experiment conducted by Belardini et al (1992) 10^{-9} g of tetradecane was injected at temperature of 300 K and initial velocity of 6 m/s through a hole of 0.28 mm diameter into a 100 cm^3 chamber. The chamber was filled with air at 1 bar, and the initial temperatures in the range from 473 K to 673 K. The evolution of droplet diameter during the evaporation process was measured starting with droplet diameter equal to 72 μm. The experimental characterization was carried out using a light scattering technique allowing the simultaneous measurement of droplet diameter, velocity and temperature. The experimental results were compared with the numerical results based on KIVA2 CFD code using the Spalding evaporation model. The comparison showed that the code underestimated the evaporation rates compared with the experimental results.

The experimental data reported in Nomura et al (1996) were obtained for a suspended *n*-heptane droplet in nitrogen atmosphere at pressure in the range between 0.1 and 1 MPa and temperatures in the range between 400 K and 800 K. Droplet initial radii varied from 0.3 mm to 0.35 mm. The authors studied experimentally the effects of ambient temperature and pressure on droplet evaporation under microgravity conditions. The results showed that, at an ambient pressure of 0.1 MPa the ratio of heat-up time to the evaporation time is almost independent of ambient temperature and the range of its value is about 0.1 - 0.2. The evaporation lifetime decreased with increasing ambient

temperature for various ambient pressures. The evaporation life time decreased with increasing ambient pressure for ambient temperature above 550 K, while it increased as ambient pressure increased at ambient temperature below 450 K. The authors suggested that the evaporation lifetime is almost independent of ambient pressure at an ambient temperature of about 480 K.

Lavieille et al (2000) developed an efficient laser-induced fluorescence technique in the liquids, to measure the temperature of monodisperse droplets. The droplets were seeded with an organic dye (rhodamine B), and the temperature dependence of the fluorescence quantum yield was used to determine droplet temperatures. The droplet velocity was measured simultaneously using LDA optics and a single argon laser source. The experimental set-up consisted of droplets generator, which can produce different droplets diameter and different initial droplet temperature, and a 1-D LDA optical device, which can obtain the droplet temperatures and velocities. The probe volume, corresponding to the intersection point of two laser beams, is adjusted on the droplet stream. The method was validated on an evaporating monodisperse ethanol droplet stream, previously heated. The technique was demonstrated to be capable of determine the droplet temperature within 1 °C in a monodisperse stream, where size changes due to evaporation were neglected. The major problem was that the fluorescence signal also depended on the droplet volume, which may change in evaporating or combusting spray. An alternative strategy was suggested by Sakakibara and Adrian (1999): a second fluorescent agent, whose fluorescence spectral band is well separated from the first one and with different temperature sensitivity, can be dissolved in the fuel. The ratio of the fluorescence signals measured on the two spectral bands can eliminate the volume dependence. Lavieille et al (2001) developed another laser-induced fluorescence technique based on a ratiometric measurement of fluorescence signals detected on two-colour bands of a single fluorescence dye (rhodamine B). This technique allowed the laser intensity, dye concentration and drop volume dependence to be eliminated, keeping the sole effect of temperature. Validation of the technique was provided on a monodisperse ethanol droplet stream either in evaporation or combustion. This technique succeeded to measure the average droplet temperature. However, with the use of small measuring volume, the technique has potential for detecting the temperature gradient inside the droplet. The two-colour laser-induced fluorescence technique was extended by Lavieille et al (2002) to measure the temperature distribution within the ethanol fuel droplets on a combustion monodisperse droplet stream, with 200 □m

droplet diameter. In this technique the droplet was scanned by a sufficiently small probe volume. The results showed that the heat transfer from the surrounding hot gas occurred at the droplet surface and the hot liquid fuel is convected from the droplet surface to the wake side of the droplet and to its central section.

Castanet et al (2002) studied experimentally heating and vaporization of a monodisperse ethanol stream, injected in a thermal boundary layer of vertical heated plate. The droplet size reduction was measured using the light scattering technique (interferential method) and the average droplet temperature was measured using the two-colour laser-induced fluorescence technique. The results showed that for distance parameter (the ratio between the inter-droplet distance and the droplet diameter) higher than 5, the droplet heating time is limited by the heat diffusion mechanism within the droplet, resulting from pure conduction in the liquid fuel and from convection due to the formation of internal circulation, while it is limited by the heat flux transferred from the gaseous phase to the liquid droplet for smaller distance parameter. This demonstrated the necessity to investigate the internal heat diffusion phenomena by measuring the temperature distribution inside the droplet. The results also showed that the convectional heat transfer coefficient is higher in the heating phase than in the vaporization phase. Castanet et al (2003) extended the technique used in Castanet et al (2002) to the measurements of the temperature distribution inside a droplet. They scanned the droplet volume by a sufficiently small probe volume compared to the droplet volume itself. The authors applied this technique to a monodisperse ethanol stream with initial droplet diameter equal to 200 □m and droplet injection velocity in the range from 2 m/s to about 10 m/s. The results showed that the heat transfer from the hot gas environment occurs at the droplet surface, and the heated liquid fuel then convected from the droplet surface to the droplet central region. These results are in qualitative agreement with the numerical simulations performed by Chiang et al (1992).

It can be noticed that the only direct observation of temperature gradient inside large (R_d > 100 μm) droplets is that reported in Laveille et al (2002), Castanet et al (2002) and Castanet et al (2003), to the best of our knowledge. This is not directly relevant to diesel engine environment as droplets are typically much smaller there. Also, the results reported by these authors refer to instantaneous measurements and cannot be used for validating of the model for droplet heating process. It seems that the only feasible validation of the model for droplet transient heating at the moment are those based on

the comparison of the predicted time evolution of droplet radius and the predicted ignition delay with experimental observations.

2.2.2 Radiation

Absorption and scattering of radiation by a particle depends on particle geometrical parameters and wavelength, as well as on complex refractive index of refraction of particle material $m = n - i\kappa$, where n is the index of refraction, κ is the index of absorption and $i = \sqrt{-1}$. For homogenous spherical particle the only geometrical characteristic which controls the absorption of thermal radiation is the size parameter $x = 2\pi R_d/\lambda$ (Dombrovsky, 1996).

The models suggested so far for radiative exchange between fuel droplets and gas can be subdivided into two main groups: those which take into account the semi-transparency of droplets in the infrared range (Lage and Range, 1993; Chang and Sheil, 1995; Dombrovsky, 1996; Dombrovsky; 2000; Dombrovsky et al, 2001, 2002, 2003) and those which assume that droplets are grey opaque spheres (Marchese and Dryer, 1997; Sazhin et al, 2000). Although the latter models are less accurate than the models of the first group, their application was justified by their computer efficiency. This is particularly important in the multidimensional modelling of combustion processes in diesel engines where the effects of thermal radiation are generally secondary when compared with conduction and convection (Sazhin et al, 2000).

Hottel et al (1955) and Berland and Hibberd (1952) have examined the effect of radiation on droplet combustion. These studies were concerned primarily with measuring the effect of radiative heat gain at the droplet surface on the burning rate. The results suggested that radiative heating is relatively unimportant for small droplets (e.g., droplet sizes representative of diesel spray combustion). Conversely, many theoretical studies like that by Chang and Shieh (1994) predicted an increase in burning rate due to radiation. Friedman and Churchill (1965) studied theoretically the absorption of the radiation heat transfer by JP-4 fuel droplets from the combustion walls (assumed to be a blackbody). The authors indicated that the fraction of infrared radiation, which is absorbed by the fuel droplet, rises continuously with increasing droplet radius.

Harpole (1980) was the first to predict complex profiles of absorption of thermal radiation in water droplets by computing the volumetric heating due to radiation absorption as a function of radial position for spherical water droplets in a black body surrounds of temperatures up to 1450 K. Lage and Rangel (1993a) studied theoretically a

single-droplet vaporization using three liquid phase heating models, the infinite-conductivity model, the conduction-limit model and the effective-conductivity model. The authors showed that the radiation absorption distribution pattern is not important in the single-droplet vaporization process, under the conditions analysed; only the total absorbance values are needed for vaporization studies. The authors also showed that absorption of thermal radiation in the *n*-decane droplet core is almost constant and predicted that most of the thermal radiation is absorbed near the droplet surface. Lage and Rangel (1993b) studied the total directional and hemispherical radiation absorption distributions, based on electromagnetic theory, for water and decane droplets irradiated by a blackbody at different temperatures. Also, they studied the total absorbance for water droplets of up to 1500 μm radius. They found that the total hemispherical absorption radial profile varied little with the blackbody temperature for the same droplet size for spherically symmetric irradiation. Also they found that the geometrical-optics approximation introduce more than 20 % of error for the absorbance of droplets with radii less than 10 μm. This error drops with increasing droplet radius to about 6 % for droplets with radii greater than 50 μm. Saitoh et al (1993) studied the effect of gas radiation on *n*-heptane droplet combustion and predicted a 25 % reduction in flame temperature due to radiation losses. Marchese and Dryer (1997) studied the effect of radiative heat loss from isolated droplet. The authors indicated that the radiative heat loss from isolated droplet of methanol is negligible for small droplet sizes ($R_d < 1$ mm). The effect of radiation becomes noticeable for fuel droplets with diameters greater than 1 mm. This model predicted a decrease in burning rate of fuel droplet with increasing its diameter.

Goldfarb et al (1999) focused on the impact of thermal radiation on the delay time of fuel droplet ignition. The authors assumed that the gas contains evaporating ideal spherical droplets of fuel with the same radii (monodisperse spray). These spheres were treated as opaque grey and the medium was considered spatially homogeneous. It was pointed out that the effect of thermal radiation could be largely ignored in the case of the thermal explosion of tetralin, while in the case of *n*-decane these effects can be important.

Yang and Wong (2001) explained the discrepancies between the experimental and theoretical results for microgravity droplet evaporation. All the experiments for microgravity droplet evaporation, such as Ristau et al (1993), were conducted in a hot furnace with the droplet suspended by a fibre. The authors proposed that the

discrepancies came from ignoring the heat conduction into the droplet through the fibre and the liquid phase absorption of radiation from the furnace wall. The model developed by the authors took into account the previous two effects. The results of this model showed a good agreement between experimental and theoretical results. Radiative absorption and fibre conduction enhanced the droplet evaporation rate significantly. At temperature of 470 K, the discrepancies are mainly due to the additional fibre conduction, while at a high temperature of 750 K, the liquid phase radiative absorption was mainly responsible for the discrepancy.

Sazhin et al (2001b) analysed the evaporation and ignition of liquid droplets in monodisperse sprays in the presence of convective and radiative heat exchanges with the surrounding hot gas. The radiative exchange between fuel droplets and hot gas was described using P-1 approximation and Marshak boundary condition (Marshak, 1947) at droplet's surfaces. As in the paper by Goldfarb et al (1999) droplets were assumed to be opaque grey spheres. The authors found a reasonably good agreement between analytical results and the results predicted by the CFD package VECTIS.

The grey medium approach for droplets, used in Goldfarb et al (1999) can lead to noticeable errors both in estimated absorption and scattering of thermal radiation, emitted in a non-isothermal enclosure, and in the integral thermal radiation flux to combustion chamber walls. These errors are related to the fact that fuel droplets absorb and scatter thermal radiation from the high temperature regions of the engine, and the spectrum of the incident radiation turns out to be considerably different from the blackbody one at local temperature (Dombrovsky et al, 2003). Dombrovsky (2000) suggested a new differential approximation for radiation heat transfer in a semi-transparent particle (droplet) called MDP_0 (modified DP_0). This approximation is much simpler than the solution of the general radiation transfer equation.

Dombrovsky et al (2001) developed a simple analytical expression to approximate absorption and transport spectral efficiency factors for spherical semi-transparent droplets. These expressions were used for calculation of the average (over wavelength in a given range) absorption and transport coefficients. These were applied to the modelling of the thermal radiation transfer in diesel engines in the presence of liquid fuel droplets. When particles (droplets) of different size are present in the medium the general equation of transfer of a non-polarized thermal radiation at position R along the s -direction can be written as (Dombrovsky et al, 2001):

$$\Omega\nabla I_\lambda(R,\Omega)+a_{\lambda(ext)}I_\lambda(R,\Omega)=\sum_i\frac{\sigma^i_{s\lambda(d)}}{4\pi}\int I_\lambda(R,\Omega)f_i(\Omega,\Omega')d\Omega'+a_{\lambda(gas)}B_\lambda(T_g)$$

$$+\sum_i a^i_{\lambda(d)}B_\lambda(T_i) \qquad (2.2.2.1)$$

where $I_\lambda = I_\lambda(\lambda, s, \Omega)$ is the spectral intensity of radiation in the unit solid angle Ω, $a_{\lambda(gas)}$ is the spectral absorption coefficient of the gas per unit volume, $a^i_{\lambda(d)}$ and $\sigma^i_{s\lambda(d)}$ are spectral absorption and scattering coefficients of the ith droplet per unit volume, $a_{\lambda(ext)} = a_{\lambda(gas)} + \Sigma(a^i_{\lambda(d)} + \sigma^i_{s\lambda(d)})$ is the spectral extinction coefficient, f_i is the scattering phase function of the ith droplet, $B_\lambda(T_{g(i)})$ is the Planck function defined as (Incropera and DeWitt, 2002):

$$B_\lambda(T_g)=\frac{C_1}{\lambda^5[\exp(C_2/(\lambda T_{g(i)})-1]}, \qquad (2.2.2.2)$$

$C_1 = 3.742\times10^8\ \mathrm{W\mu m^2}$, $C_2 = 1.439\times10^4\ \mu\mathrm{mK}$. When deriving Equation (2.2.2.1) it was assumed that the spectral density of the radiation of the medium and droplets is that of a black body. The scattering phase function f_i can be presented as a sum of isotropic component and forward scattering (Dombrovsky, 1996b):

$$f_i(\mu_0)=(1-\mu_i)+4\pi\mu_i\delta(1-\mu_0), \qquad (2.2.2.3)$$

where $\mu_0 = \Omega\Omega'$ and $\mu_i = \frac{1}{4\pi}\int(\Omega\Omega')f_i(\Omega\Omega')d\Omega'$.

The first term in Equation (2.2.2.1) describes the variation of the spectral radiation intensity in direction Ω. The second term takes into account extinction of radiation by absorption and scattering in other directions. The third term takes into account the scattering of the radiation from other directions. The fourth and fifth terms take into account the radiation of the medium (Dombrovsky, 1996a; b). Using the P-1 approximation, introducing the radiation temperature (θ_R) and taking into account the contribution of droplets, Equation (2.1.1) can be generalised to (Sazhin et al, 1996; Dombrovsky et al, 2001):

$$\frac{1}{3}\nabla\frac{1}{\bar{a}_{tr}}\nabla\theta_R^4+\bar{a}_g(T_g^4-\theta_R^4)+\sum\bar{a}_i(T_d^4-\theta_R^4)=0, \qquad (2.2.2.4)$$

where $\theta_R^4=\frac{1}{4\sigma}\int_{\lambda_1}^{\lambda_2}I_\lambda^0 d\lambda$, $I_\lambda^0(R)=\int I_\lambda(R,\Omega)d\Omega$, σ is Stefan-Boltzmann constant, $\bar{a}_i, \bar{a}_g$ and $\bar{a}_{tr}$ are average absorption coefficient of droplets, average absorption coefficient of gas and average transport extinction coefficient of the medium, respectively. In the limit

of optically thick gas ($\bar{a}_g \to \infty$) Equation (2.2.2.4) predicts $\theta_R = T_g$. The summation is over all droplets in a unit volume. To find the distribution of θ_R based on Equation (2.2.2.4) the values of droplet absorption coefficient $a^i_{\lambda(d)}$ and transport scattering coefficient $\sigma^i_{s\lambda(d)}$ have to be calculated. They can be related to droplet radii (R_{di}), absorption efficiency factor $Q_{ai\,(\lambda)}$ and transport scattering efficiency factor $Q^{tr}_{si(\lambda)}$ via the equation:

$$\left\{a^i_{\lambda(d)}, \sigma^i_{s\lambda(d)}\right\} = \frac{\pi R^2_{di}}{V}\left\{Q_{ai(\lambda)}, Q^{tr}_{si(\lambda)}\right\} \tag{2.2.2.5}$$

For individual droplets the authors approximated $Q_{ai(\lambda)}$ and $Q^{tr}_{si(\lambda)}$ as:

$$Q_{ai(\lambda)} = 1 - \exp(-2\tau_i) \tag{2.2.2.6}$$

$$Q^{tr}_{si(\lambda)} = A\left(\frac{10}{x_i}\right)^q, \tag{2.2.2.7}$$

where $\tau = 2\kappa x_i$ is the optical thickness of liquid droplets, $x_i = 2\pi R_{di}/\lambda$ is the diffraction parameter of droplets, and $A = 1\text{-}\kappa^{0.13}$ and $q = 4/(\log_{10}\kappa)^2[1+2(1.5\text{-}n)\exp(-200\kappa)]$. The average value of the droplet absorption coefficient ($\bar{a}_i$) was presented as (Dombrovsky et al, 2001):

$$\bar{a}_i = \frac{\pi R^2_{di}}{V}\Lambda, \tag{2.2.2.8}$$

where

$$\Lambda = 1 - \frac{\int_{\lambda_1}^{\lambda_2} \frac{\exp(-2a_\lambda R_{di})}{\lambda^5[\exp(C_2/(\lambda T_g)) - 1]} d\lambda}{\int_{\lambda_1}^{\lambda_2} \frac{d\lambda}{\lambda^5[\exp(C_2/(\lambda T_g)) - 1]}}, \tag{2.2.2.9}$$

the coefficient C_1 and C_2 are the same as in Equation (2.2.2.2)and $a_\lambda = 4\pi\kappa_\lambda/\lambda$.

Having substituted Equations (2.2.2.6) and (2.2.2.7) into Equation (2.2.2.9) and using the experimentally measured values of κ_λ in the ranges of λ: 0.2 – 1.1 and 2-6 □m, Dombrovsky et al (2001) found a simple analytical approximation of Λ for diesel fuel droplets with radii in the range 5- 50 μm and external temperature in the range 1000-3000K:

$$\Lambda_0 = aR^b_d \tag{2.2.2.10}$$

where $a = 0.095268 - 0.049415(T_g/1000) - 0.0072018(T_{gt}/1000)^2$,

$b = 0.38947 + 0.13089(T_g/1000) - 0.014647(T_g/1000)^2$, for unboiled white diesel fuel, R_d is in μm. It was assumed that gas was optically thick and $\theta_R = T_g$.

Equation (2.2.2.10) was implemented into research version of VECTIS CFD code of Ricardo Consulting Engineers with the P-1 thermal radiation model. It was shown that the effect of thermal radiation on heating and evaporation of realistic semi-transparent diesel fuel droplets is considerably smaller when compared with the case when droplets are approximated as black opaque spheres (Dombrovsky et al, 2001; Sazhin et al, 2002).

Dombrovsky et al (2003) studied experimentally the absorption spectra of several types of diesel fuel. The measurements were taken for diesel fuel used in cars (white) and diesel fuel used in off-road equipment in which dye was added for legislative purposes (red). Similar measurements were repeated for these diesel fuels after they had undergone a simulation of ageing process by prolonged boiling for six hours. The index of absorption of diesel fuels was measured in the ranges 0.2-1.1 and 2-6 μm. The linear interpolation of the values of index of absorption in the range 1.1-2 was used due to the absence of the measured data in this range. The index of refraction of diesel fuel $n(\lambda)$ was calculated by using the so called subtractive Kramers-Kronig analysis based on the equation:

$$n(\lambda) = n(\lambda_1) + \frac{2(\lambda_1^2-\lambda^2)}{\pi}\left[\int_{\lambda_{min}}^{\lambda_1-\delta} f(\lambda,\lambda')d\lambda' + \int_{\lambda_1+\delta}^{\lambda-\delta} f(\lambda,\lambda')d\lambda' + \int_{\lambda+\delta}^{\lambda_{max}} f(\lambda,\lambda')d\lambda'\right] + O(\delta), \quad (2.2.2.11)$$

where

$f(\lambda,\lambda') = \frac{\lambda'\kappa(\lambda')}{(\lambda^2-\lambda'^2)(\lambda_1^2-\lambda'^2)}$, δ is a small parameter, $n(\lambda_1)$ is the measured value of refractive index at a certain wavelength λ_1, and λ_{min} and λ_{max} are determined by the location of main absorption bands in the spectrum (λ_{min}=0.2 μm and λ_{max}=6 μm). The authors used the following approximation for absorption efficiency factor Q_a and the transport efficiency factor of scattering Q_s^{tr} (Dombrovsky, 2002):

$$Q_a = 4n/(n+1)^2\,[1-\exp(-4\kappa x)] \quad (2.2.2.12)$$

$$Q_s^{tr} = \begin{cases} C\xi & \text{when } \xi \le 1 \\ C/\xi^{\gamma} & \text{when } \xi > 1, \end{cases} \quad (2.2.2.13)$$

where $C = 1.5n(n-1)\exp(-15\kappa)$, $\gamma = 1.4 - \exp(-80\kappa)$, $\xi = 0.4(n-1)x$.

These equations give slightly better approximation for Q_a and Q_s^{tr} for droplet radii under consideration over the whole spectrum when compared with those given Equations

(2.2.2.6) and (2.2.2.7). It was shown that the index of refraction depends only slightly on the type of fuel and this dependence can be safely ignored in the calculation of absorption and scattering of thermal radiation by fuel droplets. For the calculations it was assumed that n (λ_1) = 1.46 for all four types of fuel. The measurements showed that the peaks of absorption practically coincide for all types of diesel fuels but there is a noticeable difference between them in the regions away from absorption peaks at $\lambda \approx 3.5$ μm. The study also showed that the absorption of the boiled diesel fuel in the ultraviolet-near infrared range is noticeably larger than that of the unboiled fuels. Their calculations were performed in the range $0.5 < \lambda < 6$ μm and droplet radii were taken in the range $5 < R_d < 50$ μm, which are realistic values for radiation heat transfer in diesel engines. They showed that the influence of the type of fuel on the values of the absorption efficiency factor Q_a and transport extinction efficiency factor Q_{tr} is strong in the range of semi-transparency ($\lambda < 2$ μm, λ close to 2.8 and 5 μm). Except near the absorption peaks, the scattering of radiation dominates over absorption. This indicates the importance of taking into account the scattering of radiation by fuel droplets in radiation heat transfer calculations in diesel engines. By comparing the calculations for polydisperse and monodisperse sprays, it was shown that the monodisperse approximation is applicable for the analysis of infrared radiative properties of realistic polydisperse diesel fuel sprays. Using the P-1 approximation and the expression for the average absorption efficiency factor $\overline{Q}_{ai}$ the droplet temperature (T_d) can be found from the equation (Sazhin et al, 2002):

$$\frac{dT_d}{dt} = \frac{3\sigma}{\rho_l c_l R_d} \overline{Q}_{ai} (\theta_R^4 - T_d^4). \qquad (2.2.2.14)$$

Variation of droplet temperature with radius inside droplets is ignored in Equation (2.2.2.14).

Dombrovsky (2002b) developed an approximate model called a wide band model (box model) with constant coefficients of absorption and extinction in each spectral band. This approximation reduces computational time by approximately three orders of magnitude in comparison with the detailed spectral calculation. This model used the approximations of absorption efficiency factor Q_a and the transport efficiency factor of scattering Q_s^{tr} by Equations (2.2.2.12) and (2.2.2.13). The spectral range was divided into seven bands with constant coefficients of absorption and extinction in each band. The comparison of the prediction of this model with the results of Mie calculations for

the conditions of diesel engine, showed that the seven bands model is rather accurate whereas the grey model, developed by Dombrovsky et al (2001), can overestimate significantly the radiation absorbed and scattered by fuel droplets and gives too low values of radiation flux to the cylinder head at small crank angles. The errors introduced by the gray approximation are related to the fact that fuel droplets absorb and scatter thermal radiation from the high temperature regions of the engine, and the spectrum of the incident radiation turns out to be considerably different from the blackbody one at local temperature (Dombrovsky et al, 2003).

Dombrovsky and Sazhin (2003b) developed a simple analytical approximation for normalised absorbed radiation power inside droplets assuming that the geometrical optics approximation is valid. When the droplet's thermal radiation could be ignored, the radiation transfer equation in a spherical droplet was presented as (Siegel and Howell, 1992):

$$\mu\frac{\partial I_\lambda}{\partial R}+\frac{1-\mu^2}{R}\frac{\partial I_\lambda}{\partial \mu}+a_{\lambda(d)}I_\lambda=0 \qquad (2.2.2.15)$$

where μ = cos θ (θ is measured from the R- direction). As the solution of Equation (2.2.2.15) is rather difficult, the authors used the simplified MDP_0 approximation (Domrovsky, 2000; 2002b). In this approximation it was assumed that in the droplet core ($R \le R_* \equiv R_d/n$) radiation intensity is constant in the angular ranges $-1 < \mu \le 0$ and $0 < \mu \le 1$. At the droplet periphery ($R_* < R \le R_d$) however, constant values of the radiation intensity were assumed only when $-1 \le \mu < -\mu_*$ and $\mu_* < \mu \le 1$, where $\mu_* = \sqrt{1-(R_*/R)^2}$. Outside of this range it was zero.

The radiation power absorbed per unit volume inside the droplet was estimated as:

$$P(R)=\frac{0.75}{R_d}\int_0^\infty Q_a w(R) I_\lambda^{0(ext)} d\lambda, \qquad (2.2.2.16)$$

where

$$w(R)=p_\lambda(R)\Big/\left[\frac{3}{R_d^3}\int_0^{R_d} p_\lambda(R)R^2 dR\right], \qquad (2.2.2.17)$$

$I_\lambda^{0(ext)}=\int_{-1}^{1} I_\lambda^{0(ext)}(\mu)d\mu$, $p_\lambda(R)=a_\lambda I_\lambda^0(R)$ and $I_\lambda^0(R)=\int_{-1}^{1} I_\lambda^0(R,\mu)d\mu$. Q_a is the same as in Equation (2.2.2.12). Equation (2.2.2.17) was simplified to (Dombrovsky and Sazhin, 2003b):

$$w(r)=\frac{[1-u_*\theta(r-1/n)](r^2+\bar{\gamma})}{[0.6(1-u_c^5)-u_c^3/n^2]+\bar{\gamma}(1-u_c^3)}, \qquad (2.2.2.18)$$

where $\bar{\gamma}=(1.5/\tau_0^2)-(0.6/n^2)$, $u_*=\sqrt{1-\left(\frac{1}{nr}\right)^2}$, $u_c=\sqrt{1-\left(\frac{1}{n}\right)^2}$,

$\tau_0=a_\lambda R_d=4\pi\kappa R_d/\lambda$, $\theta(x)=\begin{cases}0 & \text{when} \quad x<0\\ 1 & \text{when} \quad x\geq 0\end{cases}$

and

$$w(\tau)=\frac{\xi^2\tau_0^3}{3}\frac{\exp[-\xi(\tau_0-\tau)]}{\tau_0(\xi\tau_0-2)+(2/\xi)[1-\exp(-\xi\tau_0]}, \qquad (2.2.2.19)$$

where $\xi=2/(1+u_c)$. Equation (2.2.2.18) was used when $\tau_0<n\sqrt{2.5}$; otherwise Equation (2.2.2.19) was used. The power absorbed in the droplet core was shown to be rather large and almost homogeneous. Also, the absorbed power is large in the vicinity of the droplet surface, but is minimal in the intermediate region.

Dombrovsky and Sazhin (2004) developed a theoretical model of thermal radiation absorption in semi-transparent droplets at the surface and inside a fuel spray taking into account asymmetry of droplet illumination. Its results showed that the absorption of thermal radiation is inhomogeneous inside the droplet. The results also showed that, as in the case of symmetrical droplet illumination (Dombrovsky and Sazhin, 2003b), an increased absorption of thermal radiation in the central area of the droplet ($R\approx 0.65R_d$) and in a thin layer near the surface of the droplet at its illuminated side is predicted.

Liu et al (2002) studied the transient coupled radiation-conduction in a semitransparent spherical particle surrounded by isothermal black walls. The energy equation for transient coupled radiative and conductive heat transfer in a semitransparent particle was given by:

$$\rho_l c_l\frac{\partial T(R,t)}{\partial t}=\frac{k_l}{R^2}\frac{\partial}{\partial R}\left[R^2\frac{\partial T(R,t)}{\partial R}\right]+S(R,t) \qquad (2.2.2.20)$$

where $S(R, t)$ is the radiative heat source. The radiative heat source term was calculated by the radiative transfer coefficient and the transient energy equation was solved by an implicit finite difference method. They obtained the radiative transfer coefficients by using the ray tracing method (tracing an incident ray from the surroundings through the particle) with Hottel and Sarofim's zonal method (Hottel and Sarofim, 1967). The authors based their analysis on the assumptions that the space between the particle and the wall is filled by a vacuum. Hence convection heat transfer to the particle from the

surroundings is neglected. The particle emits and absorbs thermal radiation; the temperature dependence of density, specific heat and the thermal conductivity of the particle can be neglected. The results show that when the size parameter x ($x = 2\pi R_d / \lambda$) of the particle is greater than 30, the results of the ray tracing method is close to that of Mie theory, and the Mie theory can be approximated accurately with the geometrical optics if the size parameter of the particle is greater than 400. The results also show that the radial radiative heat source reaches its peak in the interior shell of the particle with small optical thickness. This phenomenon might result in the internal burst or overheating during radiant heating because the interior of particle is the first to reach the phase change temperature and undergoes phase change or overheating. For the particle or droplet with small optical thickness ($x < 1$), the particle inner temperature is larger than its surface temperature.

From the above analysis I can conclude that a number of algorithms for calculation of absorption of thermal radiation inside fuel droplets have been discussed in many reviews. It is also shown that the algorithm suggested by Dombrovsky and Sazhin (2003b) was effectively reduced to a simple analytical approximation to calculate the absorbed radiation power inside droplets. The calculations require the knowledge of the spectral optical properties of the liquid fuel: index of absorption and refractive index. The former was measured experimentally for diesel fuel in the ranges 0.2-1.1 and 2-6 μm, while the latter was calculated from the measured index of absorption using the subtractive Kramers-Kröing analysis (Ahrenkil, 1971).

2.3 Modelling of the processes in diesel engines

Computational fluid dynamics (CFD) has become an essential tool for the design and understanding of practical combustion systems. Multidimensional CFD simulations have achieved a reduction in the need for physical experimentation, the benefit of which has been a reduction in product development time and cost.

The internal combustion engine represents one of the most challenging problems to model because the turbulent flow is compressible with large density variations. There are large spatial gradients and cyclic time dependence (Reitz and Rutland, 1995).

The main events that occur during the diesel combustion were identified more than 70 years ago (Ricardo, 1930). Since that time a number of mathematical models of the combustion process have been suggested and, with varying degrees of success, used to understand the relative importance of the various phenomena involved. However, a

universally accepted model does not yet exist and the development of a predictive method for diesel combustion remains one of the most difficult tasks facing automotive researchers. There are a number of reasons for this. Firstly, many individual processes, including air motion, fuel spray dynamics and evaporation, turbulent mixing, relatively low gas temperature preceding autoignition, and high gas temperature during combustion are quite important and cannot be ignored for a realistic model. Secondly, the mechanism governing many of these phenomena, such as atomisation and detailed chemistry, are either poorly understood or too complicated to be incorporated into a comprehensive model. Finally, it is only in recent years that the computing power required for solving the equations resulting from detailed modelling has become generally available (Johns, 1990).

The studies in the simulation of the processes in diesel engine can be divided to two broad categories. The first one refers to the models, which deal with individual processes in diesel engine (e.g. heating, evaporation, break-up, etc). The second one refers to the multidimensional CFD simulation which employs the CFD codes (e.g. VECTIS, KIVA, STAR-CD, etc) to simulate most of the processes in diesel engine.

For the first category, Hiroyasu et al (1980) studied the spray characteristic in diesel engines. Spray penetration, spray angle, droplet size, vaporization rate, and ignition delay were measured in a constant volume chamber with several injection and ambient conditions. The authors expressed most of their measured data in empirical correlations providing benchmarking tool for numerical simulation of diesel engine combustion. The results showed that the spray tip penetration decreased with increasing the ambient gas pressure while the spray angle increased. Both spray tip penetration and spray angle were increased with increasing the injection pressure. The spray angle decreased with increasing the ambient gas temperature while its effect on spray tip penetration is insignificant. The experimental studies of the droplet sizes and distributions showed that higher injection pressure produces smaller droplets due to the increase in the velocity of discharge. The results also showed that the more small droplets are in the periphery of the spray and the Sauter mean diameter increased with the increasing in ambient gas pressure. Increasing the amount of fuel injection increases the droplet diameter because of the high probability of coalescence among the neighbouring droplets. The results of studying the vaporization of fuel droplets showed that the droplet bulb temperature rose with increasing ambient pressure and temperature and the evaporation rates increased with increasing the gas temperature at all gas pressures. Large expansion due to liquid

density being dependent on temperature causes the size of the droplet to exceed its initial size. This is especially pronounced for slow evaporation. The results of studying the ignition delay of fuel spray showed that the injection conditions produced a minor effect on the ignition delay compared with the effect of gas conditions. Ignition delay increased with an increase in the amount of fuel injected, which was significant at low gas temperatures. The results also showed that ignition delay was independent of nozzle opening pressure and nozzle orifice diameter.

Papageorgakis and Assanis (1996) developed a spray break-up model under low injection pressure. The authors obtained the internal pressure inside the droplet by solving the momentum equation inside it assuming the flow inside the droplet is potential and axisymmetric. When the surface of the droplet is slightly perturbed from its equilibrium position, the difference between the internal and external pressure forces acting on the droplet surface due to the internal liquid field and the aerodynamic force respectively is balanced by the pressure force due to surface tension. The authors assumed that the break-up process occurs when the radial displacement of the distorted droplet at the flow direction exceeds 8% of the radius of the undistorted spherical droplet. This break-up model was implemented in KIVA3 code and was tested based on 2-D axisymmetric simulation studies. The results showed that increasing the injection velocity leads to increase turbulent dispersion, increase spray cone angle and decrease the droplets size. For a given axial distance from the nozzle, the droplets are decelerated and decrease in size with increasing radial distance from the injector tip. Bazari (1992) formulated and developed a model for the prediction of combustion and exhaust emission of DI diesel engines. This model took into consideration details of fuel spray formation, droplet evaporation, air-fuel mixing, spray wall interaction, swirl heat transfer, self-ignition and rate of reaction. The emissions model was based on chemical equilibrium, as well as the kinetics of fuel, carbon monoxide, NO, and soot production in order to calculate the pollutant concentrations at each point in the cylinder. In this model, injection was characterised as intermittent parcel of fuel being injected through the nozzle, at a given time step. The injected fuel was distributed within the spray angle. This angle was unique to each spray parcel and varied, albeit not significantly, from one time step to the next. The author calculated the delay period time τ_z using the formula (Nishida and Hiroyasu, 1989):

$$\tau_z = 0.004.p_{cyl}^{-2.5}.\phi_z^{1.04}.\exp(6000.0/T_{cyl}) \qquad (2.3.1)$$

where p_{cyl} is in-cylinder pressure, T_{cyl} is its temperature and ϕ_z is crank angle. In this model the heat transfer from each zone was calculated taking into account both carbon (soot) radiation and convection.

Gogos et al (2003) developed an axisymmetric numerical model to study single droplet evaporation over a wide range of ambient pressure under normal and microgravity conditions. The mass, momentum, species and energy equations were solved using the finite volume method. The model was applied to *n*-hexane droplet evaporating within a high-pressure nitrogen environment. The results showed that the droplet lifetime decrease with increasing ambient pressure under normal gravity more significantly than under microgravity due to increase the effect of natural convection heat transfer. Under the normal gravity conditions, increasing ambient pressure increased the droplet surface temperature and the evaporation constant with time due to the same reason. Comparison of the results with experimental results of Matlosz et al (1972) and Nomura et al (1997) showed that the discrepancy can be attributed to the heat conduction along the wire supported the droplet and the droplet movement, in theoretical model. Hohmann and Renz (2003) studied the numerical simulation of the vaporization of an unsteady fuel spray at high ambient temperature and pressure solving the appropriate conservation equations. The author studied the effects of high ambient pressure on the vaporization motion of the diesel fuel droplet. They showed that the droplet thermal conductivity and its diffusion coefficient have to be multiplied by the correction factor χ, which is defined in Equation (2.2.1.1.1) to take into account the circulation inside the droplet in modelling its vaporization process. The results showed that for higher Biot number (the ratio of droplet internal thermal resistance to its boundary layer thermal resistance) the temperature gradient inside the droplet is significant. This effect was pronounced in high gas temperature and pressure because the gaseous thermal conductivity increases with temperature while the liquid thermal conductivity decreases with temperature. The results also showed that modelling the physical processes within the spray in diesel engine, such as primary and secondary break-up, droplet collision and coagulation, exchange of momentum and heat and mass transfer with the surrounding gas have a more pronounced influence on the droplet diameter than modelling droplet vaporization process.

As CFD studies, Amsden et al (1985) developed KIVA2 CFD code, which solved the equations of transient, two and three-dimensional, chemically reactive fluid flow with sprays. The equations solved in KIVA2 can be applied to laminar or turbulent flows,

subsonic or supersonic flows, and single-phase or dispersed two-phase flows. Evaporating liquid sprays are represented by a discrete-particle technique (Dukowicz, 1980) in which each particle represents a number of droplets of identical size, velocity, and temperature. The particles and fluid interact by exchanging mass, momentum, and energy. Droplet collisions and coalescence are accounted for (O'Rourke, 1981) and a TAB break up model is used for droplet aerodynamic breakup (O'Rourke, 1987). The number of species and chemical reactions that can be accounted for in KIVA 2 are arbitrary; they are limited only by computer time and storage considerations. The code distinguishes between slow reactions, which proceed kinetically, and fast reactions, which are assumed to be in equilibrium (Ramshaw, 1980). Two models are available to represent the effects of turbulence; a standard version of the k-ε turbulence model (Launder and Spalding, 1972) and a modified version of subgrid scale (SGS) turbulence model of KIVA (Amsden et al, 1985). The SGS model reduces to the k-ε mode near walls where all turbulence length scales are too small to be resolved by the computational mesh. KIVA2 CFD code was modified in KIVA3 (Amsden, 1993) where the grid generator extended to create more complicated grid for internal combustion engines. In this version a block-structured mesh was adopted, and the program became able to modeling geometries containing inlet and outlet ports in the cylinder wall. This development was driven by an interest in crankcase-scavenged 2-stroke engines. A new version of KIVA called KIVA 3V (Amsden, 1997) was released in 1997. In this version it was allowed to simulate the intake and exhaust valves in internal combustion engines where the grid generator was extended to support the generation of grids for valves, valve ports and runners. Also in this version a particle-based liquid wall film model and a mixing-controlled turbulent combustion model were added to the code. KIVA3V is applied to studies of port injection (PFI) and direct injection, spark-ignition (DISI) or gasoline direct-injection (GDI) engines, as well as large and small bore diesel engines. In the second release of KIVA3V (Amsden, 1999) some new features were added to the code. These new features were extensions to the particle-based liquid wall film model, a split-injection option, and new features in the grid generator to enable the code to simulate more accurately the complicated combustion chambers (e.g. complex runner, helical ports and bifurcations).

Johns (1990) developed a detailed model for diesel combustion. The model consisted of three main parts. The first part was focused on the dynamics of the gas-phase, determination of the mean flow and turbulence field. The second part was focused on the

dynamics; heat and mass transfer of the fuel spray. The third part was focused on the transport, mixing and chemical reaction, which determined the composition and temperature fields. The model based on solving equations for the composition joint probability density function (pdf) and the associated temperature pdf were developed. The joint pdf described the diesel combustion process. This model predicted that halving the droplet size reduced the ignition delay (the delay time between the start of injection and ignition) by 30%, where as the ignition delay was insensitive to an artificial reduction in fuel vapour pressure. The higher momentum exchange rate associated with the smaller droplet size produced faster mixing and the ignition delay was controlled by the rate of mixing.

Reitz and Rutland (1995) described the development and validation of computational fluid dynamic (CFD) models for diesel engine combustion and emissions. Their work consisted of two parts. The first part described the experimental study and the second part described the CFD study using the KIVA code (Amsden et al, 1985 and Amsden et al, 1987). The authors used KIVA3 for simulating the intake flow process in realistic engine geometry and moving valves of Caterpillar engine. They also used KIVA2 for modelling combustion and emissions, and the initial flow turbulence conditions at intake valve closure. The authors replaced TAB break–up model, which was originally implemented in KIVA with 'wave' break-up model (Reitz, 1987). They implemented into KIVA a spray wall impingement model in which the impact drop on the heated surface may lead to instantaneous break-up, sudden vaporization, or to developing a thin liquid film on the surface, or to sliding or rebounding of a highly distorted drop. The author also used the autoignition Shell model to predict the fuel ignition delay time and Zeldovich mechanism (Heywood, 1976) to describe nitric oxide (NO_x) formation. Good agreement between computed and measured cylinder pressure and apparent heat release rate were obtained. These models allowed good quantitative predictions of soot and NO_x emissions.

Ayoub and Reitz (1997) used an improved version of the multidimensional CFD code, KIVA2 (Amsden et al, 1985; Amsden et al, 1987 ; Amsden et al, 1992) to study the effects of multicomponent fuel vaporization on diesel engine ignition under cold-starting conditions and the parameters that influence this phenomenon. This model was applied to simulate cold starting in diesel engines. It took into account the effects of fuel residual left from previous cycles, injection timing, and its duration. In the droplet vaporization submodel, the authors assumed that droplets were spherically symmetric, pressure was

spatially uniform around the droplet, the gas-liquid interface was in thermodynamic equilibrium and gas was dissolved in a very thin liquid surface layer (i.e. gas does not diffuse into the droplet interior). The phenomenon of internal circulation of the liquid within the droplet was taken into account as internal mixing enhanced the processes of heat and mass transfer inside the droplet. The model artificially increased the heat and mass diffusivity, depending on mixing parameters. The diffusivity was increased by a factor C (Jin and Borman; 1985):

$$C = \begin{cases} 2.685 + \dfrac{3.02514\times10^{-3}}{1.9868\times10^{-3} + (D_{12}t/R_d^2)} & \text{for } \; 4\times10^{-3} \le \dfrac{D_{12}t}{R_d^2} \le 1 \\ 2.685 & \text{for } \; \dfrac{D_{12}t}{R_d^2} \ge 1 \end{cases}, \qquad (2.3.2)$$

where t is the drop lifetime and D_{12} is the binary liquid diffusivity. In the spray sub-model they assumed that the drop parcels were injected with characteristic size equal to the nozzle exit diameter. The subsequent break-up of the parcels containing parent drop of radius R_{da} was computed by assuming that the break-up process produced children drops with $R_d = B_0\lambda$ and break-up time was $t = 3.726\ B_1\ R_{da}/\lambda\vartheta$, where λ is wavelength and ϑ is wave growth rate. Drop size constant B_0 and break up time constant B_1 were related to the initial distribution of fuel droplets. The autoignition process was modelled using the Shell autoignition model. The results of this work showed that advancing injection timing improved ignition under cold-starting condition. Also the presence of a small amount of vapour fuel residual in the combustion chamber enhanced ignition and combustion. Lower injection velocity and the larger droplets reduced the amount of vaporized fuel. When the ambient air intake temperature was reduced from 273 to 254 K the onset of ignition was delayed and there was very little combustion. Finally, the study showed that split injection improved cold starting in diesel engines. In this case, a small fraction of fuel was injected early in the compression stroke to help ignition. In the same way fuel residual enhanced the ignition process.

Yamane and Shimamoto (1999) used the multidimensional engine simulation code, FREC-3D (CI), to elucidate the effects of injection rate and split injection on diesel combustion, NO and soot emission. The FREC-3D (CI) code is three-dimensional computational code for compression ignition engines and was developed by Ikegami et al (1997). It calculated gas motion, turbulence, temperature and concentrations of fuel, unburned mixture and burned gas. The program took into account turbulence, spray, ignition and combustion, NO and soot. The results showed good agreement between

measured and calculated in-cylinder pressure and rate of heat release. It also showed that a high turbulence kinetic energy caused by an initial combustion stage after fuel injection, promoted the soot oxidation process.

As already mentioned, Bertoli and Migiaccio (1999) showed that the accuracy of CFD computations of heating, evaporation and combustion of diesel fuel sprays could be substantially increased if the assumption of infinite high thermal conductivity of liquid is relaxed. The authors used a modified version of the CFD KIVA2 code. They suggested that the numerical solution of the heat conduction equation inside the droplet is added to the solution of other equations in a CFD code. The authors performed some numerical tests for a combustion bomb to analyse the influence of the modified evaporation model on droplet heating, evaporation rate and droplet lifetime. The results show that this approach is expected to increase the accuracy of CFD predictions for tetradecane, n-heptane and diesel fuel. The additional computational cost of this approach might be too high for practical applications. Also the authors did not take into account the effects of thermal radiation on heating and evaporation of fuel droplets.

Sazhina et al (2000) applied the Shell autoignition model to modelling the ignition process in a realistic diesel engine polydisperse spray. The analysis was based on the computational fluid dynamics (CFD) code VECTIS of Ricardo Consulting Engineers. The Shell autoignition model (Halstead et al, 1977) was originally designed to simulate the self-ignition properties of hydrocarbon fuels and to analyse the knock phenomenon as a self-ignition of a compressed mixture in the end-of-gas charge in spark-ignition gasoline engines. It was extended to modelling the autoignition of heavier hydrocarbons in diesel engines (Theobald, 1986; Kong et al, 1996; Sazhina et al, 1999). The authors took the value of pre-exponential factor in the rate of production of the intermediate agent in the range between $A_{f4} = 3\times10^6$ and $A_{f4} = 6\times10^6$. They studied two cases; the first was the modelling of *n*-dodecane ignition for an idealized case of premixed air-fuel mixture and the second was the modelling of the ignition of a monodisperse spray. The results showed that the total ignition delay for droplets at the periphery of a monodisperse spray was less than in its core. Hence, ignition of the spray was expected to start at its periphery. The chemical ignition delay was shown to decrease with the increase of the initial temperature in the range of temperatures from 700 K to 950 K at both pressures for *n*-dodecane. For a monodisperse spray with droplet with initial radii about or greater than 6 μm the chemical ignition delay is smaller than the physical ignition delay. The latter resulted from droplet transit time, atomisation, heating,

evaporation and mixing. The opposite took place for smaller droplets with the initial radii about or less than 2.5 μm. The results also showed that the ignition process started in one point or simultaneously in several points (nuclei) at the periphery of the spray, and spread over the combustible charge during about 7 CA. The physical ignition delay was shown to dominate over the chemical ignition delay in agreement with the prediction by Sazhina et al (1999).

Hamosfakidis and Reitz (2003) studied the ignition delay time for diesel fuel using the Shell autoignition model in KIVA3V CFD code. The study was performed for a range of conditions representative diesel engine conditions including: equivalence ration from 0.5 to 4.0, initial pressures from 4 MPa to12 MPa, initial temperatures from 650 K to 1175 K and EGR percentages from 0 to 75%. The relative error for the ignition delay times over the entire range of conditions was shown about 11.0 %. It was also shown that good agreement with measured data was achieved for long ignition delay cases where effects due to spray, vaporization and mixing were expected to be less important than chemistry effects. However, discrepancies were noted in comparisons with engine data for short ignition delay cases. The author thought that these might be introduced by other submodels that describe the vaporization and mixing processes.

As shown above, most of research studied for engine simulations are based on KIVA CFD code although there are other codes for engine simulations (e.g. FIRE (FIRE 5.1, 1993), Star-CD (Bai and Gosman, 1995), and VECTIS (Ricardo Software, 2002)). This is because the KIVA source code is available for wide academic community while the sources of commercial codes are confidential. This allows for better dissemination of results to future collaborators. The success of an engine CFD code depends on validity of its submodels. Thus, it is essential to have access to source code, like KIVA, especially for a research program focused on model development, implementation, and validation. So my CFD part of the thesis will be developed using KIVA CFD code.

2.4 Conclusions of Chapter 2

As follows from the analysis of the literature review, a considerable progress has been achieved in developing models of droplet convective and radiative heating. At the same time these models still have gaps which need to be filled before they can be recommended for implementation in CFD codes for engineering applications. Some of these gaps are summarised below:

1) The model for radiation absorption in droplets suggested by Dombrovsky et al (2001) was based on limited ranges of droplet diameters and gas temperatures and just for one type of diesel fuel. The measurements of the spectral index of absorption for four types of diesel fuel reported by Dombrovsky et al (2003) was performed in the spectral ranges 0.2 μm -1.1 μm and 2 μm -6 μm but not in the range 1.1 μm-2 μm. The latter range is particularly important as it corresponds to maximal intensities of thermal radiation in the range of temperature 1119-2635 K, as follows from Wien's law. This range is perhaps the most important for applications in diesel engines and the absence of these data was regrettable.
2) To take into account the finite thermal conductivity model for transient heating of diesel fuel droplets with temperature gradient inside them. Bertoli and Migliaccio (1999) suggested that the numerical solution of the heat conduction equation inside the droplet is added to the solution of the other equations in a CFD code. Additional computational cost of this approach might be too high for practical applications. Also the authors neglected the thermal radiation effects and the recirculation inside the fuel droplets.
3) The performances of the infinite thermal conductivity model, the effective thermal conductivity model and the parabolic model (Dombrovsky and Sazhin, 2003a) have not been compared.
4) The effects of temperature gradient inside droplets and thermal radiation effects on the heating, evaporation, break-up and the ignition of fuel vapour / air mixture in diesel engines were not investigated.

The above gaps will be filled in this work.

3. RADIATIVE HEATING OF SEMI-TRANSPARENT DIESEL FUEL DROPLETS

3.1 Introduction

As mentioned in Section (2.2.2) the model suggested by Dombrovsky et al (2001), took into account the transparency of fuel droplets but its formulation is considerably simpler when compared with the previously suggested models. Detailed Mie calculations were replaced by the approximation of the absorption efficiency factor for droplets with an analytical formula aR_d^b, where R_d is the droplet radius, a and b are quadratic functions of gas temperature. Dombrovsky et al (2001) implicitly assumed that the external gas temperature, responsible for radiative heating of droplets is equal to the ambient gas temperature, responsible for their convective heating. The coefficients a and b were found based on the comparison of prediction of Equations (2.2.2.9) and (2.2.2.10) for diesel fuel droplet radii and gas temperatures in the ranges 5 - 50 μm and 1000 - 3000 K respectively.

The main objective of this chapter is to investigate the applicability of the model suggested in Dombrovsky et al (2001) for a wider range of droplet radii, external and ambient gas temperatures using more detailed measurements of spectral properties of diesel fuels. The same types of diesel fuel as in Dombrovsky et al (2003) were used. Due to experimental restrictions, the measurements reported by Dombrovsky et al (2003) were performed in the spectral ranges 0.2 μm - 1.1 μm and 2 μm - 6 μm but not in the range 1.1 μm - 2 μm. The latter range is particularly important as it corresponds to maximal intensities of thermal radiation in the range of temperatures 1449 - 2635 K, as follows from the Wien's law. This range is perhaps the most important for applications in diesel engines and the absence of data was rather regrettable. In this chapter the measurements reported in Dombrovsky et al (2003) are supplemented by the measurements in the range 1 μm - 3 μm using a new experimental technique. Hence the whole range 0.2 μm - 6 μm is covered.

The new approximation for the absorption efficiency factor is implemented into a stand-alone code designed for modelling heating and evaporation of droplets. Using this code the influence of thermal radiation on heating and evaporation of fuel droplets is investigated.

Results of the measurements of the spectral index of absorption of diesel fuels are presented and discussed in Section 3.2. In Section 3.3 the approximation of the

absorption efficiency factor by the expression aR_d^b in various ranges of droplet radii and external gas temperatures is discussed. Results of implementation of this model into our stand-alone code and analysis of the influence of thermal radiation on droplet heating and evaporation are presented and discussed in Section 3.4. The main results of the chapter are summarized in Section 3.5.

The main results of this chapter are represented in the paper by Sazhin, Abdelghaffar et al (2004a)

3.2 Optical properties of fuel

3.2.1 Measurements of index of absorption

The index of absorption of diesel fuels was measured in the ranges 0.2 μm - 1.1 μm, 1 μm - 3 μm and 2 μm – 6 μm. Ultraviolet near-infrared spectra (0.2 - 1.1 μm) were obtained using a UV-Visible spectrophotometer Shimadzu, model 1601. The spectra were recorded versus n-hexane as a background. The latter is transparent in the studied range of wavelengths. Also in this range the diesel fuels were diluted with n-hexane to prevent saturation of the peaks act in blank (background) of n-hexane. Thus the actual Ultraviolet absorbance spectrum of diesel fuels can be obtained. The average error of measurements of absorbance was about 5 %.

In the range (1 - 3) μm the index of absorption was measured using a Fourier Transform Infrared Spectrometer (Nicolet FT-IR Nexus). This spectrometer is designed to work in the mid-infrared or near infrared range. The experimental set-up used to record the fuel spectra was optimised for analysis in the near infrared range. The program used was OMNIC E.S.P. version 5.2a set in Transmission E.S.P. experimental mode. A resolution of 4 cm^{-1} was used, recording four scans in a NaCl cell with an optical path length of 0.025 mm. The background was recorded as the empty NaCl cell. The average error of measurements of absorbance was about 5 %.

Infrared spectra (2 - 6 μm) were obtained using FTIR (Fourier Transform Infrared) spectrometer Perkin Elmer 1720-X, at 4 cm^{-1} resolutions, 4 scans, in a NaCl cell with 0.011 mm optical path length. The error of measurements of absorbance was about 5 % across the whole range of wave-lengths. The lower threshold for measurements in this spectral range is higher when compared with the measurements reported in Dombrovsky et al (2001) where it was 1.39 μm. The use of conventional FT-IR spectrometers to measure absorbance beyond the mid-range infrared (approximately 2.5 μm or less) would result in large experimental errors (10 %), due to the detection limit of the

spectrometer having been reached. This may explain some of the discrepancies in the 2 - 3 μm range obtained using different techniques. The results obtained by the Nicolet FT-IR Nexus spectrometer were used in this range.

Diesel fuels have relatively high absorption below 0.4 μm, exceeding the measuring limit of the instrument. In this range, the spectrum was recorded in a 1-cm quartz cell for samples diluted with n-hexane. The latter is transparent in the studied range of wavelengths under consideration. In the ranges of 3.33 - 3.53 μm and 6.76 - 6.94 μm, where absorption of the samples exceeded the instrument measuring limit, the spectra were recorded for samples diluted with chloroform. The correction for dilution was made in both cases. All measurements were carried out at room temperature. The resulting spectra are not expected to differ, until the boiling point of the fuel is reached. After this point, it is expected that the resulting spectra will reduce by more than 50%.

Results of the measurements of the index of absorption κ are presented in Figure (3.1). The plots are shown for low sulphur ESSO AF1313 diesel fuel used in cars (white) and BP Ford reference diesel fuel used in off road equipment in which dye has been added for legislative purposes (red). Also the plots referring to these diesel fuels after they have undergone a simulation of ageing process by prolonged (six hours) boiling are shown in the same figure. Density of the white fuel was experimentally determined as 816 kg/m^3 and the boiling point in the range of 458 - 468 K, whereas density of the red fuel was experimentally determined as 827 kg/m^3 and boiling point in the range of 468 - 478 K. The density was measured at room temperature. Both parameters were measured at atmospheric pressure.

The noticeable descripency in the measured spectra at wavelengths around 1.1 μm is related to the fact that these wavelengths refere to the higher range of the UV-Visible spectrophotometer Shimadzu and to the lower range of the Fourier Transform Infrared Spectrometer (Nicolet FT-IR Nexus). In both cases the errors in the measurements are expected to be high, and it is diffucult to estimate them quantitively. The peak of the measured spectra at wavelengths around 3.4 μm is related to the presence of the OH component in all four diesel fuels.

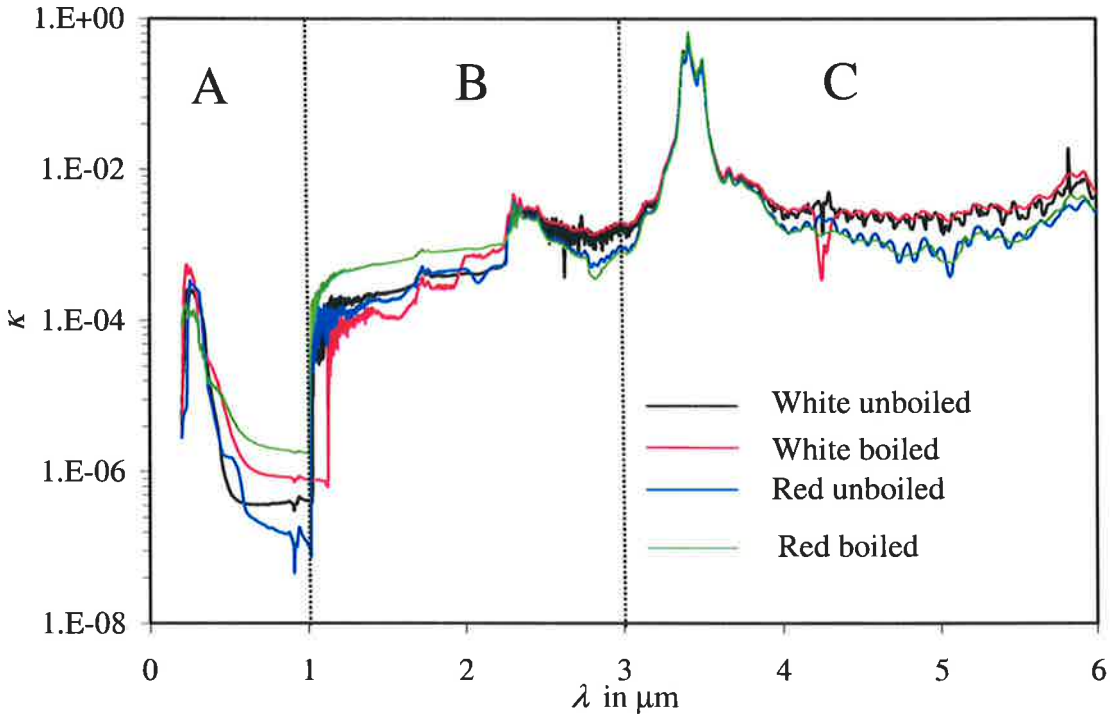

Fig. 3.1 Indices of absorption of four types of diesel fuel versus wavelength λ. White corresponds to low sulphur ESSO AF1313 diesel fuel used in cars; red corresponds to BP Ford reference diesel fuel used in off road equipment. Ranges A and C were taken from Dombrovsky et al (2001) and range B was measured experimentally.

As can be seen in Figure (3.1) the dependence of κ on the type of diesel fuel is noticeable, especially in the ranges of semi-transparency $\lambda < 3$ μm and 4 μm $< \lambda < 6$ μm. Peaks of absorption for all types of diesel fuel practically coincide. The values of κ in the ranges 0.2 μm - 1 μm and 3 μm - 6 μm coincide with those shown in Figure 3 of Dombrovsky et al (2003). The differences in the optical properties of fuels shown in Figure (3.1) are expected to be transformed in different values of the absorption efficiency factors of fuel droplets as discussed in Section 3.3.

3.2.2 Analytical presentation on index of absorption

The index of absorption for the unboiled low sulphur ESSO AF1313 diesel fuel (white unboiled) used in cars, which is shown in Figure (3.1), can be approximated by the following functions:

$$\kappa = \begin{cases} 0.00106092 \ln(\lambda) + 0.00171395 & \text{when } 0.2 \le \lambda < 0.26 \\ \exp(-29.70641403\,\lambda) \times 1.240388523 & \text{when } 0.26 \le \lambda < 0.5 \\ 10^{\zeta} & \text{when } 0.5 \le \lambda \le 1 \\ 0.0005225623501 \ln(\lambda + 5.51945445 \times 10^{-5}) & \text{when } 1 < \lambda \le 2 \\ -0.0177\lambda^3 + 0.1156\lambda^2 - 0.251\lambda + 0.1816 & \text{when } 2 < \lambda \le 2.25 \\ 10^{\zeta} & \text{when } 2.25 < \lambda \le 3.3 \\ 4.3797145 \times 10^{-26}\,\lambda^{45.427574} & \text{when } 3.3 < \lambda \le 3.4 \\ 10^{\zeta} & \text{when } 3.4 < \lambda \le 6 \end{cases} \qquad (3.2.2.1)$$

where

$\zeta = -6.4$ when $0.5 \le \lambda \le 1$

$\zeta = 11(\lambda - 2.2) - 3.4$ when $2.25 < \lambda \le 2.3$

$\zeta = 2.8\,(\lambda - 2.8)^2 - 3$ when $2.3 < \lambda \le 3.3$

$\zeta = 12.5\,(\lambda - 3.8)^2 - 2.2$ when $3.4 < \lambda \le 3.8$

$\zeta = 0.5\,[(\lambda - 4.9) / 1.1]^2 - 2.7$ when $3.8 < \lambda \le 6$

where λ is measured in μm.

Figure (3.2) shows the actually measured index of absorption versus wavelength for the unboiled low sulphur ESSO AF1313 diesel fuel and its approximation by Equation (3.2.2.1). Analytical presentation of $\kappa(\lambda)$ is convenient for practical calculations.

Table (3.1) shows the errors and CPU time requirements for the thermal radiation term calculations based on Equations (2.2.2.18) and (2.2.2.19). The errors were calculated by comparing approximation (3.2.261) and the actually measured index of absorption. From this table, it is clear that the analytical approximation can reduce the computational time by about 2 orders of magnitude. As the radiation effects are relatively small when compared with convective heating, we can calculate the radiation effect with 58 points using the analytical presentation with error less than 10 %.

The performances of the numerical algorithms described in this section are discussed in Section 5.4.

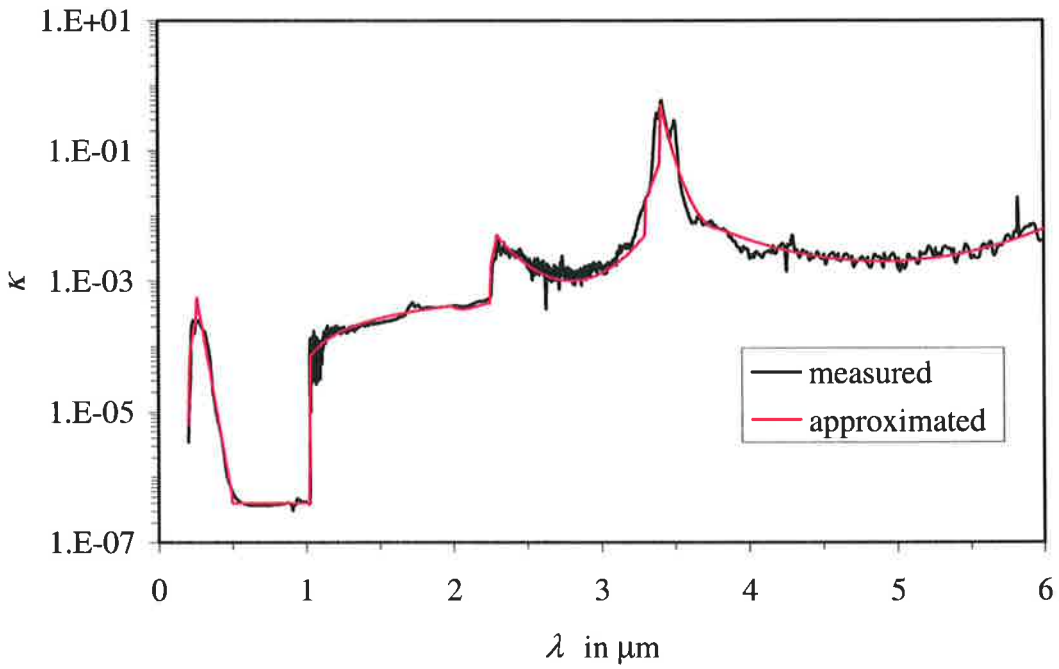

Fig. 3.2 Index of absorption of low sulphur ESSO AF1313 diesel fuel versus wavelength λ based on the measured values and the analytical approximation (3.2.2.1).

	Analytical approximation			Measured values
Number of points	15	20	58	4111
CPU time /sec	10.02	24.04	93.46	6103.2
Error %	44.35	33.2	9.35	0.0

Table 3.1 Computational time and error for the radiation term calculation using analytical approximations and based on measured values of the index of absorption.

3.3 Absorption efficiency factor of droplets

The relation between the spectral absorption coefficient due to contribution of the droplets, a_λ, and the absorption efficiency factor of individual spherical droplets (Q_a) can be presented as (Dombrovsky et al, 2003):

$$a_\lambda = 0.75 f_v \frac{\overline{Q}_a}{R_{32}}, \tag{3.3.1}$$

where

$$\overline{Q}_a = \frac{1}{R_{20}} \int_0^\infty Q_a R_d^2 F(R_d) dR_d, \tag{3.3.2}$$

$$R_{ij} = \int_0^\infty R_d^i F(R_d) dR_d \Big/ \int_0^\infty R_d^j F(R_d) dR_d,$$

$F(R_d)$ is the normalised distribution function of droplets by radii $\left(\int_0^\infty F(R_d) dR_d = 1 \right)$ and f_v is the volume fraction of droplets. Similar relations can be written for spectral transport extinction coefficient and transport extinction efficiency factor (Dombrovsky et al, 2003).

Alternatively, Equation (3.3.1) can be presented as (Dombrovsky et al, 2001):

$$a_\lambda = \sum_i a_\lambda^i = \sum_i \frac{\pi R_{di}^2}{V} Q_{ai}, \tag{3.3.3}$$

where a_λ^i describes the contributions of individual droplets, summation is assumed over all droplets in volume V, R_{di} and Q_{ai} are radii and absorption efficiency factors of individual droplets.

According to the Mie theory, Q_a depends on droplet diffraction parameter $x = 2\pi R_d / \lambda$ and complex index of refraction of the fuel $m = n - i\kappa$. These calculations are rather complicated, especially for large droplets ($x >> 1$). This stimulated attempts to develop simplified models specifically focused on the range of parameters typical for diesel fuel droplets (Dombrovsky et al, 2001, 2002, 2003). The approximation for Q_a has been suggested as in Equation (2.2.2.12). This equation gives a slightly better approximation for Q_a when compared with that suggested as in Equation (2.2.2.6). Equation (2.2.2.12) is valid in the geometrical optics limit ($x >> 1$) and small index of absorption ($\kappa << 1$). It has been shown, however, that it can be applicable even in the case when these conditions are not satisfied. The simplicity of Equation (2.2.2.12) is expected to lead to considerable simplification of the analysis of sprays based on Equations (3.3.1) and (3.3.2) or (3.3.3).

The values of n were calculated based on subtractive Kramers-Krönig analysis (Aherenkiel, 1971; Dombrovsky et al, 2003). It was shown that the results of these calculations can be accurately approximated by the following relationship (Dombrovsky et al, 2002):

$$n = n_0 + 0.02 \frac{\lambda - \lambda_m}{(\lambda - \lambda_m)^2 + 0.001}, \tag{3.3.4}$$

where $n_0 = 1.46$, $\lambda_m = 3.4$ μm, λ is the wavelength in μm. For practical calculations of κ, the dependence of n on λ can be ignored, and n can be put equal to 1.46 (Dombrovsky et al, 2003).

As in Dombrovsky et al (2001), it is assumed that the dependence of radiation intensity on λ is close to that of a black body and the averaged values of droplet absorption coefficient is calculated as:

$$\bar{a}_i = \frac{\int_{\lambda_1}^{\lambda_2} a_\lambda^i(R_{di},\lambda) B_\lambda(T_{ext}) d\lambda}{\int_{\lambda_1}^{\lambda_2} B_\lambda(T_{ext}) d\lambda} \approx \frac{\int_{\lambda_1}^{\lambda_2} a_\lambda^i(R_{di},\lambda) I_\lambda^0 d\lambda}{\int_{\lambda_1}^{\lambda_2} I_\lambda^0 d\lambda}, \tag{3.3.5}$$

where $B_\lambda(T_{ext})$ is the Planck function defined as in Equation (2.2.2.2) and T_{ext} is the external gas temperature, which controls the emission of thermal radiation absorbed by the droplets. In diesel engines this temperature can be related to the temperature of flame. It can be much higher than the ambient gas temperature, controlling the convective heating of droplets (Sazhina et al, 2000).

If the range (λ_1, λ_2) is wide enough so that most radiation energy is concentrated in it I can write:

$$\int_{\lambda_1}^{\lambda_2} B_\lambda(T_{ext}) d\lambda \approx \sigma T_{ext}^4 / \pi.$$

The combination of Equations (3.3.5) and (3.3.3) allows us to present the expression for $\bar{a}_i$ in the form:

$$\bar{a}_i = \frac{\pi R_{di}^2}{V} \frac{\int_{\lambda_1}^{\lambda_2} Q_{ai} B_\lambda(T_{ext}) d\lambda}{\int_{\lambda_1}^{\lambda_2} B_\lambda(T_{ext}) d\lambda} \tag{3.3.6}$$

Remembering Equation (3.3.6) and the definition of B_λ, expression for $\bar{a}_i$ can be presented in a more explicit form (Dombrovsky et al, 2001):

$$\bar{a}_i = \frac{\pi R_{di}^2}{V} \bar{Q}_{ai}, \tag{3.3.7}$$

where

$$\overline{Q}_{ai} = \frac{4n}{(n+1)^2}\left[1 - \frac{\int_{\lambda_1}^{\lambda_2} \frac{\exp(\frac{-8\pi\kappa R_{di}}{\lambda})}{\lambda^5[\exp(C_2/(\lambda T_{ext}))-1]}d\lambda}{\int_{\lambda_1}^{\lambda_2} \frac{d\lambda}{\lambda^5[\exp(C_2/(\lambda T_{ext}))-1]}}\right] \tag{3.3.8}$$

is the average (over wavelengths) droplet absorption efficiency factor. Equation (3.3.7) will be used to calculate the thermal radiation absorbed by the fuel droplet in the rest of the thesis.

As follows from Equation (3.3.7), the maximal values of $\overline{a}_i$ are achieved when κ is sufficiently large over the whole spectral range. For small κ, $\overline{a}_i$ is expected to be close to zero. For effective implementation of this expression for $\overline{a}_i$ into a CFD code I need to find a reasonably accurate but simple approximation of the function $\overline{Q}_{ai}(R_{di}, T_{ext})$.

Taking into account the experimentally measured values of $\kappa(\lambda)$, it was found that the best approximation for $\overline{Q}_{ai}$ in the ranges $5 \le R_{di} \le 50$ μm and $1000 \le T_{ext} \le 3000$ K is provided by the function as in Equation (2.2.2.10) where a and b are quadratic functions of T_{ext} approximated as:

$$\left.\begin{aligned} a &= a_0 + a_1(T_{ext}/1000) + a_2(T_{ext}/1000)^2 \\ b &= b_0 + b_1(T_{ext}/1000) + b_2(T_{ext}/1000)^2 \end{aligned}\right\} \tag{3.3.9}$$

In what follows the subscript 'i' for individual droplets will be omitted.

Analysis similar to that presented in Dombrovsky et al (2001) has been repeated for various ranges of droplet radii and gas temperatures for all four types of diesel fuel under consideration. It has been shown that approximation (2.2.2.10) with a and b defined by (3.3.9) is applicable for all four types of fuel in the ranges $2 \le R_d \le 200$ μm and $1000 \le T_{ext} \le 3000$ K, although it becomes less accurate for droplets with radii greater than 50 μm. Results of calculation of the coefficients in (3.3.9) for various ranges of R_d for all four types of fuel are shown in Table (3.2). As can be seen from this table the variations of the values of the coefficients depending of the range of R_d and type of fuel are substantial and need to be taken into account.

Type of fuel	R_{min}/ μm	R_{max}/ μm	a_0	$a_1(K^{-1})$	$a_2(K^{-2})$	b_0	$b_1(K^{-1})$	$b_2(K^{-2})$
White unboiled	5	50	0.10400	-0.054320	0.008000	0.49162	0.098369	-0.007857
White unboiled	5	100	0.12358	-0.066360	0.010000	0.42402	0.115583	-0.009886
White unboiled	5	200	0.01689	-0.094840	0.014800	0.31518	0.146189	-0.014057
White unboiled	2	50	0.10350	-0.053210	0.007980	0.49590	0.096781	-0.007632
White unboiled	2	200	0.15412	-0.085400	0.013200	0.33988	0.138394	-0.013029
Red unboiled	5	50	0.08876	-0.046280	0.006800	0.44544	0.131457	-0.013714
Red unboiled	5	100	0.09654	-0.050609	0.007457	0.41346	0.136374	-0.014029
Red unboiled	5	200	0.11596	-0.061626	0.009171	0.35694	0.141951	-0.014143
Red unboiled	2	50	0.09040	-0.046110	0.006724	0.44300	0.129870	-0.012980
Red unboiled	2	200	0.11116	-0.058757	0.008714	0.36804	0.138994	-0.013829
White boiled	5	50	0.10930	-0.056446	0.008171	0.50826	0.079017	-0.007314
White boiled	5	100	0.13188	-0.069380	0.010200	0.44010	0.087643	-0.007686
White boiled	5	200	0.18430	-0.100843	0.015286	0.33048	0.109137	-0.009714
White boiled	2	50	0.10800	-0.054320	0.008014	0.51330	0.078932	-0.007312
White boiled	2	200	0.16624	-0.090011	0.013543	0.35550	0.104551	-0.009343
Red boiled	5	50	0.07160	-0.031469	0.004057	0.44202	0.177531	-0.022343
Red boiled	5	100	0.07786	-0.033474	0.004229	0.41654	0.169563	-0.021686
Red boiled	5	200	0.09168	-0.035854	0.004029	0.38168	0.139197	-0.016714
Red boiled	2	50	0.07250	-0.030875	0.004032	0.44220	0.017540	-0.022120
Red boiled	2	200	0.08784	-0.034866	0.003971	0.38976	0.141946	-0.016771

Table 3.2 Constants in Equation (3.3.9)

The accuracy of approximation (2.2.2.10) with the coefficients given by Equation (3.3.9) and Table (3.2) is illustrated in Figure (3.3) for the white unboiled fuel and two ranges of R_d. As can be seen from this figure, the approximation (3.3.9) is very good for

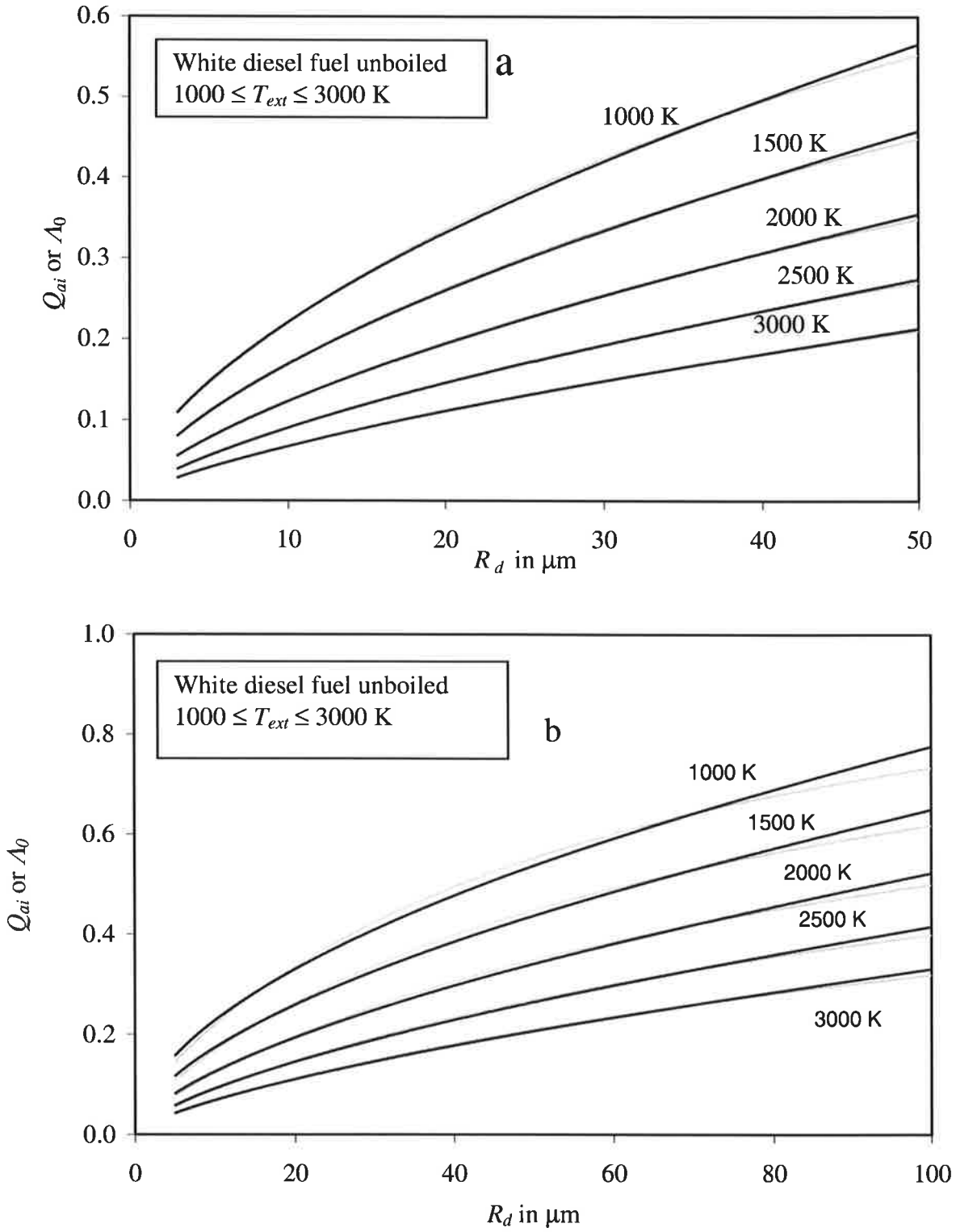

Fig. 3.3 $\overline{Q}_{ai}$ versus R_d (black) and Λ_0 versus R_d (grey) for $1000 \leq T_{ext} \leq 3000$ K (indicated near the curves) for white unboiled diesel fuel. Coefficients a and b are defined by Equation (3.3.9). Plots shown in Fig.3.2a are based on the values of coefficients found for external temperatures in the range $1000 \leq T_{ext} \leq 3000$ K and droplet radii in the range $2 \leq R_d \leq 50$ μm. Plots shown in Fig.3.2b are based on the values of coefficients found for external gas temperatures in the range $1000 \leq T_{ext} \leq 3000$ K and droplet radii in the range $5 \leq R_d \leq 100$ μm.

$2 \leq R_d \leq 50$ μm, but less accurate (although acceptable in most practical applications) for $5 \leq R_d \leq 100$ μm

For 500 K $\leq T_{ext} \leq$ 3000 K approximations (3.3.9) appeared to be poor for all types of fuel under consideration. Considerably better accuracy was obtained when approximations (3.3.9) were replaced by the following approximations:

$$\left.\begin{aligned} a &= a_0 + a_1(T_{ext}/1000) + a_2(T_{ext}/1000)^2 + a_3(T_{ext}/1000)^3 + a_4(T_{ext}/1000)^4 \\ b &= b_0 + b_1(T_{ext}/1000) + b_2(T_{ext}/1000)^2 + b_3(T_{ext}/1000)^3 + b_4(T_{ext}/1000)^4 \end{aligned}\right\} \quad (3.3.10)$$

The values of coefficients in Equation (3.3.10) for 500 K $\leq T_{ext} \leq$ 3000 K and various ranges of R_d for all four types of fuel are shown in Table (3.3). As in the case of Table (3.2), the variation in the values of the coefficients depending on the range of R_d and type of fuel are sometimes substantial and need to be taken into account.

Type of fuel	R_{min}/μm	R_{max}/μm	a_0	a_1 (K^{-1})	a_2 (K^{-2})	a_3 (K^{-3})	a_4 (K^{-4})	b_0	b_1 (K^{-1})	b_2 (K^{-2})	b_3 (K^{-3})	b_4 (K^{-4})
White unboiled	5	50	-0.0417	0.28362	-0.26836	0.09526	-0.011767	0.9671	-0.9761	0.84533	-0.28534	0.034233
White unboiled	5	100	-0.0442	0.32398	-0.31034	0.11081	-0.013733	0.8819	-0.9163	0.80674	-0.27215	0.032533
White unboiled	5	200	-0.0463	0.40945	-0.40219	0.14532	-0.018133	0.7496	-0.8308	0.75706	-0.25621	0.030533
White unboiled	2	50	-0.0440	0.27981	-0.25981	0.09478	-0.011520	0.9798	-0.9698	0.85673	-0.27982	0.033134
White unboiled	2	200	-0.0474	0.38577	-0.37553	0.13517	-0.016833	0.7824	-0.8579	0.77432	-0.26198	0.031267
Red unboiled	5	50	-0.0565	0.29014	-0.26793	0.09457	-0.011667	0.9862	-1.1016	0.97560	-0.33451	0.040567
Red unboiled	5	100	-0.0621	0.31707	-0.29294	0.10345	-0.012767	0.9636	-1.1152	0.98742	-0.33765	0.040833
Red unboiled	5	200	-0.0720	0.37382	-0.34642	0.12240	-0.015100	0.8995	-1.0880	0.96582	-0.32892	0.039600
Red unboiled	2	50	-0.0570	0.29030	-0.26583	0.09352	-0.011392	0.9681	-1.1009	0.96537	-0.27613	0.042184
Red unboiled	2	200	-0.0689	0.35806	-0.33151	0.11706	-0.014433	0.9063	-1.0819	0.95965	-0.32700	0.039400
White boiled	5	50	-0.0395	0.28796	-0.27275	0.09658	-0.011900	0.9388	-0.9035	0.78188	-0.26714	0.032433
White boiled	5	100	-0.0409	0.33132	-0.31734	0.11285	-0.013933	0.8375	-0.8168	0.71621	-0.24414	0.029533
White boiled	5	200	-0.0410	0.42355	-0.41523	0.14897	-0.018467	0.6954	-0.7176	0.64863	-0.22082	0.026567
White boiled	2	50	-0.0420	0.27893	-0.26731	0.09367	-0.016721	0.9596	-0.9007	0.76258	-0.25817	0.031425
White boiled	2	200	-0.0432	0.39663	-0.38514	0.13767	-0.017033	0.7331	-0.7515	0.67277	-0.22896	0.027567
Red boiled	5	50	-0.0850	0.32863	-0.28769	0.09964	-0.012200	1.4481	-2.1310	1.84306	-0.63536	0.077600
Red boiled	5	100	-0.0848	0.34028	-0.29836	0.10326	-0.012633	1.2870	-1.8292	1.59459	-0.55092	0.067333
Red boiled	5	200	-0.0906	0.38067	-0.33095	0.11353	-0.013800	1.1103	-1.5294	1.32851	-0.45711	0.055700
Red boiled	2	50	-0.0970	0.31872	-0.27829	0.09872	-0.021091	1.6235	-2.5023	0.18522	-0.63022	0.085020
Red boiled	2	200	-0.0973	0.38854	-0.33685	0.11562	-0.014067	1.2056	-1.7258	1.48863	-0.51140	0.062300

Table 3.3 Constants in Equation (3.3.10)

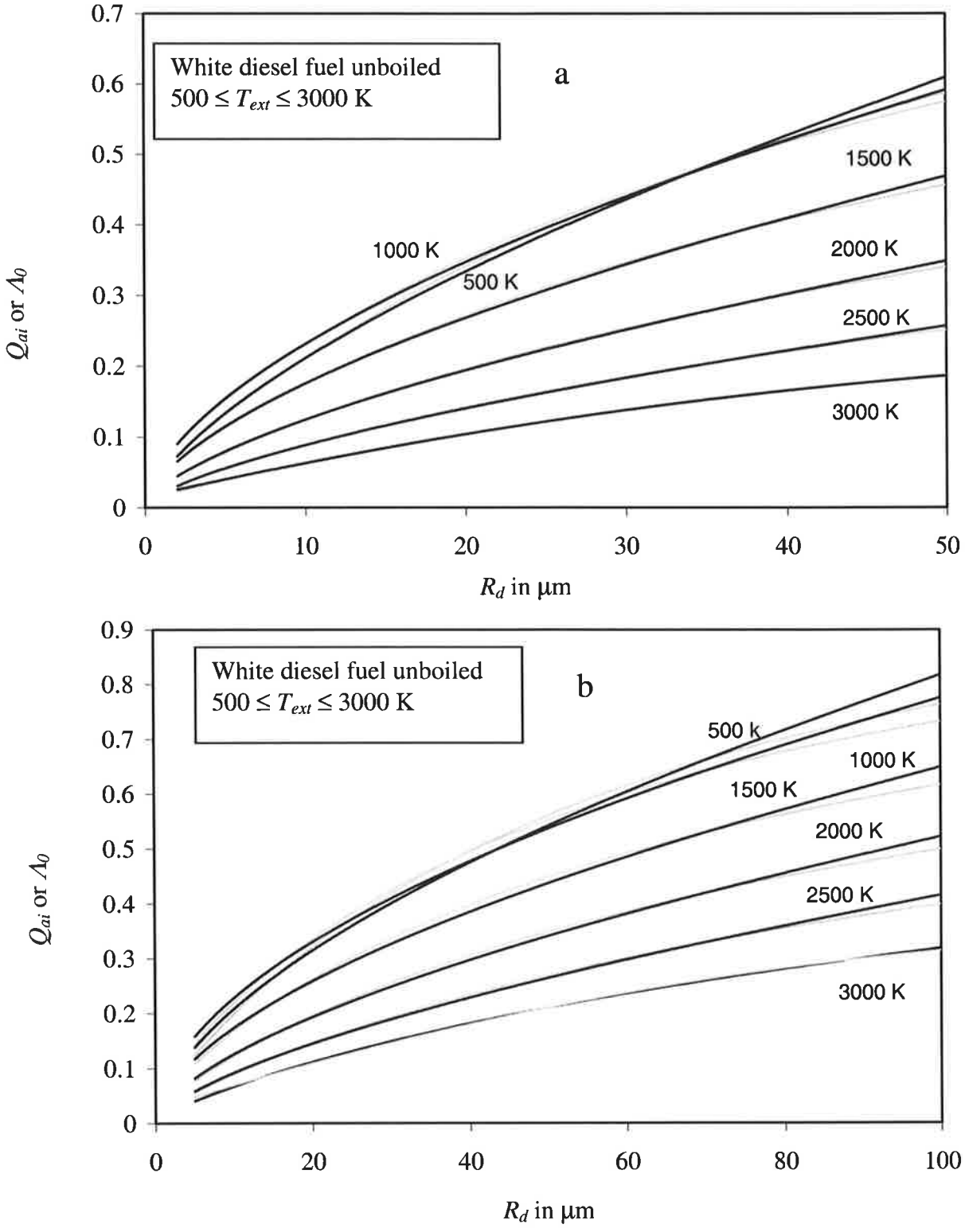

Fig. 3.4 The same as in Figure (3.3) but for the range 500 K ≤ T_{ext} ≤ 3000 K, when the coefficients *a* and *b* are defined by Equation (3.3.10).

The accuracy of approximation (2.2.2.10) with the coefficients given by Equation (3.3.10) and Table (3.3) is illustrated in Figure (3.4) for the white unboiled fuel and two

ranges R_d similar to those shown in Figure (3.3). As in the case shown in Figure (3.3), the approximation (3.3.10) is very good for $2 \leq R_d \leq 50$ μm, but less accurate (although acceptable in most practical applications) for $5 \leq R_d \leq 100$ μm.

The contribution of external gas radiation at temperatures close to 500 K is expected to be much smaller than the contribution of radiation from gas at temperatures higher than 1000 K. Hence approximation (3.3.10) is less important for practical applications than approximation (3.3.9). The values of the coefficients can be chosen from Tables (3.2) or (3.3) depending on the type of fuel and the range of droplet radii and gas temperatures required.

3.4 Heating and evaporation of droplets

To illustrate the importance of the effects described in the previous section, a stand-alone code describing droplet heating and evaporation has been developed. A single droplet was placed in a hot gas at constant temperature. Droplet thermal conductivity was assumed much greater than that of gas ($k_l = \infty$), and temperature gradients inside the droplets were ignored.

As a result the problem of heating and evaporation of droplets was reduced to the solution of the following system of equations (Chin and Lefebvre, 1983; Lefebvre, 1989):

$$\frac{4}{3}\pi R_d^3 \rho_l c_l \frac{dT_d}{dt} = 4\pi R_d^2 h\left(T_g - T_d\right) + 4\pi R_d^2 \sigma \varepsilon_d \left(T_{ext}^4 - T_d^4\right) + 4\pi R_d^2 \rho_l L \frac{dR_d}{dt} \qquad (3.4.1)$$

$$\frac{dR_d}{dt} = -\frac{\rho_g D_{12} \ln\left(1 + B_M\right)}{\rho_l R_d}, \qquad (3.4.2)$$

where T_d is the droplet temperature, $B_M = Y_{fs}/(1-Y_{fs})$ is the Spalding mass number, Y_{fs} is the mass fraction of fuel vapour near the droplet surface:

$$Y_{fs} = \left[1 + \left(\frac{p}{p_{Fs}} - 1\right)\frac{M_a}{M_f}\right]^{-1}, \qquad (3.4.3)$$

p and p_{Fs} are ambient pressure and the pressure of saturated fuel vapour near the surface of droplets respectively, M_a and M_f are molar masses of air and fuel vapour; p_{Fs} can be calculated from the Clausius-Clapeyron equation presented in the form (Chin and Lefebvre, 1983; Lefebvre, 1989):

$$p_{Fs} = \exp\left[a_v - \frac{b_v}{T_s - 43}\right], \qquad (3.4.4)$$

where p_{Fs} is in kPa. The coefficients a_v and b_v as functions of droplet surface temperature were taken the same as in VECTIS CFD code of Ricardo Consulting Engineers. They are close to those reported in (Lefebvre, 1989) for DF-2 (see page 319). $\rho_g D_{12}$ in Equation (3.4.2) can be replaced by k_g/c_{pg} assuming that the Lewis number is unity ($\mathrm{Le} = k_g/(\rho_g c_{pg} D_{12}) = 1$, k_g and c_g are thermal conductivity and specific heat capacity of gas respectively.

I consider the case when the droplet is stationary, or almost stationary, which allows us to assume that Nusselt number Nu = 2 and write

$$h = k_g / R_d \tag{3.4.5}$$

When deriving Equation (3.4.1) temperature gradients inside the droplet were ignored. For benchmarking purpose, two solvers were implemented for the solution of the system of Equations (3.4.1) and (3.4.2). The first was a stand-alone code based on the Runge-Kutta method with adaptive step size control (Press et al, 1989). The second solver was taken from the public domain site of LLNL (http://www.llnl.gov/CASC/odepack/). Both methods gave practically the same results as shown in Figure (3.4).

Values of parameters typical for a diesel engine were taken as follows: gas pressure p was taken equal to 6 MPa, droplet initial temperature and radius were taken equal to 300 K and 10 μm, respectively. Plots of droplet temperature and radius as functions of time for white unboiled fuel are shown in Figure (3.4). In this Figure the values of initial droplet radius, gas temperature and external temperature were taken equal to 10 μm, 1000 K and 2000 K respectively.

These plots refer to the cases when the effects of thermal radiation are ignored altogether (Case A), when the thermal radiation is accounted for based on Equations (3.3.7) and (2.2.2.10) (semi-transparent droplets) (Case B) using the actual measured points of index of absorption shown in Figure (3.1), and when thermal radiation is accounted for based on the assumption that ε_d = 1 in Equation (3.4.1) (black opaque droplets) (Case C). As follows from Figure (3.4) the effect of thermal radiation on semi-transparent droplets is noticeably smaller when compared with this effect on black opaque droplets. In the former case, the temperature remained subcritical (T_{cr} = 725.9 K) all the way through (until the droplets evaporated) in all cases. The difference between black and semi-transparent droplets is even more clearly seen for droplet radii. The initial increase of droplet radius is due to droplet thermal expansion. For realistic semi-transparent droplets the effects of radiation would lead to a small (less than 8.5 %)

decrease of their evaporation time when compared with the case without thermal radiation.

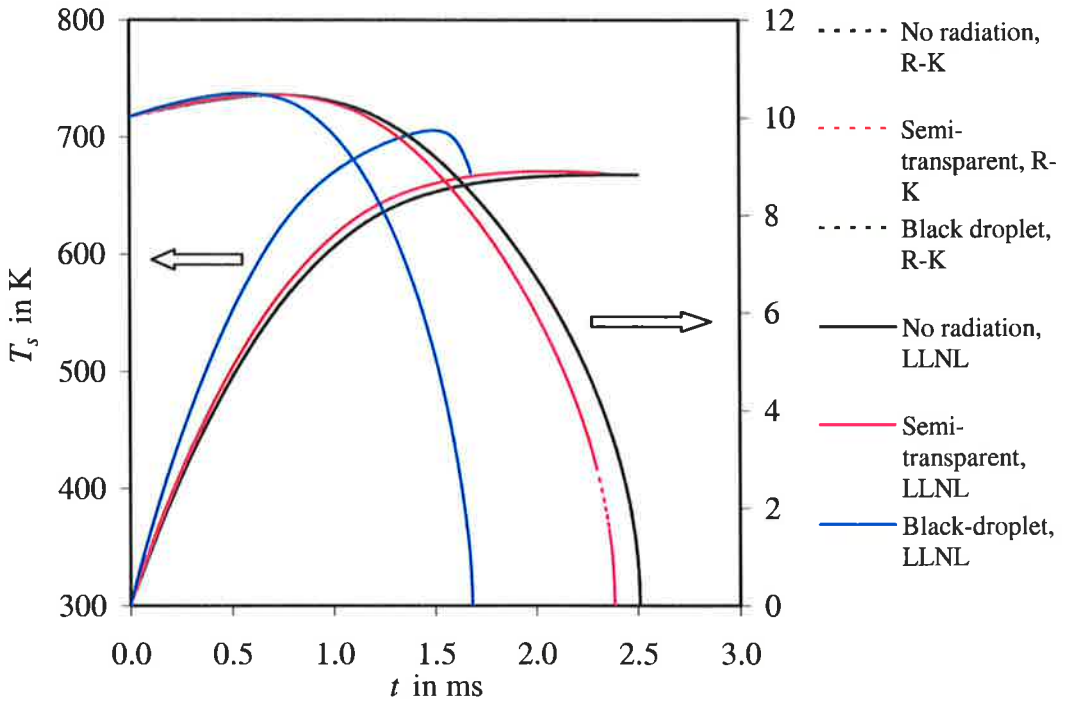

Fig. 3.5 Droplet temperatures and droplet radii versus time as calculated by a stand-alone code with Runge-Kutta (R-K) and LLNL solvers for a stationary droplet. The cases are: A) the effects of thermal radiation have been ignored, B) they are taken into account based on Equations (3.3.7) and (2.2.2.10) (semi-transparent droplets), C) they are taken into account based on Equation (3.3.7) with $\overline{Q}_{ai}$ = 1 (black opaque droplets). T_{s0}=300 K and p_g = 6 MPa. R_{d0} = 10 μm, T_g = 1000 K and T_{ext} = 2000 K.

Note that the evaporation time predicted by Figure (3.4) can be unrealistically long for real-life diesel engines. This is related to the fact that our analysis is not comprehensive at this stage and a number of important processes including droplet break-up and non-zero velocity were not taken into account. These will be considered in detail in Chapters 6 and 7.

Results similar to those shown in Figure (3.5) have been obtained for other gas temperatures, external temperatures and droplet radii as shown in Figure (3.6). As expected, the effects of thermal radiation and the difference between the cases of black and semi-transparent droplets became more prominent for larger droplets, larger external temperatures and lower gas temperature. Based on these results I can conclude that thermal radiation leads to increased heating of semi-transparent droplets and reduction of their evaporation times. These effects, however, are considerably weaker than similar effects for black opaque droplets in agreement with results in Dombrovsky et al (2001).

The effect of thermal radiation in Figure (3.6a) still appears to be rather weak. Note, however, that the analysis so far was based on the assumption that gas into which droplets are injected is homogeneous and $T_{ext} = T_g$. In a realistic diesel engine environment this assumption is almost always questionable. I might expect that the droplets be injected into a relatively cold gas (cooled down due to evaporation of previously injected droplets), while the remote flame has a relatively high temperature ($T_{ext} > T_g$). Nearer to the end of the injection process I can expect that combustion has already started, and the radiation responsible for radiative heating of droplets is generated by the hot flame. The temperature of the flame (T_{ext}) can reach up to 2500 K, while the temperature of gas in the vicinity of droplets (T_g) remains about 700 K or less (Sazhina et al, 2000). In this case the convective heating of droplets is controlled by a relatively low temperature about or less than 700 K, while its radiative heating is controlled by a much higher temperature up to 2500 K. Results of calculations similar to those presented in Figure (3.6a) but for the case when this difference in temperatures is taken into account are shown in Figure (3.5d). In the latter case I assumed that the temperature of gas responsible for convective heating is equal to T_g =700 K while the temperature of flame responsible for radiative heating is equal to T_{ext} = 2000 K. The initial radius of droplet is assumed equal to 10 μm (the most realistic value for diesel engines). This is according to the experimental results of ICEG (Internal Combustion Engines Group) in University of Brighton. As can be seen from this figure, the effect of radiative heating leads to decrease of evaporation time by 11.82 %. This effect of radiation appears to be even stronger for larger droplets, lower ambient gas temperature (responsible for convective heating) and higher flame temperature (responsible for radiative heating) as shown in Figure (3.6). In Figures (3.6b) and (3.6c), in the case of black droplets the droplet surface temperature reached the critical value of 725.9 K for diesel fuel droplet when its radius dropped to about 22 μm and 9.2 μm, respectively.

It seems that this effect was first observed by Sazhina et al (2000). The T_{ext} can be identified with the so-called radiative temperature, introduced in connection with the P-1 model. Note that the results shown in Figures (3.5) and (3.6) may look unrealistic for diesel engines due to rather long evaporation time. This occurred because the simplified model used did not address droplet break-up processes and relative velocity between droplets and gas. Both these effects will be accounted for in Chapters 6 and 7 where the

results of coupled solution of droplet and gas equations will be presented.

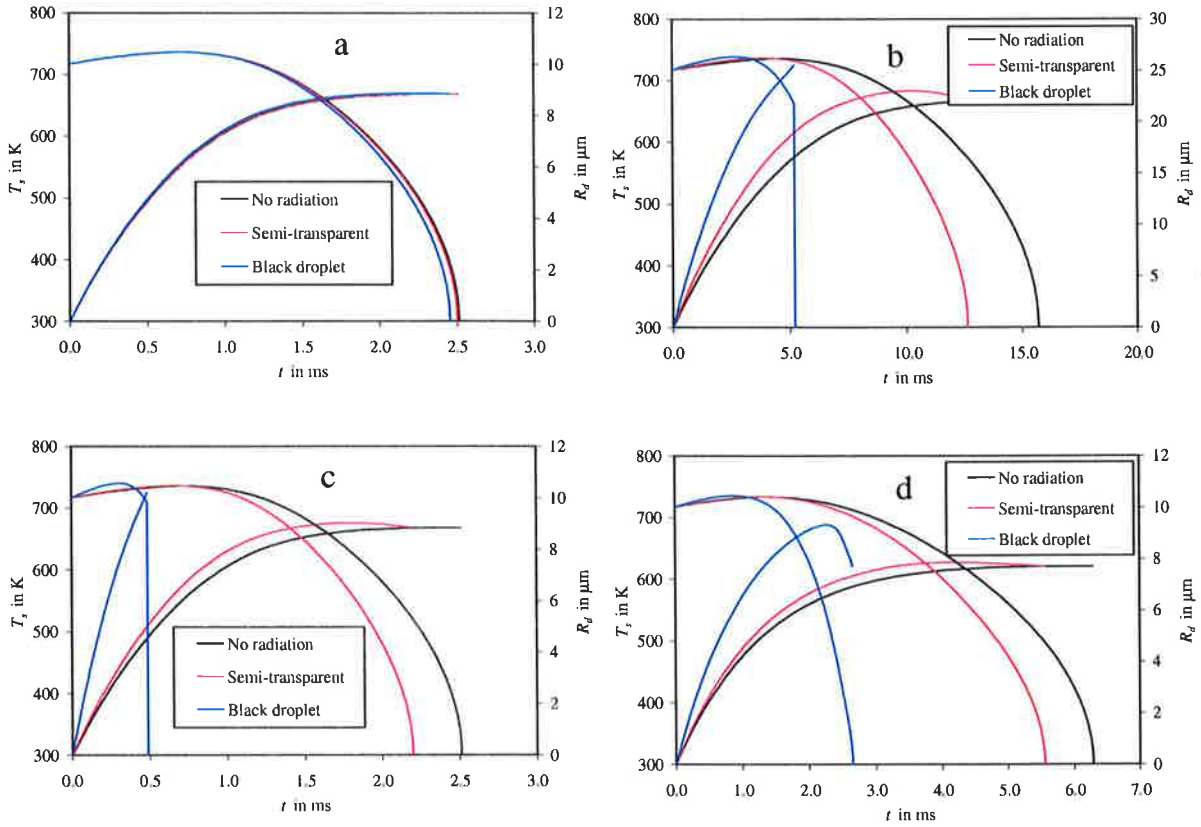

Fig. 3.6 The same results as in Figure 3.4 but as calculated with Runge-Kutta solver for different droplet radii gas temperature and external temperature. Results shown in (a) are based on R_{d0} = 10 μm, T_g = 1000 K and T_{ext} = 1000 K. Results shown in (b) are based on R_{d0} = 25 μm, T_g = 1000 K and T_{ext} = 2000 K. Results shown in (c) are based on R_{d0} = 10 μm, T_g = 1000 K and T_{ext} = 3000 K. Results shown in (d) are based on R_{d0} = 10 μm, T_g = 700 K and T_{ext} = 2000K.

3.5 Conclusions of Chapter 3

Results of the measurements of the index of absorption of four types of diesel fuel in the range of wavelengths 0.2 μm – 6 μm are presented. The types of diesel fuel analysed include two samples for which the 'ageing' process of fuels was simulated by prolonged boiling.

It is shown that the approximation of the average absorption coefficient of droplets by the function aR_d^b, where R_d is the droplet radius, and a and b are polynomial functions of external gas temperature, is applicable for all types of fuel in the reasonable range of these temperatures and droplet radii. In the case when the external temperature range is 1000 - 3000 K, these polynomials are quadratic functions. In the case when this range is

500 - 3000 K, the polynomials are of the fourth power. The accuracy of this approximation is good for droplet radii in the range 2-50 μm, but can be worse for droplet radii in the range 5-200 μm. However, even in the latter case it can be applicable for practical engineering applications. Empirical values of the coefficients are presented for all four types of diesel fuel and for various ranges of droplet radii and gas temperatures.

In agreement with the previous results, it has been shown that the effect of thermal radiation on heating and evaporation of semi-transparent diesel fuel droplets is considerably smaller when compared with the case when droplets are approximated as black opaque spheres. The effect of thermal radiation increases with increasing droplet radii and external temperature and decreases with increasing the gas temperature. This approximation combines the simplicity and reasonable accuracy required for modelling thermal radiation transfer within the framework of numerical modelling of combustion processes in diesel engines.

The effect of radiative heating of droplets is shown to be particularly strong when the difference between the gas temperature responsible for droplet convective heating and flame temperature responsible for its radiative heating, is taken into account.

4. TRANSIENT HEATING OF DIESEL FUEL DROPLETS: MATHEMATICAL MODELS

4.1 Introduction

In Chapter 3 the focus was on the radiative heating of diesel fuel droplets assuming that there is no internal temperature gradient. In this chapter the analysis will be generalized to the case when this temperature gradient is accounted for. The analytical solution of the transient heat conduction equation inside a spherical droplet will be obtained. Three cases will be considered; constant, almost constant and arbitrary convection heat transfer coefficient.

The previously suggested analytical solutions of the heat conduction equation in a sphere were limited to the case when the convection heat transfer coefficient was constant, and the heat source depended on time, but spatially homogeneous (Luikov, 1968). A number of analytical solutions for specific heat source distributions in a sphere are presented in Carslaw and Jaeger (1986), but no convection has been accounted for. The analytical solutions discussed in this chapter are generalisations of the solutions reported by Carslaw and Jaeger (1986), Luikov (1968), Kartashov (2001), Sazhin and Krutitskii (2003) and Mukhopadhyay and Sanyal (2005). At first the explicit solution of the problem with constant convection heat transfer coefficient, but arbitrary distribution of radiative heat inside droplets, and arbitrary initial temperature distribution inside droplets, is constructed in the form of a convergent series. This solution is used as an auxiliary tool to solve the problem with the time-dependent heat transfer coefficient. The latter problem is reduced to the solution of an integral equation. This solution is unique and can be obtained numerically. The numerical algorithm is discussed. An approximate solution of the integral equation is obtained using the perturbation method for the case of almost constant heat transfer coefficient. An arbitrary initial distribution of temperature inside droplets is assumed. The effect of evaporation is taken into account via a non-zero time derivative of droplet radius in the enthalpy equation. The solution, however, is based on the assumption that the changes in droplet surface area are negligibly small. This assumption is justified when the time interval is small, while the latent heat of evaporation is large. Its range of applicability is investigated. The contribution of the radiation term is calculated using the simplified model developed by Dombrovsky and Sazhin (2003b, c) and the results of the original measurements of the diesel fuel absorption coefficient reported in Chapter 3.

The basic equations and approximations used in our analysis are discussed in Section 4.2. Details of the analytical solutions of the heat conduction equation are presented in Section 4.3. The application of one of the solutions to the practical problem of heating of diesel fuel droplets is discussed in Section 4.4. The main results of the chapter are summarised in Section 4.5.

The main results presented in this chapter have been published in the paper by Sazhin, Abdelghaffar et al (2004b)

4.2 Basic equations and approximations

Assuming that the temperature distribution inside a droplet (T) is spherically symmetrical the transient heat conduction equation inside this droplet in the presence of thermal radiation can be written as (Carslaw and Jaeger, 1986; Luikov, 1968):

$$c_l \rho_l \frac{\partial T}{\partial t} = k_l \left(\frac{\partial^2 T}{\partial R^2} + \frac{2}{R} \frac{\partial T}{\partial R} \right) + P_1(R), \tag{4.2.1}$$

where P_1 (R) is the power generated in unit volume inside the droplet due to external radiation, and c_l, ρ_l, and k_l are assumed to be constant.

If the droplet is heated by convection from the surrounding gas, and cooled down due to evaporation, the energy balance equation at the droplet surface can be written as:

$$h(T_g - T_s) = -\rho_l L \dot{R}_d + k_l \left. \frac{\partial T}{\partial R} \right|_{R=R_d}, \tag{4.2.2}$$

where $h = h(t)$ is the convection heat transfer coefficient (time dependent in the general case). We took into account that $\dot{R}_d < 0$ during the evaporation process. Equation (4.2.2) can be considered as a boundary condition for Equation (4.2.1) at $R = R_d$. This needs to be complemented by the boundary condition at $R = 0$:

$$\left. \frac{\partial T}{\partial R} \right|_{R=0} = 0,$$

and the initial condition $T(t = 0) = T_0(R)$.

Introducing the normalised radius $r = R/Rd$, Equation (4.2.1) can be rewritten as:

$$\frac{\partial T}{\partial t} = K \left(\frac{\partial^2 T}{\partial r^2} + \frac{2}{r} \frac{\partial T}{\partial r} \right) + P(r) \tag{4.2.3}$$

where

$$K = \frac{k_l}{c_l \rho_l R_d^2}, \quad P(r) = P_1(rR_d)/(c_l\rho_l) = \left[\frac{3\pi}{R_d} \int_{\lambda_1}^{\lambda_2} w(r,\lambda) Q_a B_\lambda(T_{ext}) d\lambda \right] /(c_l\rho_l),$$

$B_\lambda(T_{ext})$ is the Planck function defined as in Equation (2.2.2.2), λ is the wavelength in μm. T_{ext} is assumed to be constant. Q_a is estimated using Equation (2.2.2.12), w (r) is the normalised spectral power of radiation per unit volume absorbed inside the droplet (Dombrovsky and Sazhin, 2003b), λ_1 and λ_2 are the lower and upper limit of the spectral range of thermal radiation which contributes to droplet heating. The values of $w(r)$ were calculated based on the Equations (2.2.2.18) and (2.2.2.19).

Equation (4.2.2) can be rearranged to:

$$T_{eff} - T_s = \frac{k_l}{hR_d} \left. \frac{\partial T}{\partial r} \right|_{r=1}, \tag{4.2.4}$$

where:

$$T_{eff} = T_g + \frac{\rho_l L \dot{R}_d}{h}$$

Equation (4.2.4) is complemented by the boundary condition at r = 0 and the corresponding initial condition mentioned above.

T_{eff} is time dependent in the general case to account for the effects of droplet evaporation and gas cooling. Although we take into account non-zero $\dot{R}_d$ due to evaporation, we assume that R_d is constant in all terms except in the definition of T_{eff}. This assumption would certainly be not acceptable if we attempted to describe the whole process of droplet evaporation by a single analytical formula. Our solutions, however, are suggested with a view of incorporation into a CFD code, where it will be applied over relatively small time steps. Due to the large value of the coefficient $\rho_l L/h$, the correction to T_g leading to T_{eff} can be justified even if the solutions are considered over small time intervals. In the realistic situation the temperature dependence of ρ_l needs to be taken into account. This would lead to the initial increase, rather than decrease of droplet radii despite the effect of evaporation (Sazhin et al, 2001).

The value of $\dot{R}_d$ is controlled by fuel vapour diffusion from the droplet surface. It can be found from Equation (3.4.2). A more general kinetic approach to the problem is based on the solution of the Boltzmann equation in the Knudsen layer surrounding the droplet. In diesel engines this kinetic model predicts up to 5-10% larger evaporation times when compared with the evaporation times predicted by the hydrodynamic model on which

Equation (3.4.2) is based (Kryukov et al, 2004). Analysis of the kinetic model is beyond the scope of this thesis.

Equations (4.2.3) and (3.4.2) can be solved by iterations. At first one can assume that $T_s = T_{s0}$ in Equation (3.4.4) and obtain the solution of Equation (4.2.3) as $T_s = T_{s1}(t)$. Then this solution is substituted into Equation (3.4.4). When T_s approaches the boiling temperature T_b then the assumptions $Y_{fs} << 1$ and R_d = const become no longer applicable. The solution of the problem in this case is beyond the scope of this chapter (see (Crespo and Liñan, 1975).

For application in CFD codes we can assume that K is constant during the small time steps when the equations for droplet motion, evaporation and heat exchange with surrounding gas are solved. In this case the solution of the problem at the end of the time step can be considered as the initial condition for the next time step.

Introduction of the new variable $u = T r$ allows us to rewrite Equation (4.2.3) as:

$$\frac{\partial u}{\partial t} = K\frac{\partial^2 u}{\partial r^2} + \tilde{P}(r) \tag{4.2.5}$$

with the boundary and initial conditions:

$$\left.\begin{array}{ll} \dfrac{\partial u}{\partial r} + H(t)u = M(t) & \text{when } r = 1 \\ u = 0 & \text{when } r = 0 \\ u(t=0) = rT_0(rR_d) \equiv \tilde{T}_0(r) & \text{when } 0 \le r \le 1 \end{array}\right\} \tag{4.2.6}$$

where

$$H(t) = \frac{h(t)R_d}{k_l} - 1, \qquad M(t) = \frac{h(t)T_{eff}(t)R_d}{k_l}, \qquad \tilde{P}(r) = rP(r).$$

4.3 Analytical solutions

4.3.1 Case $h(t)$ = const

The analytical derivation for this case was mainly developed by P. A. Krutitskii (Sazhin et al, 2004b). At first we consider the case $h(t) \equiv h$ = const. Hence, $H(t) \equiv h_0 = (hR_d / k_l) - 1 = \text{const}$. Introducing a new parameter

$$\mu_0(t) = \frac{hT_{eff}(t)R_d}{k_l}$$

we can rewrite Equation (4.2.6) as:

$$\left.\begin{array}{ll} \dfrac{\partial u}{\partial r} + h_0 u = M(t) = \mu_0(t) & \text{when } r = 1 \\ u = 0 & \text{when } r = 0 \\ u(t=0) = rT_0(rR_d) \equiv \tilde{T}_0(r) & \text{when } 0 \le r \le 1 \end{array}\right\} \qquad (4.3.1.1)$$

Remembering that $h_0 > -1$, let us look for the solution of Equation (4.2.5) in the form:

$$u(r,t) = \frac{1}{1+h_0} r\mu_0(t) + W(r,t). \qquad (4.3.1.2)$$

Having substituted function (4.3.1.2) into Equation (4.2.5) we find the equation for W:

$$\frac{\partial W}{\partial t} = K\frac{\partial^2 W}{\partial r^2} + \tilde{P}(r) - \frac{r}{1+h_0}\frac{d\mu_0(t)}{dt} \qquad (4.3.1.3)$$

with the boundary and initial conditions:

$$\left.\begin{array}{l} W\big|_{r=0} = \left(\dfrac{\partial W}{\partial r} + h_0 W\right)\Big|_{r=1} = 0 \\ W\big|_{t=0} = \tilde{T}_0(r) - \dfrac{r}{1+h_0}\mu_0(0) \end{array}\right\}. \qquad (4.3.1.4)$$

We look for the solution of Equations (4.3.1.3) subject to (4.3.1.4) in the form:

$$W(r,t) = \sum_{n=1}^{\infty} c_n(t)\upsilon_n(r), \qquad (4.3.1.5)$$

where functions $\upsilon_n(r)$ form the full set of non-trivial solutions of the equation:

$$\frac{d^2\upsilon}{dr^2} + \lambda^2\upsilon = 0 \qquad (4.3.1.6)$$

subject to boundary conditions:

$$\upsilon\big|_{r=0} = \left(\frac{d\upsilon}{dr} + h_0\upsilon\right)\Big|_{r=1} = 0. \qquad (4.3.1.7)$$

The general solution of Equation (4.3.1.6):

$$\upsilon(r) = A\cos\lambda r + B\sin\lambda r \qquad (4.3.1.8)$$

satisfies the boundary conditions (4.3.1.7) when $A = 0$ and:

$$\lambda\cos\lambda + h_0\sin\lambda = 0. \qquad (4.3.1.9)$$

The solution of Equation (4.3.1.9) gives a set of positive eigenvalues λ_n numbered in ascending order (n = 1, 2,...). If $h_0 = 0$, then $\lambda_n = \pi\,(n - 1/2)$. Assuming that $B = 1$, expressions for eigenfunctions υ_n can be written as:

$$\upsilon_n(r) = \sin\lambda_n r \qquad (4.3.1.10)$$

The value of B is implicitly accounted for by the coefficients $c_n(t)$ in series (4.3.1.5). The functions υ_n form a full set of eigenfunctions which are orthogonal for $r \in [0,1]$. The orthogonality of functions υ_n follows from the relation:

$$\int_0^1 \upsilon_n(r)\upsilon_m(r)dr = \delta_{nm}\|\upsilon_n\|^2, \tag{4.3.1.11}$$

where:

$$\delta_{nm} = \begin{cases} 0 & n \neq m \\ 1 & n = m \end{cases},$$

$$\|\upsilon_n\|^2 = \frac{1}{2}\left(1 - \frac{\sin 2\lambda_n}{2\lambda_n}\right) = \frac{1}{2}\left(1 + \frac{h_0}{h_0^2 + \lambda_n^2}\right). \tag{4.3.1.12}$$

The eigenvalue $\lambda_0 = 0$ describes the trivial eigenfunction $\upsilon_0(r) = 0$. The orthogonality of υ_n allows us to expand known functions in Equations (4.3.1.3) and (4.3.1.4) in the series:

$$\tilde{P}(r) = \sum_{n=1}^{\infty} p_n \upsilon_n(r), \qquad \tilde{T}_0(r) = \sum_{n=1}^{\infty} q_n \upsilon_n(r), \qquad f(r) \equiv -\frac{r}{1+h_0} = \sum_{n=1}^{\infty} f_n \upsilon_n(r).$$

where:

$$p_n = \frac{1}{\|\upsilon_n\|^2}\int_0^1 \tilde{P}(r)\upsilon_n(r)dr, \qquad q_n = \frac{1}{\|\upsilon_n\|^2}\int_0^1 \tilde{T}(r)\upsilon_n(r)dr,$$

$$f_n = \frac{1}{\|\upsilon_n\|^2}\int_0^1 f(r)\upsilon_n(r)dr = -\frac{\sin\lambda_n}{\|\upsilon_n\|^2\lambda_n^2}.$$

This allows us to rewrite Equation (4.3.1.3) as:

$$\sum_{n=1}^{\infty}\left(\frac{dc_n(t)}{dt} + c_n(t)K\lambda_n^2\right)\upsilon_n(r) = \sum_{n=1}^{\infty}\left(p_n + f_n\frac{d\mu_0(t)}{dt}\right)\upsilon_n(r). \tag{4.3.1.13}$$

Both sides of Equation (3.3.1.13) are Fourier series of functions $\upsilon_n(r)$. Two Fourier series are equal if and only if their coefficients are equal. This implies that:

$$\frac{dc_n(t)}{dt} + c_n(t)K\lambda_n^2 = p_n + f_n\frac{d\mu_0(t)}{dt} \tag{4.3.1.14}$$

The initial condition for $c_n(t)$ follows from the initial condition for W:

$$c_n(0) = q_n + f_n\mu_0(0). \tag{4.3.1.15}$$

The solution of Equation (4.3.1.14), subject to initial condition (4.3.1.15), can be written as:

$$c_n(t) = \frac{p_n}{K\lambda_n^2} + \exp[-K\lambda_n^2 t]\left(q_n + f_n\mu_0(0) - \frac{p_n}{K\lambda_n^2}\right) + f_n\int_0^t \frac{d\mu_0(0)}{d\tau}\exp[-K\lambda_n^2(t-\tau)]d\tau. \tag{4.3.1.16}$$

Having substituted functions (4.3.1.16) and (4.3.1.10) into series (4.3.1.5) we obtain:

$$W(r,t) = \sum_{n=1}^{\infty}\{\frac{p_n}{K\lambda_n^2} + \exp[-K\lambda_n^2 t]\left(q_n + f_n\mu_0(0) - \frac{p_n}{K\lambda_n^2}\right) + f_n\int_0^t \frac{d\mu_0(\tau)}{d\tau}\exp[-K\lambda_n^2(t-\tau)]d\tau\}\sin\lambda_n r \tag{4.3.1.17}$$

and

$$u(r,t) = \frac{1}{1+h_0}r\mu_0(t) + \sum_{n=1}^{\infty}\{\frac{p_n}{K\lambda_n^2} + \exp[-K\lambda_n^2 t]\left(q_n + f_n\mu_0(0) - \frac{p_n}{K\lambda_n^2}\right) + f_n\int_0^t \frac{d\mu_0(\tau)}{d\tau}\exp[-K\lambda_n^2(t-\tau)]d\tau\}\sin\lambda_n r. \tag{4.3.1.18}$$

Remembering the definitions of f_n and u, the final solution of Equation (4.2.3) can presented in the form:

$$T(r,t) = \frac{1}{r}\sum_{n=1}^{\infty}\left\{\frac{p_n}{K\lambda_n^2} + \exp\left[-K\lambda_n^2 t\right]\left(q_n - \frac{p_n}{K\lambda_n^2}\right) - \frac{\sin\lambda_n}{\|v_n\|^2\lambda_n^2}\mu_0(0)\exp\left[-K\lambda_n^2 t\right] - \frac{\sin\lambda_n}{\|v_n\|^2\lambda_n^2}\int_0^t \frac{d\mu_0(\tau)}{d\tau}\exp\left[-K\lambda_n^2(t-\tau)\right]d\tau\right\}\sin\lambda_n r + T_{eff}(t). \tag{4.3.1.19}$$

We took into account that $T_{eff}(t) = k_l\mu_0(t)/(hR_d)$. If $T_0(r)$ is twice differentiable, then the series in (4.3.1.17), (4.3.1.18) and (4.3.1.19) converge absolutely and uniformly for all $t \geq 0$ and $r \in [0,1]$ since

$$|p_n| < \text{const}, \qquad |q_n| < \frac{\text{const}}{\lambda_n^2}, \qquad |\sin\lambda_n r| \leq 1, \qquad \exp(-K_0\lambda_n^2 t) \leq 1$$

and $\lambda_n^{-2} < n^{-2}$ for $n > 1$. It can be shown that $\lambda_n > \pi(n-1)$. Hence for $n > 1$:

$$\lambda_n > n\pi(1-\frac{1}{n}) > \frac{n\pi}{2} > n. \tag{4.3.1.20}$$

When μ_0 = const, $P(r) = 0$, T_{eff} = const and $k_l \to \infty$ Equation (4.3.1.19) reduces to (Sazhin and Krutitskii, 2002):

$$T_s = T_g + (T_{s0} - T_g)\exp\left(-\frac{3ht}{c_l\rho_l R_d}\right). \tag{4.3.1.21}$$

where $T_s\,(t=0) = T_{s0}$.

The same expression could be obtained directly from the energy balance at the surface of the droplet, assuming that there is no temperature gradient inside the droplet:

$$\frac{4}{3}\pi R_d^3 \rho_l c_l \frac{dT_s}{dt} = 4\pi R_d^2 h\left(T_g - T_s\right) \tag{4.3.1.22}$$

4.3.2 Case h $(t) \neq$ const (general case)

Let us assume that:

$$H(t) = h_0 + h_1(t), \tag{4.3.2.1}$$

where h_0 = const $\neq$ -1 and $h_1(t)$ is an arbitrary function of time. This enables us to use the results obtained in the previous section for the general analysis. If $h_0 = 0$ then $H(t) = h_1(t)$.

Having substituted (4.3.2.1) into conditions (4.2.6) we can generalise conditions (4.3.1.1) as:

$$\left.\begin{array}{ll} \dfrac{\partial u}{\partial r} + h_0 u = -h_1(t)u + \mu_0(t) \equiv \mu_{g0}(t) & \text{when } r = 1 \\ u = 0 & \text{when } r = 0 \\ u(t=0) = rT_0(rR_d) \equiv \tilde{T}_0(r) & \text{when } 0 \le r \le 1 \end{array}\right\} \tag{4.3.2.2}$$

If $\mu_{g0}(t)$ is a known function then conditions (4.3.2.2) reduce to conditions (4.3.1.1) with $\mu_0(t)$ replaced by $\mu_{g0}(t)$. The analytical solution of the problem would then be given by series (4.3.1.18) with $\mu_0(t)$ replaced by $\mu_{g0}(t)$. Integration of the last term of this equation by parts allows us to write:

$$u(r,t) = \frac{r\mu_{g0}(t)}{1+h_0} + U(r,t) + \sum_{n=1}^{\infty}\{f_n\mu_{g0}(t) - K\lambda_n^2 f_n \int_0^t \mu_{g0}(\tau)\exp[-K\lambda_n^2(t-\tau)]d\tau\}\sin\lambda_n r, \tag{4.3.2.3}$$

where:

$$U(r,t) = \sum_{n=1}^{\infty}\left\{\frac{pn}{K\lambda_n^2} + \exp[-K\lambda_n^2 t]\left(q_n - \frac{pn}{K\lambda_n^2}\right)\right\}\sin(\lambda_n r). \tag{4.3.2.4}$$

Remembering the definition of f_n and Equation (4.3.1.13) we can rewrite (4.3.2.3) as:

$$u(r,t) = U(r,t) - \int_0^t \mu_{g0}(\tau)G(t-\tau,r)d\tau, \tag{4.3.2.5}$$

where:

$$G(t,r) = K\sum_{n=1}^{\infty}\lambda_n^2 f_n \exp[-K\lambda_n^2 t]\sin\lambda_n r = -K\sum_{n=1}^{\infty}\frac{\sin\lambda_n}{\|v_n\|^2}\exp[-K\lambda_n^2 t]\sin\lambda_n r. \tag{4.3.2.6}$$

One can show that $G(t, r)$ is continuous at $t > 0$. For $t \to +0$ the following inequality holds:

$$|G(t,r)| < \frac{c}{\sqrt{t}} \tag{4.3.2.7}$$

uniformly with respect to $r \in [0,1]$ (see Appendix 1).

Remembering that

$$\mu_{g0}(t) = M(t) - h_1(t)u(1,t)$$

we can rewrite (4.3.2.5) in the form:

$$u(r,t) = U(r,t) - \int_0^t [M(\tau) - h_1(\tau)u(1,\tau)]G(t-\tau,r)d\tau\,. \tag{4.3.2.8}$$

This formula gives us an integral representation of the solution of the problem (4.2.5), (4.3.2.2). For $r = 1$ integral representation (4.3.2.8) reduces to the integral equation for the function $u(1, t)$:

$$u(1,t) = U(1,t) - \int_0^t [M(\tau) - h_1(\tau)u(1,\tau)]G(t-\tau,1)d\tau, \tag{4.3.2.9}$$

where:

$$G(t,1) = -K\sum_{n=1}^{\infty}\frac{\sin^2\lambda_n}{\|\upsilon_n\|^2}\exp[-K\lambda_n^2 t] = -2K\sum_{n=1}^{\infty}\frac{\lambda_n^2}{h_0^2+h_0+\lambda_n^2}\exp[-K\lambda_n^2 t]. \tag{4.3.2.10}$$

When deriving Equation (4.3.2.10) we took into account that:

$$\sin^2\lambda_n = \frac{1}{1+\cot^2\lambda_n} = \frac{1}{1+(h_0/\lambda_n)^2} = \frac{\lambda_n^2}{\lambda_n^2+h_0^2}.$$

If $h_0 = 0$ then $G(t,1) = -2K\sum_{n=1}^{\infty}\exp[-K\lambda_n^2 t]$, where $\lambda_n = \pi(n-\frac{1}{2})$. As shown in Appendix 1, the kernel $G(t, 1)$ is continuous if $t \neq 0$. It has integrable singularity $G(t, 1) \propto t^{-1/2}$ when $t \to +0$. The integral Equation (4.3.2.9) is the so-called Volterra integral equation of the second kind. This equation has a unique solution, although this solution cannot be found in an explicit form. The scheme of its numerical solution is described in Appendix 2. Once the solution of this equation has been found we can substitute it into integral representation (4.3.2.8) and find the required solution of the initial and boundary value problem (4.2.5), (4.3.2.2). The required distribution of T is found as $T = u/r$. In the case when $h_1(t) = 0$ this solution reduces to that given by (4.3.1.19). To simplify the numerical solution of the equation it is reasonable to take $h_0 = 0$. In this case $\lambda_n = \pi(n-(1/2))$ and $\|\upsilon_n\|^2 = 1/2$ in all equations.

4.3.3 Case of almost constant h (t)

In the case of almost constant $h(t)$ we can use represent it as (4.3.2.1) and assume that $h_1(t) = \varepsilon\eta(t)$, where ε is a small parameter. In this case the perturbation theory can be applied to the analysis of Equation (4.3.2.9). We look for the solution $u(1, t)$ of this equation in the form:

$$u(1,t) \equiv \nu(t) = \nu_0(t) + \varepsilon\nu_1(t) + \varepsilon^2\nu_2(t) + \ldots\ldots = \sum_{j=0}^{\infty} \varepsilon^j \nu_j(t). \qquad (4.3.3.1)$$

The convergence of series (4.3.3.1) is discussed in Appendix 3.

The substitution of series (4.3.3.1) into the integral Equation (4.3.2.9) gives:

$$\sum_{j=0}^{\infty} \varepsilon^j \nu_j(t) = U(1,t) - \int_0^t \left[M(\tau) - \eta(\tau) \sum_{j=0}^{\infty} \varepsilon^{j+1} \nu_j(\tau) \right] G(t-\tau,1)\,d\tau. \qquad (4.3.3.2)$$

The terms with the same powers of ε in the left-hand and the right-hand sides of Equation (4.3.3.2) should be equal. Hence, Equation (4.3.3.2) reduces to the following system of equations:

$$\varepsilon^0: \qquad \nu_0(t) = U(1,t) - \int_0^t M(\tau) G(t-\tau,1)\,d\tau \qquad (4.3.3.3)$$

$$\varepsilon^1: \qquad \nu_1(t) = \int_0^t \eta(\tau)\nu_0(\tau) G(t-\tau,1)\,d\tau \qquad (4.3.3.4)$$

.....

.....

$$\varepsilon^j: \qquad \nu_j(t) = \int_0^t \eta(\tau)\nu_{j-1}(\tau) G(t-\tau,1)\,d\tau \qquad (4.3.3.5)$$

Formulae (4.3.3.3)-(4.3.3.5) allow us to find all functions $\nu_j(t)$ step-by-step. Substitution of these functions into series (4.3.3.1) gives the solution of the integral Equation (4.3.2.9) in the form of a power series in ε. One can show that this series converges absolutely and uniformly for $t \in [0, t_0]$, if t_0 is a fixed number and ε (depending on t_0) is small enough (see Appendix 3). Substitution of this solution into integral representation (4.3.2.8) gives the solution of the problem (4.2.5), (4.3.2.2) for $u(r, t)$. The solution of the original problem for $T(r, t)$ is $T(r, t) = u(r, t)/r$.

Keeping only linear terms in the series (4.3.3.1) we obtain the approximate solution of Equation (4.3.2.9) with accuracy $O(\varepsilon^2)$:

$$u(1,t) = U(1,t) - \int_0^t M(\tau) G(t-\tau,1) d\tau + \varepsilon \int_0^t \eta(\tau) \upsilon_0(\tau) G(t-\tau,1) d\tau. \qquad (4.3.3.6)$$

4.4 Applications

The theory developed in the previous sections is applied to a specific problem of heating fuel droplets in diesel engines (Sazhin et al, 2001; Sazhina et al, 2000). We take gas pressure p = 6 MPa, $T_g = T_{ext}$ = 1000 K and 2000 K, k_g = 0.061 W/(m K), T_{s0} = 300 K, ρ_l = 846 kg/m^3, M_a = 28.97 kg/kmol, M_f = 198 kg/kmol, k_l = 0.14 W/(m K), c_l = 2 kJ/(kg K), a_v =15.5274, b_v = 5383.59, L = 254 kJ/kg and R_d = 50 μm and R_d = 25 μm (Chin and Lefebvre, 1983; Lefebvre, 1989; Pitcher et al, 1990; Comer et al, 1999). Experimental values of the index of absorption κ were presented in Chapter 3 (see Figure 3.1). Droplets are assumed to be stationary (Re_d = 0). The generalisation of the results to the case of moving droplets would require the modification of h and introducing k_{eff} instead of k_l as discussed in Chapter 2 (Section 2.2.1.1). We consider the case h = const, which allows us to focus the analysis on formula (4.3.1.19). This formula needs to be used in combination with formula (3.4.2) for $\dot{R}_d$ and remembering the definition of T_{eff}. As a first step of the iterative process, it is assumed that $\dot{R}_d$ = 0. This leads to the conditions: μ_0 = const and T_{eff} = const. As a result, formula (4.3.1.19) can be considerably simplified as the integral in its right hand side becomes equal to zero. This solution is exact when the effects of evaporation can be ignored (initial stage of droplet heating). The calculated values of droplet surface temperature allow us to find the expressions for $\dot{R}_d$ and T_{eff} as functions of time and substitute them into the right hand side of formula (4.3.1.19). Thus we find a more accurate value of $T(r, t)$. As follows from our calculations, the iterations converge quite quickly, and subsequent iterations practically do not increase the accuracy of the results.

We start with calculating the radial distribution of the radiation power absorbed inside droplets. The approximations for $w(r)$ presented in Equations (2.2.2.18) and (2.2.2.19) have been used, using the actual measured points of index of absorption shown in Figure (3.1). We restrict our analysis to the unboiled low sulphur ESSO AF1313 diesel fuel used in cars. Analysis of other types of fuel leads to essentially similar results. The plots of $P(r)$ versus r for R_d = 50 μm, R_d = 25 μm and $T_g = T_{ext}$ = 1000 K, $T_g = T_{ext}$ = 2000 K are shown in Figure (4.1). The shape of these curves is rather similar to the one reported in Dombrovsky and Sazhin (2003b), where slightly less accurate results of

measurements of κ of diesel fuel and the simplified approximation of κ have been used. The difference between the values of κ predicted by Dombrovsky and Sazhin (2003b) and our calculations did not exceed 9%. A typical feature of all plots is the presence of two maxima in $P(r)$: one near the surface of the droplet, and another at $r = 1/n \approx 1/1.46 = 0.68$. The discontinuity of the slope at $r = 1/n$ is related to the fact that all rays entering the droplet from outside, will concentrate in the cone with the half angle $\theta = \sin^{-1}(1/n)$ after refraction at the surface. The spheres of radii $r = 1/n$ are the maximal spheres inside this cone. The results show that increasing the size of droplet radii leads to an increase in the value of $P(r)$. Hence, larger droplets are expected to absorb more thermal radiation due to their size, and also to have a larger concentration of absorbed radiation. These results are consistent with the prediction of the overall absorption efficiency factor reported in Dombrovsky et al (2001). As expected, the increase in external temperature leads to a considerable increase of $P(r)$.

The application of formula (4.3.1.19) requires truncation of the series. As will be shown later, this series converges rather quickly. As a starting point, however, we take 25 terms of this series (the higher order terms are in most cases less than the round-up errors of the computer). Assuming $T_{\text{eff}} = T_{\text{ext}} = \text{const} = 2000$ K, $T(r, t = 0) = T_d = 300$ K and $R_d = 50$ μm the plots of $T(r, t)$ versus r are presented in Figure (4.2) for $t = 0.01$, 0.1, 1 and 5 ms both with and without radiation. As follows from this figure, the effect of radiation leads to a small (about 10%) increase in the droplet temperature at $t = 5$ ms. At shorter times this increase is smaller. Note that radiation leads to an increase in temperature throughout the whole droplet as expected. At shorter times, droplet temperature increases in the immediate vicinity of its surface only, in agreement with Lavieille et al (2002).

The plots of droplet surface temperature versus time for the same values of gas temperature, initial droplet temperature and droplet radii, as in Figure (4.2), are shown in Figure (4.3). Similarly to Figure (4.2), the plots taking and not taking into account the effects of thermal radiation are presented. In contrast to Figure (4.2), the cases $T_{\text{eff}} = T_{\text{ext}} = \text{const}$ (zeroth iteration) and $T_{\text{eff}} = T_{\text{eff}}$ (t), but $T_{\text{ext}} = \text{const}$ (first iteration) are presented. The plots for the second and higher iterations are practically indistinguishable from those for the first iteration.

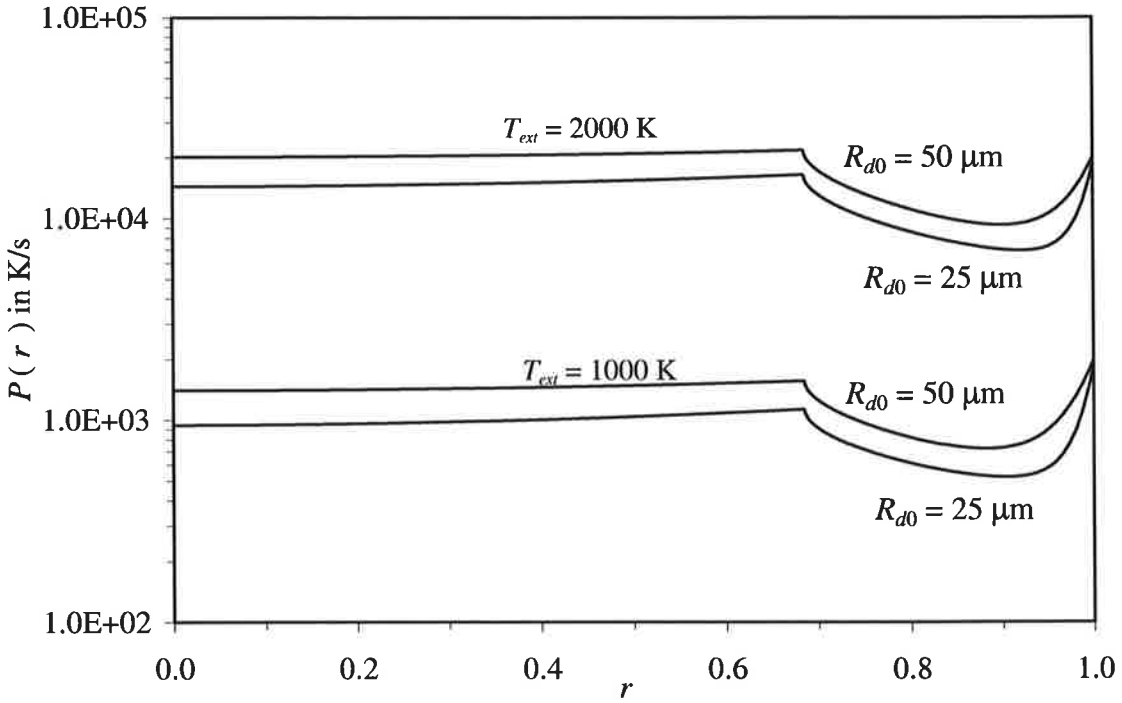

Fig. 4.1 Plots of thermal radiation power density absorbed by diesel fuel droplets normalized by the product $c_l\rho_l$ versus normalised radius. Droplet radii are taken equal to 25 μm and 50 μm; external temperatures are taken equal to 1000 K and 2000 K (indicated near the curves). The curves are presented for unboiled low sulphur ESSO AF1313 diesel fuel used in cars.

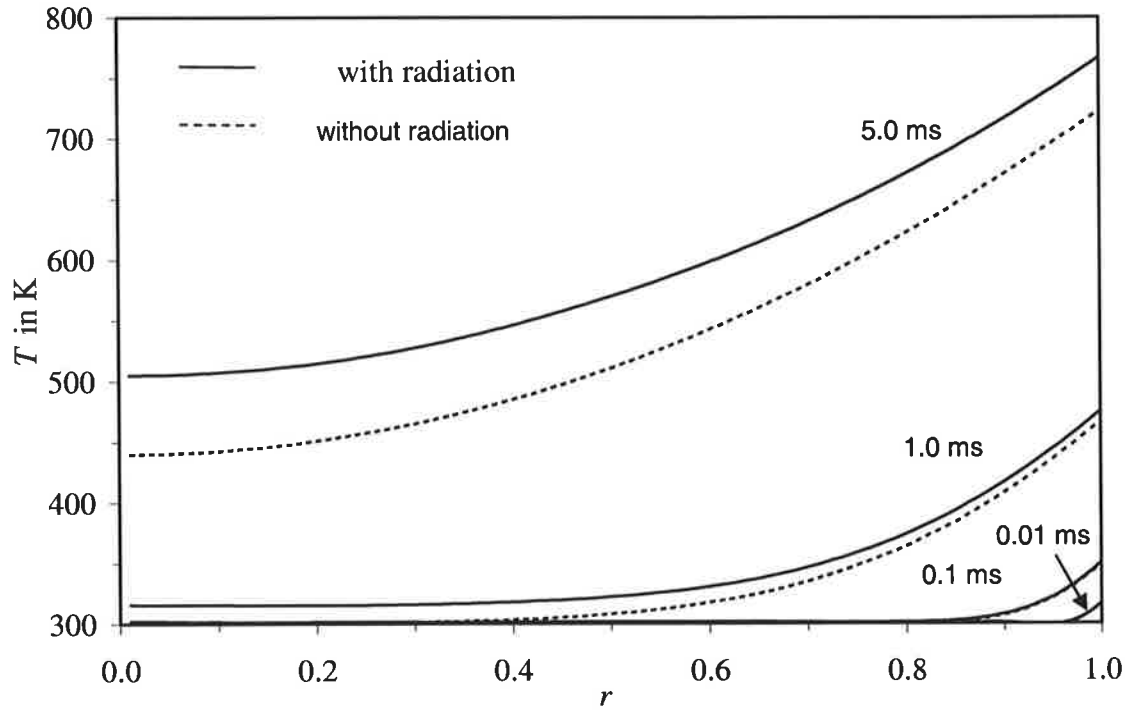

Fig. 4.2 Plots of droplet temperature versus normalized radius r for various times (indicated near the curves). Droplet radius is taken equal 50 μm. Gas and external temperatures are taken equal 2000 K. Curves for the cases when thermal radiation was ignored (dashed) and taken into account (solid) are presented.

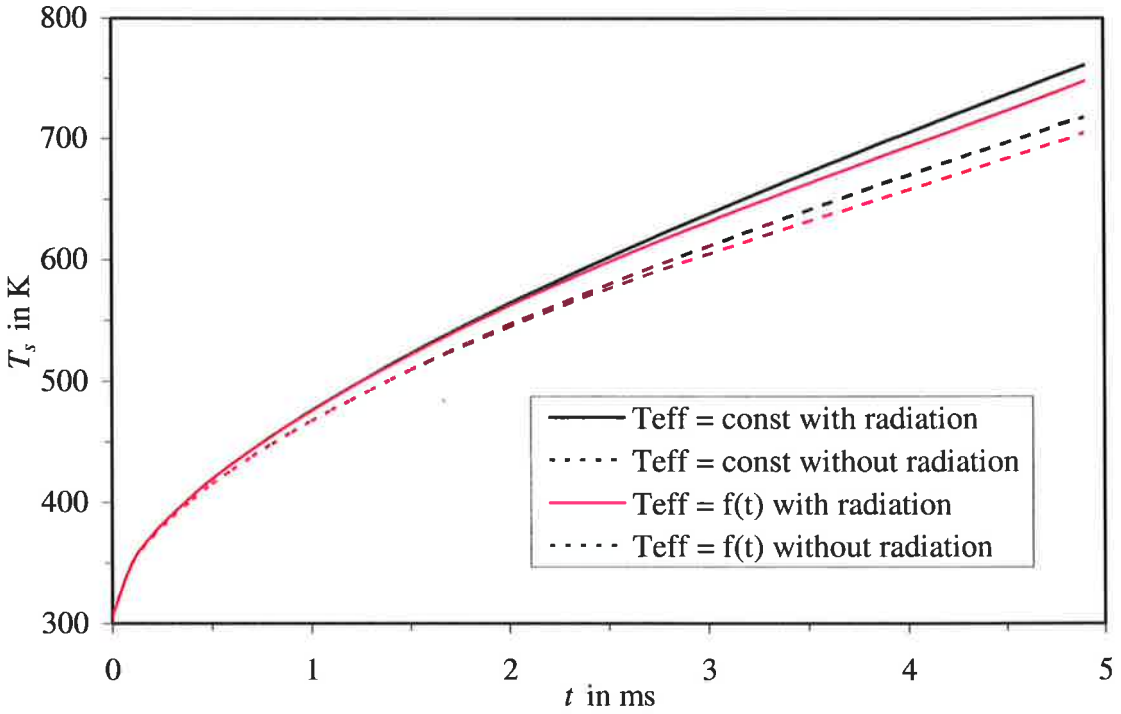

Fig. 4.3 Plots of droplet surface temperature versus time for the case when T_{eff} = const (zeroth iteration) and T_{eff} = T_{eff} (t) (first iteration). Droplet radius and gas and external temperatures are taken equal 50 μm and 2000 K respectively. Curves for the cases when thermal radiation was ignored (dashed) and taken into account (solid) are presented.

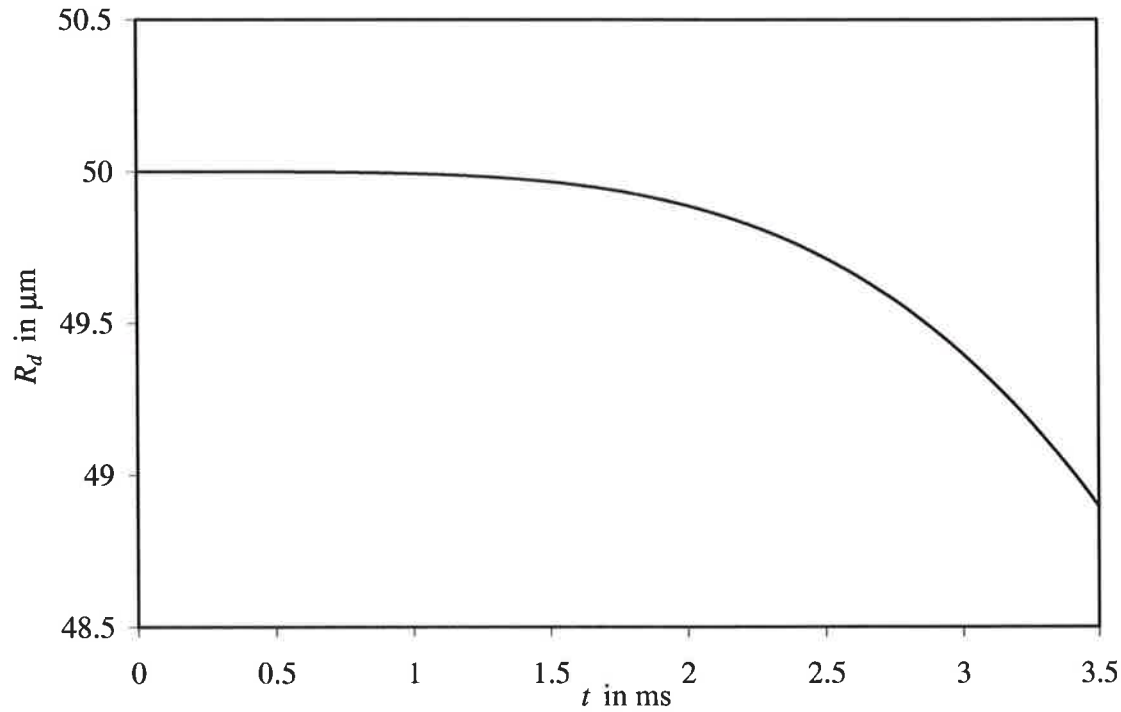

Fig. 4.4 Plots of droplet radius versus time for the case when the initial droplet radius and gas and external temperatures are equal 50 μm and 2000 K respectively. Effects of thermal radiation are taken into account.

In agreement with Figure (4.2), Figure (4.3) shows that the effect of thermal radiation leads to a noticeable (up to about 10 %) increase in droplet surface temperature. This effect is even more pronounced for higher gas temperatures. Comparing the predictions of the zeroth and first approximations, we can see that at $t \leq 2$ ms they are practically undistinguishable. This means that the effects of droplet evaporation at $t \leq 2$ ms can be ignored. This is confirmed by Figure (4.4) where the plot of R_d versus time, as predicted by formula (3.4.2), is shown. As follows from this figure, the decrease in droplet radius at $t \leq 2$ ms is less than 0.3 %. This justifies our approximation that R_d = const.

Now we can investigate the influence of the number of terms in the series taken on the accuracy of the predicted values of droplet temperature. The plots of $T(r)$ versus r for t = 1 ms, $T_{eff} = T_{ext}$ = const = 2000 K, $T(r, t = 0) = T_d$ = 300 K, R_d = 50 μm and several numbers of terms in the series taken are shown in Figure (4.5). The effect of radiation was taken into account. As can be seen in this figure, the prediction of the series with just 3 terms is practically indistinguishable from the prediction of the series with 25 terms. This agrees with the prediction of Table (4.1), where the results of our analysis of the number of terms required for $T_{eff} = T_{ext}$ = 2000 K and the average errors are shown.

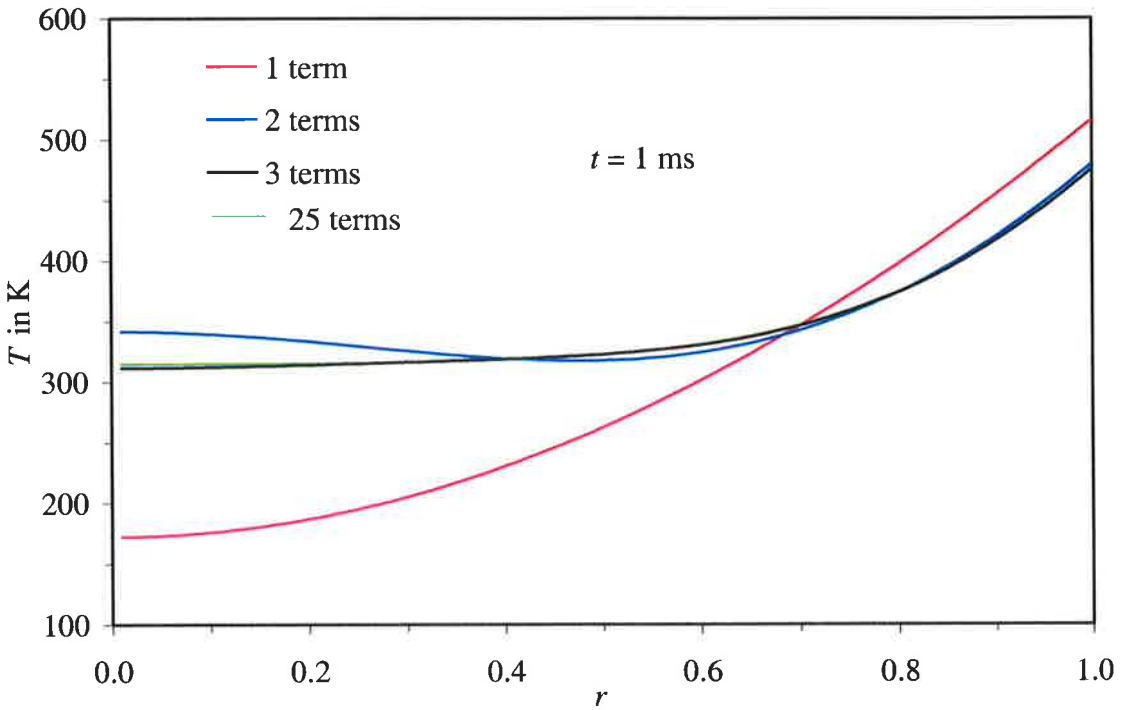

Fig. 4.5 Plots of droplet temperature versus normalized radius r for t =1 ms. The plots refer to the case when 1, 2, 3 and 25 terms in the series are taken. Droplet radius and gas and external temperatures are taken equal 50 μm and 2000 K respectively. The contribution of thermal radiation is taken into account.

The line 'number of terms' indicates the number of terms required in order for the average error in the estimate of the series does not exceed 1%. The actual average error is indicated in the same table. Note that if we consider the errors in the estimate of T_s rather than average errors, then the number of terms required to meet the same criterion would be slightly different. For R_d = 50 μm and t = 0.01, 0.1, 1 and 5 ms these numbers would be 12, 5, 2 and 1 respectively. For R_d = 25 μm and t = 0.01, 0.1, 1 and 5 ms these numbers would be 8, 3, 1 and 1 respectively. Similar results to those in Table (4.1) are shown in Table (4.2) for R_d = 10 μm and R_d = 5 μm.

R_d (μm)	50				25			
t (ms)	0.01	0.1	1	5	0.01	0.1	1	5
Number of terms	6	5	3	2	6	4	2	2
Average error (%)	0.94	0.61	0.14	0.16	0.63	0.22	0.07	0.02

Table 4.1 Number of terms and the predicted average error from series (4.3.1.19). T_{eff} = T_g = 2000 K, R_d = 50 μm, 25 μm.

R_d (μm)	10				5			
t (ms)	0.01	0.1	1	5	0.01	0.1	1	5
Number of terms	5	4	3	2	4	4	2	2
Average error (%)	0.51	0.83	0.75	0.04	0.93	0.45	0.21	0.08

Table 4.2 Number of terms and the predicted average error from series (4.3.1.19). T_{eff} = T_g = 2000 K, R_d = 10 μm, 5 μm.

The corresponding number of terms, if we consider the errors in the estimate of T_s are also slightly different from the average errors. For R_d = 10 μm and t = 0.01, 0.1, 1 and 5 ms these numbers would be 11, 7, 3 and 2 respectively. For R_d = 5 μm and t = 0.01, 0.1, 1 and 5 ms these numbers would be 8, 4, 2 and 2 respectively. As follows from these tables, the required number of terms increases with decreasing time and increasing R_d.

In Table (4.3) the results similar to those shown in Table (4.1), but for the initial distribution of droplet temperature predicted by Equation (4.3.1.19) for t = 1 ms are shown. This can approximate further heating of an initially preheated droplet.

R_d (μm)	50				25			
t (ms)	0.01	0.1	1	5	0.01	0.1	1	5
Number of terms	3	2	2	2	2	2	2	2
Average error (%)	0.38	0.92	0.45	0.14	0.05	0.07	0.04	0.02

Table 4.3 Number of terms and the predicted average error from series (4.3.1.19). T_{eff} = T_g = 2000 K, R_d = 50 μm, 25 μm. The initial distribution of droplet temperature at t = 1 ms

As can be seen from this table, the number of terms in the series required for practical applications is noticeably less than that in the case of modelling of heating of a cold droplet. As in the case shown in Table (4.1), the number of terms required decreases with decrease of droplet radius. In fact if droplet radii less than 10 μm are considered then just one term in the series would be sufficient to ensure the error of less than 1 %. If we consider the errors in the estimate of T_s rather than average errors, then the number of terms required to get an error of less than 1 % would be slightly different. For R_d = 50 μm and t = 0.01, 0.1, 1 and 5 ms these numbers would be 3, 2, 2 and 1 respectively. For R_d = 25 μm and all times one term would be sufficient. This has an important implication when we incorporate the results into a CFD code. If we ignore the effects of very initial heating of droplets, then 3 terms of the series in (4.3.1.19) would be more than enough to ensure that the error of calculations is well below 1 %.

Plots similar to those shown in Figures (4.2)-(4.5) can be shown for other values of T_{eff} and T_{ext} and R_d. One of the most important characteristics following from these curves would be the upper time limit (t_{up}) over which the approximations T_{eff} = const and R_d = const are valid. The values of t_{up} for various T_{eff} and R_d are shown in Table (4.4)

The values of t_{up} have been estimated as those for which the decrease in R_d has not exceeded 0.2 %. As follows from this table, the values of t_{up} decrease with decreasing R_d and increasing T_{eff}. Note that even in the most unfavourable situation the values of t_{up} are large enough to play an important role in the process of droplet heating in diesel engines (Sazhin et al, 2001; Sazhina et al, 2000). Note that taking into account the contribution of $\dot{R}_d$ leads to a much larger decrease in T_s than in R_d as expected. This provides additional support to our assumption that R_d = const, but $\dot{R}_d \neq 0$.

R_d (μm)	50		25	
T_{eff} (K)	1000	2000	1000	2000
t_{up} (ms)	6.4	2.0	1.6	0.5
Decrease in predicted T_{eff} (%)	1.19	0.99	1.19	1.71

Table 4.4 The upper time limit (t_{up}) for the approximation T_{eff} = const and R_d = const.

As in Chapter 3, the lifetimes of droplets predicted by Figures (4.2) - (4.4) are longer than those, which we would expect in diesel engines. This is attributed to a simplified formulation of the problem used in this chapter to illustrate the processes described by the analytical solutions. In CFD simulations of the real-life diesel engine, using the solution described in this chapter, and taking into account droplet break-up processes, the predicted droplet life times correspond to those actually observed (see Chapters 6 and 7)

4.5 Conclusions of Chapter 4

Analytical solutions of the heat conduction equation inside a spherical droplet have been suggested. The droplet has been assumed to be heated by convection and radiation from

the surrounding hot gas - a situation typical in many engineering applications (e.g. in-cylinder applications in IC engines). Initial droplet evaporation, the effects of time dependent gas temperature and the convection heat transfer coefficient have been taken into account. Three approximations for the convection heat transfer coefficient have been considered. Firstly, this coefficient has been assumed constant and an explicit formula for the time dependent distribution of temperature inside droplets has been derived. Secondly, the general case of time dependent convection heat transfer coefficient has been considered. In this case the solution of the original differential equation has been reduced to the solution of the Volterra integral equation of the second kind. A numerical scheme for the solution of this equation has been suggested. Thirdly, the case of almost constant convection heat transfer coefficient has been considered. In this case the problem has been solved using the perturbation theory. A set of solutions corresponding to ascending approximations have been obtained.

Results referring to the case of constant convection heat transfer coefficient have been applied to a typical problem of fuel droplet heating in a diesel engine. Results of the measurements of index of absorption of low-sulphur ESSO AF1313 diesel fuel used in cars have been used in the analysis. Results referring to other types of diesel fuel (see Chapter 3 Section 3.2) are expected to lead to similar conclusions. It has been shown that the effects of radiation lead to a noticeable increase in droplet temperature, especially at larger times and larger droplet radii. The distribution of temperature inside droplets has been shown to be different from constant values, as assumed in the isothermal model. This implies that finite thermal conductivity of fuel droplets and the effects of radiation need to be taken into account when modelling droplet heating in diesel engines. It has been shown that the range of times when the model is applicable decreases with decreasing droplets' initial radii, and increasing ambient gas temperature.

5. TRANSIENT HEATING AND EVAPORATION OF DIESEL FUEL DROPLETS: NUMERICAL ALGORITHMS

5.1 Introduction

Since the pioneering monograph by Spalding (1963), the problem of modelling heating and evaporation of droplets has been widely discussed in the literature (Faeth, 1983; Kuo, 1986; Lefebvre, 1989; Abramzon and Sirignano, 1989; Griffiths, 1995; Aggarwal, 1998; Borman and Ragland, 1998; Sirignano, 1999; Mukhopadhyay and Sanyal, 2001; Bird et al, 2002; Miliauskas, 2003; Abramzon and Sazhin, 2005). In most practical engineering applications in CFD codes, however, only rather simplistic models for droplet heating have been used. These models have been based on the assumption that the thermal conductivity of liquid is infinitely high and the temperature gradient inside droplets can be ignored (see e.g. Sazhin et al, 2001; Sazhina et al, 2000; Utyuzhnikov, 2002). This simplification of the model was required because of the fact that droplet heating and evaporation had to be modelled alongside the effect of turbulence, combustion, droplet break-up and related phenomena in realistic 3D enclosures. Hence, finding a compromise between the complexity of the models and their computational efficiency is the essential precondition for successful modelling. Bertoli and Migiaccio (1999) were perhaps the first who drew attention to the fact that the accuracy of CFD computations of heating, evaporation and combustion of diesel fuel sprays could be substantially increased if the assumption of infinitely high thermal conductivity of liquid is relaxed. They suggested that the numerical solution of the heat conduction equation inside the droplets is added to the solution of other equations in a CFD code. Although this approach is expected to increase the accuracy of CFD predictions, the additional computational cost might be too high for practical applications.

An alternative approach to taking into account the effect of finite thermal conductivity and recirculation inside the droplets have been suggested by Dombrovsky and Sazhin (2003a). This model is based on the parabolic approximation of the temperature profiles inside the droplets. This approximation does not satisfy the heat conduction equation with appropriate boundary conditions, but satisfies the equation of thermal balance at the droplet surfaces. Comparison with numerical solutions of the transient problem for moving droplets has shown the applicability of this approximation to modelling the heating and evaporation processes of fuel droplets in diesel engines. The simplicity of the model makes it practically convenient for implementation into multidimensional CFD codes to replace the abovementioned model of isothermal droplets. Preliminary

results of the implementation of the simplified version of this model into a research version of the CFD code VECTIS of Ricardo Consulting Engineers have been demonstrated in Sazhin et al (2002).

Instead of solving numerically the heat conduction equation inside a droplet, or using a simplified model based on the parabolic approximation, we think about the development of a numerical code based on the analytical solutions of this equation. A number of analytical solutions for a spherically symmetric problem have been obtained and discussed in Carslaw and Jaeger (1986), Luikov (1968), Kartashov (2001), Sazhin and Krutitskii (2003) and Sazhin et al (2004b). In most cases these analytical solutions have been presented in the form of converging series. Extensive analysis of these solutions and their generalizations in view of specific applications to the problem of diesel fuel droplet heating were discussed in Chapter 4. A semi-analytical model for droplet evaporation reported in Mukhopadhyay and Sanyal (2005) is similar to that reported in Chapter 4, although the effects of thermal radiation were not taken into account, and a simplified form of the analytical solution was used. The problem of modelling of heating and evaporation of droplets taking into account the effect of finite liquid thermal conductivity is closely linked with the problem of modelling of heating and evaporation of multicomponent droplets (e.g. Sirignano, 1999; Zeng and Lee, 2002; Torres et al, 2003). It is anticipated that the solutions obtained in Chapter 4 could be generalized to take into account the effects of multicomponent droplets, although the discussion of these possible generalization is beyond the scope of this thesis.

The finite liquid thermal conductivity models (based on numerical or analytical solutions of the spherical symmetrical heat conduction equation) could be generalised to take into account the internal recirculation inside droplets. This could be achieved by replacing the actual thermal conductivity of liquid k_l by the so called effective thermal conductivity $k_{eff} = \chi k_l$, where the coefficient χ can be approximated by Equation (2.2.1.1.1).

The main objective of this chapter is to investigate the applicability of the results of the analysis of the new numerical algorithms to the problem of numerical modelling of heating and evaporation of droplets in engineering CFD codes. They are based on the incorporation of new analytical solutions of the heat conduction equation inside the droplets into a numerical code (constant or almost constant h), or replacement of the numerical solution of this equation by the numerical solution of the integral equation (arbitrary h), which were discussed in Chapter 4. The prediction of these numerical

algorithms are compared with other numerical algorithms based on the numerical solution of the discretised heat conduction equation (NSDE) inside the droplet, the parabolic temperature profile model and the assumption of no temperature variation inside the droplet. Both convective and radiative heating will be taken into account.

As in Chapters 3 and 4 the testing of the numerical algorithms will be undertaken for idealized situations (no droplet break-up) and sometimes for extreme rather than typical values of parameters. The latter will allow facilitate a better view of the difference in the performance of different algorithms. This approach to testing will help to separate the effects of heating and evaporation from other processes, which take place in diesel engines (air entrainment by droplets and droplet break-up).

I will start with the analysis of droplet heating and evaporation based on the assumption of no temperature variation inside the droplet ($k_l = \infty$) in Section 5.2. The numerical algorithms, based on NSDE, the analytical solutions of the heat conduction equation inside the droplets for constant or almost constant h, the numerical solution of the integral equation (arbitrary h) and the parabolic temperature profile model, for incorporation into CFD codes are discussed in Section 5.3. The performances of these algorithms are discussed in Section 5.4. In Section 5.5 the comparative analysis of these algorithms is given. The main results of the chapter are summarised in Section 5.6.

Some preliminary results of this chapter were published in Sazhin, Abdelghaffar et al (2004c) and Sazhin, Abdelghaffar et al (2005a).

5.2 Conventional algorithm ($k_l = \infty$)

We start with the analysis of a single droplet placed in a hot gas at given temperature T_g. The influence of the droplet on the state of the surrounding gas is ignored. This can be generalized to the mondisperse spray case when a number of identical droplets are considered. The temperature variation inside the droplet is ignored. This is similar to the assumption that the droplet thermal conductivity is large when compared with the gas thermal conductivity. In this case modelling of the heating of droplets by convection and radiation from the surrounding hot gas and their evaporation is reduced to the solution of the system of Equations (3.4.1) and (3.4.2).

An assumption was made that the fuel molar mass fraction far from the droplet is negligible. We also took into account the temperature dependence of liquid fuel density, its specific heat capacity and latent heat of evaporation. The temperature dependence of liquid fuel, fuel vapour, gas viscosity, air and gas thermal conductivity and gas and fuel

vapour specific heat capacity at constant pressure were taken into account. Reference temperature for fuel vapour-air mixture near droplet surface T_{ref} was approximated as (Lefebvre, 1989; Hubbard et al, 1975):

$$T_{ref} = \frac{T_g + 2T_d}{3} \tag{5.2.1}$$

In most CFD codes, including the most recent version of VECTIS (VECTIS 3.6) the fuel droplets are assumed to be grey and opaque. In the code presented, a model which takes into account the semi-transparency of droplets based on Equation (2.2.2.10) (Dombrovsky et al, 2001) was used. In this model the emissivity of fuel droplets ε_d in Equation (3.4.1) is replaced by the Λ_0, defined as in Equation (2.2.2.10).

Dombrovsky et al (2001) obtained the functions a (T_g) and b (T_g) in the expression Λ_0 based on measurements of the index of absorption of a typical diesel fuel. More detailed measurements of the index of absorption of liquid diesel fuel in the range of wavelength 0.2-6 μm and in a wider gas temperature range were used by present work. This allowed us to get more accurate expressions for a (T_g) and b (T_g) as discussed in Chapter 3.

Three cases were considered: $\varepsilon_d = 0$ (no radiation); $\varepsilon_d = 1$ (black opaque droplet) and $\varepsilon_d = \Lambda_0$ (semi-transparent droplet).

Two solvers were used for the solution of this system of Equations (3.4.1)-(3.4.2). The first was based on the Runge-Kutta method with adaptive step size control (Press et al, 1989). The second solver was taken from the public domain site of LLNL (http://www.llnl.gov/CASC/odepack/). Both methods gave practically the same results as shown in Figure (3.5).

The value of thermal conductivity of liquid diesel fuel changes from 0.145 W / (m K) to 0.02 W / (m K) when the droplet temperature increases from 300 to 725.9 K (Reid et al, 1997). Based on these values, the ratio of the internal thermal resistance of the droplet to the boundary layer thermal resistance increases with temperature. In this case the temperature variation inside the droplet has to be taken into account. Hence the applicability of the model described above to diesel engines environment can be questioned because it is based on the assumption of no temperature variation inside the droplets. In the next sections new algorithms of heating and evaporation of diesel fuel droplets based on realistic values of diesel fuel thermal conductivity and, taking into account the temperature variation inside the droplet, are described.

5.3 Numerical algorithms ($k_l \neq \infty$)

Assuming that the temperature distribution inside a droplet is spherically symmetrical and taking into account the effects of radiation, the transient heat conduction equation inside the droplet (4.2.1) can be used. If the droplet is heated by convection from the surrounding gas, and cooled down due to evaporation, the boundary and initial condition of Equation (4.2.1) can be written as in Equation (4.2.2).

We assume that the temperature of gas T_g (t) is given. The influence of droplets on its value is ignored. This approximation would be justified in the case when the concentration of droplets is low. In realistic situation gas temperature can be calculated by enthalpy transport equation with the source term describing the contribution of droplets. The values of the convection heat transfer coefficient depend on gas parameters (velocity and viscosity) and droplet radius. The latter is calculated using Equation (3.4.2) and taking into account droplet swelling due to the decrease of liquid fuel density with increasing temperature. Under these assumptions the calculation of droplet temperature reduces to the solution of Equation (4.2.1) subject to appropriate initial and boundary conditions. When calculating droplet radius I take into account the conservation of mass of liquid droplet during its swelling and evaporation. The first requirement leads to the condition:

$$R_d(T) = R_d(\overline{T}_{d0})\left(\frac{\rho(\overline{T}_{d0})}{\rho(\overline{T})}\right)^{1/3}, \tag{5.3.1}$$

where $\overline{T}$ is the average droplet temperature defined as:

$$\overline{T}_d = \frac{3}{R_d^3}\int_0^{R_d} R^2 T(R)dR. \tag{5.3.2}$$

In what follows, five numerical algorithms for the solution of the problem of droplet heating and evaporation will be considered. These will be based on NSDE, the solutions discussed in Chapter 4 and the solution based on the parabolic temperature profile model (Dombrovsky and Sazhin, 2003a).

5.3.1 Numerical solution of the discretised heat conduction equation (NSDE)

Equation (4.2.1) can be simplified by introducing a new variable $u = Tr$. This allows us to rewrite this equation as Equation (4.2.5) with its boundary and initial condition as in Equation (4.2.6). I define the source term S as $S = \tilde{P}(r)$ where $\tilde{P}(r) = rP(r)$. This equation is the one-dimensional unsteady heat conduction equation in cartesian

coordinates and can be solved numerically by various algorithms widely discussed in CFD literature. I use the finite difference technique with fully implicit marching in time (Patankar, 1980; Versteeg and Malalasekera, 1995). The details are described in Appendix 4.

5.3.2 Numerical algorithm using the solution for h (t) = constant

In the case when h (t) $\equiv h$ = const the analytical solution of Equation (4.2.1) is given by Equation (4.3.1.19). The solution is based on the assumption that the changes in droplet surface area are small. This is always true when the time step is small enough. The analytical solution (4.3.1.19) enables us to get the temperature distribution inside the droplet $T(r, t)$ as a function of normalised radius r at the end of each time step. For the first time step I use specified initial conditions $T_{d0}(r, t = 0)$. Then the solution at the end of the first time step is used as the initial condition for the second time step etc.

If the time step over which the droplet temperature and radius are calculated is small, I can assume that h (t) = const over this time step. In this case I calculate $\dot{R}_d(t = 0)$ from Equation (3.4.2) and T_{eff} (t = 0) from Equation (4.2.4). Then the initial condition at t = 0 will allow us to calculate T (R, t) at the end of the first time step ($T(R, t_1)$ using Equation (4.3.1.19). Droplet radius at time t_1, R_d (t_1) is calculated based on Equation (3.4.2) with the correction swelling of the droplet (see Equation (5.3.1)).

The same procedure is repeated for all the following time steps until the droplet is evaporated. The number of terms in the series in Equation (4.3.1.19) which needs to be taken into account depends on the timing of the start of droplet heating and the time when the value of droplet temperature is calculated. For parameters relevant to diesel engine environments, just three terms in the series can be used with possible errors of not more than about 1 % (Chapter 4, Section 4.4).

Note that the integrals over r, used to estimate $\overline{T}$ and q_n, can be calculated analytically as described in Appendix 5.

At the very initial stage of droplet heating, before the boundary layer around the droplet has had time to establish, the description of droplet heating in terms of the convection heat transfer coefficient may not be adequate (Feng and Michaelides, 1996; Sazhin et al, 2001a).

5.3.3 Numerical algorithm using the solution for almost constant h (t)

In the case of almost constant h (t) we can use representation (4.3.2.1) and assume that $h_1(t) = \varepsilon\eta(t)$, where ε is a small parameter and h_0 is constant.

In this case the approximation solution of Equation (4.2.1) can be written as:

$$T(r,t) = \frac{1}{r}\left\{U(1,t) - \int_0^t M(\tau)G(t-\tau,1)d\tau + \varepsilon\int_0^t \eta(\tau)\nu_0(\tau)G(t-\tau,1)d\tau\right\}, \qquad (5.3.3.1)$$

where $\nu_0(t)$ defined as in Equation (4.3.3.3).

When the change of h (t) over a time step is small but still needs to be taken into account then the analytical solution for almost constant h (t) can be applied. The difficulty in the application of this analytical solution is that the value of $\varepsilon\eta(t)$ cannot be *a priori* established in the general case, and iterations are required. The general scheme for the solution in this case starts with the first step for the case when h (t) = constant. Droplet radius is calculated taking into account droplet swelling and evaporation. If the relative gas-droplet velocity is low then $h(t_1) = k_g / R_d(t_1)$. In the case where this velocity needs to be taken into account then the exchange of momentum between droplets and gas needs to be considered (Sazhina et al, 2000). At the next stage I assume that h (t) is a linear function of t in the range (0, t_1). This allows us to assume that $\eta(t)$ = t and calculate ε as:

$$\varepsilon \equiv \varepsilon_1 = (h(t_1) - h_0)/t_1, \qquad (5.3.3.2)$$

where ε_1 indicates the value of ε for the first iteration. Then I calculate all parameters used in Equation (5.3.3.1) and find the value of T (r, t_1) from this equation. The updated values of R_d (t_1) and h (t_1) are calculated similarly to the case of h (t) = constant. The value of h (t_1) is expected to be close to the one predicted by the analysis based on the assumption that h (t) = constant. In the event of this not being the case a further iteration is needed. Based on experience, the prediction of the second iteration is practically undistinguishable from the prediction of the first iteration for realistic diesel engine conditions.

When considering the next time step from t_1 to t_2 I assume that η (t) = t (as at the previous step). Then I assume that $\varepsilon = \varepsilon_1$, that is the value of ε at the second time step is the same as at the first time step. After that, the value of T (r, t_2) is calculated based on Equation (5.3.3.1) and using the values of T (r, t_2) as the initial condition. As a result, the values of h (t_2) and $\varepsilon_2 = (h(t_2) - h(t_1))/(t_2 - t_1)$ are obtained. The calculations of T (r, t_2) are repeated for the $\varepsilon = \varepsilon_2$. The updated values of R_d (t_2) and h (t_2) are calculated

similarly to the case of h (t) = const. The same procedure is repeated for all the following time steps until the droplet is evaporated.

5.3.4 Numerical algorithm for arbitrary h (t)

It is assumed that h is an arbitrary function as defined in Equation (4.3.2.1). In this case the solution of Equation (4.2.1) can be written as:

$$T(r,t) = \frac{1}{r}\left\{U(r,t) - \int_0^t [M(\tau) - h_1(\tau)u(1,\tau)]G(t-\tau,r)\,d\tau\right\} \qquad (5.3.4.1)$$

where u (1, t) is found from the solution of Equation (4.3.2.9). The numerical solution of the latter equation is described in Appendix 2.

It is unlikely that numerical algorithm for arbitrary h (t) is used in CFD codes. It can, however, be useful for calculating heating of slowly evaporating individual droplets in a prescribed gas flow. Using the prescribed functions h_0 and h_1 (t) Equation (4.3.2.9) is solved numerically for u (1, t), using the algorithm described in Appendix 2. In the case of fast moving droplets the values of h_0 and h_1 (t) are calculated from known values of droplet radius, gas thermal conductivity and the calculated time dependence of droplet relative velocity. Then the values of $T(r, t)$ are obtained from Equation (5.3.4.1) for T_{eff} = T_g. At the next stage the values of $\dot{R}_d$ are calculated from Equation (3.4.2) and the updated value of T_{eff} is found. The change of R_d over time of calculation should be small. Otherwise, Equations (5.3.4.1), (4.3.2.9) are not applicable.

5.3.5 Numerical algorithm for the parabolic temperature profile model

In the case of constant T_g the solution (4.3.1.19) can be reasonable accurately approximated by a parabolic function of r as in Equation (2.2.1.1.5). This presentation of $T(r, t)$ takes into account the difference between the temperatures in the centre and at the surface of the droplet. The boundary condition at R = 0 is satisfied. The boundary condition at $R = R_d$ and the condition for the thermal balance of the droplet leads to the following equation (Dombrovsky and Sazhin, 2003a):

$$T_s = (\overline{T} + 0.2\xi T_g)/\varphi + 0.2\xi\rho_l R_d \dot{R}_d(T_s)L/(k_l\varphi). \qquad (5.3.5.1)$$

where $\varphi = 1 + 0.2\xi$, ξ = 0.5 Nu k_g / k_l, Nu can be obtained from the correlation (2.2.1.2.23).

Although the algorithms described in Sections 5.3.1-5.3.4 are likely to describe the heating of droplets more accurately compared with the case where the temperature

gradients inside the droplet are ignored altogether, they might be CPU intensive. A reasonable compromise between accuracy and CPU time requirements can be achieved for the parabolic temperature profile model. The effect of thermal radiation is ignored at this stage. It can be included as a perturbation if required (Sazhin et al, 2000).

The application of this model starts with finding the average droplet temperature ($\overline{T}$) from the Equation (5.3.2). Then the value of T_s is calculated from Equation (5.3.5.1) assuming that $\dot{R}_d = 0$. Using this value of T_s the updated value of $\dot{R}_d$ is obtained. Then this updated value of $\dot{R}_d$ allows more accurate estimate of T_s by inserting it into Equation (5.3.5.1).

It is worth to point out that in this algorithm we do not need to take into account the differential radiation heating of droplets as described by the function w (r, λ) (see Chapter 2, Section 2.2.2), as the parabolic temperature profile model is not interested in the details of the temperature distribution inside droplets. Instead, the global heating of droplets needs to be accounted for as described by Sazhin et (2002), Dombrovsky et al (2001) and Sazhin et al (2004a).

5.4 Performance of numerical algorithms

In this section the performance of the numerical algorithms discussed in Section 5.3 will be investigated for the parameters relevant to diesel engines. The initial droplet radius is taken equal to 10 μm, and its initial temperature is taken equal to 300 K. The droplet thermal conductivity is taken equal to 0.14 W / (m^2 K) and its temperature dependence is ignored when considering the heating process alone. It will be taken into account when considering the heating and evaporation processes. Molar mass of air is M_a =28.97 kg/mol; for fuel it is taken as M_f = 206 kg/ kmol (Poling et al, 2000). The time dependent convective heat transfer coefficient h is approximated as:

$$h = h_{in} - \frac{h_{in} - h_f}{\tau} t \tag{5.4.1}$$

where h_{in} is the heat transfer coefficient at the start of fuel injection, which is assumed equal to $1.377 k_g / R_d$ and h_f is its value when the fuel droplet stops ($h_f = k_g / R_d$) and τ is taken 1 ms. This can approximate the reduction of droplet relative velocity from 0.45 m/s to zero. This situation is relevant to diesel engines when air entrainment by a fuel spray is taken into account (Flynn et al, 1999; Sazhin et al, 2003). The detailed calculation of fuel droplet velocities is beyond the scope of the analysis of this chapter.

The approximation of h (t) in Equation (5.4.1) is just used for comparative analysis of the effectiveness of numerical algorithms described in Section 5.3.

The runs were performed on a Pentium 4 CPU 2.00 GHz PC with 512 MB of RAM. The computer programs for the numerical algorithms are written in FORTRAN 90.

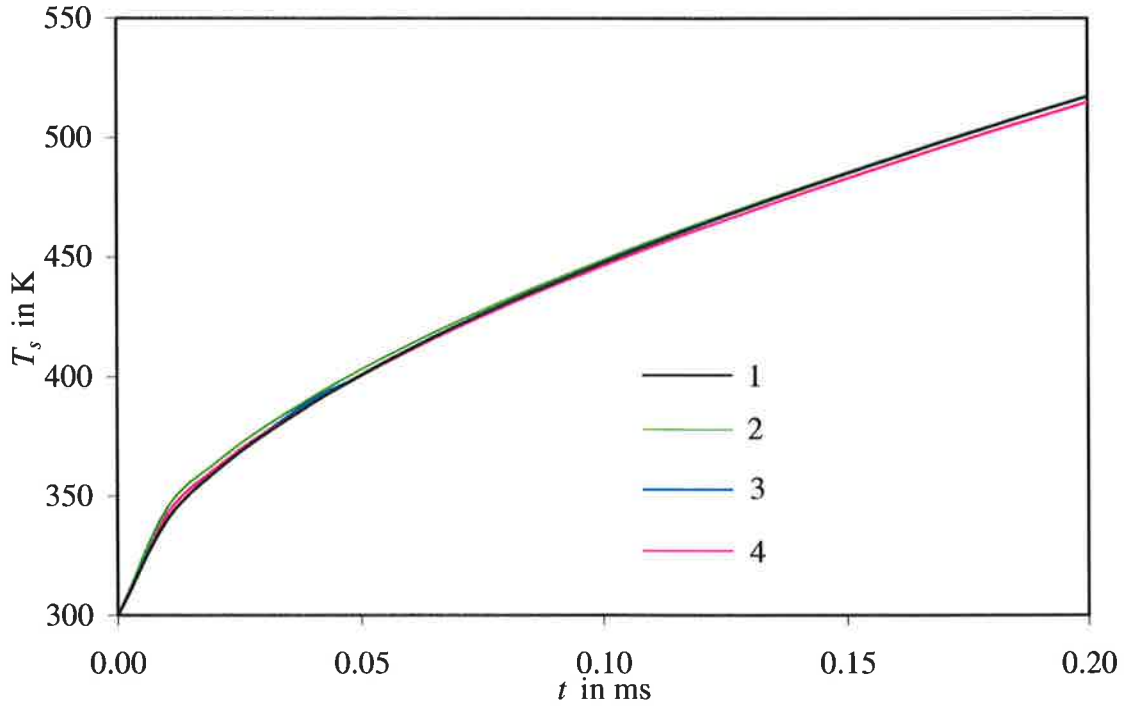

Fig. 5.1 Plots of droplet surface temperature T_s versus time. The calculation have been performed using the numerical algorithm based on NSDE (1), the numerical algorithms based on the analytical solution for constant h (2), almost constant h (3) and an arbitrary h (4) without thermal radiation effects with timestep Δt = 10 μs, number of nodes along the radius $r/\Delta r$ =100, T_g =1000 K and R_{d0} = 10 μm. The contribution of radiation is ignored.

Figure (5.1) shows the droplet surface temperature versus time using all algorithms described above without taking into account the thermal radiation effect, swelling and evaporation. The gas temperature was taken equal to 1000 K. Time step (Δt) is taken equal to 10 μs and the number of nodes along the radius $r/\Delta r$ is taken equal to 100. The time dependent convective heat transfer coefficient h is taken in the form (5.4.1). The results predicted by all numerical algorithms are almost identical. These results are shown just at $t < 0.2$ ms when the effects of evaporation are expected to be weak.

The performance of all algorithms described in Section 5.3 will be analysed in Section 5.4.1- 5.4.4 without taking into account evaporation and swelling. The calculations shall be performed based on a hypothetical case when the droplet is heated up to more than 800 K without swelling and evaporation during 1 ms (the full range is not shown in

Figure (5.1)). This allowed us to calculate the CPU time more accurately compared with the case when this time is estimated just over 0.2 ms.

5.4.1 Numerical solution of the discretised heat conduction equation (NSDE)

Results of our calculations of droplet surface temperature as a function of time, using NSDE when the thermal radiation effects, swelling and evaporation are ignored are shown in Figure (5.2). The time dependent convective heat transfer coefficient h is taken in the form (5.4.1).

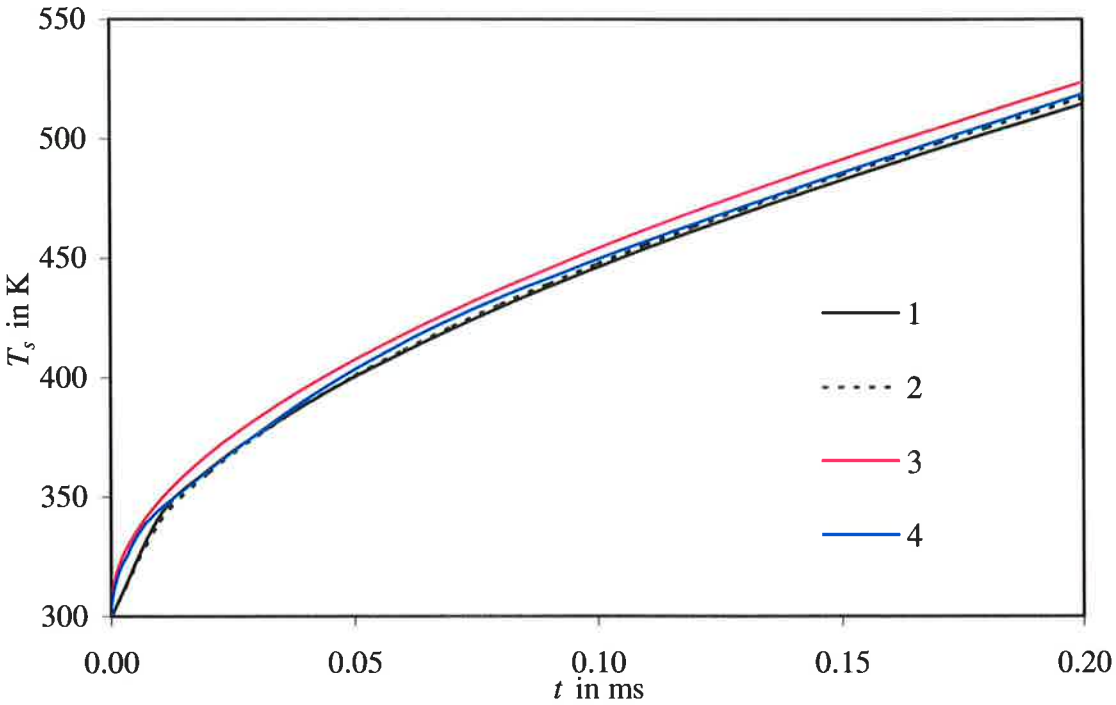

Fig. 5.2 The same as in Figure (5.1) using the numerical algorithm based on the analytical solution for constant h (1), NSDE based on fully implicit method (2), Crank-Nicolson method (3) and explicit method (4).

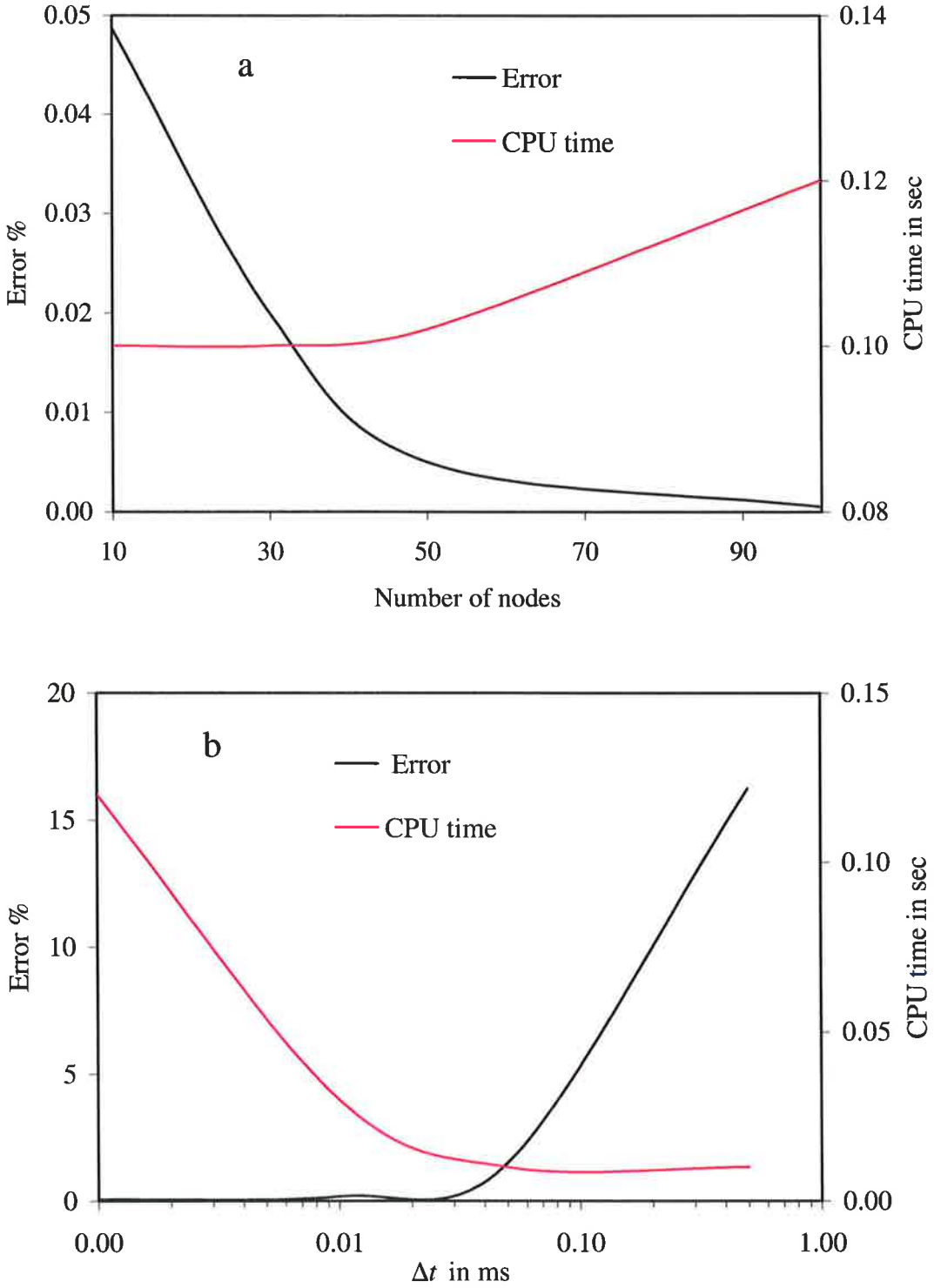

Fig 5.3 Plots of errors and CPU times of droplet surface temperature versus number of nodes ($r/\Delta r$) (a) and time step (b) for NSDE; the calculations have been performed based on NSDE for Δt = 1 μs (a) and for $r/\Delta r$ = 100 (b). The errors were calculated relative to the prediction of NSDE with Δt = 1 μs and $r/\Delta r$ = 1000.

NSDE are developed using central-difference scheme for explicit, Crank-Nicolson and fully implicit time-marching algorithms. In the same figure the results of calculations using the numerical algorithm based on the analytical solution for constant h are shown. As follows from this figure, results predicted by both algorithms are almost identical. The implicit algorithm appeared to be the most effective from the point of view of computer efficiency and stability of calculations (it is unconditionally stable). This allows us to discard both explicit and Crank-Nicolson algorithms as possible candidates for implementation in CFD codes and focus our attention on the implicit algorithm.

The plots of errors and CPU times versus number of nodes along radius (Δt = 1 μs) and time step Δt ($r/\Delta r$ = 100), using the numerical algorithm based on NSDE (fully implicit algorithm and central-difference scheme) are shown in Figures (5.3a) and (5.4b), respectively. The errors were calculated relative to the prediction of NSDE with 1000 nodes along droplet radius and time step Δt = 1 □s. Figure (5.3a) shows that 100 nodes along radius provides an error less than 0.01 % and CPU time for droplet surface temperature calculations using less than 50 nodes along radius is almost the same. The smaller errors can be related to that they are calculated based on only droplet heating without taken into account thermal radiation effects, evaporation and swelling. The CPU time was estimated by FORTRAN 90 function. As shown in Figure (5.3b), the errors are significant for time step > 0.05 ms, while their values are close to zero for smaller values of time step.

5.4.2 New approaches for solutions of the heat conduction equation inside droplets without thermal radiation

The plots of errors for droplet surface temperature calculations and CPU requirements as functions of the number of terms in series (4.3.1.19) using the analytical solution for h = const are shown in Figure (5.4a). Thermal radiation effects, swelling and evaporation are ignored. Time step Δt is taken equal 1 μs; the calculations are independent of number of nodes along radius because the analytical presentation of q_n is used (Appendix 5). The results show that 3 terms are sufficient for an error less than 0.01 %. The errors are slightly small when compared with the results obtained in Figure (4.5). This can be related to smaller droplet radius (10 □m), smaller time step (Δt = 1 μs) and analytical presentation of q_n.

Figure (5.4b) shows the errors for droplet surface temperature calculations and CPU requirements as functions of the number of terms in series (4.3.2.8) using the numerical

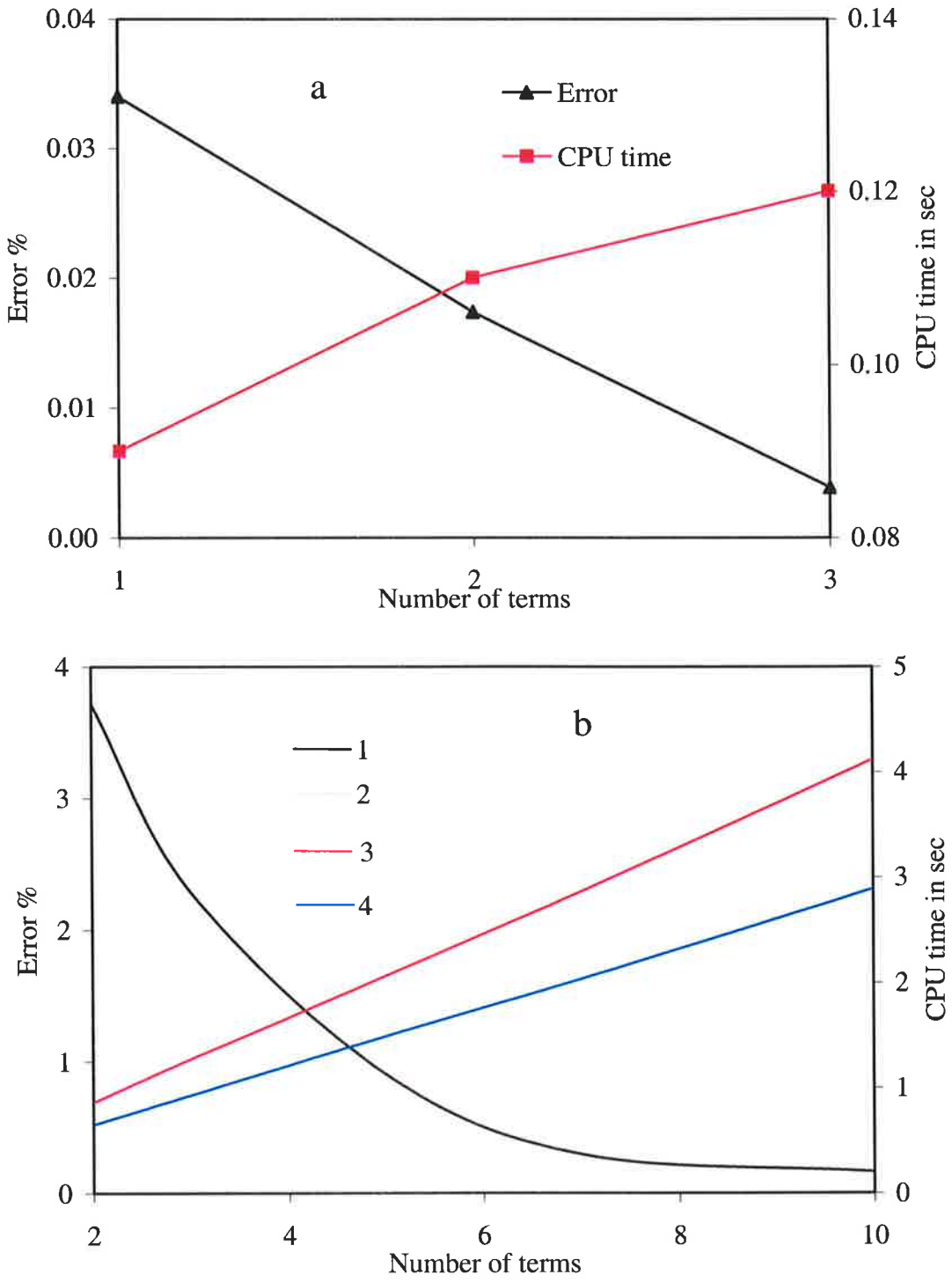

Fig. 5.4 Plots of errors and CPU times of droplet surface temperature versus number of terms used in series (4.3.1.19) for the numerical algorithm based on the analytical solution for constant h (a) and versus number of terms used in series (4.3.2.8) for the numerical algorithm based on the analytical solution for almost constant h and an arbitrary h (b) without thermal radiation effects. The plots of errors are presented using the numerical algorithms based on the analytical solution for almost constant h (1) and the solution for an arbitrary h (2). CPU times required by these numerical algorithms based on the analytical solution for almost constant h (3) and the solution for an arbitrary h (4). Δt = 1 μs, T_g =1000 K and R_{d0} = 10 μm. Plots 1 and 2 are undistinguishable in this figure.

algorithm based on the solution for an arbitrary h (general case) and numerical algorithm based on the analytical solution for almost constant h without the thermal radiation effects. Time step Δt is taken equal 1 μs and nodes along radius are taken equal to 100. The results shows that both numerical algorithms predict results with similar level of accuracy but the computational time for the numerical algorithm based on the solution for an arbitrary h is always less than that based on the analytical solution for almost constant h regardless the number of terms. The results also show that 10 terms are sufficient for an error less than 0.2 % for both numerical algorithms. The errors in Figure (5.4a, b) were calculated relative to the prediction of NSDE with 1000 nodes along droplet radius and time step Δt = 1 μs.

Note the number of terms used in the numerical algorithms based on the analytical solution for almost constant h and the solution for an arbitrary h is larger than that used for the numerical algorithm based on the analytical solution for constant h. This is due to the sinusoidal functions, which are used in the first algorithms (Equations (4.3.2.4), (4.3.2.6)). These sinusoidal functions required large number of terms to reduce the predicted error in calculating the temperature distribution inside the droplet.

The plots of errors and CPU times versus time step Δt for the numerical algorithms based on the new approaches are shown in Figure (5.5). 10 terms series (4.3.2.8) and 100 nodes along radius are taken for the numerical algorithms using the solution for almost constant h and an arbitrary h. The results show that the errors of the numerical algorithm based on the analytical solution of heat conduction equation for h = const are generally less than the errors of the numerical algorithms based on the solution for almost constant h and an arbitrary h for $\Delta t < 0.5$ ms. The former is close to zero for $\Delta t < 0.1$ ms. This can be due to the integral form of the final Formulae (8.3.2.8) and (8.3.2.9), the contribution of $G(t, 1)$ (Formula (8.3.2.10)) at small t cannot be ignored. The errors were calculated relative to the prediction of NSDE with 1000 nodes along droplet radius and time step Δt = 1 μs. The CPU requirements of the numerical algorithm based on the analytical solution for h = const are always less than those required by the other two numerical algorithms.

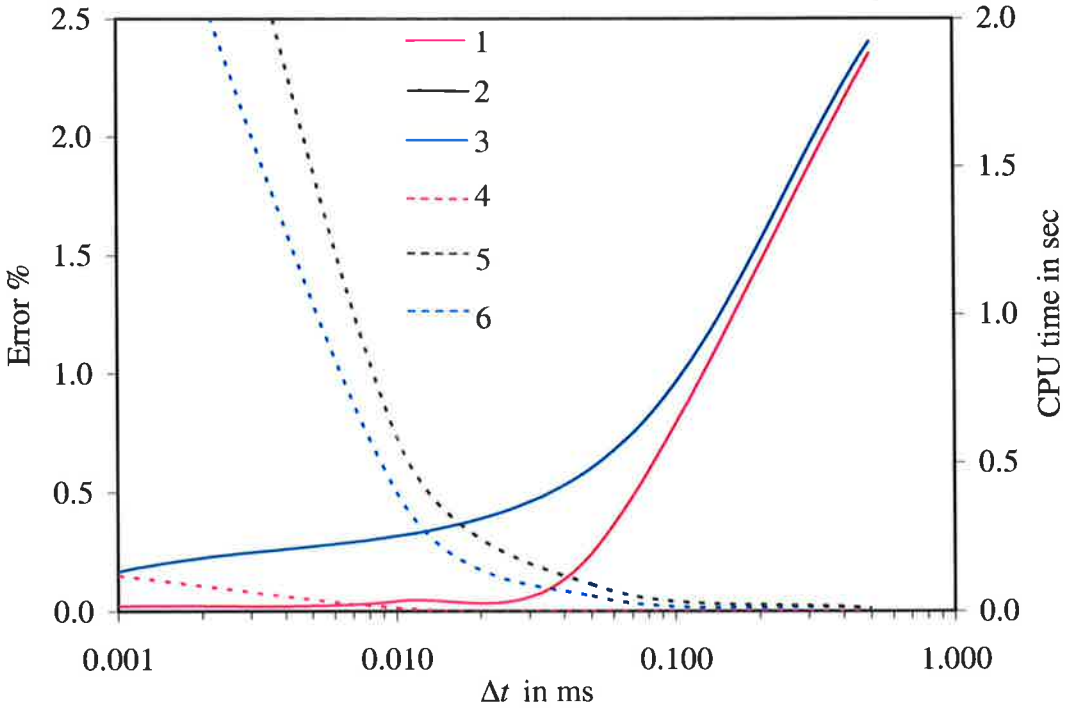

Fig. 5.5 Plots of errors and CPU times of calculation of droplet surface temperature versus time step. The errors were calculated relative to the result given by the numerical algorithm based on NSDE with Δt = 1 μs and $r/\Delta r$ = 1000. The plots for errors are presented for the numerical algorithms based on the analytical solution for h = const (1), the analytical solution for almost constant h (2) and the solution for an arbitrary h (3). Plots 2 and 3 are undistinguishable in this figure. CPU times required by the numerical algorithms based on the analytical solution for h = const (4), the analytical solution for almost constant h (5) and the solution for an arbitrary h (6). Gas temperature is taken as T_g =1000 K, and initial droplet radius is taken as R_{d0} = 10 μm.

5.4.3 New approaches for solutions of the heat conduction equation inside droplets with thermal radiation

In this section the analysis in Section 5.4.2 will be repeated but with the thermal radiation effects taken into account. The plots of errors for droplet surface temperature calculations and CPU requirements as functions of the number of terms in the series (4.3.1.19) using the analytical solution for h = const are shown in Figure (5.6a). Thermal radiation effects are taken into account using Equations (2.2.2.18) and (2.2.2.19). Time step Δt is taken equal 1 μs and nodes along radius are taken equal to 100. The results show that 3 terms are sufficient for an error less than 0.01 %.

Figure (5.6b) shows the errors for droplet surface temperature calculations and CPU requirements as functions of the number of terms in series (4.3.2.8) using the numerical algorithm based on the solution for an arbitrary h (general case) and numerical algorithm based on the analytical solution for almost constant h. The results show that both

numerical algorithms predict results with similar level of accuracy but the computational time for the numerical algorithm based on the solution for an arbitrary h is always less than that based on the analytical solution for almost constant h regardless the number of terms.

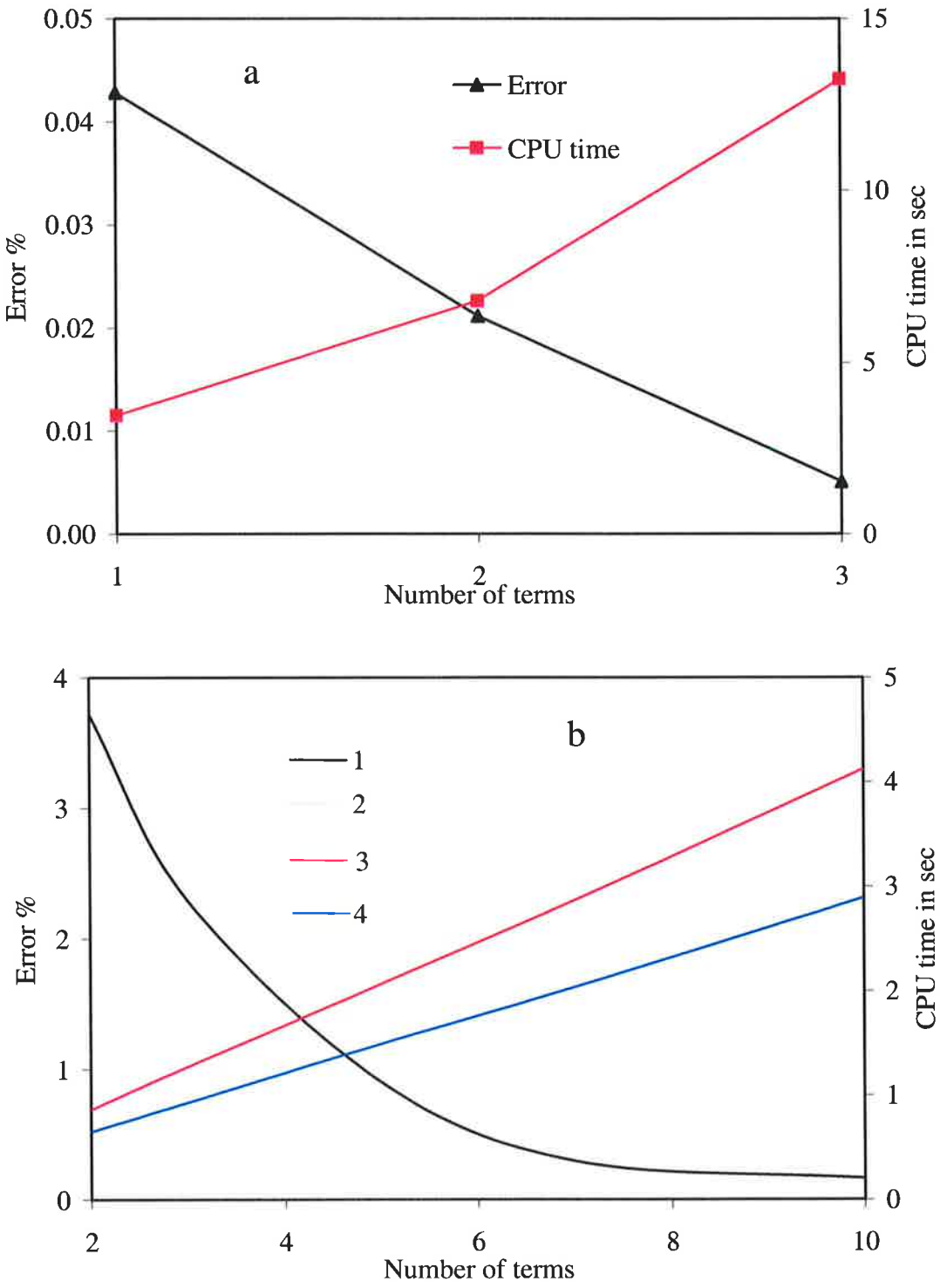

Fig. 5.6 The same as in Figure (5.4) but with thermal radiation effects.

The results also show that 10 terms are sufficient for an error less than 0.2 % for both numerical algorithms.

The plots of errors and CPU times versus time step Δt for the numerical algorithms based on the new approaches with thermal radiation effects are shown in Figure (5.7). 10 terms in series (4.3.2.8) and 100 nodes along radius are taken for the numerical algorithms using the solution for almost constant h and an arbitrary h. The results show that, as in the case without thermal radiation, the errors of the numerical algorithm based on the analytical solution of heat conduction equation for h = const are generally less than the errors of the numerical algorithms based on the solution for almost constant h and an arbitrary h. The former is close to zero for $\Delta t < 0.1$ ms. This can be related to the same reason, which was explained in Section 5.4.2. The errors were calculated relative to the results given by the numerical algorithm based on NSDE with 1000 nodes along the droplet radius, time step Δt = 1 μs. The CPU requirements for the numerical algorithm based on the analytical solution for h = const are always less than those required by the other two numerical algorithms.

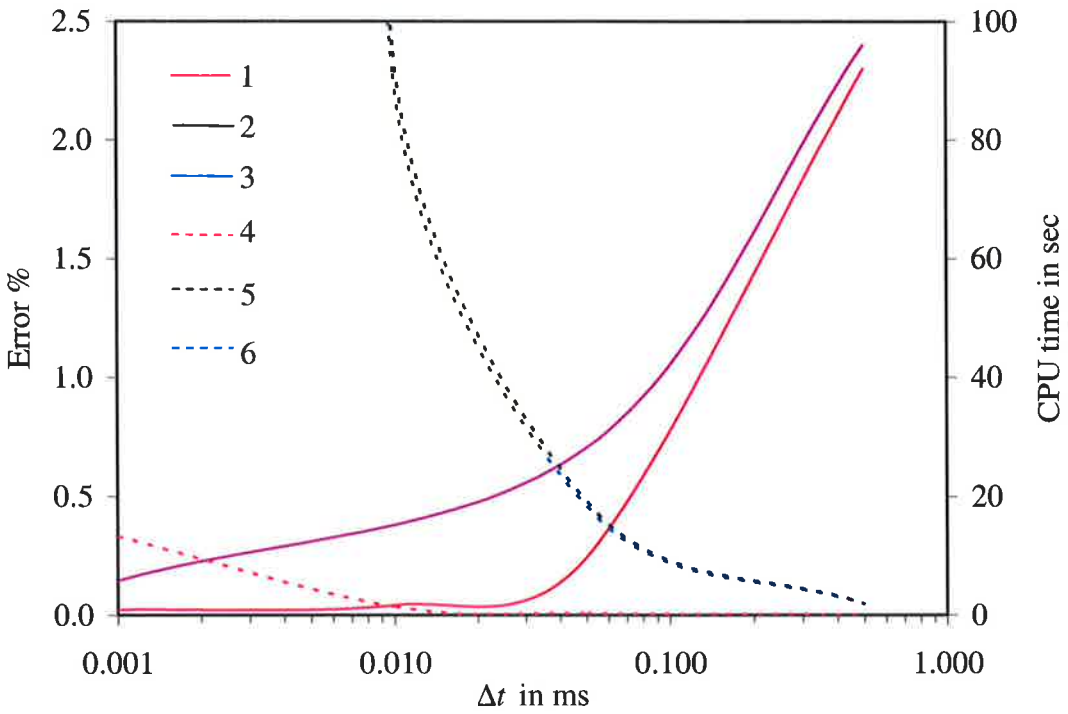

Fig 5.7 The same as in Figure (5.5) but with thermal radiation effects. The errors were calculated relative to the prediction of numerical algorithms using analytical solution for h = const with 1000 nodes along droplet radius, time step Δt = 1 μs and 25 terms in series (4.3.1.19).

From the discussion above, the algorithms for the three solutions predict almost the same dependence of droplet surface temperature on time. From a computer efficiency standpoint, however, the algorithm using the analytical solution for h = const, has clear advantages over other algorithms when the radiation effect is ignored and taken into account. The CPU time required by this algorithm has been about an order of magnitude less than the CPU time required by the algorithms with transient h. Three terms in the analytical solution have been taken by the algorithm. This introduces an error of the solution less than 1%. In practice it turned out to be much less than 1% (0.02 %) for sufficiently small time steps (less than 0.01 ms) and for the values of parameters under consideration. This results allows us to focus on the algorithm using the solution for h = const for the implementation in CFD codes.

As follows from the analysis in Chapter 4 the thermal radiation effect does not have a significant influence on the predicted error in the droplet surface temperature using all the three numerical algorithms, while it has a large effect on the computational time consumed. This allows the simplification of the radiation term as will be discussed later in Section (5.6).

5.4.4 Numerical algorithm for the parabolic temperature profile model

This algorithm is based on the assumption of the parabolic temperature profile inside the droplet. Figure (5.8) shows the droplet surface temperature versus time during the heating process using the numerical algorithm based on the parabolic temperature profile model and the numerical algorithm based on the assumption that there is no temperature gradient inside the droplet. The droplet is stationary as described before. The results obtained using the numerical algorithm based on the solution for constant h are shown in the same figure. The predicted errors in calculating the droplet surface temperature using the first algorithm are relatively large at the beginning of heating process but decrease later. They reach 0.9 % at time equal to t = 0.4 ms, when the error for the second algorithm is equal 4.2 %. The errors are calculated relative to the numerical algorithm based on NSDE with time step equal 1μs and 1000 nodes along droplet radius.

Although the predicted errors from the numerical algorithm based on the parabolic temperature profile model can be relatively high in the realistic condition of diesel engines it is very computer efficient. The calculations for the parabolic model were performed based on adaptive time step. The CPU requirements of this model are expected to be less than for numerical algorithm based on NSDE and numerical

algorithm based on analytical solution for heat conduction equation for h = const for the same time step. It is also straight forward for implementation in CFD codes.

In the next sections the comparison of the numerical algorithms based on the analytical solution for h = const, NSDE, the parabolic temperature profile model and the assumption that there is no temperature gradient (inside the droplet) model are discussed. At first I consider the case when the contribution of thermal radiation is ignored. Then the contribution of thermal radiation is discussed.

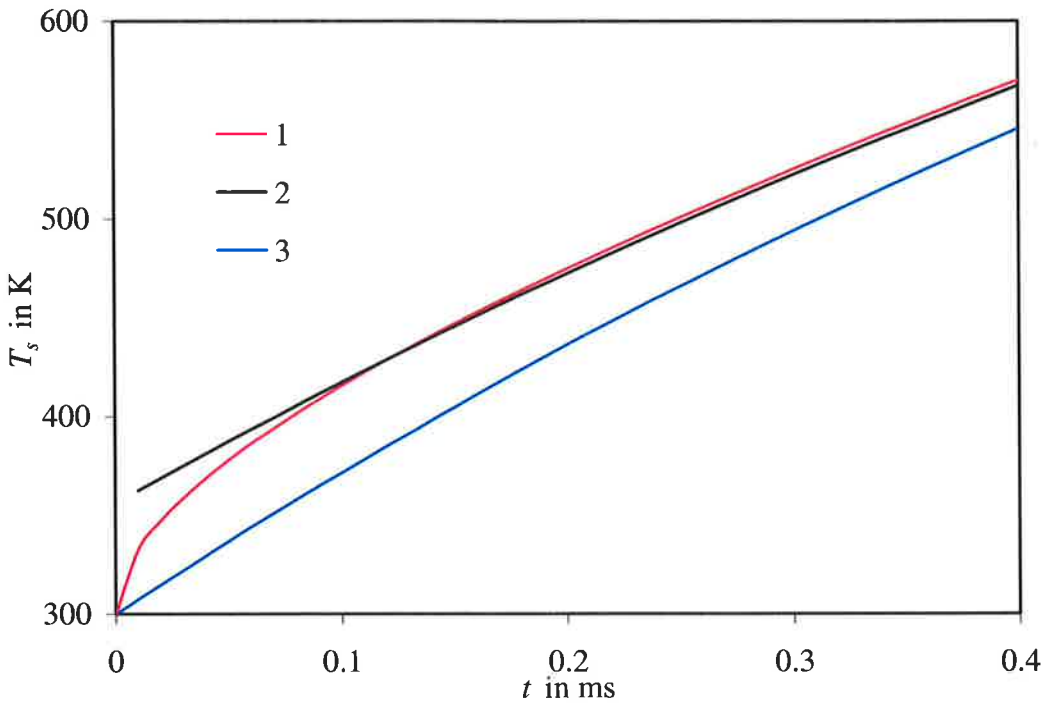

Fig. 5.8 Plots of droplet surface temperature T_s versus time for T_g =1000 K and R_d = 10 μm. The calculations have been performed using the numerical algorithm based on the analytical solution for constant h (1), the numerical algorithm based on the parabolic temperature profile model (2) and the numerical algorithm based on the assumption of no temperature gradient inside the droplet (3).

5.5 Comparison of numerical algorithms without thermal radiation

5.5.1 Heating of diesel fuel droplets

If the surface temperature and the temperature distribution inside the droplet is required at a specified time during the droplet heating process, without taking into account the evaporation processes, the analytical solution of heat conduction Equation (4.2.1) for h = const, which was developed in Chapter 4 is more accurate and computer efficient than the analytical solution for almost constant h, the numerical solution for an arbitrary h and NSDE. The calculations take less than 0.01 sec of CPU times.

As this algorithm has to be implemented in a CFD code its performance has to be compared with the performance of NSDE. As in previous section, the convection heat transfer coefficient h is assumed to change according to Equation (5.4.1) from 1.377 k_g/R_d to k_g/R_d over 1 ms. The initial droplet radius is taken 10 μm, and its initial temperature is taken equal to 300 K. The droplet thermal conductivity is taken 0.14 W/ (m K). Gas temperature is taken equal to 1000 K. The effects of thermal radiation, evaporation and swelling are ignored. The plots of errors and CPU times versus time step Δt for the numerical algorithm based on the analytical solution for h = const and NSDE are shown in Figure (5.9). 100 nodes along radius were considered for the latter solution. All errors were calculated relative to the prediction of the NSDE with 1000 nodes along droplet radius and time step Δt = 1 μs. From Figure (5.9), the errors of calculation based on the algorithm using the analytical solution for h = const are consistently lower when compared with the errors of calculations based on the numerical solution of NSDE for $\Delta t > 0.005$ ms. At smaller Δt these errors are close to zero for both solutions. This can be related to the fact that NSDE is based on the assumption that non-linear terms can, with respect to the time step, be ignored, while the algorithm using the

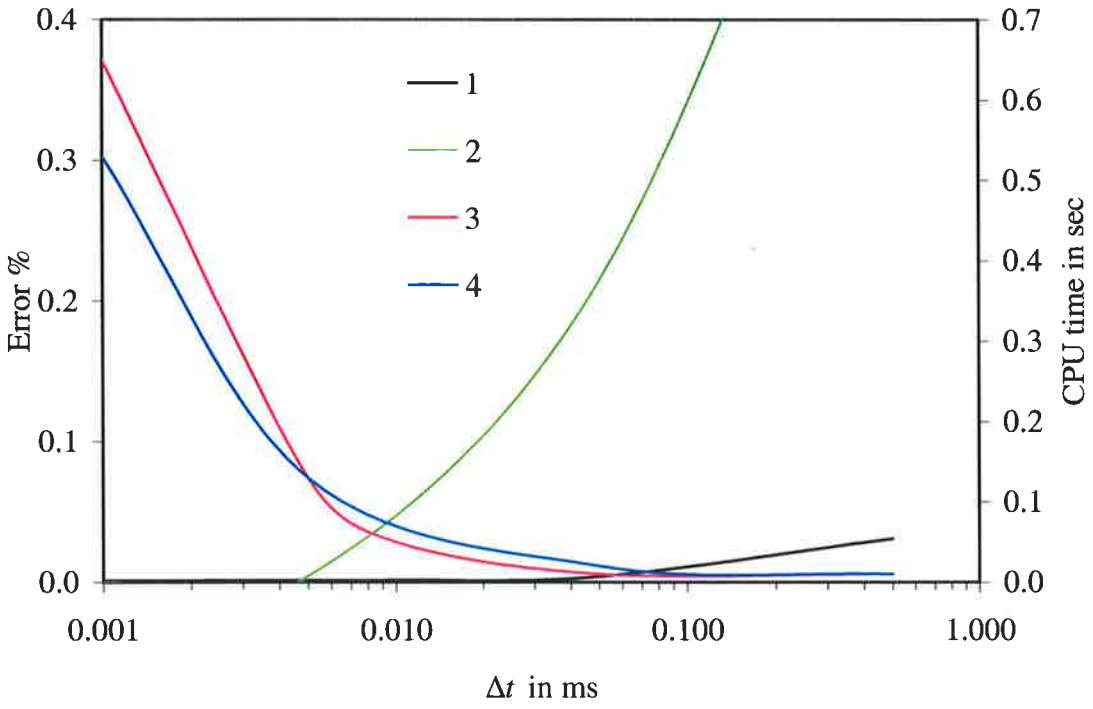

Fig. 5.9 Plots of errors and CPU times of calculation of droplet surface temperature versus time step. The errors were calculated relative to the prediction of NSDE with Δt = 1 μs and $r/\Delta r$ = 1000. The plots of errors are presented for numerical algorithm based on the analytical solution for h = const (1) and NSDE (2). Plots of CPU times are presented for the numerical algorithm based on the analytical solution for h = const (3) and NSDE (4). T_g =1000 K and R_{d0} = 10 μm.

analytical solution for h = const implicitly retains these terms. The CPU requirements of the algorithm using the analytical solution for h = const are lower than the CPU requirements of the algorithm based on NSDE for $\Delta t > 0.005$ ms. When computing errors and CPU times we considered a hypothetical case when droplet is heated up without evaporation to more than 800 K in 5 ms.

5.5.2 Heating and evaporation of a diesel fuel droplet

At this stage I compare the performance of the numerical algorithm based on the analytical solution for h = const with the performance of the numerical algorithm based on NSDE, the numerical algorithm based on the parabolic temperature profile model and the numerical algorithm based on the assumption that there is no temperature gradient inside the droplet (conventional algorithm). As in the previous analysis I assumed that T_g = 1000 K, but allowed droplets to evaporate and swell. The initial droplet radius is taken equal to 10 □m and its initial temperature is equal to 300 K. The temperature dependent liquid fuel heat capacity, latent heat of evaporation and droplet thermal conductivity are taken into account. The latter decreases from 0.145 W/ (m K) to 0.02 W/(m K) when the droplet temperature increased from 300 K to 725 K (Ried et al, 1987). The effect of droplet break-up will not be taken into account, and this might lead to unrealistically long droplet lifetimes. It is however, essential to separate the effects of droplet heating and evaporation from other processes to get a better insight into advantages and limitations of various algorithms.

Results of our calculations of the droplet surface temperature and radius as functions of time, using the abovementioned 4 algorithms, are shown in Figure (5.10). From this figure, the predictions of the numerical calculations based on NSDE and the algorithm using the analytical solution for h = const almost coincide for both surface temperature and droplet radius. Both these solutions differ noticeably from the predictions of the model based on the assumption of no temperature gradient inside the droplet. The predictions of the parabolic model are between the abovementioned solutions. This means that from the point of view of potential accuracy, NSDE and the solution based on the algorithm using the solution for h = const (keeping 3 terms in the series) are practically identical and superior to the numerical solutions based on the parabolic temperature profile model and the model with no temperature gradient inside the droplet. Accuracy, however, is not the only parameter, which determines the applicability of the

model for the implementation into CFD codes. Another parameter, which needs to be accounted for, is CPU requirements.

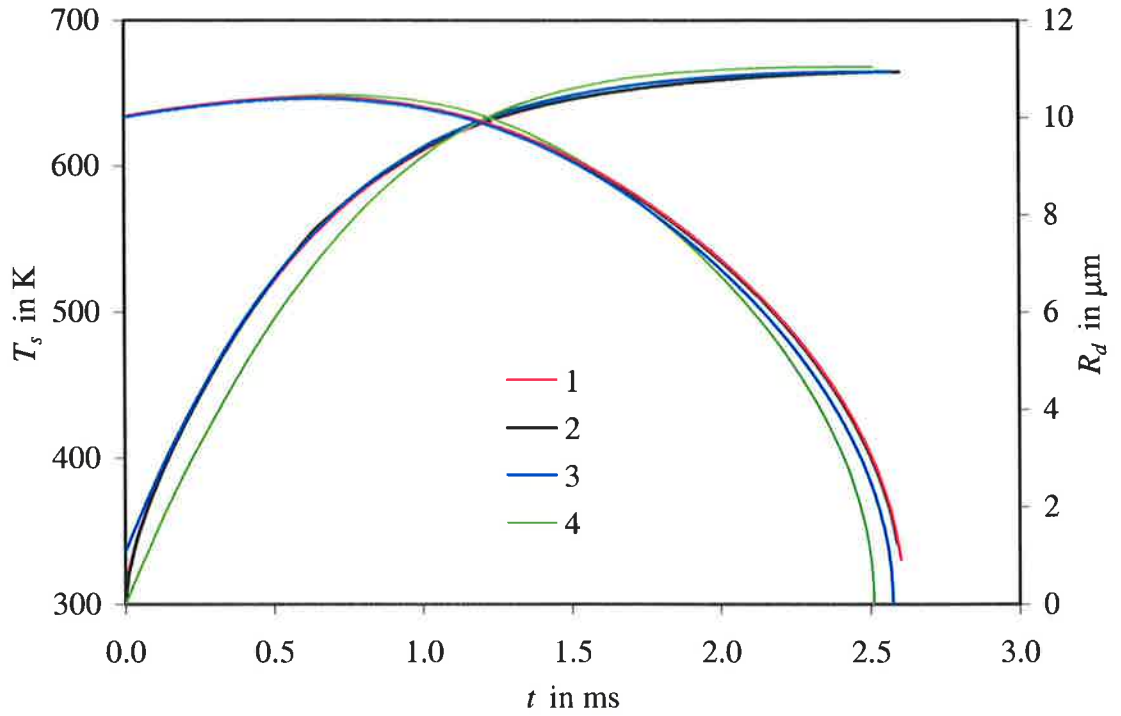

Fig 5.10 Plots of droplet surface temperature T_s and radius R_d versus time for T_g = 1000 K, without taking into account the effect of thermal radiation. The calculation have been performed using the numerical algorithms based on the analytical solution for h = const (1), NSDE (2), the numerical solution based on the parabolic temperature profile model (3) and the numerical solution based on the assumption that there is no temperature gradient inside the droplet (4). Curves 1 and 2 coincide within the accuracy of plotting.

The plots of errors and CPU times versus time step Δt for the numerical algorithm based on the analytical solution for h = const and NSDE are shown in Figure (5.11). Spatial resolution of 100 nodes along radius was considered for the latter solution to provide calculations with relative errors of less than about 0.5%. The calculations for the numerical algorithm based on the parabolic temperature profile model and the numerical algorithm based on the assumption that there is no temperature gradient inside the droplet were performed using the adaptive time step. The errors of these calculations relative to the prediction of NSDE were 1.2% and 3.6% respectively. All errors were calculated relative to the prediction of the NSDE with 1000 nodes along droplet radius and time step Δt = 1 µs. As follows from Figure (5.11), the errors of calculations based on the algorithm using the analytical solution for h = const are consistently lower when compared with the errors of calculations based on the numerical solution of NSDE for Δt > 0.01 ms. At smaller Δt these errors are close to zero for both solutions.

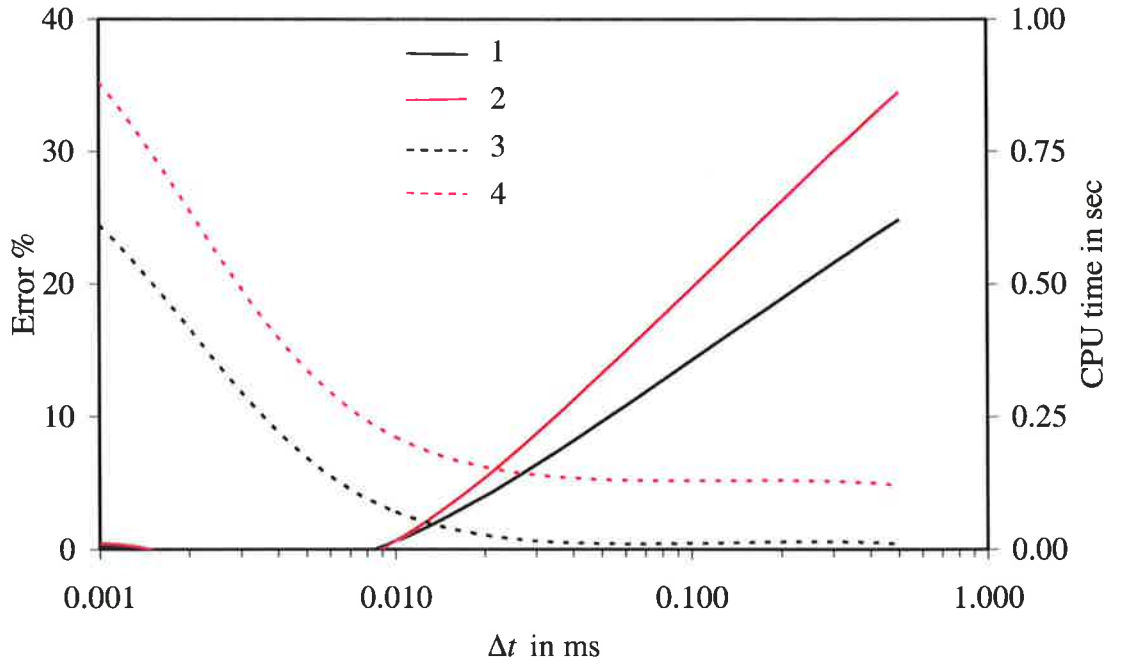

Fig 5.11 Plots of errors and CPU times of calculation of evaporation time versus time step for the calculations presented in Figure (5.10). The errors were calculated relative to the prediction of NSDE with Δt = 1 μs and $r/\Delta r$ = 1000. The plots of errors are presented for numerical algorithm based on the analytical solution for h = const (1) and NSDE (2). Plots of CPU times are presented for the numerical algorithm based on the analytical solution for h = const (3) and NSDE (4). The calculations for the parabolic temperature profile model and the numerical solution based on the assumption that there is no temperature gradient inside the droplet were performed using the adaptive time step. The errors of these calculations relative to the prediction of NSDE were 1.2 % and 3.6 % respectively.

As mentioned above, the errors of the numerical algorithm based on the parabolic temperature profile model are generally less than the errors of the numerical algorithm based on the assumption that there is no temperature gradient inside droplets. The CPU requirements of the parabolic temperature profile model, however, are larger than those of the model based on the assumption of no temperature gradients inside droplets. In both cases, however, they are expected to be less than for more rigorous models for the same time step. It is recommended that the numerical algorithm based on parabolic temperature profile model is used in CFD codes if the high accuracy of calculations is not essential. Figure (5.11) shows also that the CPU requirements of the algorithm using the analytical solution for h = const are consistently lower than the CPU requirements of the algorithms based on NSDE.

Results of the errors and the CPU times of calculation of the evaporation time at different gas temperatures (700 K-1200 K) and a wide range of initial droplet diameters

(5μm, 50 μm) without the contribution of radiation are shown in Table (5.1). The errors were calculated relative to the prediction of the NSDE with Δt =1 μs using 1000 nodes along the droplet radius. The errors and CPU times are presented for the numerical algorithm based on the analytical solution for h = const (A) and NSDE (N) using 100 nodes along the droplet radius. From the results it is observed that the predicted errors and CPU time for the algorithm based on the analytical solution are always much less than the predicted errors and CPU time for the algorithm based on NSDE.

Δt /ms	0.0 01								0.01							
R_{d0} /μm	2.5				25.0				2.5				25.0			
	Erro r%		CPU time /ms		Erro r%		CPU time /ms		Erro r%		CPU time /ms		Erro r%		CPU time /ms	
T_g /K	A	N	A	N	A	N	A	N	A	N	A	N	A	N	A	N
700	0.25	0.50	0.11	0.23	0.02	0.40	9.96	12.3	0.01	2.56	0.02	0.13	0.03	0.40	0.94	1.52
750	0.32	0.32	0.08	0.22	0.02	0.45	7.25	9.72	0.01	3.23	0.01	0.12	0.03	0.45	0.74	1.03
800	0.38	0.76	0.07	0.20	0.03	0.46	6.39	8.03	2.85	4.70	0.01	0.11	0.04	0.46	0.62	0.88
880	0.48	0.96	0.06	0.19	0.02	0.29	5.10	6.40	0.01	4.76	0.01	0.1	0.05	0.43	0.50	0.72
1000	0.61	0.61	0.04	0.17	0.02	0.43	3.91	4.98	2.14	4.29	0.01	0.08	0.01	0.43	0.38	0.59
1200	0.82	0.82	0.03	0.16	0.02	0.35	2.95	3.71	0.01	4.33	0.01	0.06	0.01	0.41	0.29	0.47

Table 5.1 Errors and CPU times of calculation of evaporation time at various gas temperatures without thermal radiation. The errors were calculated relative to the prediction of NSDE with Δt =10^{-6} sec using 1000 grid nodes along droplet radius. The errors and CPU times are presented for the numerical algorithm based on the analytical solution for h = const (A) and NSDE (N) using 100 nodes along droplet radius.

5.6 Comparison of numerical algorithms with thermal radiation

There can be two different approaches to modelling the effects of thermal radiation on heating and evaporation of droplets. If I intend to take into account the distribution of thermal radiation absorption inside the droplets I first need to model the term $P_1(R)$ in Equation (4.2.1) as defined in Equation (4.2.3). If I ignore the distribution of thermal radiation absorption inside droplets then a much simpler approach can be used as suggested in (Dombrovsky et al, 2001; Sazhin et al, 2002):

$$P_1(R) = 3\times10^6 a\sigma R_{d(\mu m)}^{b-1}(\theta_R^4 - \overline{T}^4), \qquad (5.6.1)$$

where θ_R is the radiation temperature (assumed equal to external temperature), $\overline{T}$ is the average droplet temperature defined by Equation (5.3.2), $R_{d(\mu m)}$ is the droplet radius in μm, a and b are polynomials of external temperature (quadratic function in the first

approximation). The expression for these coefficients for a typical automotive diesel fuel (low sulphur ESSO AF1313 diesel fuel) in the range of external temperatures 1000-3000 K was used in this analysis (see Chapter 3 Section 3.3). Note that the assumption that θ_R is equal to the external temperature is valid in the case of optically thin gas. In the case of optically thick gas we can assume that θ_R is equal to the gas temperature in the vicinity of the droplet. In all cases the contribution of $\overline{T}^4$ in Equation (5.6.1) is ignored when compared with the contribution of θ_R^4 in the same equation.

Expression for $P_1(R)$ in Equation (4.2.3) is certainly more accurate than Expression (5.6.1), but its application requires much more CPU time than the application of Expression (5.6.1). Most of the CPU time is actually spent on the calculation of the integral over λ in this expression as shown in Section (3.2.2). The most accurate calculation of this integral is based on all experimentally measured values of absorption coefficient a_λ (4111 points). Our analysis showed that the reduction of the number of these point to just 58, allow us to reduce CPU time by almost two orders of magnitude with the introduction of an error less than 10 %. This error can be tolerated in most cases, and this approach is used in our analysis. The analysis of Dombrovsky and Sazhin (2003b) was based on the results of measurements of λ in the range 0.5 – 1.1 μm and 0.2 - 6.0 μm, while our results are based on the measurements in the range 0.2 – 6.0 μm (see Chapter 3 Section 3.3). Note that when I use $P_1(R)$ in the form (5.6.1), the expression for p_n used in Equation (4.3.1.12) can be simplified considerably (see Appendix 5).

To illustrate the effect of thermal radiation on droplet heating and evaporation we consider modelling droplet heating and evaporation in the gas at temperature 700 K near the droplet and external temperature 2500 K (this temperature can be identified with the temperature of remote flame). These values of temperature are extreme rather than typical, but they are used to illustrate the effect of thermal radiation as shown in Chapter 3, Section 3.4. As we did in the previous section we took a droplet radius equal to 10 μm and its initial temperature is equal to 300 K. The convection heat transfer coefficient is assumed equal to $k_g/R_d(t)$ throughout the droplet lifetime (this refers to stationary or almost stationary droplets relative to the surrounding gas). The problem has been solved in the following approximations:

a) Temperature gradient inside the droplet, and contribution of radiation are not taken into account Equation (3.4.1) ($\varepsilon_l = 0$).

b) Temperature gradient inside the droplet is not taken into account. The contribution of radiation is taken into account based on the presentation of P_1 in the form (5.6.1)

c) No contribution of radiation, but the temperature gradient inside the droplet is taken into account. Numerical algorithm of the solution of Equation (4.2.1) is based on the analytical solution corresponding to constant h (Equation (4.3.1.19)), applied at each time step.

d) The same as case (c) but with contribution of radiation taken into account based on the presentation of P_1 in Equation (4.2.3)

e) The same as case (c) but with contribution of radiation taken into account based on the presentation of P_1 in the form (5.6.1)

f) The temperature gradient inside the droplet is taken into account. NSDE with radiation term in the form (5.6.1) is performed using the finite difference technique with fully implicit marching in time.

In Figure (5.12) the surface temperature and radii of droplets predicted by the models based on approximation 'd' and 'e' are compared. The values of Δt were taken equal to 1 μs. As can be seen from this figure, the time evolution of surface temperature predicted by both models practically coincide. The time evaluation of droplet radii predicted by these models differs slightly, but this difference can be ignored in most practical applications. Note that the values of P_1 (R) obtained based on Equation (4.2.3), already contained an error of about 10% (see the discussion in Section 3.2.2). Recall that the values of parameters used for our comparison are extreme rather than typical for diesel engine environment. In more realistic cases this difference between the curves is expected to be even smaller. Under these circumstances, the application of the radiation term in the form (5.6.1) seems to have clear advantages when compared with the application of the radiation term in the form (4.2.3), due to simplicity of the former. This allows us to recommend the application of radiation term in the form (5.6.1) for practical calculations in CFD codes.

The plots of droplet surface temperature and radius predicted by the models based on approximations 'a'-'c' and 'e'-'f'' are shown in Figure (5.13). The values of Δt were taken equal to 10^{-5} sec and for the case 'f', the number of nodes $r/\Delta r$ was taken equal to 100 as in the case without radiation. As can be seen from this figure, the effect of radiation tends to increase droplet evaporation due to the additional heat source, as expected. The effect of temperature gradient is expected to lead to an increase in droplet

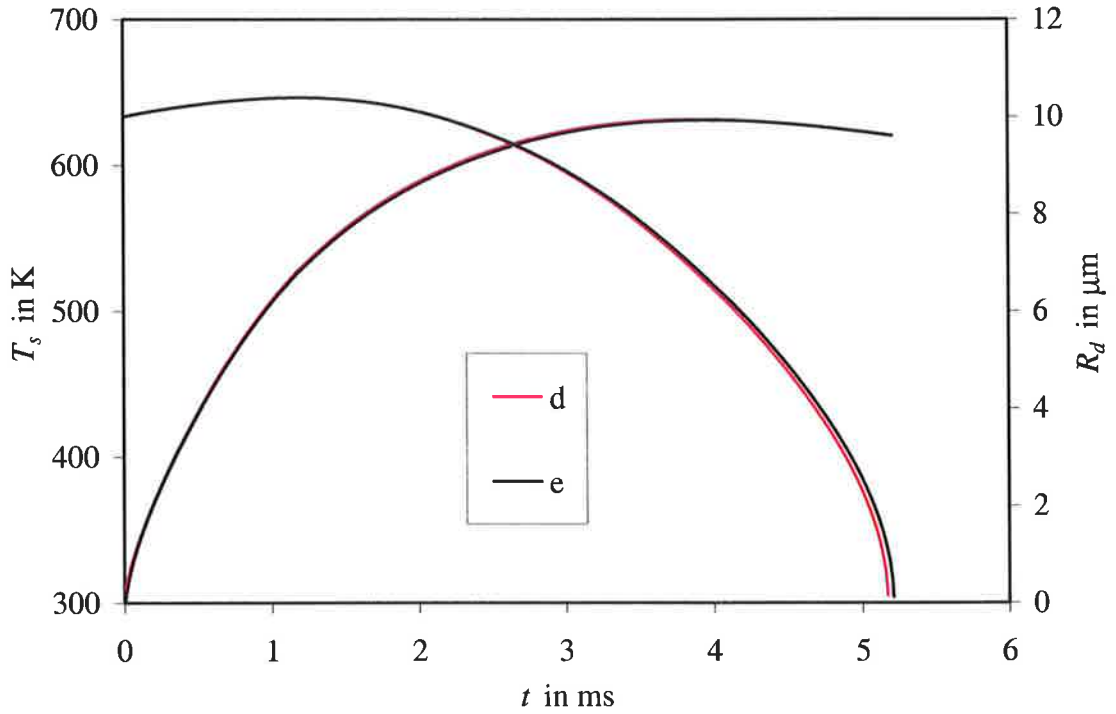

Fig. 5.12 Plots of droplet surface temperature T_s and radius R_d versus time taking into account the effects of thermal radiation. The letters 'd' and 'e' corresponding to the numerical algorithms used as indicated in the text. T_g = 700 K and T_{ext} = 2500 K.

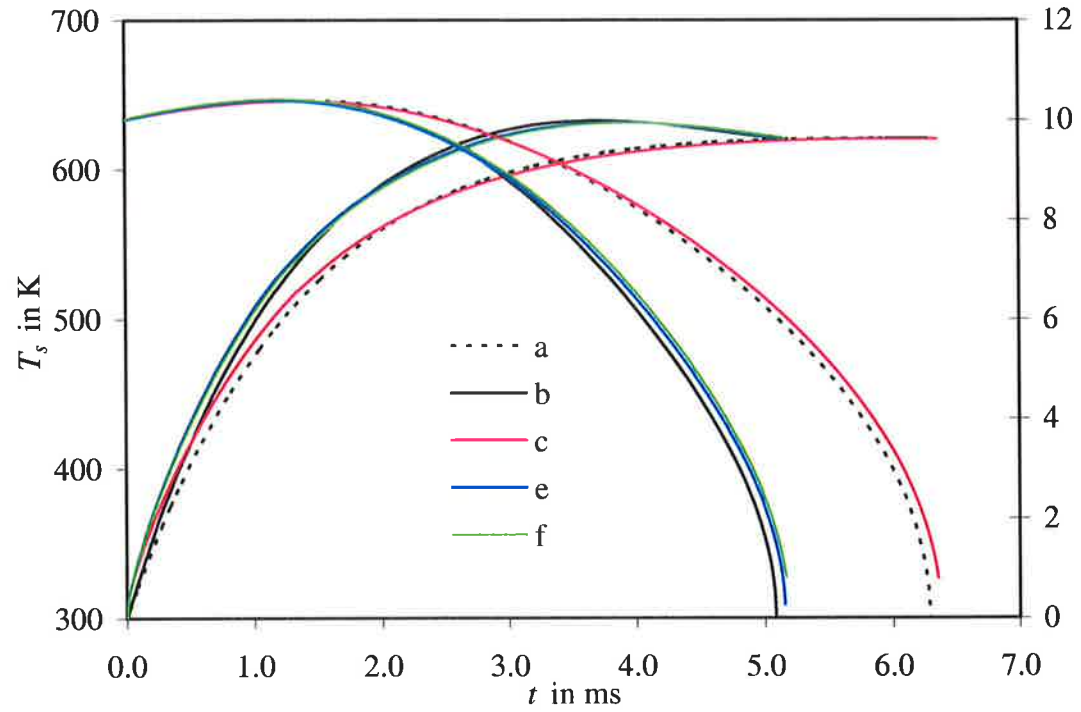

Fig. 5.13 The same as Fig 5.13 but for numerical algorithms 'a' – 'c' and 'e' –'f'.

surface temperature when compared with the droplet average temperature. This would lead to an increase in droplet evaporation due to the direct temperature effect, and its decrease due to decrease of convective heat supply to droplet surface. As follows from Figure (5.13), the second effect dominates over the first, and the rate of droplet evaporation decreases. The curves 'b', 'e' and 'f' in Figure (5.13) appear to be rather close to each other. This means that the predictions of the numerical algorithm of the solution of Equation (4.2.1) based on the analytical solution corresponding to constant h and NSDE with the radiation terms taken into account give rather similar results.

The errors in evaporation time as the functions of Δt for the cases 'c', 'e' and 'f' are shown in Figures (5.14). The errors in all cases are calculated relative to the predictions of NSDE with $\Delta t = 1$ μs and $r/\Delta r = 1000$. From Figure (5.14), the largest errors are those for the curve 'c', which corresponds to the case when the effect of radiation is not taken into account. Hence, the radiation cannot be ignored in this case. The errors for other curves increase with increasing Δt. This error in the predicted evaporation times is negligibly small at $\Delta t < 10^{-5}$ sec and can be tolerated in most practical applications.

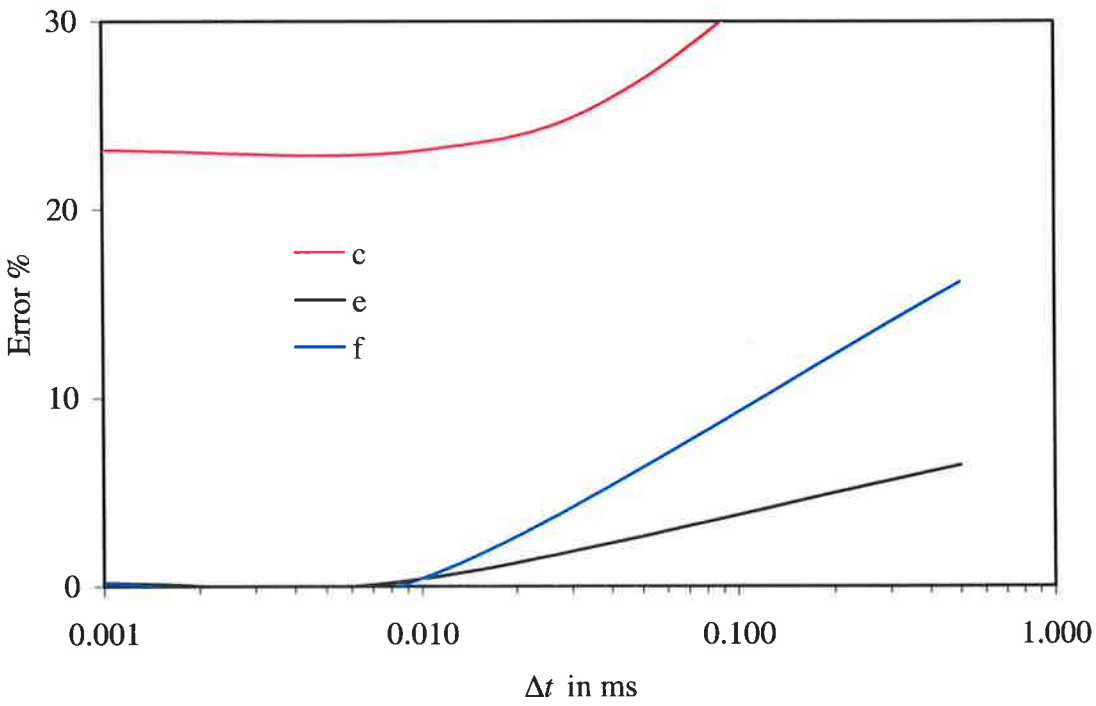

Fig 5.14 Plots of errors of calculation of evaporation time versus time step for the curves 'c', 'e' and 'f' presented in Figure (5.13). These errors were calculated relative to the prediction of NSDE with $\Delta t = 1$ μs and $r/\Delta r = 1000$. The letters correspond to the numerical algorithms used as indicated in the text.

As follows from Figure (5.15), the CPU requirements for the case 'd' are more than an order of magnitude larger than for other curves. This CPU requirement is difficult to justify in view of the very small improvement of the accuracy of calculations. Comparing curves 'e' and 'f' we can see that the CPU time for the algorithm based on the analytical solution is always much less than CPU time for the algorithm based on NSDE.

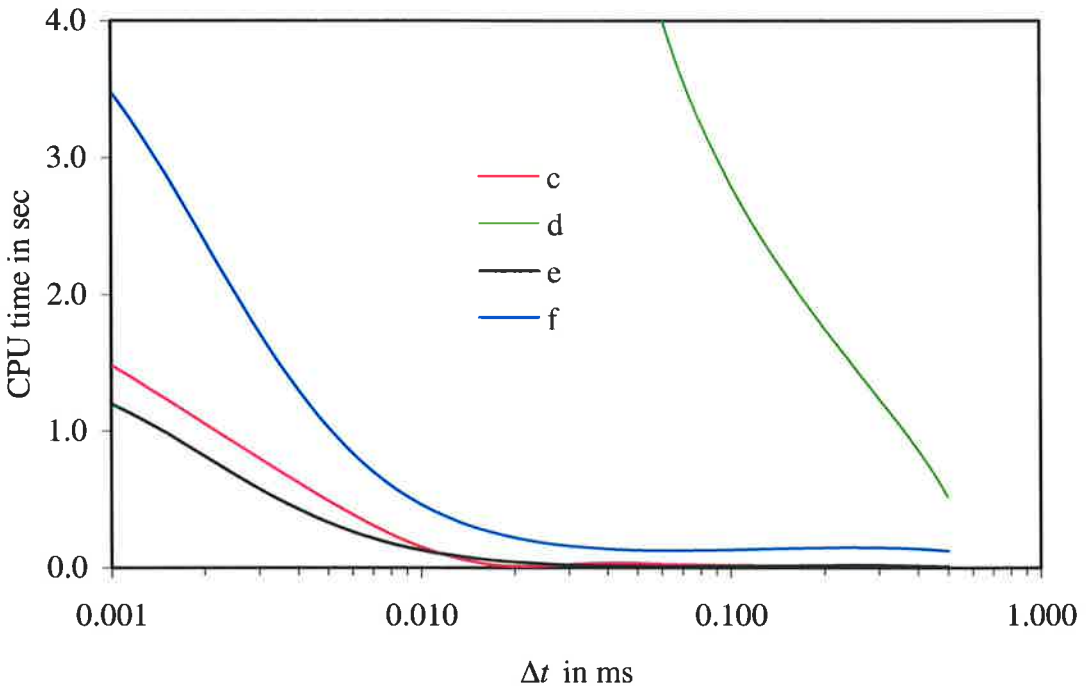

Fig. 5.15 Plots of CPU time versus time step for the curves 'c' – 'f' presented in Figure (5.13). The letters correspond to the numerical algorithms used as indicated in the text.

Note that the CPU time required for the case without radiation (curve 'c') is slightly larger than that for the case when the radiation is taken into account and the radiation term is taken in the form (5.6.1). This is related to the fact that in the case without radiation droplet needs longer time to evaporate.

Results of the errors and the CPU times of calculation of the evaporation time at various external temperatures (700 K - 2500 K) and a wide range of initial droplet diameters (5μm, 50 μm) with the contribution of radiation are shown in Table (5.2). Gas temperature is taken equal to 700 K. The errors were calculated relative to the prediction of the NSDE with Δt =1 μs using 1000 nodes along droplet radius. The errors and the CPU times are presented for the numerical algorithm based on the analytical solution for h = const (A) and NSDE (N) using 100 nodes along droplet radius. It can be noticed from the results that the predicted errors and CPU time for the algorithm based on the

analytical solution for h = const is always much less than the predicted errors and CPU time for the algorithm based on NSDE. This allows us to recommend the former algorithm with the radiation term of Equation (5.6.1) for practical applications, including possible implementation into CFD codes.

Δt /ms	0.001								0.01							
R_{d0} /μm	2.5				25.0				2.5				25.0			
	Erro r%		CPU time /ms		Erro r%		CPU time /ms		Erro r%		CPU time /ms		Erro r%		CPU time /ms	
T_{ext}	A	N	A	N	A	N	A	N	A	N	A	N	A	N	A	N
700	0.25	0.50	0.1	0.38	0.02	0.39	9.82	26.7	0.01	2.56	0.02	0.13	0.05	0.38	0.93	2.70
1000	0.25	0.51	0.1	0.38	0.02	0.40	8.75	25.5	0.01	2.56	0.02	0.13	0.02	0.40	0.88	2.59
1500	0.01	0.51	0.1	0.38	0.02	0.40	7.78	21.3	0.01	2.56	0.01	0.11	0.06	0.38	0.75	2.20
2000	0.26	0.26	0.1	0.38	0.02	0.46	5.96	16.6	0.01	2.63	0.01	0.11	0.04	0.45	0.57	1.71
2500	0.01	0.52	0.1	0.37	0.03	0.47	4.61	12.2	0.01	2.63	0.01	0.10	0.05	0.94	0.63	1.30

Table 5.2 Errors and CPU times of calculation of evaporation time at various external temperatures. Thermal radiation effects are taken into account. The errors were calculated relative to the prediction of NSDE with $\Delta t = 10^{-6}$ sec using 1000 nodes along droplet radius. The errors and CPU times are presented for the numerical algorithm based on the analytical solution for h = const (A) and NSDE (N) using 100 nodes along droplet radius, T_g = 700 K.

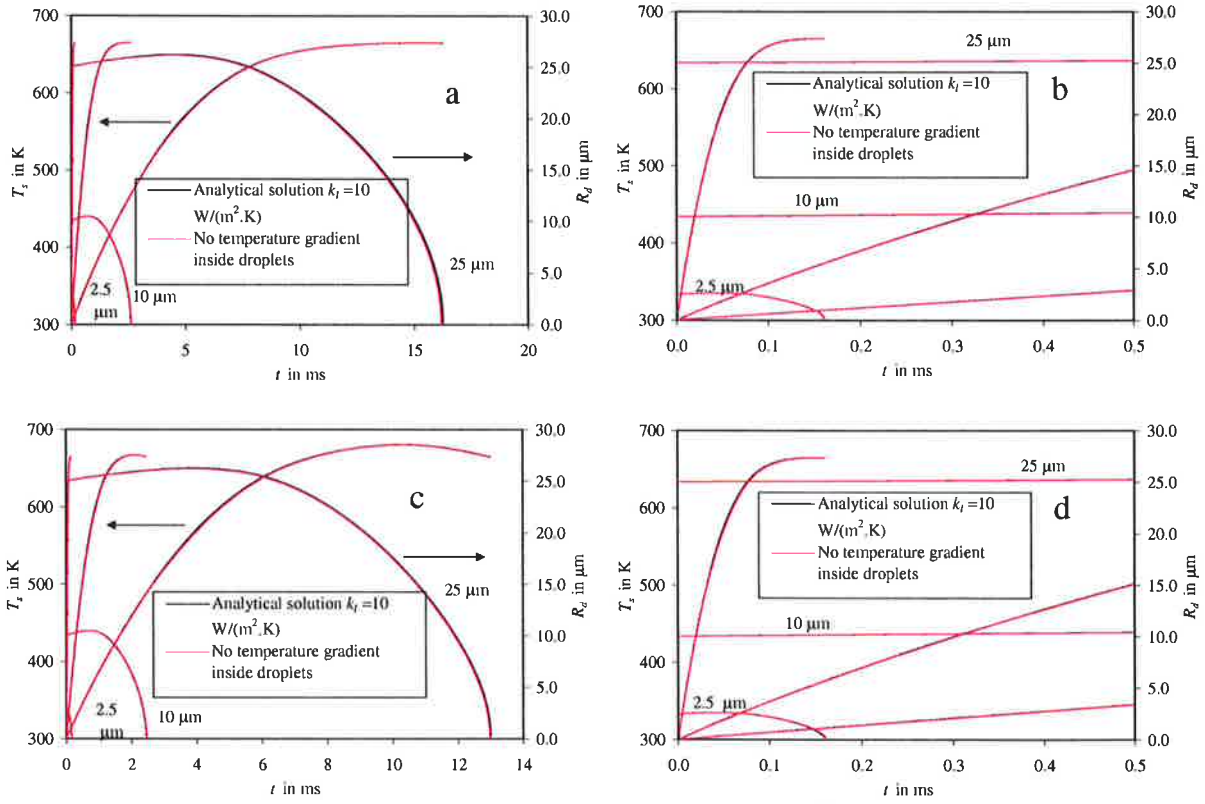

Fig. 5.16 Plots of droplet surface temperature T_s and radius R_d versus time, without taking into account the effect of thermal radiation (a and b) and with taking into account the effect of thermal radiation (c and d). T_g = 1000 K, T_{ext} = 2000 K. The calculation have been performed using the numerical algorithms based on the analytical solution for h = const with k_l = 10 W m^{-2} K^{-1} and the numerical solution based on the assumption that there is no temperature gradient inside the droplet. Initial droplet radius is indicated near the plots. Figures (b, d) are zoomed for Figures (a, c), respectively.

Note that the solution predicted by the algorithm using the analytical solution for h = const reduces to that predicted by the numerical algorithm based on the assumption that there is no temperature gradient inside the droplet in the limit $k_l \to \infty$ if the value k_l = 10 W / (m^2 K) was used as shown in Figure (5.16).

5.7 Conclusions of Chapter 5

Several new approaches to numerical modeling of droplet heating and evaporation by convection and radiation from the surrounding hot gas have been suggested. Finite thermal conductivity of the droplets and internal recirculation in them have been taken

into account via the introduction of the effective thermal conductivity of the droplets k_{eff}. Gas temperature T_g and convective heat transfer coefficient h have been taken as arbitrary functions of time. Our approaches have been based on the incorporation of the solutions of the heat conduction equation inside the droplet (see Chapter 4) into a numerical code, when gas temperature and convection heat transfer coefficient vary with time. It has been shown that the solution based on the assumption of constant convective heat transfer coefficient is the most efficient for the implementation into numerical codes. Initially, this solution is applied at the first time step, using the initial distribution of temperature inside the droplet. The results of the analytical solution over this time step are used as the initial condition for the second time step etc. This approach has been compared with the approaches based on the numerical solution of the discretised heat conduction equation, those based on the assumption that there is no temperature gradient inside the droplet, and those based on the assumption that the temperature distribution inside the droplet has a parabolic profile. All these approaches have been applied to the numerical modeling of fuel droplet heating and evaporation in conditions relevant to diesel engines, but without taking into account the effects of droplet break-up. The algorithm based on the analytical solution for constant h has been shown to be more effective (from the point of view of the balance of accuracy and CPU time requirement) than the approach based on the numerical solution of the discretised heat conduction equation inside the droplet, and more accurate than the solution based on the parabolic temperature profile model. The relatively small contribution of thermal radiation to droplet heating and evaporation allows us to describe it using a simplified model, which takes into account their semi-transparency, but does not consider the spatial variations of radiation absorption inside droplets.

6. TRANSIENT HEATING, EVAPORATION AND IGNITION OF DIESEL FUEL DROPLETS: COUPLED SOLUTIONS

Models for heating and evaporation of a semi-transparent fuel droplet taking into account the temperature gradient inside the droplet and the thermal radiation effects were described in Chapters 3-5. These models were tested in various conditions and their performance was tested and validated.

This chapter is focused on further development of the numerical algorithm based on the analytical solution of the heat conduction Equation (4.2.1) inside the droplet (the algorithm described in Chapters 3-5), its testing and application to modelling the processes of heating, evaporation, ignition, and break-up of diesel fuel droplets. In contrast to Chapter 5, the effects of droplets' velocities, heating and evaporation on the surrounding gas is taken into account (coupled solutions). The surrounding gas will be accelerated by movement of the droplets. Then the gas will cool with accompanying heating and evaporation of droplets. The fuel vapour will diffuse through the gas culminating in ignition of the fuel vapour / air mixture. These effects are expected to be accelerated significantly via droplet break-up (Sazhin et al, 2003). The new algorithm is implemented into a zero dimensional code in which all values of gas parameters (velocity, temperature, fuel vapour concentration etc) are assumed to be homogeneous. Parameters typical for a diesel engine combustion chamber will be used.

Naturally, while the main focus of this chapter is on the effects produced by the temperature gradient in droplets, a number of important processes will be beyond its scope. These include the effects of real gases (Hohmann and Renz, 2003), near critical and supercritical droplet heating (Bellan, 2000; Givler; Abraham, 1996), analysis of droplets' collisions and coalescence (Loth, 2000; Orme, 1997).

The droplets dynamics effects are discussed in Section 6.1. The effects of internal circulation inside the droplets are discussed in Section 6.2. The gas phase heat and mass exchange with fuel droplets is discussed in Section 6.3. In Section 6.4 the break-up model is discussed. The Shell autoignition model is discussed in Section 6.5. In Section 6.6 a description of the zero dimensional code is given. In Section 6.7 this code is tested against several available experimental data sets. Results of sensitivity studies of the effects of temperature gradient inside droplets and radiation on droplet evaporation time, ignition delay in the absence and present of the break-up process are discussed in Section 6.8. The main results of the chapter are summarized in Section 6.9.

Some preliminary results of this chapter were published in Sazhin, Abdelghaffar et al (2005b).

6.1 Dynamics of droplets

The initial velocity of fuel droplets injected from a nozzle is typically much greater than the velocity of in-cylinder air. The droplets are rapidly decelerated due to the drag force, while the air in the vicinity of the spray is accelerated (Sazhin et al, 2001b; 2003). The dynamics of fuel droplets has to be taken into account in numerical algorithms of heating and evaporation of diesel fuel droplets to investigate the effects of the temperature gradient inside the droplet. In this case the convective heat transfer coefficient increases and the droplets boundary layer thermal resistance decreases. The ratio of the internal thermal resistance of the fuel droplet to its boundary layer thermal resistance (Biot number) increases. Hence, the effect of the temperature gradient inside the droplet on modelling heating and evaporation of diesel fuel droplet is expected to be larger than in the case of stationary droplets.

The droplet dynamics is described by the following equation (Sirignano, 1999 and Sazhin et al, 2001):

$$m_d \frac{d\vec{U}_d}{dt} = -\frac{1}{2} C_d \rho_g \left(\vec{U}_d - \vec{U}_g\right) \left|U_d - U_g\right| A_d, \tag{6.1.1}$$

where m_d, $\vec{U}_d$, $A_d = \pi R_d^2$ are droplet's mass, velocity and cross-sectional area, respectively, $\vec{U}_g$ is gas velocity and C_d is the drag coefficient for non evaporating droplets.

The solution of Equation (6.1.1) requires the knowledge of C_d, which depends on temperature and droplet Reynolds number (Chiang et al, 1992; Panton, 1996). Our analysis will be restricted to spherical droplets. A number of approximations have been suggested (Putnam, 1961; Wallis, 1969; Morsi and Alexander, 1972; Borman and Regland, 1998). Expressions for C_d suggested by these authors can be used for numerical analysis of Equation (6.1.1), but they are not suitable for analytical estimates (Sazhin et al, 2003). A much simpler approximation for the drag coefficient was suggested by Putnam (1961):

$$C_d = \begin{cases} \dfrac{24}{\mathrm{Re}_d}\left(1 + \dfrac{1}{6}\mathrm{Re}_d^{\frac{2}{3}}\right) & \text{when } \mathrm{Re}_d \le 1000 \\ 0.424 & \text{when } \mathrm{Re}_d > 1000 \end{cases} \tag{6.1.2}$$

where Re_d is Reynolds number of a droplet defined as in Equation (2.2.1.2.2). An alternative approximation was suggested by Douglas et al (1995):

$$C_d = \begin{cases} \dfrac{24}{Re_d} & Re_d \le 2 \quad \text{(Stokes flow)} \\ \dfrac{18.5}{Re_d^{0.6}} & 2 < Re_d \le 500 \quad \text{(Allen flow)} \\ 0.44 & 500 < Re_d \le 10^5 \quad \text{(Newton flow)} \end{cases} \tag{6.1.3}$$

There seems to be an error in Douglas et al (1995) where the transition between Stokes and Allen flows was identified with $Re_d = 0.2$. This was corrected by Sazhin et al (2003) where the authors found that predictions of C_d for Stokes and Allen flows match for $Re_d = 2$ but not for $Re_d = 0.2$. The value of C_d for Re = 2 (Stokes flow) is consistent with the results presented in Robertson and Crowe (1997) and White (1999). It is sometimes recommended to use $C_d = 24/ Re_d$ for $Re_d < 0.5$ (Robertson and Crowe, 1997), the error in the prediction of C_d by this formula does not exceed about 20% for $Re_d < 2$ (Robertson and Crowe, 1997; White, 1999). More accurate approximation for C_d for $Re_d < 2$ can be obtained from the formula in Equation (6.1.2) or from the formula $C_d = (24/ Re_d) [1+ 3 Re_d /16]^{1/3}$ (Douglas et al, 1995).

Equation (6.1.2) is used for the droplets' trajectory calculation in the present work due to its simplicity and predicting more accurate values for C_d for $Re_d < 2$. Not that Re_d is close to zero over most of lifetimes for small droplets (Renksizbulut and Haywood, 1988).

The expressions for C_d given above do not take into account the effects of droplet acceleration, internal recirculation, burning, non-spherical shape and vibrations and heating process. They cannot be applied when Mach number is close to or greater than 1 (Borman and Ragland, 1998). The condition $Re_d < 10^5$ is always satisfied for realistic droplets in diesel engine (Sazhin et al, 2003). For the case of an evaporating sphere, the drag coefficient is reduced and can be replaced by (Abramzon and Sirignano, 1989):

$$C_{df} = \frac{C_d}{(1+B_M)^{\alpha}} \tag{6.1.4}$$

where C_{df} is drag coefficient with evaporation effect,

$$\alpha = \begin{cases} 1 & \text{for } B_M < 0.78 \\ 0.75 & \text{for } B_M \ge 0.78 \end{cases}$$

The initial droplet velocity U_{di} can be calculated from the pressure drop at the nozzle (ΔP) (Borman and Ragland, 1998):

$$U_{di} = C_{do}\sqrt{\frac{2\Delta P}{\rho_l}}, \tag{6.1.5}$$

where C_{do} is the orifice discharge coefficient, $\Delta P = P_{inj} - P_{cyl}$, P_{inj} is injection pressure and P_{cyl} is in-cylinder pressure. There is some uncertainty regarding the value of C_{do} because it depends on the nozzle type. Both Chehroudi and Bracco (1988) and Reitz and Diwakar (1987) recommended that this value could be assumed 0.7, while Lefebvre (1989) and Borman and Ragland (1998) believe that this value is close to 0.39. Paál (1992) and Sazhin et al (2001) assumed that this value equals 0.62 and 0.8, respectively.

6.2 Effects of internal circulation inside the droplets

When the droplets move, the heat and mass transport over the boundary layer is enhanced. Furthermore, the shear force on the liquid surface causes internal recirculation that enhances the heating of the liquid (Sirignano, 1999). In this case the convection heat transfer inside the droplet can dominate over conduction. The finite liquid thermal conductivity models can be generalised to take into account the internal circulation inside droplets. As mentioned before, this could be achieved by replacing the thermal conductivity of liquid k_l by the so-called effective thermal conductivity $k_{eff} = \chi k_l$, where the coefficient χ varies from about 1 (at droplet Peclet number $Pe_d < 10$) to 2.72 (at $Pe_d > 500$) (Abramzon and Sirignano, 1989). It can be approximated by Equation (2.2.1.1.1).

Binary diffusion coefficient D_{12} for multicomponent fuel droplets should be replaced by the so-called effective binary diffusion coefficient $D_{12eff} = \chi D_{12}$ in order to take into account the internal circulation inside the multicomponent fuel droplets (Hohmann and Renz, 2003).

6.3 Gas phase heat and mass exchange with diesel fuel droplets

A detailed calculation of the flow around the droplets during the evaporation process is rather difficult and is usually not performed in CFD calculations. Rather an average gas velocity is taken into account to estimate the drag force. We assume that there are no spatial gradients inside a computational cell. The problem is unsteady as the droplet size is continuously changing due to swelling and evaporation. Relative droplet velocity is also changing due to droplet drag, and droplet temperature is changing due to heating and evaporation (Sirignano, 1999).

The mass vaporization rate from the droplet surface is described by the following equation (Sirignano, 1999):

$$\frac{dm_d}{dt} = -2\pi R_d \rho_g D_{12} \mathrm{Sh}\, B_M, \tag{6.3.1}$$

where Sh can be obtained using the Equation (2.2.1.2.24).

The analytical solution of the heat conduction equation inside droplets (4.2.1) for constant h, Equation (4.3.1.19), is used to calculate the droplet temperature.

A number of correlations for Nusselt number (Nu) and Sherwood number of moving and evaporating droplets were discussed in Chapter 2. In the absence of evaporation, Correlations (2.2.1.2.3) and (2.2.1.2.4) are believed to be more accurate than Correlations (2.2.1.2.1) and (2.2.1.2.2) at $\mathrm{Re}_d < 10$ (Abramzon and Sirignano, 1989). However, the difference between the predictions of these correlations for $1 < \mathrm{Re}_d \leq 400$ does not exceed about 10%. This is well within the margins of errors of experimental measurements of parameters used in these equations. In the presence of evaporation, following widely used practice (see e.g. Faeth, 1983; Lefebvre, 1989) the simplified Correlations (2.2.1.2.23) and (2.2.1.2.24) will be used in our analysis. This is justified by the fact that the focus of the chapter is on the investigation of the effect of temperature gradient inside droplets on evaporation, break-up and ignition processes, and not on the most accurate modelling of these processes. The corrections introduced by Equations (2.2.1.2.16) and (2.2.1.2.17) are not expected to influence the conclusions of this chapter. Moreover they can, on some occasions, even marginally decrease the accuracy of calculations of the mass flow rate of evaporated fuel (Yao et al, 2003).

When the initial temperature of the droplet is lower than the surrounding gas temperature, and does not exceed its own boiling temperature, the net heat transfer Q from the surrounding gas to the film surrounding the droplet, prior to ignition, has three effects: (1) to heat up the liquid droplet Q_L; (2) to vaporize the liquid, Q_λ ; and (3) to be carried back with diffusing vapour in the form of superheat, Q_S. The heat that arrives at the droplet surface is $Q_V = Q - Q_S$. Hence, (El Wakil et al, 1954):

$$Q_V = Q - Q_S = Q_L + Q_\lambda. \tag{6.3.2}$$

The following relation between Q and Q_V can be obtained (El Wakil et al, 1954):

$$Q_V = Q\left(\frac{z}{e^z - 1}\right), \tag{6.3.3}$$

where $z = \dfrac{\dot{m}_v c_v}{h A_d}$, $\dot{m}_v$ is mass rate of fuel vaporization, c_v is fuel vapour heat capacity at constant pressure and A_d is the droplet surface area.

The factor $z/(e^z-1)$ shows the fraction of the total heat transfer Q from the air that finally arrives at the surface of the liquid droplet This factor therefore represents a correction factor to the heat transfer coefficient h (El Wakil et al, 1954).

Equation (6.3.3) leads to the following modification of h due to the effect of superheat (El Wakil et al, 1954):

$$\tilde{h} = h\left(\frac{z}{e^z - 1}\right) \tag{6.3.4}$$

For a stationary droplet Equation (6.3.4) is identical with Equation (2.2.1.2.23). Indeed, Equation (6.3.1) can be rearranged to:

$$\ln(1 + B_M) = \frac{\dot{m}_d}{4\pi\rho_g D_{12} R_d}$$

If $\mathrm{Le} = \dfrac{\overline{k_g}}{D_{12} c_v \rho_g} = 1$ then

$$\ln(1 + B_M) = \frac{\dot{m}_d c_v}{4\pi \overline{k_g} R_d} = \frac{\dot{m}_d c_v}{h A_d} = z$$

and $B_M = e^z - 1$. Hence:

$$\frac{\ln(1 + B_M)}{B_M} = \frac{z}{e^z - 1} = \frac{\mathrm{Nu}}{\mathrm{Nu}_0} = \frac{\tilde{h}}{h}$$

Heat removed from the gas is described by Equation (2.2.1.2.1). Gas temperature was calculated from the definition of the heat lost by the gas side:

$$\frac{dT_g}{dt} = -2\pi \frac{k_g}{m_g c_g} \sum_i \mathrm{Nu}_{0i} R_{di} (T_g - T_{si}), \tag{6.3.5}$$

where m_g is the total mass of gas, subscripts i indicate individual droplets, and summation is performed over all droplets. Gas mass and droplets' radii are updated at each time step to take into account droplet evaporation.

It can be seen from Equation (6.3.5) gas temperature decreases with time due to the transfer of energy from ambient air to droplets.

The momentum transferred from gas to droplets has the same value but the opposite sign to the momentum transferred from droplets to gas. Gas velocity is calculated from the momentum conservation equation, which can be presented in the form:

$$\frac{d(m_g U_g)}{dt} = -\sum_i \frac{d(m_{di} U_{di})}{dt} \tag{6.3.6}$$

Equations (6.3.5) and (6.3.6) are applied at each time step to get the new values of gas temperature and velocity. These values are used as initial values for the next time step.

6.4 Droplets' break-up model

Droplet break-up influences spray penetration, evaporation and mixing in high-pressure sprays. If the effect of evaporation is ignored (heating-up period) the spray droplets size is the outcome of a competition between droplet break-up (which decreases with time due to reduction of relative velocity between the droplet and entrained gas) and droplet coalescence (which also decreases with increasing the distance from the nozzle because of the expansion of spray) (Reitz and Diwakar, 1987). Droplet break-up dominates in hollow-cone sprays as coalescence is minimized by the expanding spray geometry. Droplet sizes in solid-cone sprays are influenced by both droplet coalescence and break-up (Reitz and Diwakar, 1987). Since evaporation rates depend on droplet size, this implies that droplet break-up and coalescence influence the fuel vapour distribution and mixing. Reitz and Diwakar (1986) concluded that the distribution of fuel in practical devices could be controlled by exploiting the competition between droplet break-up and coalescence. This can be accomplished even with a relatively simple injector, since the spray droplet sizes are determined mostly by droplet break-up and coalescence, but not the size of injector nozzles.

A number of droplet break-up models have been suggested (Borman and Ragland, 1998; Lefebvre, 1989; Shraiber et al, 1996; Lin, 1998; Gorokhovski, 2001; Gorokhovski and Saveliev, 2003). The model developed by Reitz and Diwakar (1986, 1987), is widely used in CFD codes (VECTIS and STAR CD CFD codes). In this model two different mechanisms to break up the fuel spray into smaller droplets are taken into account. The first mechanism is the bag break-up, which occurs when a high pressure is exerted on the front of the droplet, and a low pressure is on the wake of the droplet. Thus a spherical droplet is deformed into a bag shape, and eventually breaks into small droplets. The second mechanism is the stripping break-up, which occurs when a droplet is sheared by a relative velocity between the droplet and ambient air, and is stripped into smaller droplets. This can also be viewed as the result of tangential stress acting on the moving droplets, which leads to stripping break-up.

The bag break-up occurs when (Reitz and Diwakar, 1987):

$$\mathrm{We} = \frac{\rho_g (U_d - U_g)^2 R_d}{\sigma_s} > C_{b1} = 6, \qquad (6.4.1)$$

where We is the Weber number (ratio of aerodynamic forces to surface tension forces), σ_s is the droplet surface tension, We is defined following the original papers by Reitz and Diwakar (1986, 1987), although this definition differs from the one used by Lefebvre (1989) and Borman and Ragland (1998). The factor C_{b1} is an empirical coefficient in the range 3.6 to 8.4 (Reitz and Diwakar, 1987), $C_{b1} = 6$ will be used in our analysis, following Reitz and Diwakar (1986, 1987) and Sazhin et al (2003).

The bag break-up time is assumed to be proportional to the inverse frequency of the main harmonic of droplet oscillations. The lifetime of an unstable droplet as estimated as (Reitz and Diwakar, 1987):

$$t_b = C_{b2}\left(\frac{\rho_l R_d^3}{2\sigma_s}\right)^{1/2}, \tag{6.4.2}$$

where the factor $C_{b2} = \pi$.

The stripping break-up occurs when (Reitz and Diwakar, 1987):

$$\frac{We}{\sqrt{\mathrm{Re}_d}} > C_{s1} = 0.5, \tag{6.4.3}$$

Note that Borman and Ragland (1998) used C_{s1} =0.7.

The stripping break-up lifetime is estimated as (Reitz and Diwakar, 1987):

$$t_s = C_{s2}\left(\frac{\rho_l}{\rho_g}\right)^{1/2}\frac{R_d}{(U_d - U_g)}, \tag{6.4.4}$$

where C_{s2} is an empirical coefficient in the range 2 to 20. The value of this coefficient is determined by fitting the predictions of the model with experimental data. This is the reason why different values were reported: C_{s2} = 20 by STAR CD CFD code, 13 by Sazhin et al (2003) and VECTIS CFD code and 2, 20 and 5 by Reitz and Diwakar (1987). The reduction of C_{s2} increases the rate of droplet break-up, but the stable droplet size is independent of C_{s2} because the relative velocities are the same.

In practical applications of this model, the stability criteria, conditions (6.4.1) and (6.4.3) were checked for each droplet parcel at each time step. If either of the two criteria is met for the time equal to the corresponding time defined in Equations (6.4.2) and (6.4.4), then stable droplet size for the parcel was specified from Equations (6.4.1) or (6.4.3). In both cases, the reduction of droplet radii is described by the equation:

$$\frac{dR_d}{dt} = \begin{cases} 0 & \text{when } R_d \le R_{db(s)} \\ -\dfrac{R_d - R_{db(s)}}{t_{b(s)}} & \text{when } R_d > R_{db(s)} \end{cases}, \tag{6.4.5}$$

where $t_{b(s)}$ are characteristic times of the development of bag (stripping) break-ups and defined by Equations (6.4.2) and (6.4.4), respectively and $R_{db(s)}$ are threshold radii of marginally stable droplets with respect to bag (stripping) break-ups. $R_{db(s)}$ are determined by the condition $We = 6, We/\sqrt{\mathrm{Re}_d} = 0.5$, respectively. This approximation is justified by the fact that the contribution of smaller droplets generated during the break-up is relatively small and can be ignored (Reitz and Diwakar, 1986). Also Equation (6.4.5) implies that droplets preserve their spherical shape during the break-up process. This is the limitation of the model, which was appreciated by the authors (Reitz and Diwakar, 1986; 1987).

With each change in droplet size, the droplet number is changed to ensure the conservation of liquid mass:

$$n_n R_{dn}^3 = n_o R_{do}^3 \tag{6.4.6}$$

The energy and momentum correction due to break-up were found to be insignificant (Reitz and Diwakar, 1986; 1987).

The contribution from catastrophic break-up has been ignored. This is likely to occur at rather large We (greater than about 350 (Liu and Reitz, 1993; Tanner, 2004)), and is not expected to be observed for small droplets in diesel engines away from the immediate vicinity of the nozzle. An alternative equation for the evolution of droplet mass during the development of break-up has been discussed in Tanner (2004) (see his Equation (3)). A detailed analysis of the latter equation and its comparison with Equation (6.4.5) is beyond the scope of this chapter.

6.5 The Shell autoignition model

Autoignition can be defined as an onset of combustion in a reactive medium raised to a certain temperature and pressure, without any external agents (e.g. electric spark) (Spalding, 1979; Kuo, 1986). It is sometimes called heterogeneous ignition, self-ignition or spontaneous ignition (Kuo, 1986). It happens in diesel engines by rapid compression of fuel-oxidizer mixture (positive combustion) or in gasoline engine as end-gas combustion or knock (Kuo, 1986; Bradley et al, 1996a, 1996b, 2002; Bradley and Morley, 1997).

The initial temperature at which the autoignition can be developed and the time delay before the start of autoignition is considered to be the main characteristic parameters for the autoignition process (Brady, 1996). These parameters strongly depend on the condition of internal surface of the engine, pressure, fuel composition and other

parameters. Modelling of autoignition phenomenon is very important for predicting the initiation of combustion in diesel engines. The autoignition model should be simple and adequately describe the main features of the combustion process.

The detailed kinetic mechanism of the autoignition process includes hundreds of chemical reactions and over a hundred of species (Sazhina et al, 1999). The lack of accurate kinetic data for many reactions is a major problem in constructing the detailed kinetic mechanism. This encouraged many authors to develop reduced chemical models (Basevich et al, 1994; Halstead et al, 1973; Griffiths, 1995; Poppe et al, 1993; Basevich and Frolov, 1994). Poppe et al (1993) have considered a model based on 30 reactions and 21 species. Basevich and Frolov (1994) reduced the number of reactions and species to 21 and 13, respectively. Müller et al (1992) suggested four-step model with adjusted rate coefficients. The practical application of this model was questioned because the ignition was produced entirely by thermal feedback, while the chain branching process was ignored (Griffiths, 1995).

The group of researchers from Shell Research Ltd developed an autoignition model, which is now widely used (Shell model). This model introduces generic species with kinetic rate constants deduced from experimental data (Halstead et al, 1975; Halstead et al, 1977). In the Shell model the autoignition process is reduced to the eight-step chain branching reaction scheme. The main advantage of the Shell model is its simplicity combined with a generalized description of the kinetic mechanism, which proves to be adequate for many applications. Although this model was developed to simulate the autoignition properties of a number of hydrocarbon fuels for spark-ignition gasoline engines, it was successfully extended to modelling the combustion of diesel fuels (Sazhina et al, 1999).

This study is based on the formulation for the Shell model developed by Sazhina et al (1999) with A_{f4} in the range between 3×10^6 and 6×10^6. Details of the Shell model are discussed in Appendix 6.

6.6 Zero dimensional code: implementation of the coupled algorithms

The model of heating a semi-transparent fuel droplet based on the analytical solution of heat conduction equation inside the droplet (4.2.1) was implemented into a zero dimensional code. A number of processes in diesel engines (swelling, evaporation, internal circulation inside the droplets, dynamics of the droplets, effects of the droplets on the gas phase, droplets break up and the autoignition based on the Shell model) have

been taken into account. Effects of turbulence and coalescence processes have been ignored.

As the first step we assume that the temperature of gas T_g (t = 0) and initial droplet velocity U_d (t = 0) are given. The values of the convection heat transfer coefficient depend on the external gas properties (thermal conductivity and viscosity) alongside with droplet radius. The latter is calculated using Equation (3.4.2) and taking into account swelling due to decrease of liquid fuel density with increasing temperature. Under these assumptions the calculation of droplet temperature reduces to the solution of Equation (4.2.1) subject to appropriate initial and boundary conditions. When calculating droplet radius I take into account the conservation of mass of liquid droplets during its swelling.

The analytical solution (4.3.1.19) enables us to get the temperature distribution inside the droplet $T(r, t)$ as a function of normalised radius r at the end of each time step. For the first time step we use specified initial conditions $T_{d0}(r, t = 0)$. Then the solution at the end of the first time step is used as the initial condition for the second time step etc. If the time step over which the droplet temperature and radius are calculated is small, we can assume that h (t) = const over this time step. In this case we calculate $\dot{m}_d(t=0)$ using Equation (6.3.1). $\dot{R}_d(t=0)$ is calculated as:

$$\frac{dR_d}{dt} = \frac{\dot{m}_d}{4\pi R_d^2 \rho_l} - \frac{R_d}{3\rho_l}\frac{d\rho_l}{dt}, \tag{6.6.1}$$

T_{eff} (t = 0) was calculated from Equation (4.2.4). Then the initial condition at t = 0 allowed us to calculate T (r, t) at the end of the first time step ($T(r, t_1)$) using Equation (4.3.1.19). In calculating $\mu_0(t)$ the heat transfer coefficient h was replaced by $\tilde{h}$ in Equation (6.3.3) to take into account the effect of fuel vapour superheating. The heat transfer coefficient is calculated as h (t) = Nu k_g / 2 R_d (t). Nusselt number can be obtained using Equation (2.2.1.2.23).

The effect of internal circulation inside the droplet is taken into account by multiplying the liquid thermal conductivity by the factor χ, which is calculated using Equation (2.2.1.1.1).

The system of Equations (6.1.1) and (6.3.1) were solved by using the Runge-Kutta method with adaptive step size control (Press et al, 1989) to obtain the droplet mass and velocity at $t = t_1$. When solving Equation (6.1.1), Equation (6.1.5) was used to obtain the

drag coefficient C_{df} while Equation (6.1.2) was used to obtain C_d. The fuel vapour mass was calculated as:

$$\Delta m_v = n_o m_d (t = 0) - n_o m_{dv} (t = t_1) \tag{6.6.2}$$

where m_{dv} is droplet mass obtained by solving Equation (6.3.1) and n is the number of droplets.

It was checked that the second term in Equation (6.6.1) is relatively small and can be neglected with error less than 0.1 % in evaporation time calculations.

In the break up model, the stability criteria, conditions (6.4.1) and (6.4.3) were checked for each droplet parcel at each time step. If either of the two criteria is met for the time equal to the corresponding time defined in Equations (6.4.2) and (6.4.4), then stable droplet size for the parcel was specified from Equations (6.4.1) or (6.4.3). The size of an unstable droplet was allowed to change continuously with time following the rate Equation (6.4.5) where $R_{db(s)}$ are marginally stable radii determined by the conditions We = 6 and $\mathrm{We}/\sqrt{\mathrm{Re}_d} = 0.5$ respectively. With each change in droplet size, the droplet number n is changed to ensure the conservation of liquid mass in Equation (6.4.6).

As the evaporation process and break up process can happen simultaneously, the mass of liquid droplet was calculated as:

$$m_d (t_1) = \left(n_0 m_d (0) - \Delta m_v\right) / n_n \tag{6.6.3}$$

$R_d (t_1)$ is calculated as:

$$R_d (t_1) = \left(3 m_d (t_1) / 4\pi\rho(\overline{T}(t_1))\right)^{\frac{1}{3}}, \tag{6.6.4}$$

The gas temperature $T_g(t_1)$ was obtained algebraically from Equation (6.3.5) while the gas velocity $U_g(t_1)$ was obtained from the momentum exchange between fuel droplets and their surrounding gas in Equation (6.3.7).

If the equivalence ratio (actual fuel / air ratio divided by stoichiometric fuel / air ratio) reaches the lower flammability range of the fuel, the Shell model is activated in the calculation of gas temperature and new concentrations of the fuel vapour, oxygen and inert gas mass fractions in the surrounding gas.

For the second time step, the values of variables obtained at the end of first time step ($t = t_1$) $T(r, t_1)$, $R_d(t_1)$, $T_g(t_1)$, $U_d(t_1)$, $U_g(t_1)$, $m_d(t_1)$, $n(t_1)$ and concentrations of the fuel vapour, oxygen and inert gas in surrounding gas are used as initial conditions to integrate the equations in the range (t_1, t_2). The previous calculations are repeated based on the new initial conditions to get the results at $t = t_2$.

The same procedure is repeated for all subsequent time steps until the autoignition starts at T_g = 1100 K (Sazhina et al, 1999). The number of terms in the series in Equation (4.3.1.19), which needs to be taken into account, depends on the timing of the start of droplet heating and the time when the value of droplet temperature is calculated. For parameters relevant to diesel engines environment just three terms in the series can be safely used with possible errors of not more than about 1 %, as discussed in Chapters 4 and 5.

Note that the calculation of integrals over r in order to estimate $\overline{T}$ and q_n can be replaced by analytical solution as described in Appendix 5.

The gradients of temperature and fuel vapour concentration in the gas phase are ignored. This has been introduced with a view to the future implementation of the algorithm into a computational fluid dynamics (CFD) code, where this assumption refers to individual computational cells. The number of droplets in the enclosure can be arbitrary, but the direct interaction between droplets is not taken into account at this stage. All transport coefficients for the gas phase were calculated at reference temperature, T_{ref} defined as (Lefebvre, 1989; Hubbard et al, 1975):

$$T_{ref} = \frac{T_g + 2T_s}{3} \tag{6.6.5}$$

The concentration of fuel vapour is assumed to be so small that its effect on transport coefficients can be ignored. This effect could be taken into account as described in Appendix 3 of Sazhin et al (1993).

The ignition of the fuel vapour / air mixture is based on the version of the Shell model described in Sazhina et al (1999, 2000a) (see Appendix 6).

The flow chart of the zero dimensional code is shown in Figure (6.1).

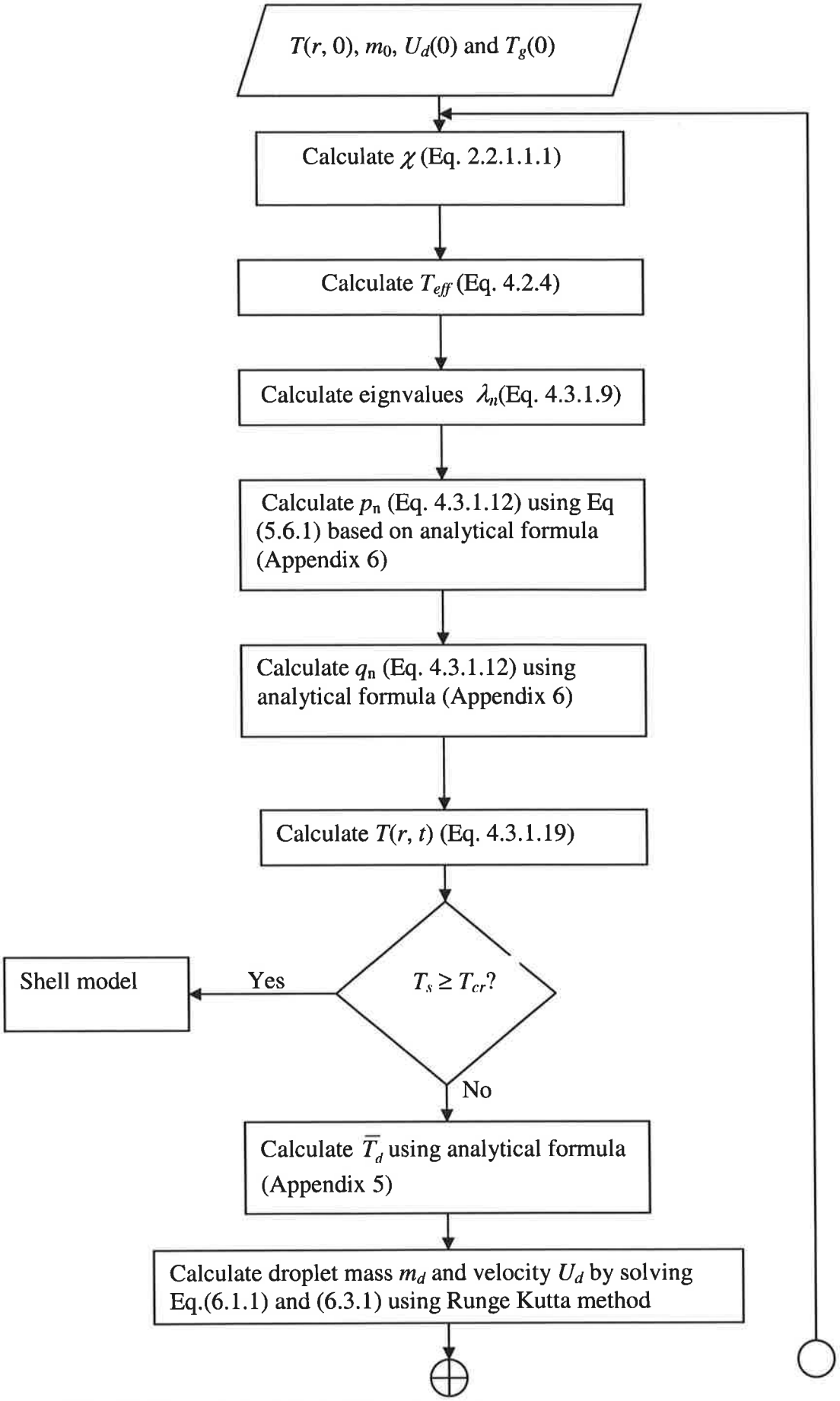

Fig. 6.1 Flow chart of Zero-dimensional code.

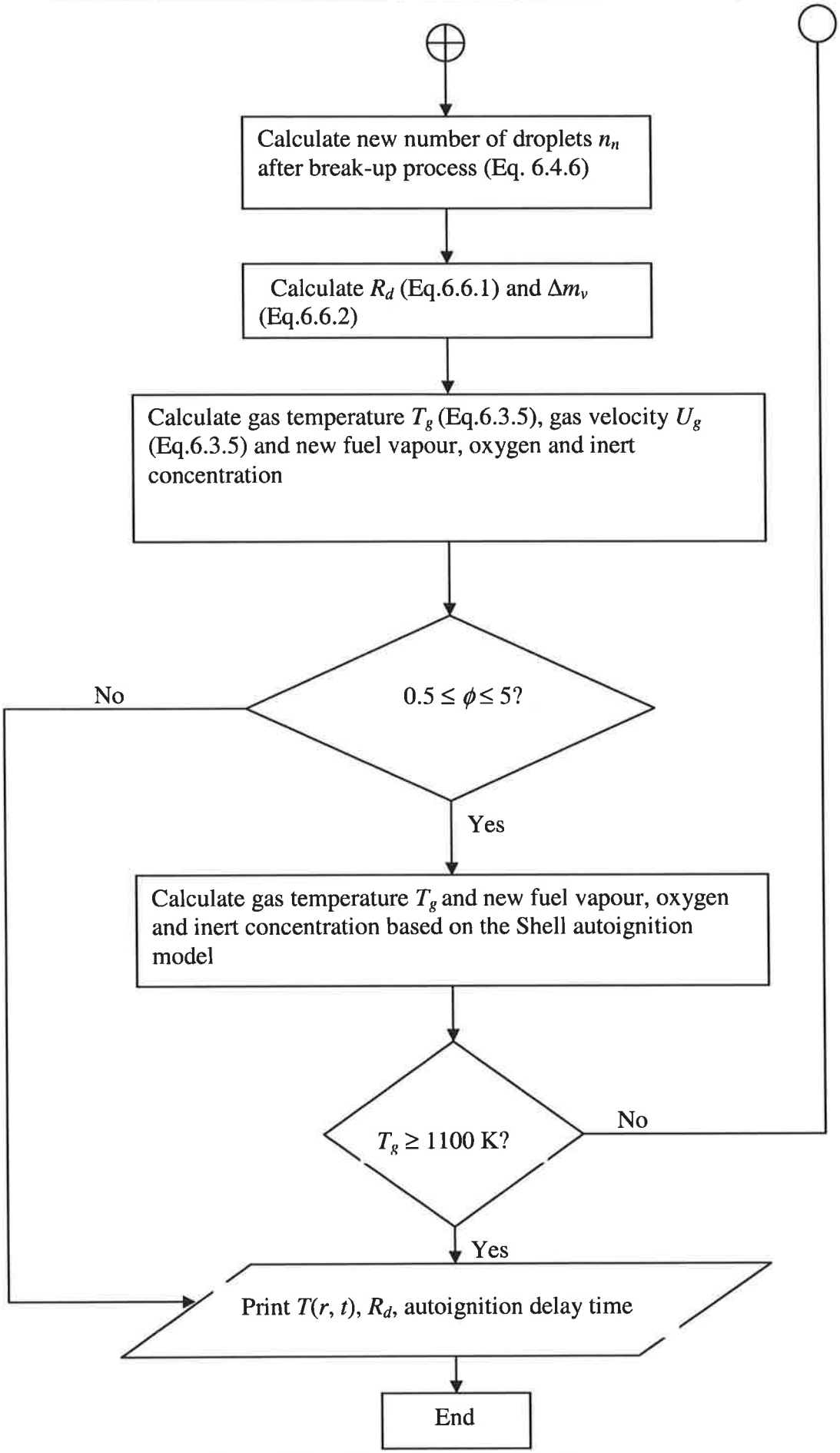

Fig. 6.1 Flow chart of Zero-dimensional code (cont).

6.7 Validation of the numerical algorithm

The only direct observations of temperature gradient inside large (R_d > 100 μm) droplets are those reported in Laveille et al (2002), Castanet et al (2002) and Castanet et al (2003), to the best of our knowledge. These sizes of droplets are not directly relevant to diesel engine environment as droplets are typically much smaller there. Also, the results reported by these authors refer to instantaneous measurements and cannot be used for validating of the model for droplet heating process described above. In this section we shall validate our model by comparing the predicted time evolution of droplet radius and the predicted ignition delay with experimental observations. This seems to be the only feasible approach.

In the experiment conducted by Belardini et al (1992) 10^{-9} g of tetradecane was injected at temperature of 300 K and initial velocity of 6 m/s through a hole of 0.28 mm diameter into a 100 cm^3 chamber. The chamber was filled with air at 1 bar, and the initial temperatures in the range from 473 K to 673 K. The evolution of droplet diameter during the evaporation process was measured starting with droplet diameter equal to 72 μm. The results of measurements were presented in the form of a plot of $(R_d/R_{d0})^2$ versus time t and are shown in Figure (6.2). In the same figure, the time evolution of this variable, predicted by the algorithm described above are presented. The calculations were performed using the effective thermal conductivity model (hereafter referred to as ETC model), based on the analytical solution of the heat conduction equation inside droplets for constant heat transfer coefficient, and the infinite thermal conductivity model (hereafter referred to as ITC model). The physical properties of tetradecane, used in calculations, are given in Appendix 7.

As follows from Figure (6.2) the results of calculations for both ITC and ETC models show reasonable agreement with the measurements for both temperatures 473 K and 673 K. In fact the predictions of the ETC and ITC models are practically indistinguishable. This difference would have been observed for the surface temperature at the initial stage of heating but this is not translated into the time evolution of droplet radius. The plots of $(R_d/R_{d0})^2$ versus t are non-linear functions of time after the completion of the heat-up period, in contrast to the prediction of the d^2-law (this is particularly clearly seen for the curve referring to T_s = 673 K) . This is attributed to the effect of thermal radiation which was not taken into account when deriving this law (cf. the following discussion referring to Figure (6.4)). The effect of thermal radiation generally decreases with decreasing droplet radius (Sazhin et al, 2004).

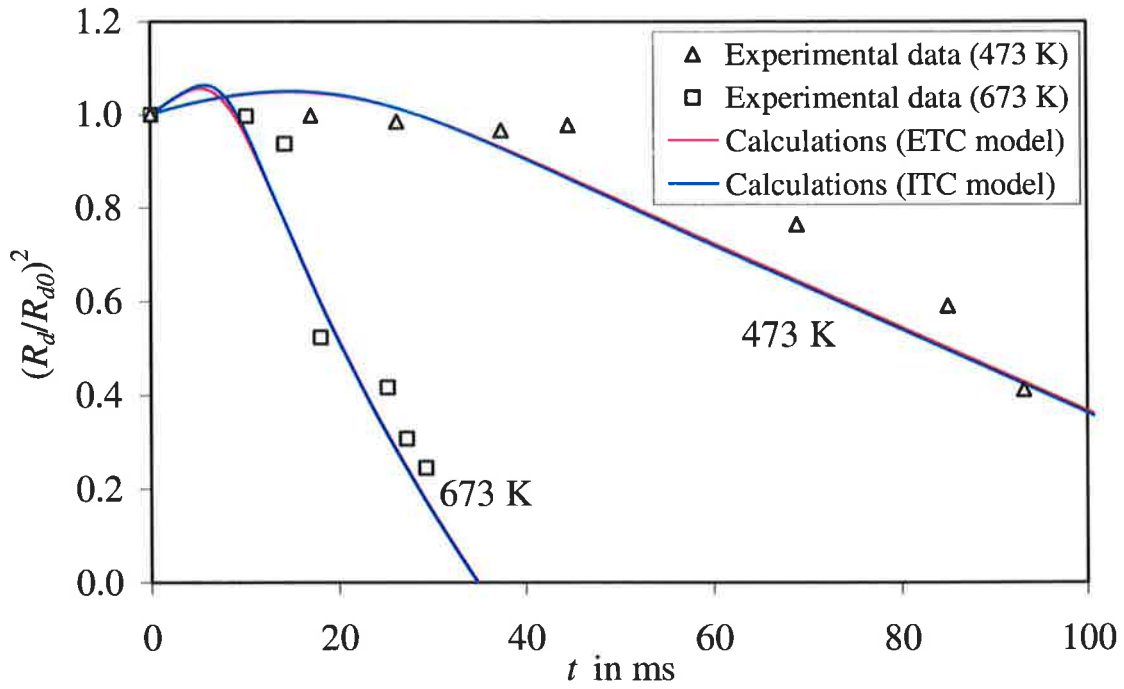

Fig. 6.2 The values of $(R_d / R_{d0})^2$ for evaporating tetradecane droplets versus time, as measured by Belardini et al (1992), and the results of calculations based the ETC (effective thermal conductivity) and the ITC (infinite thermal conductivity) models implemented into the zero dimensional code. The values of the initial gas temperature 473 K and 673 K are indicated near the plots.

Data for initial gas temperature T_{g0} = 673 K presented in Figure (6.2) was used in Bertoli and Migliaccio (1999) to validate various models for droplet heating. The comparison was between: a model which includes the effect of finite thermal conductivity inside droplets (but not recirculation) combined with the effect of droplet swelling; and a model which did not take into account the effect of swelling. As expected, the prediction of the first model was practically indistinguishable from that shown in Figure (6.2). Ignoring the effect of swelling led to visibly poorer agreement between experimental data and prediction of the model.

The experimental data reported in Nomura et al (1996) were obtained for a suspended *n*-heptane droplet in nitrogen atmosphere at pressure in the range between 0.1 and 1 MPa and temperatures in the range between 400 K and 800 K. Droplet initial radii varied from 0.3 mm to 0.35 mm. The experiments were performed under microgravity conditions. The experimentally observed values of $(R_d/R_{d0})^2$ versus t for pressure 0.1 MPa, initial gas temperature 471 K, 55K, 648 K, 741 K and the initial droplet radii equal to 0.3 mm, are shown in Figure (6.3). Also, the results of calculations based on ETC and

ITC models for the same values of parameters are shown. The physical properties of *n*-heptane used in calculations are described in Appendix 7.

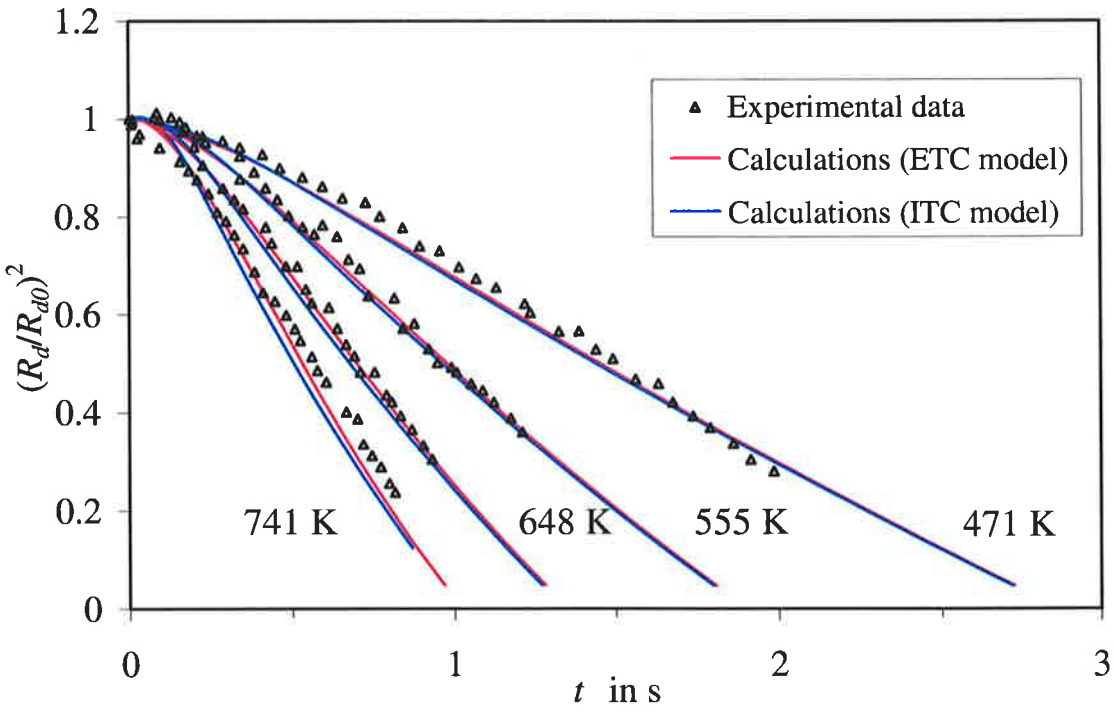

Fig. 6.3 The values of $(R_d/R_{d0})^2$ for evaporating *n*-heptane droplets versus time for the initial pressure 0.1 MPa, as measured by Nomura et al (1996), and the results of calculations based on the ETC and the ITC models implemented into the zero dimensional code. The values of initial gas temperature 471 K, 555 K, 647 K and 741 K are indicated near the plots.

As follows from Figure (6.3) both ITC and ETC models show good agreement with experimental data. For T_{g0} = 471 K and T_{g0} = 555 K the predictions of the models practically coincide. At higher temperatures, however, the predictions of the ETC model are in marginally better agreement with experimental data, compared with the ITC model, as expected. At lower initial gas temperature droplets evaporate more slowly and the temperature inside droplets has sufficient time to become almost homogeneous. Hence, the closeness of evaporation times predicted by the ETC and ITC models. Stronger effect of droplet finite thermal conductivity on the evolution of their size shown in Figure (6.3), compared with Figure (6.2), is related to much larger droplets studied in Nomura et al (1996) compared with Belardini et al (1992).

Plots of droplets surface temperatures T_s versus t for the same parameters as in Figure (6.3) are shown in Figure (6.4). As follows from this figure, the ETC model predicts much quicker rise of surface temperature compared with the ITC model at the initial

stage. This is related to the fact that the heat reaching the surface of the droplet is spent on heating the whole droplet in the ITC model, and on heating of a relatively thin layer near the droplet surface in the ETC model. Then the surface temperature predicted by the ETC model becomes lower than the one predicted by the ITC model.

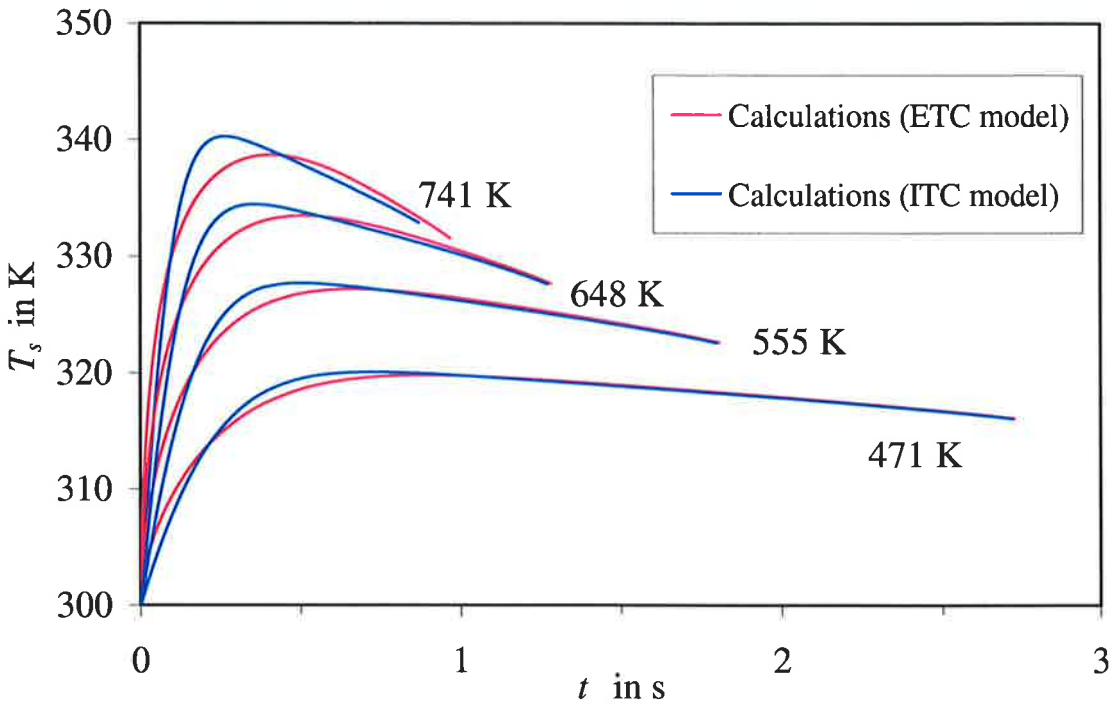

Fig. 6.4 The plots of T_s versus time for the same values of parameters as in Figure (6.3), calculated using the ETC and the ITC models implemented into the zero dimensional code.

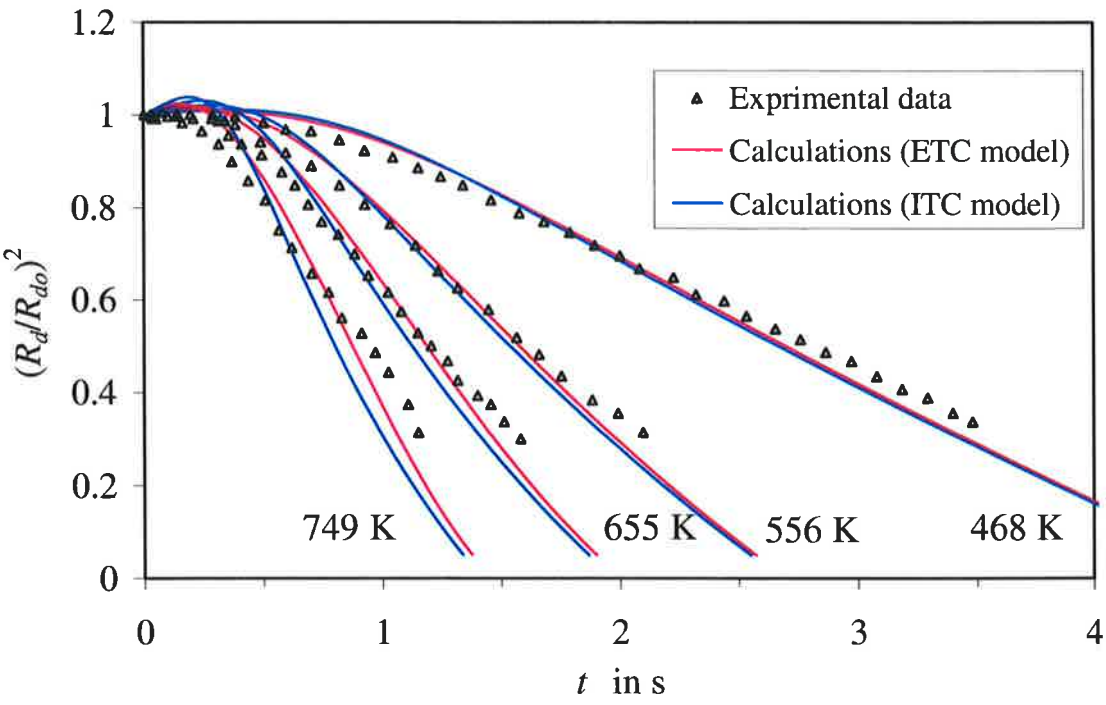

Fig. 6.5 The same as in Figure (6.3) but for the initial gas pressure 0.5 MPa.

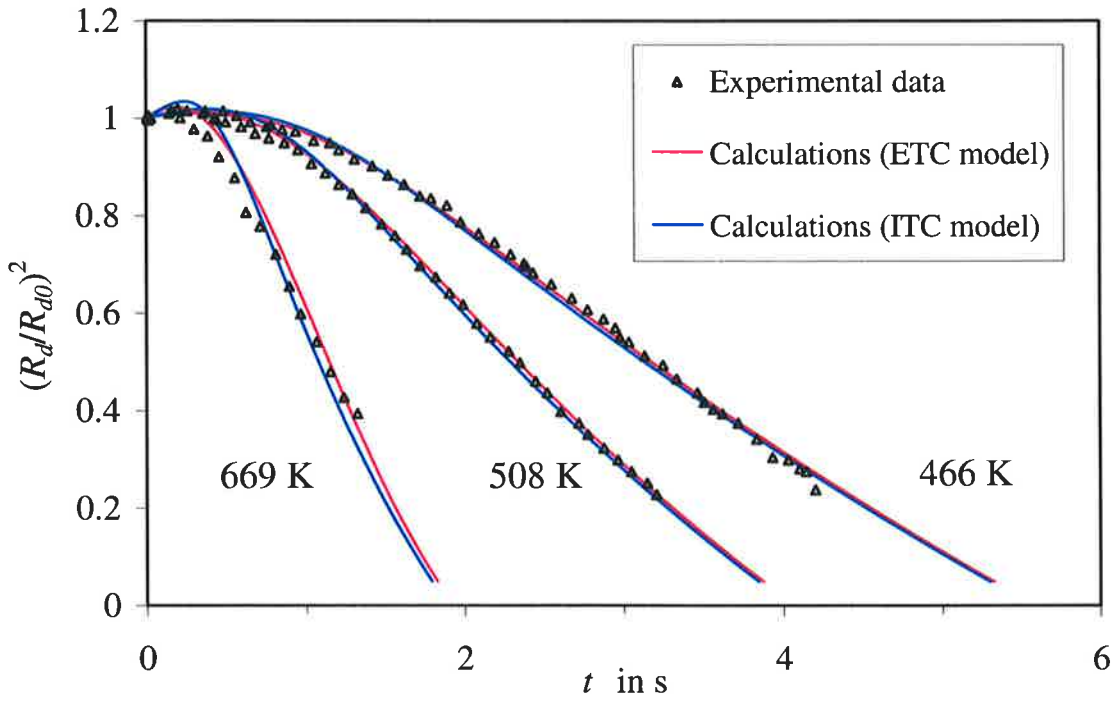

Fig. 6.6 The same as in Figure (6.3) but for the initial gas pressure 1 MPa

This is related to the fact that the increased surface temperature predicted by the ETC model will lead to decrease of the amount of heat supplied to the droplet. Eventually, the surface temperatures predicted by both models become practically indistinguishable, as in the case considered earlier. Note that both ITC and ETC models predict the maximal values of droplet surface temperature at certain moments of time. These maxima are related to the contribution of thermal radiation. This result agrees with that reported in Abramzon and Sazhin (2005). The detailed physical explanation of this phenomenon is given in Abramzon and Sazhin (2005). In the absence of radiation the droplet surface temperature is expected to increase asymptotically to the wet bulb temperature. Note that temperatures shown in this figure are well below the *n*-heptane boiling temperature 371.4 K.

The plots similar to those shown in Figure (6.3) but for pressures 0.5 MPa and 1 MPa, and various initial gas temperatures are shown in Figures (6.5) and (6.6). As follows from these figures, the ETC model predicts marginally more accurate results compared with the ITC one, similarly to the case of lower pressure (see Figure (6.3)). The corresponding plots of T_s versus t have the properties similar to those shown in Figure (6.4) for pressure 0.1 MPa.

The experimental data discussed so far is relevant to understanding heating and evaporation processes — it does not give us much information about the influence of droplets on gas. In what follows, I compare experimental data on the total ignition delay times reported in Tanabe et al (1995) and the prediction of the models. In the experiment described in this paper, *n*-heptane droplets with the initial radii of 0.35 mm were injected in air at pressure 0.5 MPa. The droplets' diameters were measured with possible errors ±0.05 mm. A furnace able to generate almost uniform gas temperature (from room temperature to 1100 K) was constructed and used for this experiment. The igniting droplets were observed by a Michelson interferometer so that the time dependent temperature distribution around the droplets could be estimated. Interferometric images were stored on an 8 mm video tape with a frame rate of 50 s^{-1} and were analyzed by computer image processing. The experiment was performed under the microgravity conditions by using the 110 m drop tower. This enabled the authors to observe spherically symmetrical phenomenon that could be compared with the one-dimensional theoretical analysis (Tanabe et al, 1995).

The volume of air used in the experiment was not specified, but it can be assumed that this volume was rather large. Hence, we took lean ignition limit when the equivalence ratio equal to 0.5 for the initial gas temperature T_{g0} = 600 K (Sazhina et al, 2000a). This corresponds to the case when the volume of air is equal to 19.1 radii of droplets. This volume could be identified with the so called 'cooling zone' (Todes, 1966; Sazhin et al, 2001a). The observed total ignition delay times (physical + chemical ignition delays) versus initial gas temperature are shown in Figure (6.7). In the same figure the total ignition delay times predicted by the ETC and ITC models are shown. The calculations were based on the Shell model with $A_{f4} = 3 \times 10^6$.

As follows from Figure (6.7), the influence of the temperature gradient in droplets on the total ignition delay is noticeably greater than its influence on droplet evaporation time discussed earlier. This is related to the fact that the chemical part of the total ignition delay is a strongly non-linear function of the gas temperature in the vicinity of droplets determined by Equation (6.6.5). As shown earlier (see Figure (6.4)), the droplet surface temperature strongly depends on the temperature gradient inside the droplet, especially at the initial stages of heating. Hence, this temperature gradient cannot be ignored when calculating the total ignition delay of fuel droplets. If the ETC model is replaced by the ITC one for the same set of parameters then the agreement between the predicted and observed total ignition delays becomes much worse for $T_{g0} > 650$ K (see

Figure (6.7)). This shows that the effects of temperature gradient inside droplets influence significantly the total ignition delay and need to be taken into account when modelling this phenomenon.

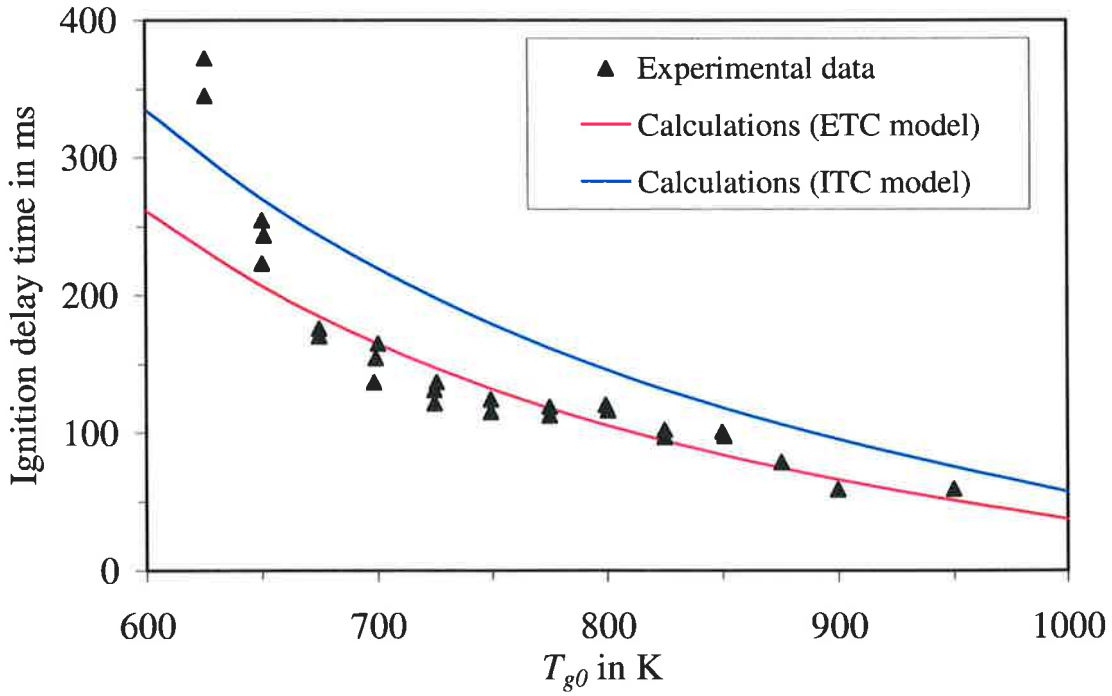

Fig. 6.7 The values of the total ignition delay time for evaporating *n*-heptane droplets versus initial gas temperature, as measured by Tanabe et al (1995), and the results of calculations based on the ETC and the ITC models implemented into the zero dimensional code. The version of the Shell autoignition model described in Sazhina et al (1999) and Sazhina et al (2000) was used with the coefficient $A_{f4} = 3 \times 10^6$. The ratio of the volumes of air and liquid droplet was taken equal to $19.1^3 = 6967.871$ to provide the equivalence ratio 0.5 for $T_{g0} = 600$ K.

The rapid increase of the ignition delay with decrease of T_{g0} in the range 600 K- 650 K is not reproduced well by either model. This could be related to the fact that both models do not take into account the heat losses from the combustion chamber. In the case of short total ignition delays at large gas temperatures, these effects of heat loss can be ignored, but they need to be taken into account in the case of relatively long total ignition delays at low gas temperatures (cf. the results reported by Sazhina et al (1999)). The analysis of this phenomenon is beyond the scope of this chapter.

6.8 Application to a monodisperse spray

This section will focus on the investigation of temperature gradient inside droplets and recirculation in them on droplet velocity, break-up, heating and evaporation, and the

ignition of fuel vapour / air mixture in a monodisperse spray. The algorithm described in Section (6.6) and validated in Section (6.7) will be used. The fuel was approximated by *n*-dodecane, and the 'average' diesel fuel, the characteristics of which were taken from various sources (see Appendix 7).

The overall volume of injected liquid fuel was taken equal to 1 mm^3, and the volume of air where the fuel was injected was taken equal to 883 mm^3. In this case, provided that the fuel is injected at room temperature (T_d = 300 K) into air at temperature 880 K and pressure of 3 MPa, and when all the fuel has evaporated without combusting, the fuel vapour / air mixture is expected to become close to stoichiometric. More precisely, the equivalence ratio for *n*-dodecane in these conditions was calculated as 0.98, while for diesel fuel it was calculated as 1.01. This calculation took into account the relevant physical properties including temperature dependence of the liquid fuel density. The liquid fuel physical properties were calculated based on the droplet average temperature $\overline{T}_d$. Their initial velocities were taken in the range from 0 to 100 m/s. Droplet initial diameters were taken equal to 5, 20 and 50 μm. The initial gas pressure and temperature were taken in the range from 1 to 5.5 MPa and from 700 to 1200 K, respectively. In this case the equivalence ratios of the mixture of evaporated fuel and air are expected to change accordingly, and are shown in Figures (6.8a, b). External temperatures, responsible for radiative heating of droplets, were taken in the range from 880 K to 2500 K. The flammability equivalence ratio of fuel was taken in the range from 0.5 and 5 (Kuo, 1986; Sazhina et al, 2000). The autoignition process was modelled based on the version of the Shell model described in Sazhina et al (1999, 2000a) (see Appendix 6) with the constant A_{f4} in the range between 3×10^6 and 6×10^6. The autoignition was assumed to be completed when fuel vapour / air temperature reached 1100 K (Sazhina et al, 1999).

To illustrate the effect of initial droplet velocities on the time evolution of the relative droplet velocities and their surface temperatures I consider the case when the initial gas temperature is equal to 880 K, initial gas pressure equal to 3 MPa, and n-dodecane droplet initial temperature and radius equal to 300 K and 10 μm respectively. The ETC model is used and the effect of thermal radiation is ignored (this effect is illustrated in Figure (6.4)). In Figure (6.9a) the plots of relative droplet velocities $|U_d - U_g| / |U_{d0}|$ (U_{d0} is the initial droplet velocity) versus time for $|U_{d0}|$ = 10 m/s, 50 m/s, 100 m/s and 200 m/s, are presented. The initial gas velocity is assumed equal to zero. As follows from this figure, the rate of decrease of the relative velocity increases with increasing $|U_{d0}|$.

As a result, regardless of the values of the initial velocities, the velocities of all droplets approach to the gas velocity. The plots of the droplet surface temperature T_s versus time for $|U_{d0}|$ = 0, 10 m/s, 50 m/s and 100 m/s are presented in Figure (6.9b). As follows from this figure, the rate of increase of this temperature increases with increasing droplet

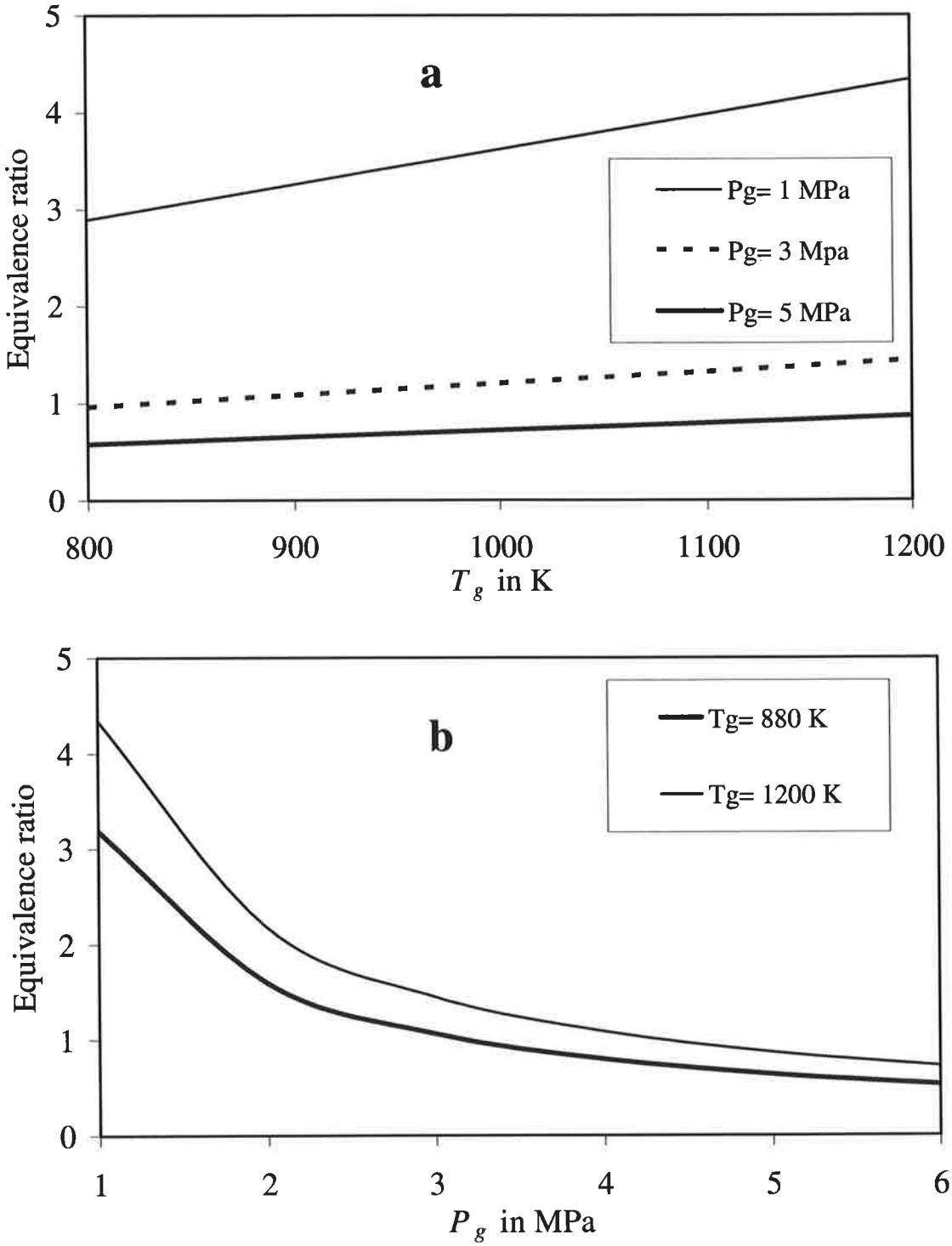

Fig. 6.8 The values of the equivalence ratio versus gas temperature for various gas pressures (a), and the values of the equivalence ratio versus gas pressure for various gas temperatures (b). 1 mm^3 of liquid *n*-dodecane injected into 883 mm^3.

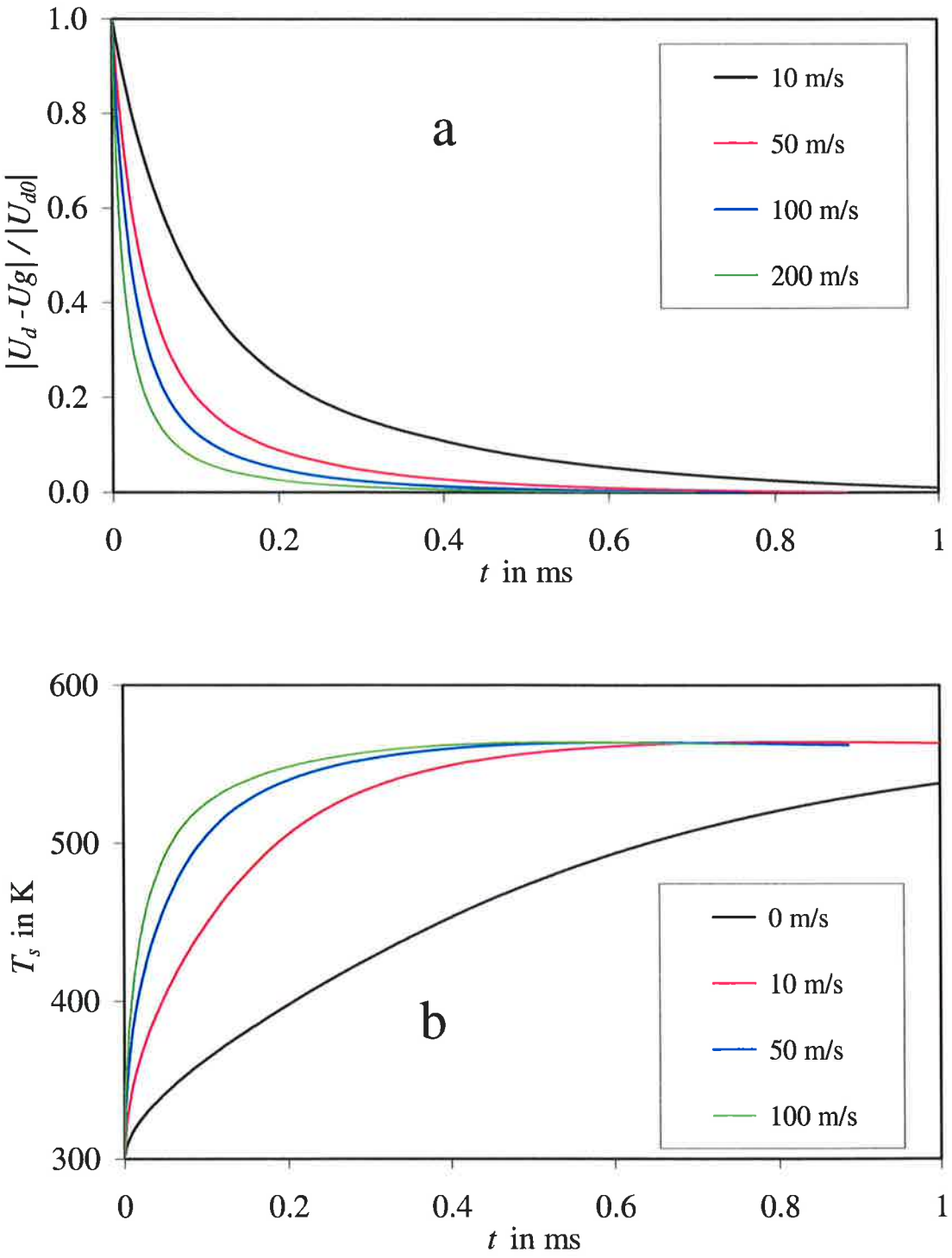

Fig. 6.9 Plots of $|U_d - Ug| / |U_{d0}|$ (U_{d0} is the initial droplet velocity) versus time for $|U_{d0}|$ = 10 m/s, 50 m/s, 100 m/s and 200 m/s (a), and plots of the droplet surface temperature T_s versus time for $|U_{d0}|$ = 0, 10 m/s, 50 m/s and 100 m/s (b). In all cases $U_{g0} = 0$. The initial gas temperature is equal to 880 K, initial gas pressure is equal to 3 MPa, and n-dodecane droplet with initial temperature and radius equal to 300 K and 10 μm respectively are taken. The ETC model is used and the effect of thermal radiation is ignored.

initial velocity. This would be expected as the convective heat transfer coefficient increases with increasing Re and the initial droplet velocities (see Equation (2.2.1.2.1)). Also, as expected in the absence of thermal radiation, in all cases the droplet surface temperature asymptotically approach the wet bulb temperature. All the above mentioned properties of the curves shown in Figure (6.9) can be observed for the initial values of droplet diameters equal to 5 μm and 50 μm and other values of the initial gas temperature and pressure.

The effects of thermal radiation, gas temperature, and gas pressure on evaporation time are discussed in Section (6.8.1). The effects of thermal radiation, gas temperature, and gas pressure on total ignition delay time are discussed in Section (6.8.2). The effects of gas temperature on evaporation time and total ignition delay time taking into account the break up process are discussed in Section (6.8.3).

6.8.1 The effects of thermal radiation, gas temperature and gas pressure on evaporation time without break-up

Firstly, we assume that gas temperature and pressure are equal to 880 K and 3 MPa respectively, and consider *n*-dodecane droplets with diameters 5 μm, 20 μm and 50 μm, moving with velocities 0 (stationary droplets), 10 m/s, 50 m/s, and 100 m/s. These are typical values of parameters for diesel engines (Sazhina et al, 2000). Also, we consider the values of external temperatures in the range from 880 K (gas temperature) to 2500 K (maximal temperature of remote flames in the engines) (Sazhina et al, 2000).

Figures (6.10a, b, c) show the droplets evaporation time versus external temperature for droplet initial diameters equal to 5, 20 and 50 μm, respectively based on the ETC model and the ITC model (neglecting temperature gradient inside droplets) for *n*-dodecane. Droplet initial velocities are shown near the plots. As expected, the results show that evaporation time decreases with increasing external temperature and initial velocity and decreasing droplets initial diameter. The data show that the effect of thermal radiation on droplet evaporation time increased with increasing external temperature and droplet diameter while it decreased with increasing droplets initial velocity. The evaporation time decreased by less than 1.19 % and 1.2 % for droplet initial diameter equals to 5 μm and external temperature equals to 2500 K based on the ETC model and the ITC model, respectively. These values are equal to 12.9 % and 13.5 % for droplet initial diameter equal 20 μm while they are equal to 42 % and 43.9 % for droplet initial diameter equal to 50 μm. The effect of taking into account temperature

gradient inside the droplet on evaporation time are less than 1.7 %, 1.9 % and 3 % for droplet initial diameters 5, 20 and 50 μm, respectively for the conditions under consideration.

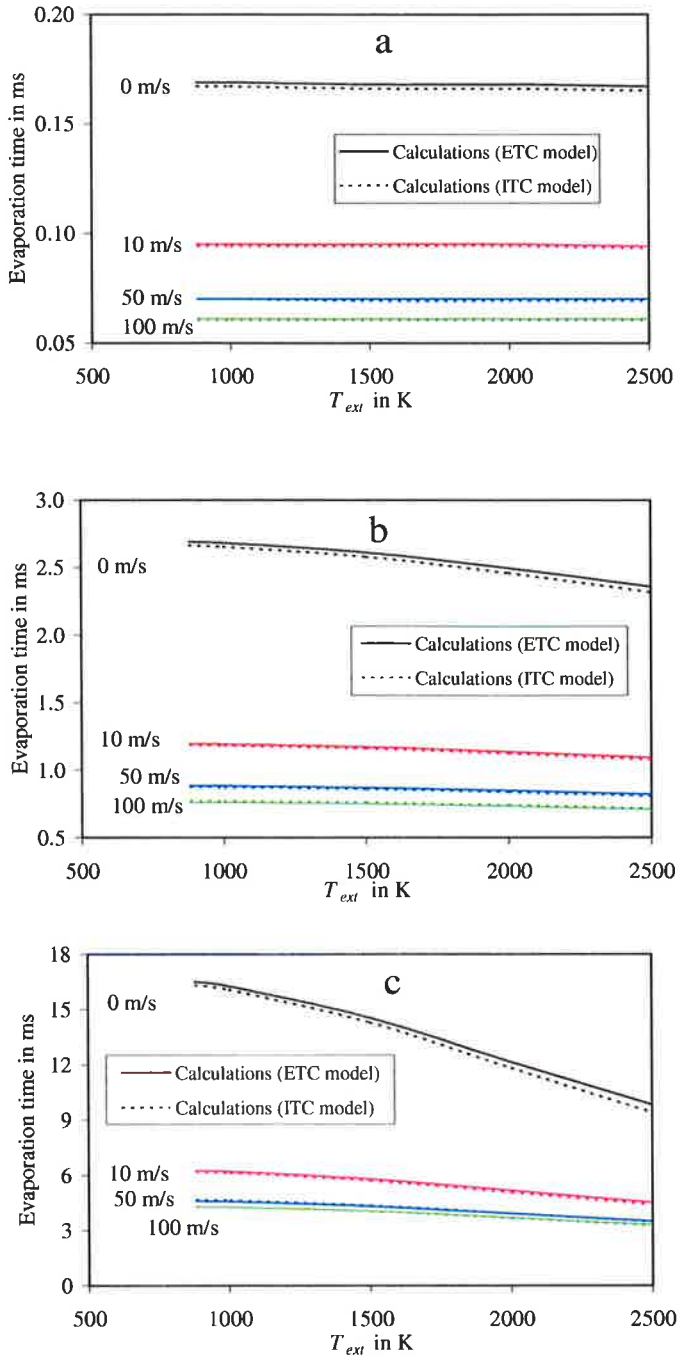

Fig. 6.10 The values of the evaporation time for *n*-dodecane droplets versus external temperature calculated based on the ETC and ITC models implemented into the zero dimensional code. The initial gas pressure and temperature are taken equal to 3 MPa and 880 K respectively. The initial droplet diameters are taken equal to 5 μm (a), 20 μm (b) and 50 μm (c). The initial droplet velocities are indicated near the curves (0 (black), 10 m/s (red), 50 m/s (blue) and 100 m/s (green)).

The data in Figure (6.10b) show that the effect of taking into account temperature gradient inside droplets slightly increased evaporation time for droplet initial diameter 20 μm when initial velocity is less than 50 m/s. This effect is reversed for droplet initial velocity 100 m/s. A similar effect can be seen in Figure (6.10c) for droplet initial diameter equal to 50 μm and initial velocity equal to 50 m/s and 100 m/s. This could be related to the fact that the effect of temperature gradient inside the droplet can lead mainly to increase of droplet surface temperature rather than the droplet average temperature. This effect would lead to an increase of the droplet evaporation due to the direct temperature effect, and a reduction due to a decrease of convective heat supply to the droplet surface. When the first effect dominates over the second effect then, taking into account temperature gradient inside droplets will lead to decrease of evaporation time. Conversely if the second effect dominates over the first effect, then, taking into account temperature gradient inside droplets will lead to decrease evaporation time.

Figure (6.11) show the percentage reduction on evaporation time versus external temperature for droplet initial diameter equal to 50 μm for *n*-dodecane based on the ETC model. Droplet initial velocities are shown near the plots.

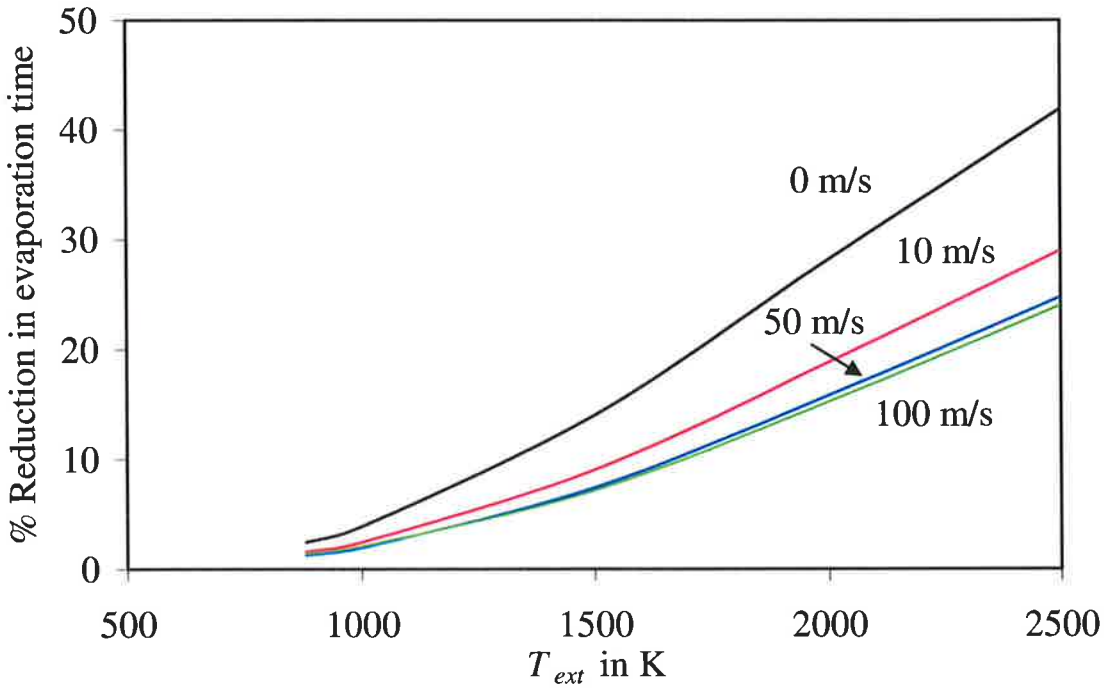

Fig. 6.11 Plots of percentage reduction of evaporation time due to thermal radiation versus external temperature calculated based on the ETC and ITC models implemented into the zero dimensional code, relative to the case without thermal radiation. Initial gas pressure and temperature are taken equal to 3 MPa and 880 K respectively. The initial droplet diameter is taken 50 μm. The initial droplet velocities are indicated near the curves (0 (black), 10 m/s (red), 50 m/s (blue) and 100 m/s (green)).

The results show that the effect of thermal radiation on evaporation time increased with decreasing initial velocity of droplets.

Results similar to those shown in Figure (6.10c) but for diesel fuel are presented in Figure (6.12). The evaporation time decreased by less than 40.7 % and 42.1 % for droplet initial diameter equals to 50 μm and external temperature equals to 2500 K based on the ETC model and the ITC model, respectively. The effect of taking into account temperature gradient inside the droplet on evaporation time are less than 3 % for droplet initial diameter 50 μm for the conditions under consideration.

A similar analysis of these droplets evaporation without the contribution of radiation, but for gas temperatures in the range (700 K- 1200 K) was developed. Figures (6.13a, b, c) show droplets evaporation time versus gas temperature for droplet initial diameters 5 μm, 20 μm and 50 μm, respectively based on the ETC model and the ITC model for *n*-dodecane. Droplets initial velocities were taken in the range from 0 (stationary

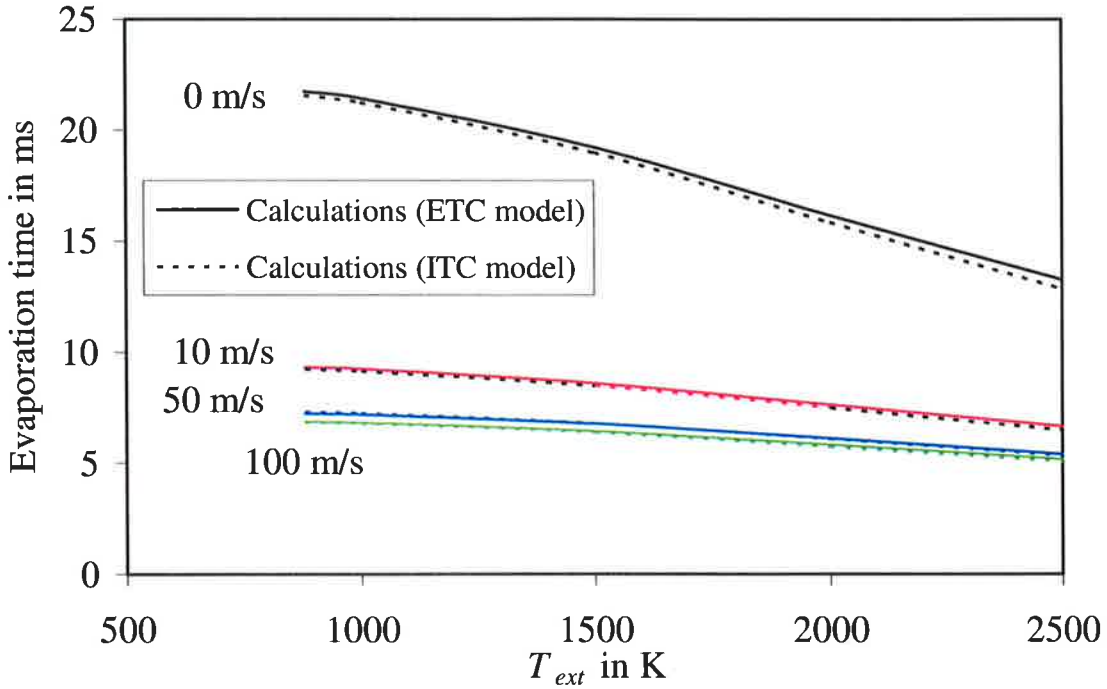

Fig. 6.12 The same as in Figure (6.10c) but for diesel fuel.

droplet) to 100 m/s for droplet initial diameters 5 μm and 20 μm, and in the range from 0 (stationary droplet) to 200 m/s (shown near the plots) for droplet initial diameter 50 μm. Gas pressure was taken 3 MPa. As expected, the results show that evaporation time decreases with increasing gas temperature and initial velocity and decreasing droplet initial diameter. These results qualitatively agree with experimental results obtained by

Belardini et al (1992) and Nomura et al (1996). It can be noticed that the effect of gas temperature on evaporation time is more visible at lower gas temperature. This could be related to the fact that increasing gas temperature from 700 K to 800 K leads to increase in *n*-dodecane vapour thermal conductivity by 28.2 % while increasing gas temperature from 1100 K to 1200 K leads to increase in dodecane vapour thermal conductivity by 11.25 % (Maxwell, 1950). The effect of gas temperature on vapour thermal conductivity leads to visible increase in convective heat supply at lower gas temperature. The effect of taking into account temperature gradient inside the droplet on evaporation time, when gas temperature is changed, is rather complex, as mentioned above. Evaporation increases due to the increase of droplet surface temperature and decreases due to the decrease of convective heat supply. The results show that the first effect is the dominant for the initial droplet diameter equal to 5 μm. For droplet initial diameter equal to 20 μm, the first effect dominates for initial velocity up to 50 m/s and gas temperature less than 1100 K. For initial velocity equal 100 m/s, however it dominates for gas temperature less than 880 K. For droplet initial diameter equal to 50 μm, the first effect dominates over the second one for initial velocity up to 10 m/s and for initial velocity equal to 100 m/s when gas temperature is less than 880 K. The effect of taking into account temperature gradient inside droplets on evaporation time are less than 2.5 %, 3.5 % and 5 % for initial droplet diameters 5 μm, 20 μm, and 50 μm, respectively. The effect of initial velocity on evaporation time is negligible for initial velocity greater than 50 m/s, as shown in Figure (6.13c). This can be related to the fact that after 0.25 ms the relative velocities between droplets and gas does not influence the results significantly as shown in Figure (6.14). The higher decrease in relative velocity could be related to increasing drag coefficient due to high initial Reynolds number for initial velocity greater than 50 m/s as predicted by Equation (6.1.2). For droplet initial diameter equal to 50 μm, gas temperature equal to 880 K and gas pressure equal to 3 MPa initial Reynolds numbers 1931, 3781, 5570 and 7307 for initial velocities 50 m/s, 100 m/s, 150 m/s and 200 m/s, respectively. Results similar to those shown in Figure (6.13c) for *n*-dodecane were obtained for diesel fuel, as shown in Figure (6.15). This figure shows droplets evaporation time versus gas temperature for droplet initial diameter 50 μm based on the ETC model and the ITC model for diesel fuel. Droplets initial velocities are taken in the range from 0 (stationary droplet) to 100 m/s and the gas pressure was taken to be 3 MPa.

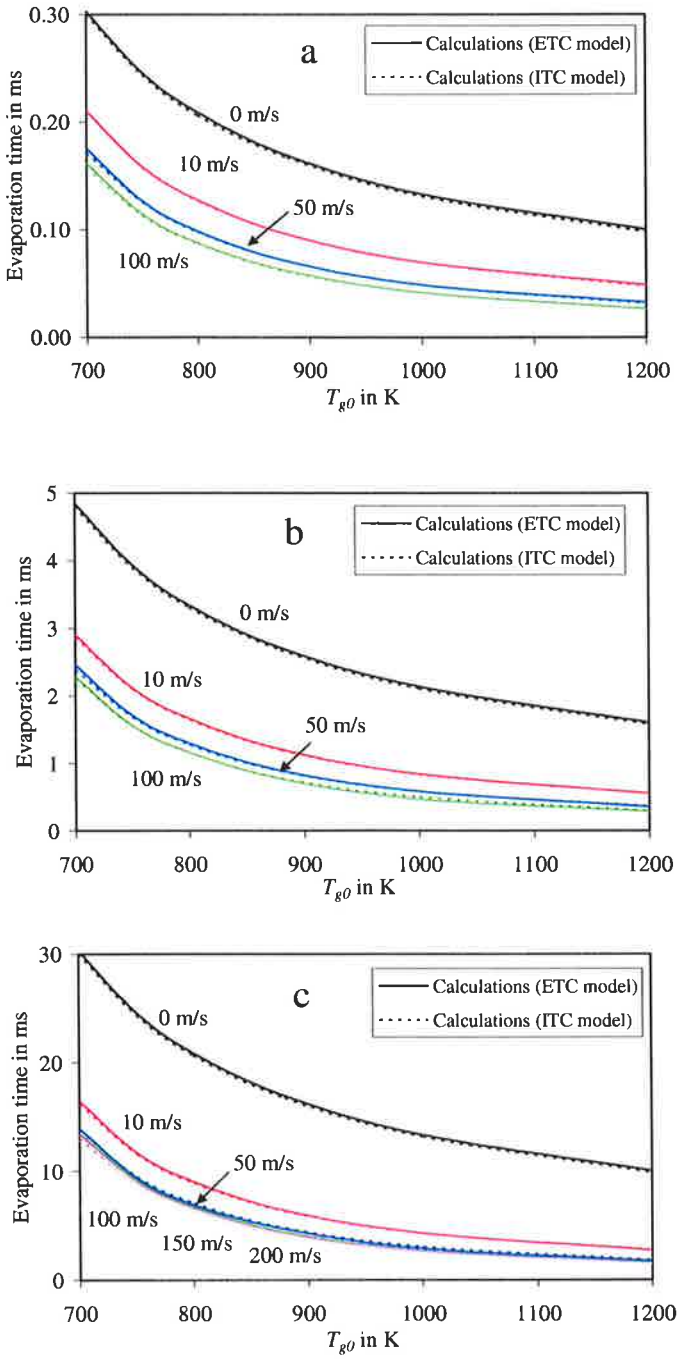

Fig. 6.13 The values of the evaporation time for *n*-dodecane droplets versus initial gas temperature calculated based on the ETC and ITC models implemented into the zero dimensional code. Initial gas pressure is taken equal to 3 MPa. The initial droplet diameters are taken 5 μm (a), 20 μm (b) and 50 μm (c). The initial droplet velocities are indicated near the curves (0 (black), 10 m/s (red), 50 m/s (blue) and 100 m/s (green)).

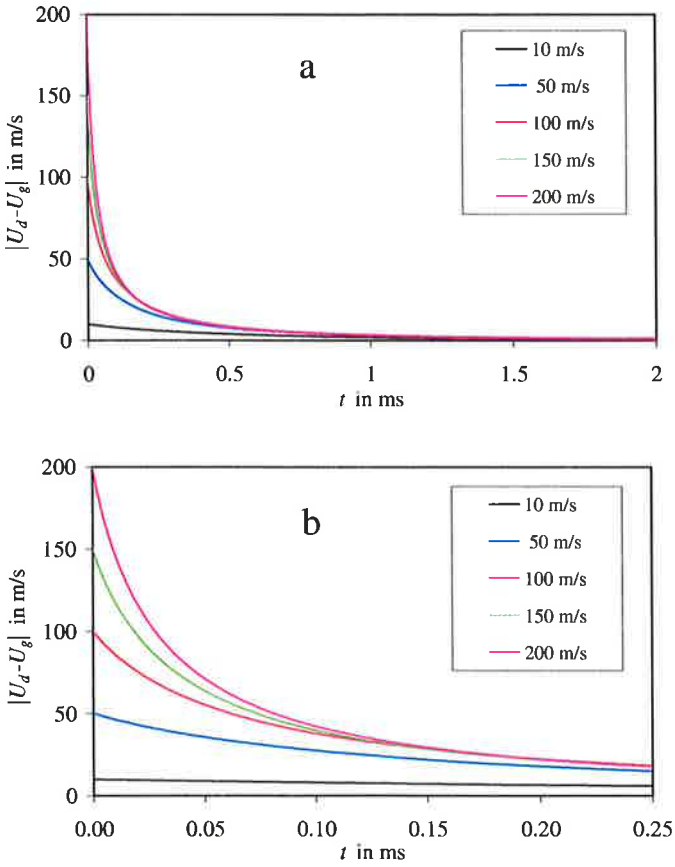

Fig. 6.14 Plots of $|U_d - U_g|$ versus time for $|U_{d0}|$ = 10 m/s, 50 m/s, 100 m/s, 150 m/s and 200 m/s. U_{g0} = 0. The initial gas pressure is equal 3 MPa, initial gas temperature is equal 880 K, *n*-dodecane droplet with initial temperature and radius equal to 300 K and 25 μm respectively are taken. The ETC model is used and the effect of thermal radiation is ignored. The results shown in Figure (a) up to 0.25 ms are zoomed in Figure (b).

Also, a similar analysis for fixed gas temperature without radiation but for pressures in the range (1-5.5) MPa were developed. Figures (6.16a, b and c) show droplets evaporation time versus gas pressure for droplet initial diameters 5 μm, 20 μm and 50 μm, respectively based on the ETC model and the ITC model for *n*-dodecane. Droplet initial velocities are shown near the plots. Gas temperature is taken to be 880 K. The results show that evaporation time decreased with increasing gas pressure due to increase of convective heat supply to droplets. This is consistent with the results reported by Gogos et al (2003) and Nomura et al (1996). According to Kim and Sung (2003) the droplet life time decreases with pressure when gas temperature is higher than 800 K which agreed with the results shown in Figure (6.16).

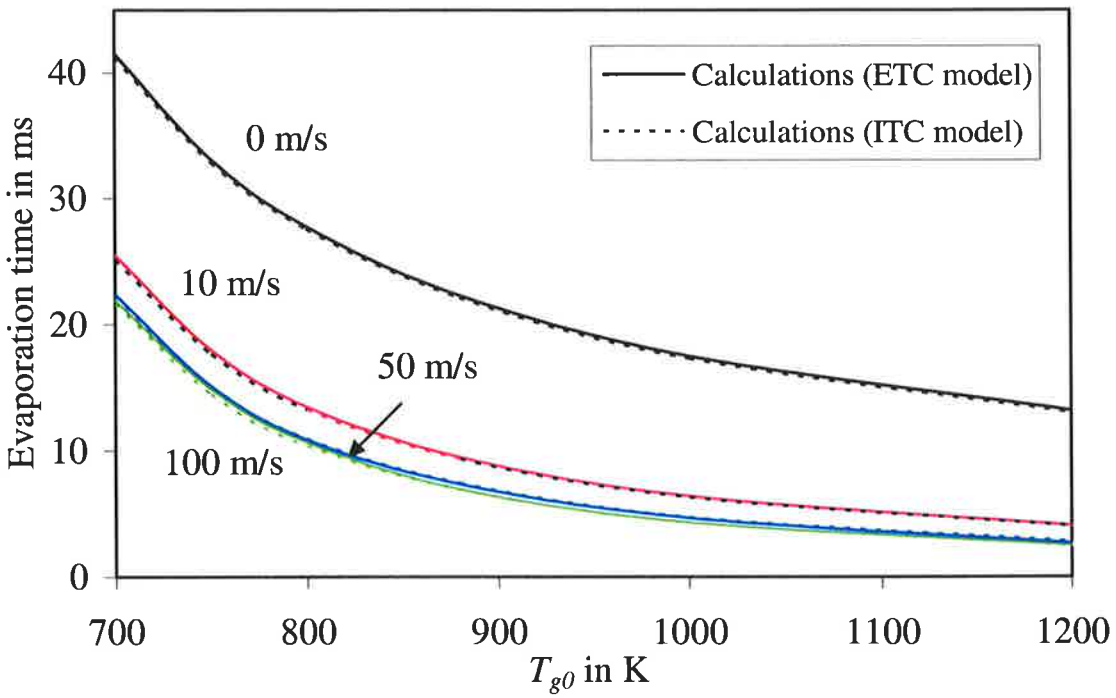

Fig. 6.15 The same as in Figure (6.13c) but for diesel fuel.

It can be noticed that the effect of gas pressures on evaporation time is more visible at lower gas pressures than that at higher pressure. This could be related to the fact that increasing gas pressure results in a decrease in droplet velocity and fuel vapour diffusion to gas side and therefore an increase in evaporation time. This effect is enhanced because of increasing saturation temperature at elevated pressures which increases the initial liquid preheating time (Renksizbulut and Haywood, 1988). On the other hand, an increase in ambient gas viscosity and an increase in convective heat supply to droplets lead to an increase in droplet surface temperature. The later leads to a reduction of the latent heat of vaporization and decrease the evaporation time (Hiroyasu et al, 1980; Nomura et al, 1996; Kim and Sung, 2003). From the results presented here, the second effect dominates at gas pressure less than 2.5 MPa while the first effect is significant at higher pressures. Results in Figure (6.16c) show that the effect of initial velocity on evaporation time is rather small for the initial velocity greater than 50 m/s as (Figure (6.13c)). The effect of taking into account temperature gradient inside the droplet on evaporation time, when gas pressure is changed, is rather complex because of many opposing effects.

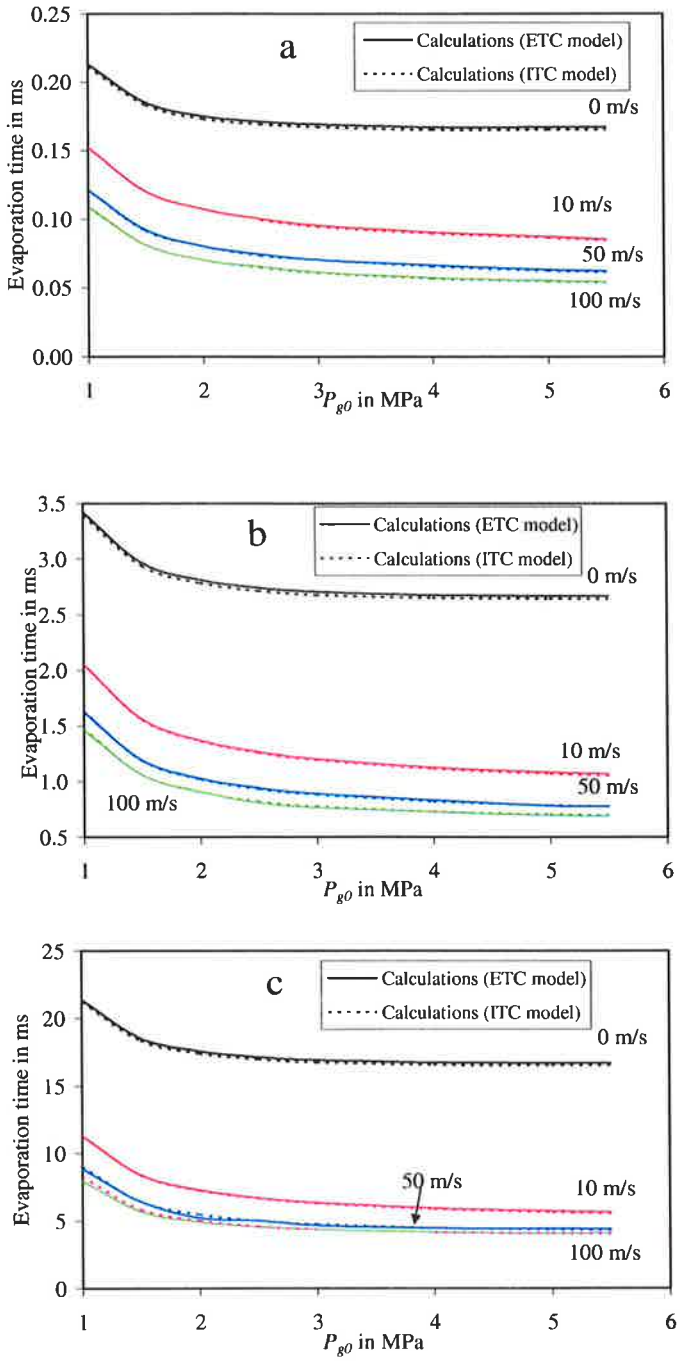

Fig. 6.16 The values of the evaporation time for *n*-dodecane droplets versus initial gas pressure calculated based on the ETC and the ITC models implemented into the zero dimensional code. Initial gas temperature is taken equal to 880 K. The initial droplet diameters are taken 5 μm (a), 20 μm (b) and 50 μm (c). The initial droplet velocities are indicated near the curves (0 (black), 10 m/s (red), 50 m/s (blue) and 100 m/s (green)).

The heat supply effect dominates for low initial velocities and low droplets initial diameters while the direct temperature effect dominates over heat supply effect for larger initial droplets diameters and higher initial velocities. The percentage effects of taking into account temperature gradient inside droplets are less than 1.9 %, 2.1 % and 4 % for

initial droplet diameters 5, 20, 50 μm, respectively when gas pressure changed from 1 to 5.5 Mpa and gas temperature is taken 880 K. Figure (6.17) shows droplet evaporation time versus gas pressure for droplet initial diameter 50 μm based on the ETC and the ITC models for diesel fuel. Droplet initial velocities are taken in the range from 0 to 100 m/s as shown near the plots. Gas temperature is taken to be 880 K. The results show that changing gas pressure has similar effects on *n*-dodecane and diesel fuel. Hence, the effect of temperature gradient inside droplets can be ignored in most diesel engines applications.

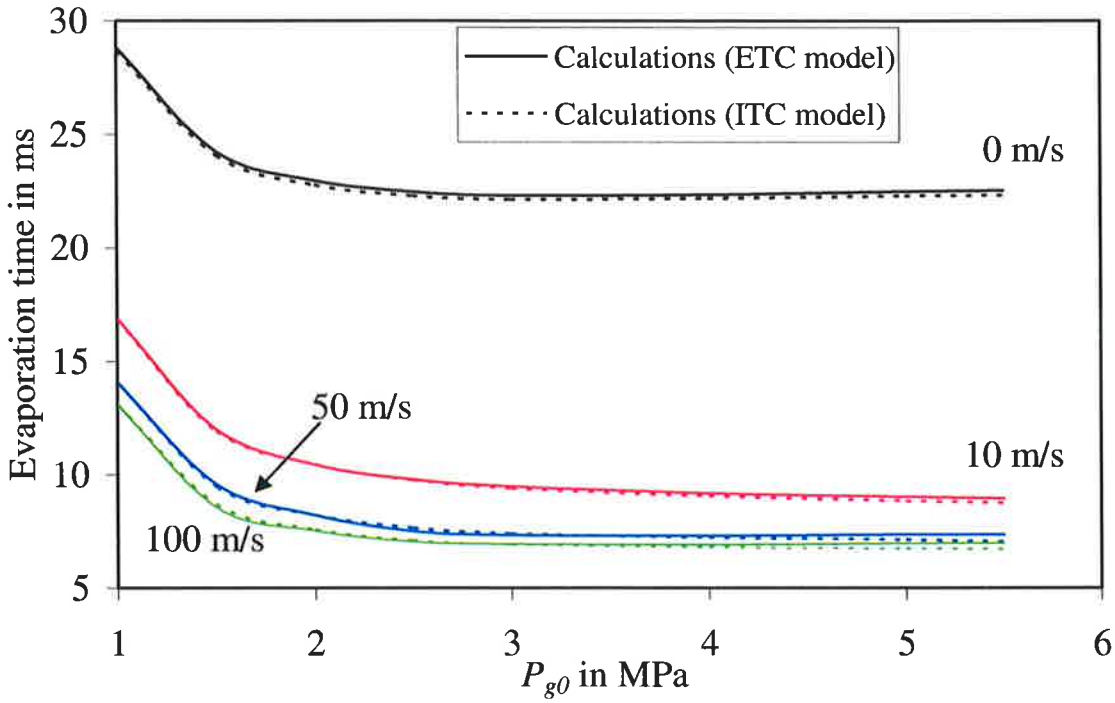

Fig. 6.17 The same as in Figure (6.16c) but for diesel fuel.

6.8.2 The effects of thermal radiation, gas temperature and gas pressure on total ignition delay time without break-up

In the previous section, we saw that the effect of temperature gradient inside droplets on evaporation time is small. The situation appears to be different when the total ignition delay is considered. Plots of the total ignition delay versus T_{ext} for the values of parameters similar to those in Figure (6.10) are shown in Figure (6.18). The Shell model with $A_{f4} = 3 \times 10^6$ was used. From these figures it can be observed that the ignition delay decreases with increasing T_{ext} and droplet velocity as expected. The effect of temperature gradient inside droplets and recirculation in them appears to be rather complex, especially for stationary droplets (see Figure (6.18a, b)). For rapidly moving droplets

this effect leads to a decrease of the total ignition delay by up to 14.5% and 20.25% for initial droplet diameters of 20 μm and 50 μm, respectively.

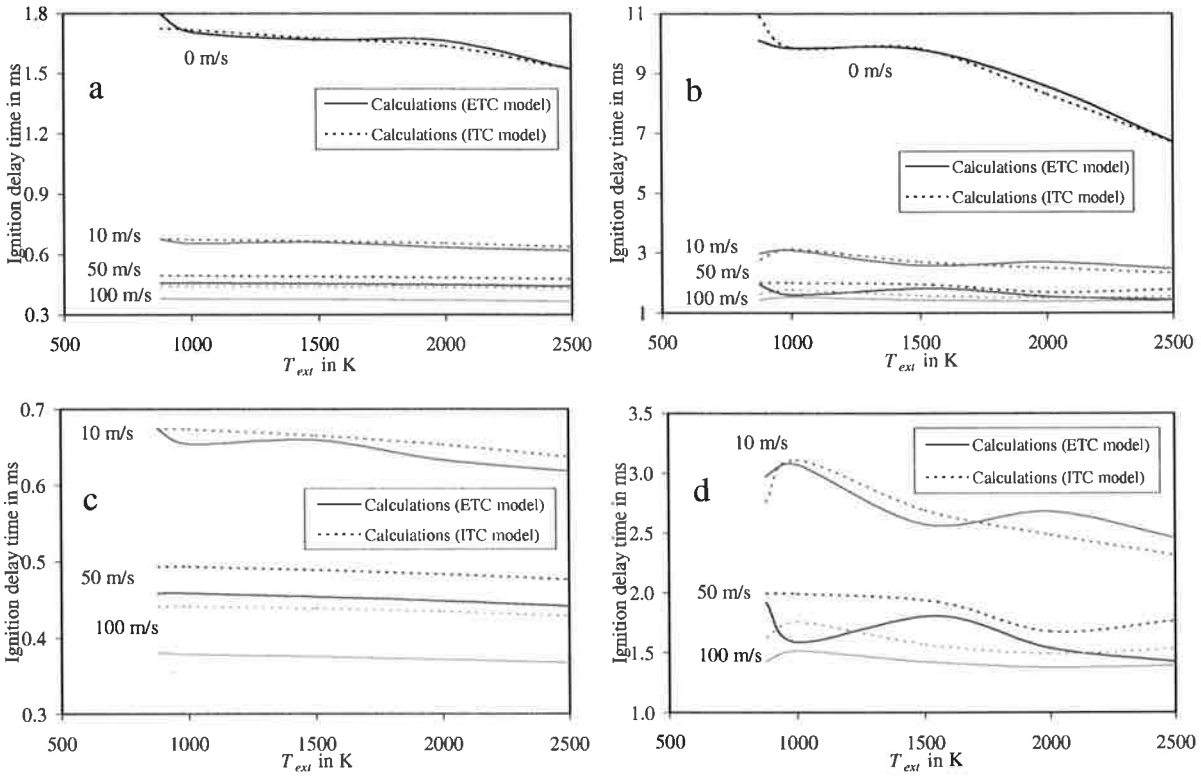

Fig. 6.18 The values of the total ignition delay time for *n*-dodecane droplets versus external temperature calculated based on the ETC and ITC models implemented into the zero dimensional code. Initial gas temperature and pressure are taken equal to 880 K and 3 MPa, respectively. The initial droplet diameters are taken 20 μm (a) and 50 μm (b). Figures (c, d) show a magnified view of initial part of Figures (a, b), respectively. The initial droplet velocities are indicated near the curves (0 (black), 10 m/s (red), 50 m/s (blue) and 100 m/s (green)).

Similar analysis for droplets with initial diameters 5 μm predicted the decrease of this time by 5%. This strong effect of temperature gradient and recirculation inside droplets on the total ignition delay is consistent with that predicted in Figure (6.7). The relative contribution of the chemical ignition delay time to the total ignition delay time is expected to increase with increasing droplet velocities, which is consistent with the results shown in Figures (6.18a, b, c). In agreement with Sazhina et al (1999) and Sazhina et al (2000), it was shown that the predicted total ignition delay is a relatively weak function of A_{f4}. For droplets of 50 μm initial diameter moving with the initial velocity of 50 m/s through gas at 3 MPa and initial temperature 880 K, the predicted

total ignition delay decreased from 0.51 ms to 0.46 ms when A_{f4} increased from 3×10^6 to 6×10^6, as predicted by the ETC model. The ITC model predicted the values of this delay about 7.9% higher for $A_{f4} = 3 \times 10^6$, and about 7.1% higher for $A_{f4} = 6 \times 10^6$.

A similar analysis of these droplets ignition without the contribution of radiation, but for gas temperatures in the range (700-1200 K) were developed. Figures (6.19a, b, c) show the total ignition delay time versus gas temperature for droplet initial diameters 5 μm, 20 μm and 50 μm respectively based on the ETC and the ITC models for *n*-dodecane. Droplets initial velocities are shown near the plots. Gas pressure was taken equal to 3 MPa. The results show that ignition delay time decreases with increasing gas temperature and initial velocity and decreasing droplet initial diameter. These results are in qualitative agreement with those reported by Tanabe et al (1995), Schnaubelt et al (2000) and Yang and Wong (2001). The results also show that the effect of gas temperature on the ignition delay time is more visible at low gas temperature. These results agreed with experimental results reported by Tanabe et al (1995), Tanabe et al (1996) and Schnaubelt et al (2000). It can be noticed that the effect of taking into account temperature gradient and recirculation inside the droplets on ignition delay time, tends to increase with increasing droplet initial diameter and initial velocity. This effect reduced the ignition delay time by up to 13%, 31.7% and 37.8% for droplet initial diameters 5 μm, 20 μm and 50 μm, respectively for the conditions under consideration. It can be noticed that the influence of the temperature gradient in droplets on the total ignition delay is noticeably greater than its influence on droplet evaporation time (cf. Figure (6.13) and (6.19)). As mentioned in Figure (6.7), this is related to the fact that the chemical part of the total ignition delay is a strongly non-linear function of gas temperature in the vicinity of droplets (T_{ref}). As shown earlier (see Figure (6.4)), the droplet surface temperature strongly depends on the temperature gradient in droplets, especially at the initial stages of heating. It can be also noticed that sometimes, especially for larger droplets, the autignition happened before completing droplets evaporation (cf. Figure (6.13) and (6.19)). This leads to make the ignition delay time more sensitive to droplet surface temperature than evaporation time for condition under consideration. In this case the autoignition process started as soon as equivalence ratio reached the lower flammability limit. This means that the dominant factor on starting the autoignition is gas temperature.

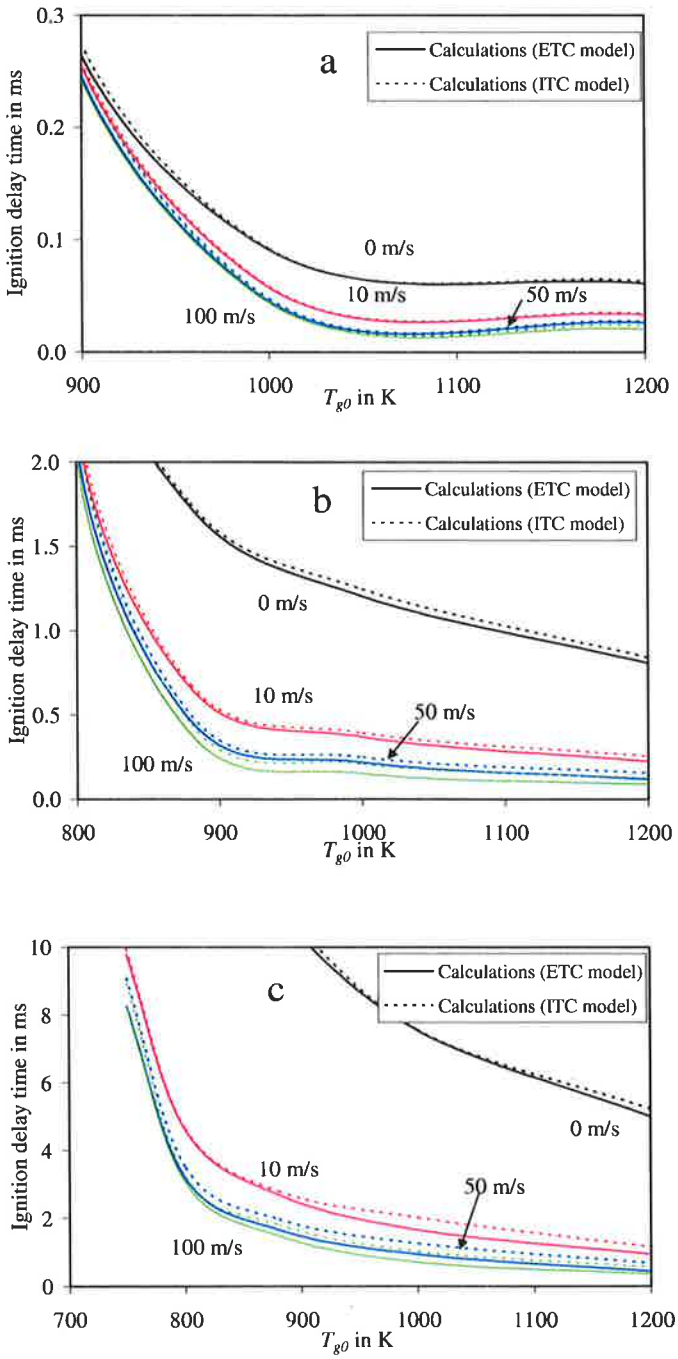

Fig. 6.19 The values of the total ignition delay time for *n*-dodecane droplets versus initial gas temperature calculated based on the ETC and the ITC models implemented into the zero dimensional code. Initial gas pressure is taken equal to 3 MPa. The initial droplet diameters are taken 5 μm (a), 20 μm (b) and 50 μm (c). The initial droplet velocities are indicated near the curves (0 (black), 10 m/s (red), 50 m/s (blue) and 100 m/s (green)). Radiation model is disabled.

As mentioned before, temperature gradient inside droplets increased droplet surface temperature because of decreasing liquid fuel thermal conductivity. Hence, increasing droplet surface temperature leads to decrease convective heat supply to droplets. As a result, gas temperature increases and this leads to decrease autoignition delay time. This

can be confirmed by the results in Figure (6.20). In this figure the gas temperature at the beginning of the autoignition and the corresponding equivalence ratio are plotted versus initial gas temperature based on the ETC and the ITC models. Gas pressure, initial droplets diameter and initial droplets velocity were taken 3 MPa, 50 μm and 50 m/s, respectively. The results show that taking into account temperature gradient inside droplets allows autoignition to start at gas temperatures higher than that when this effect is neglected. Based on the results in Figures (6.20) and (6.19c), I can conclude that gas temperature dominates over the equivalence ratio in the onset of the autoigniton process.

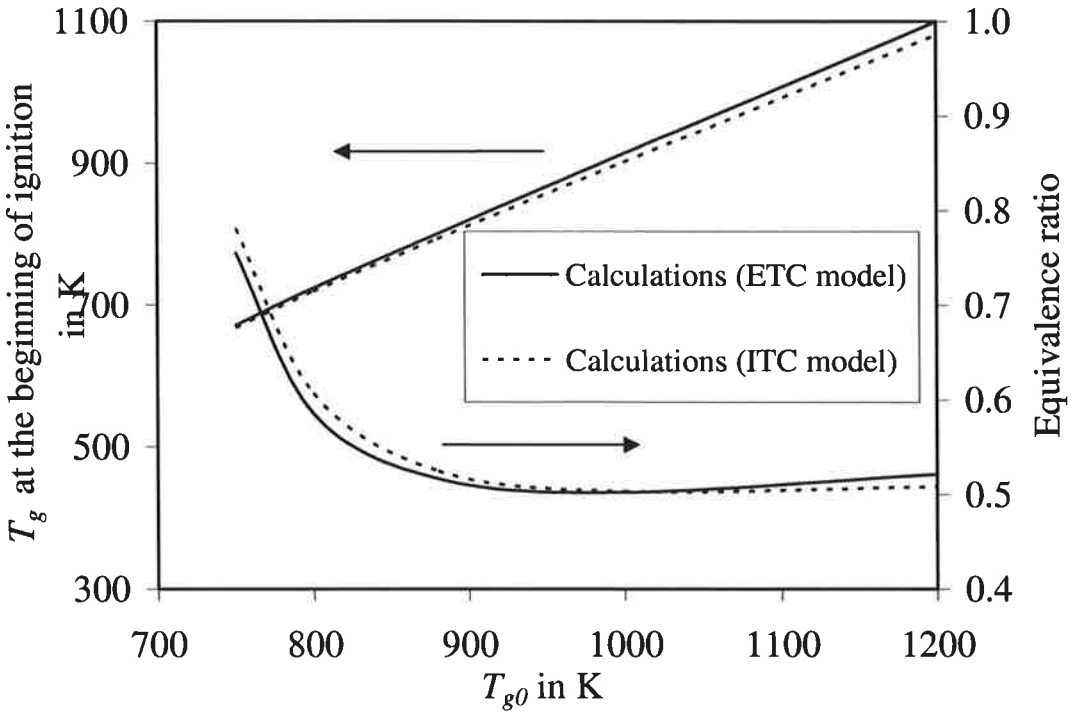

Fig. 6.20 Plots of gas temperature and the corresponding equivalence ratio at the start of ignition for *n*-dodecane versus initial gas temperature calculated based on the ETC and the ITC models implemented into the zero dimensional code. The initial droplet diameter, velocity and pressure are taken equal to 50 μm, 50 m/s and 3 MPa respectively.

A similar analysis but for fixed initial gas temperature, and pressure varying in the range (1-5.5) MPa, was developed. As before, the radiation model was disabled. Figures (6.21a, b, and c) show the total ignition delay time versus initial gas pressure, for droplet initial diameters 5 μm, 20 μm and 50 μm, respectively based on the ETC and the ITC models for *n*-dodecane. Droplets initial velocities are shown near the plots. Initial gas temperature was taken 880 K. The results show that the total ignition delay time decreased with decreasing droplet initial diameter and with increasing initial velocity, as expected. The results also show that the ignition delay time decreased with increasing

gas pressure for the droplet with the initial diameter 5 μm. This effect is reversed for the droplet of initial diameter 50 μm. For droplet with initial diameter equal to 20 μm the picture is more complex.

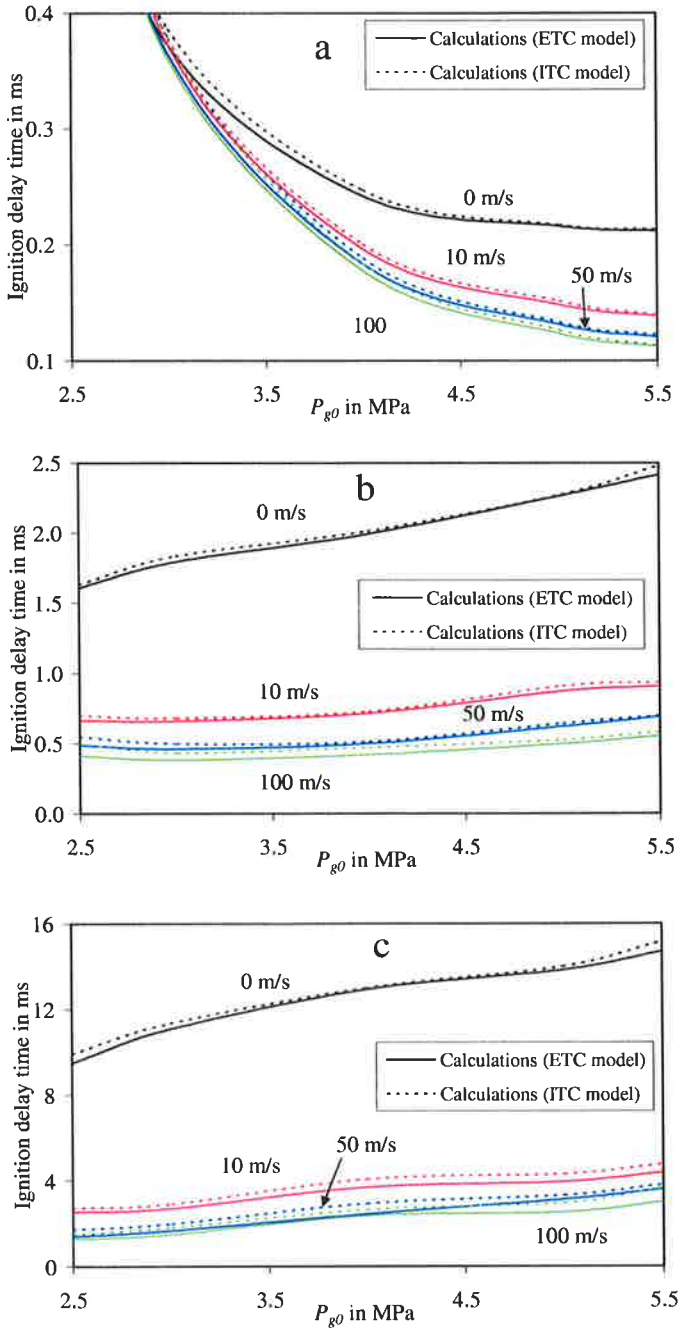

Fig. 6.21 The values of the total ignition delay time for *n*-dodecane droplets versus initial gas pressure calculated based on the ETC and the ITC models implemented into the zero dimensional code. Initial gas temperature is taken equal to 880 K. The initial droplet diameters are taken 5 μm (a), 20 μm (b) and 50 μm (c). The initial droplet velocities are indicated near the curves (0 (black), 10 m/s (red), 50 m/s (blue) and 100 m/s (green)).

For stationary droplets ignition delay tends to increase with pressure. For moving droplets, it is almost constant (or slightly decreasing) with pressure until 3 MPa. For higher pressures, the ignition delay tends to increase with pressure.

Decrease of ignition delay time with increasing gas pressure for smaller droplets could be related to the fact that the droplet life time is less than ignition delay time. In this case the ignition delay time is independent of the droplets initial diameters and decrease with increasing gas pressure (Yang and Wong, 2003). The increase in ignition delay time with increasing gas pressure for larger droplets could be related to the fact that the droplets started to ignite before evaporation completes (cf. Figures (6.16) and (6.21)). The latter are in qualitative agreement with experimental data in diesel engine reported by Crua et al (2004) at elevated pressure (P_g > 8 MPa). It can be noticed that the effect of initial velocity on ignition delay time is not visible for the droplets of initial diameter 50 μm (Figure (6.21c)). These results in the small effect of initial velocity on evaporation rate as shown above (see Figure (6.14)). Taking into account temperature gradient and recirculation inside droplets reduced the total ignition delay time by up to 6%, 13% and 17% for droplet initial diameters 5 μm, 20 μm and 50 μm respectively for the conditions under consideration. It is clear that the effect of taking into account temperature gradient inside droplets increased when the total ignition delay time is less than the evaporation time (D_{d0} = 20 , 50 μm).

6.8.3 The effects of gas temperature on evaporation time and total ignition delay time with break up

Effect of a ETC model on droplet evaporation time at various initial gas temperatures in the presence of break-up is illustrated in Figure (6.22). The initial droplet diameter and velocity are assumed equal to 50 μm and 50 m/s, respectively. If the conditions for both bag and stripping break-up are satisfied simultaneously, then if $t_b < t_s$ then it is assumed that only bag break-up takes place and vice versa. Symbols in the figure indicate the values of gas temperature for which calculations of the evaporation time were performed.

As one can see from Figure (6.22), in the presence of break–up the ETC model predicts noticeably shorter evaporation times when compared with the ITC model, especially at higher initial gas temperatures. This result can be related to rather strong dependence of the surface tension coefficient on droplet surface temperature T_s, which is translated into the corresponding dependence of $R_{db(s)}$ and $t_{b(s)}$ on T_s.

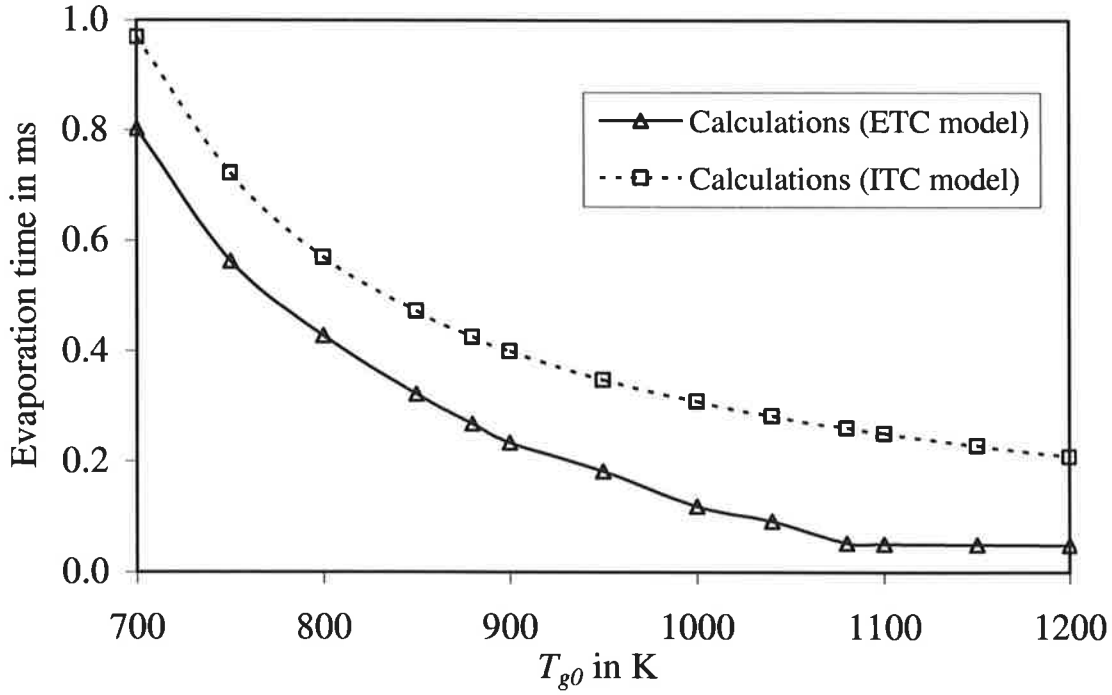

Fig. 6.22 The values of the evaporation time for *n*-dodecane versus initial gas temperature calculated based on the ETC and the ITC models implemented into the zero dimensional code. Bag and stripping droplet break-up were taken into account. The initial droplet diameter and velocity are taken equal to 50 μm and 50 m/s respectively. Symbols indicate the values of the initial gas temperature for which the computations were times were calculated.

Remembering Equations (6.4.1-6.4.5), ignoring the temperature dependence of ρ_l and assuming that U_g and U_d are constant, I can find the following expressions for the ratios:

$$\tilde{R}_{db} \equiv \frac{R_{db}(T_s)}{R_{db}(T_s = 300\,\mathrm{K})} = \frac{\sigma_s(T_s)}{\sigma_s(T_s = 300\,\mathrm{K})} \times \frac{T_g + 2T_s}{T_g + 600};$$

$$\tilde{R}_{ds} \equiv \frac{R_{ds}(T_s)}{R_{ds}(T_s = 300\,\mathrm{K})} = \tilde{R}_{db}^2;$$

$$\tilde{t}_b \equiv \frac{t_b(T_s)}{t_b(T_s = 300\,\mathrm{K})} = 1/\sqrt{\frac{\sigma_s(T_s)}{\sigma_s(T_s = 300\,\mathrm{K})}};$$

$$\tilde{t}_s \equiv \frac{t_s(T_s)}{t_s(T_s = 300\,\mathrm{K})} = \sqrt{\frac{T_g + 2T_s}{T_g + 600}} \qquad (6.8.3.1)$$

The plots of $\tilde{R}_{db}$, $\tilde{R}_{ds}$, $\tilde{t}_b$ and $\tilde{t}_s$ versus T_s for n-dodecane are shown in Figures (6.23a, b). As can be seen from Figure (6.23a), both $\tilde{R}_{db}$ and $\tilde{R}_{ds}$ decrease rather rapidly with increasing T_s, mainly due to the fact that surface tension decreases with increasing T_s. Since the ETC model predicts more rapid initial increase of T_s compared with the ITC

model, one can expect that the break-up process is predicted by the ETC model for a wider range of droplet radii, compared with the prediction of the ITC model.

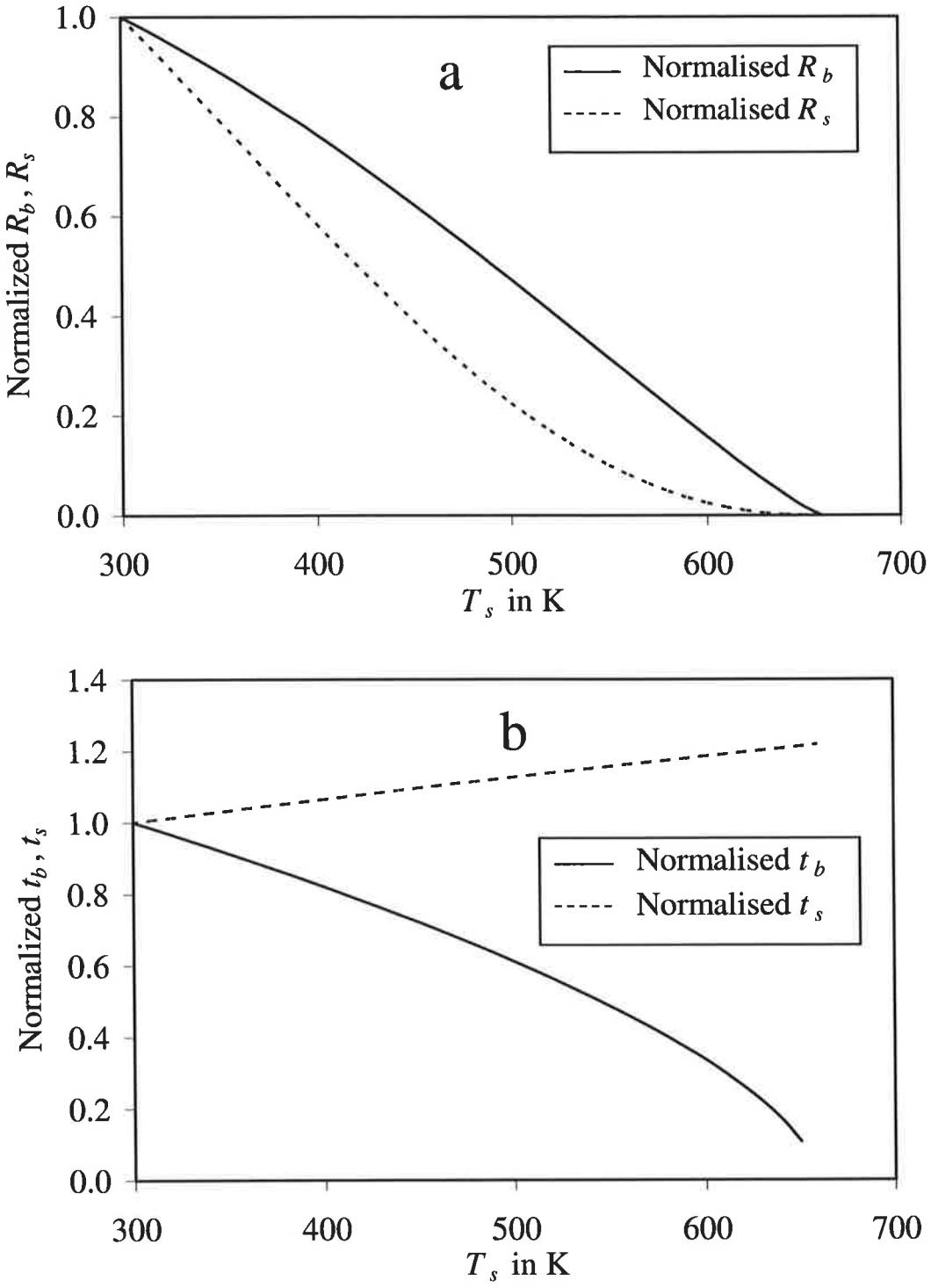

Fig. 6.23 Values of $\tilde{R}_{db} \equiv R_{db}(T_s)/R_{db}(T_s = 300K)$, $\tilde{R}_{ds} \equiv R_{ds}(T_s)/R_{ds}(T_s = 300K)$ (a), $\tilde{t}_b \equiv t_b(T_s)/t_b(T_s = 300K)$ and $\tilde{t}_s \equiv t_s(T_s)/t_s(T_s = 300K)$ (b) versus droplet surface temperature.

Hence the evaporation of droplets, as predicted by the ETC model, is expected to be more rapid when compared with the prediction of the ITC model. This is consistent with the results shown in Figure (6.22).

As follows from Figure (6.23b), the increase of $\tilde{t}_s$ with increasing T_s is rather weak and can be ignored in most practical application. $\tilde{t}_b$ decreases with T_s. In the case shown in Figure (6.22), the intensification of the stripping break-up process due to the reduction of $\tilde{R}_{ds}$ seems to dominate the slow down due to increase of $\tilde{t}_s$. As to the bag break-up both reduction of $\tilde{R}_{db}$ and $\tilde{t}_b$ lead to intensification of the break-up process. Similar results were obtained for diesel fuel.

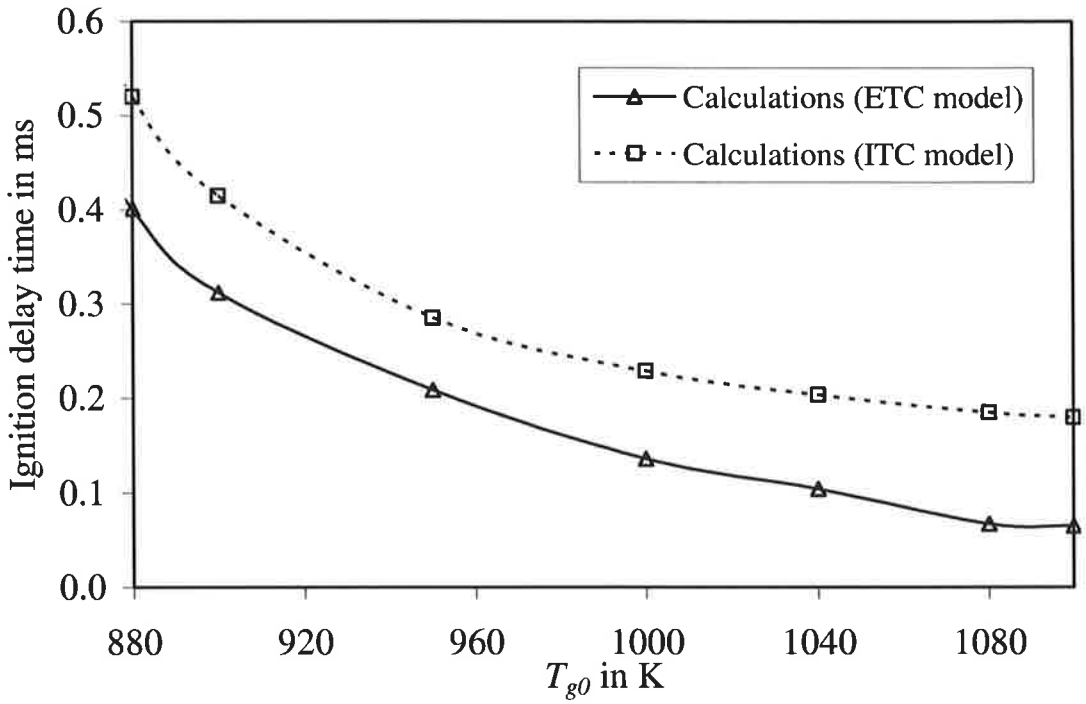

Fig. 6.24 The plots of the total ignition delay versus T_{g0} in the presence of the break-up for the same droplets as used in Figure (6.22), when calculated based on the ETC and the ITC models implemented into the zero dimensional code. Symbols indicate the values of the initial gas temperature for which the ignition delay times were calculated.

The plots of the total ignition delay versus T_s in the presence of the break-up for the same droplets as used in Figure (6.22) are shown in Figure (6.24). The Shell model with $A_{f4} = 3 \times 10^6$ was used. As can be seen from this figure, the ignition delay decreases with increasing T_g. The effect of temperature gradient inside droplets and recirculation in them on the total ignition delay is consistent with the predictions of Figure (6.7). As in Figure (6.22), symbols indicate the values of initial gas temperature for which the calculations were performed.

Strong influence of the temperature gradient inside droplets on droplet break-up, evaporation and the ignition of evaporated fuel / air mixture, allows us to recommend that this effect is taken into account in computational fluid dynamics codes designed to model fluid dynamics, heat transfer and combustion processes in internal combustion engines. So far this effect has been almost universally ignored, with the only exception of this, to the best of our knowledge, being the paper by Bertoli and Migliaccio (1999).

It should be mentioned that the zero dimensional analysis presented in this chapter has well known limitations in predicting the actually observed total ignition delay of fuel droplets. At least a one-dimensional analysis of the gas phase would be required to describe adequately the fuel vapour diffusion around droplets. This would ultimately control the ignition process of the fuel vapour / air mixture (see Tanabe et al, 1995; Schnaubelt et al, 2000). Nevertheless I see the importance of the current work in the following directions. Firstly, it can be considered as the first step and motivation to continue the started work of introducing the temperature gradient in modeling of droplet evaporation and break-up for appropriate conditions. Secondly the model described in this chapter is presented in a form suitable for implementation into multidimensional CFD codes, where the individual computational cells are assumed to be free from spatial inhomogeneities.

6.9 Conclusions of chapter 6

A zero dimensional code taking into account the temperature gradient inside droplets, the coupling between liquid and gas phases and describing the autoignition process based on the Shell autoignition model has been developed. This code was used to study the effects of temperature gradient inside fuel droplets on droplet evaporation, break-up and the ignition of fuel vapour / air mixture. The predictions of the code are validated against experimental data published by Belardini et al (1992), Nomura et al (1996), and Tanabe et al (1995). In the absence of break-up, the influence of temperature gradient on droplet evaporation in realistic diesel engines conditions is generally small (1 - 3%). In the presence of the break-up process, however, the temperature gradient inside droplets can lead to a significant decrease in the evaporation time under the same conditions. This is attributed to the fact that the effect of temperature gradient inside droplets leads to a substantial increase in droplet surface temperature at the initial stages of its heating. This increase, in turn, leads to a decrease of droplets surface tension and a decrease in the threshold radii at which break-up occurs, assuming that bag and stripping break-ups

are the dominant mechanisms of the droplet break-up. Even in the absence of break-up, the effect of temperature gradient inside droplets leads to a noticeable (up to about 20 %) decrease of the total ignition delay time (comprising the physical and chemical ignition delays). In the presence of break-up, this effect is enhanced substantially, leading to more than halving of the total ignition delay. This reduction of the total ignition delay time is understood to be the combined effect of the influence of increased droplet surface temperature on the chemical ignition delay, and the influence of this temperature on droplet evaporation (in the presence of break-up processes). It is recommended that the effects of temperature gradient inside droplets are taken into account in computational fluid dynamics codes describing droplet break-up and evaporation processes, and the ignition of the evaporated fuel / air mixture.

7. IMPLEMENTATION OF THE ETC MODEL INTO KIVA CFD CODE

In a typical internal combustion engine environment, the duration of the transient droplet heating is comparable with the droplet vaporization time. Therefore the temperature gradient inside droplets cannot be ignored in CFD calculations (Bertoli and Migliaccio, 1999). The ETC model (based on the analytical solution of heat conduction equation inside droplets for constant heat transfer coefficient), which takes into account temperature gradient and recirculation inside droplets as discussed in Chapters 4-6, has been formulated to remove some over simplifying assumptions in the original Spalding model (Spalding, 1953), thus leading to a better understanding of the evaporation process in diesel engines. One of the most important hypotheses of the Spalding model is that the thermal conductivity of the droplet is "infinite" and the temperature inside the droplet is uniform and equal to its surface temperature value. This model also neglected the thermal radiation effects and the circulation inside droplets. In order to introduce a more realistic transient heating of the droplet, the new heating model allows for the calculation of the internal temperature distribution of the droplet taking into account the circulation inside it and the thermal radiation effects.

The effects of temperature gradient inside droplets are described by the ETC model based on the analytical solution of the heat conduction Equation (4.2.1) inside the droplets for h = constant, on heating, evaporation, ignition and break-up of diesel fuel droplets were discussed in Chapter 6. These were obtained by using a zero dimensional code in which all values of gas parameters (velocity, temperature, fuel vapour concentration etc) were assumed to be homogeneous. This code took into account the coupling between liquid and gas phases and described the autoignition process based on the Shell model. The effects of thermal radiation on the same parameters using Equation (5.6.1) were discussed.

This chapter is focused on the implementation of the ETC model into KIVA2 CFD code to study the effects of the contribution of temperature gradients and recirculation inside fuel droplets on the diesel engine processes. Thermal radiation is neglected. All other models describing turbulence, coalescence, break-up and chemical reactions processes are used as they were in the original KIVA2 CFD code.

A brief description of KIVA2 code is presented in Section 7.1. In Section 7.2 the spray modelling in KIVA2 is summarized. The implementation of the ETC model into KIVA2 code is described in Section 7.3. The results are discussed in Section 7.4. The main results of the chapter are briefly summarised in the conclusions section.

Some preliminary results of this chapter were published in Abdelghaffar et al (2005).

7.1 Introduction to KIVA2 CFD code

KIVA2 CFD code solves governing equations of transient, two and three-dimensional, chemically reactive fluid flow, with sprays modelled by Lagrangian approach. The equations solved in KIVA2 can be applied to laminar or turbulent flows, subsonic or supersonic flows, and single-phase or dispersed two-phase flows. Evaporating liquid sprays are represented by a discrete-particle technique (Dukowicz, 1980) in which each particle represents a number of droplets of identical size, velocity, and temperature. The particles and fluid interact by exchanging mass, momentum, and energy. Accurate calculation of mass and energy exchange is ensured by automatic reductions in the time step when the exchange rates become large. Turbulence effects on the droplets are accounted for in one of two ways. When the time step is smaller than the droplet turbulence correlation time, a fluctuating component is added to the local mean gas velocity when calculating each particle's mass, momentum, and energy exchange with the gas (Dukowicz, 1980). When the time step exceeds the turbulence correlation time, turbulent changes in droplet position and velocity are chosen randomly from analytically derived probability distributions for these changes (O'Rourke, 1987). Droplet collisions and coalescence are accounted for (O'Rourke, 1981) and a TAB break-up model is used for droplet aerodynamic break-up (O'Rourke, 1987).

The number of species and chemical reactions that can be accounted for in KIVA 2 can be arbitrarily assigned. It is limited only by CPU requirements and storage considerations. The code distinguishes between slow reactions, which proceed kinetically, and fast reactions, which are assumed to be in equilibrium (Ramshaw, 1980). The chemical kinetic model for combustion is a single step oxidation model (Ramshaw, 1980). The real combustion processes would be much more complex than a single step mechanism; therefore the accuracy will be limited. Chemical kinetic equations with rate expressions, which are Arrhenius in form, are evaluated by two equation solvers, which are available to compute chemical equilibrium: a fast algebraic solver for hydrocarbon/air combustion (Meintjes and Morgan, 1987) and an iterative solver for more general circumstances (Ramshaw and Amsden, 1985). The latter solver is general but more CPU intensive.

Two models are available to represent the effects of turbulence. The user has the option to use a standard version of the k-ε turbulence model (Launder and Spalding,

1972), modified version of this model to include volumetric expansion effects (Reynolds, 1981) and spray/turbulence interactions (Reitz and Diwakar, 1987) or to use a modified version of subgrid scale (SGS) turbulence model of KIVA (Amsden et al, 1985). The SGS model reduces to the k-ε mode near walls where all turbulence length scales are too small to be resolved by the computational mesh. Boundary layer drag and wall heat transfer are calculated by matching to the turbulent law of the wall. KIVA2 does not take into account the effects of turbulence on the main chemical reaction rates.

KIVA2 solves the equations of motion of a turbulent, chemically reactive mixture of ideal gases, coupled to the equations for a single-component vaporizing fuel spray. The solution procedure is based on the ALE (Arbitrary Lagrangian-Eulerian) finite volume method (Hirt et al, 1974; Pracht, 1975). Spatial differences are formed on a finite-difference mesh that subdivides the computational region into small cells that are hexahedrons. The mesh can conform to arbitrary curved boundaries, and it can move with time following changes in combustion chamber geometry. The strength of the method is that the mesh needs not to be orthogonal. The time marching scheme in KIVA2 is fully implicit (Patankar, 1980) allowing timesteps to be calculated based on accuracy, not stability, criteria. This results in requiring less computing time in many problems. The coupled PDEs (Partial Differential Equations) are solved iteratively with pressure equation using a method similar to the SIMPLE algorithm (Patankar, 1980). Explicit time-marching methods are used to calculate convection in the rezone phase (when the piston moves in internal combustion engine calculations), but the convection calculation can be subcycled an arbitrary number of times, and thus the main computational timestep is not restricted by the Courant stability condition of explicit methods.

In KIVA2, the solution of droplets and gas governing equations is performed in three stages or phases (A, B and C). In phase A, the calculations related to the droplets are performed. Droplet collision and oscillation/break-up is taken into account. The droplets ODEs for mass and temperature are calculated. The droplets positions and velocities are also calculated in Phase A. The droplets then exchange mass, momentum and energy with the gas in the computational cell in which they are located. Phase A calculations are completed with the update of droplets radii and temperatures due to break-up heating and evaporation. The gravitational acceleration terms are taken into account for the droplets velocities.

The implicit solution of governing equations (Patankar, 1980) for the conservation of mass, momentum, internal energy, turbulent kinetic energy and dissipation of turbulent kinetic energy is performed in Phase B. Also computational cell volume change is taken into account in Phase B for moving geometries (e.g. piston in internal combustion engine cylinder) (Amsden et al, 1989). The SIMPLE method (Patankar, 1980) as a two-step iterative procedure is used to solve the pressure – momentum equations in Phase B. Up to 10 chemical species can be calculated in KIVA2 CFD code.

Phase C is the rezone phase, in which the flow field is frozen and rezoned or remapped onto a new computational mesh for moving geometries (Amsden et al, 1989).

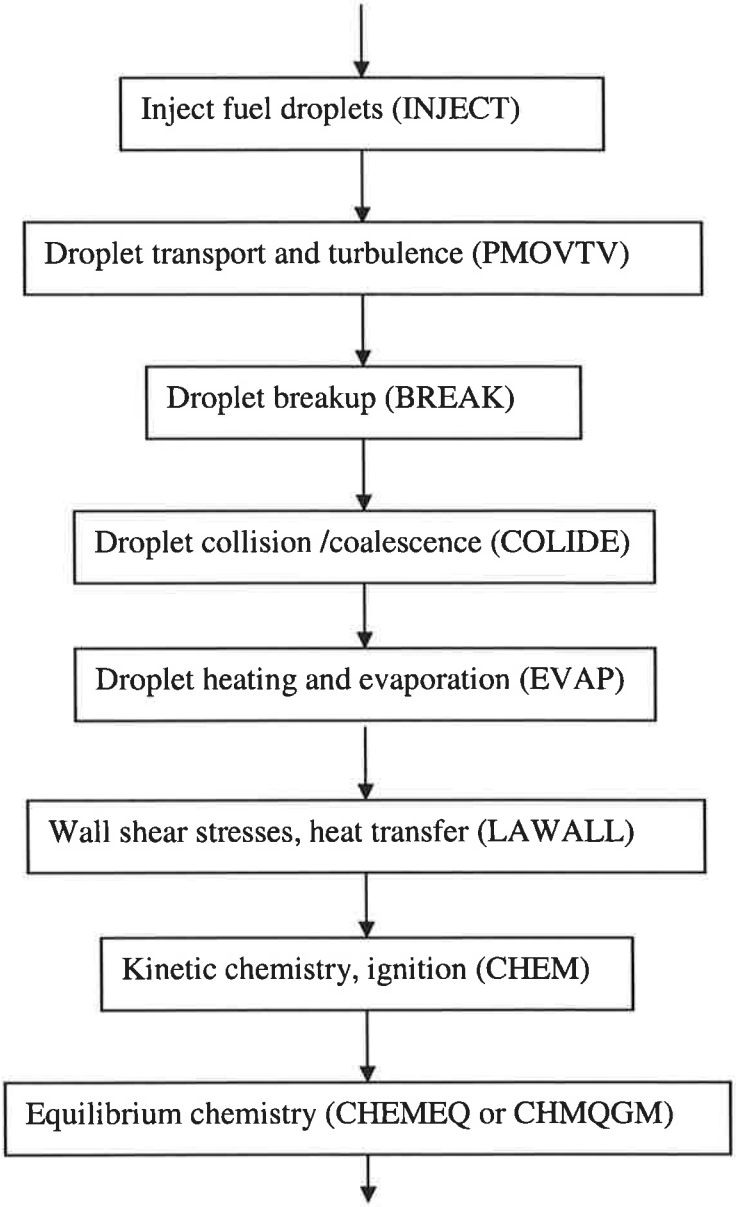

Fig. 7.1 Block diagram for the subroutine related to droplets in KIVA2 code.

Figure (7.1) shows a block diagram of the subroutines related to droplets in KIVA2 (Amsden et al, 1989). The name of the subroutine which calculates the related process is written between the brackets.

7.2 Spray modelling in KIVA2

The dynamics of a spray, and its interaction with the in-cylinder gas, is a complex problem. To calculate the mass, momentum and energy exchange between the spray and the gas in a real diesel engine, one must account for a distribution of droplet sizes, velocities and temperatures. In many sprays, droplet Weber numbers are larger than unity (Hinze, 1948), and droplet oscillations, distortions and break-up must be considered. Droplet collisions and coalescences have also been found to be important in many engine sprays (O'Rourke, 1981). A mathematical formulation that is capable of representing these complex physical processes, leads to a system of ODEs (Ordinary Differential Equations). Its solution will provide source terms for the gas phase PDEs.

In what follows, a brief description of droplets heating, evaporation and break-up models in KIVA2 CFD code are presented.

7.2.1 Droplet heating model

A classic droplet vaporization model, widely used in CFD codes, is the Spalding model (Spalding, 1953). This model is based on several simplifying assumptions: gas boundary layer is assumed to be quasi-steady; spherical symmetry is employed; thermal radiation is neglected; air and fuel vapour behave as ideal gases; vapour/liquid phase equilibrium occurs at the fuel surface; "1/3 rule" is used for gas properties; both circulation and temperature gradient inside the fuel droplets are neglected (Spalding, 1953).

The energy balance at the droplet's surface is expressed as:

$$\frac{4}{3}\pi R_d^3 \rho_l c_l \frac{dT}{dt} - 4\pi R_d^2 \dot{R}_d \rho_l L = 4\pi R_d^2 Q_l , \qquad (7.2.1.1)$$

where Q_l is the rate of heat conduction to the droplet surface per unit area (W / m^2). It was given by the Ranz-Marshall correlation (Faeth, 1977):

$$Q_l = \mathrm{Nu}\frac{k_{air}(T_{ref})(T_g - T_d)}{2R_d}, \qquad (7.2.1.2)$$

where Nu is calculated from Equation (2.2.1.2.23),

$$\mathrm{Pr} = \frac{\mu_{air}(T_{ref})c_{air}(T_{ref})}{k_{air}(T_{ref})}, \qquad k_{air}(T_{ref}) = \frac{K_1 T_{ref}^{3/2}}{T_{ref} + K_2}, \qquad \mu_{air} = \frac{A_1 T_{ref}^{3/2}}{T_{ref} + A_2},$$

K_1 = 252 g cm / (sec^3 K$^{3/2}$), K_2 = 200 K, A_1 = 1.457E-5 g/(sec cm K$^{1/2}$), A_2 = 110 K, k_{air} is the air thermal conductivity at T_{ref}, c_{air} is air specific heat capacity at constant pressure at T_{ref} and μ_{air} is air viscosity (Amsden et al, 1987).

The droplet temperature is given by the solution of Equation (7.2.1.1) using an iterative solver in KIVA2 code.

7.2.2 Droplet evaporation model

The mass vaporization rate from the droplet surface is described by Equation (6.3.1); but it can be represented as (Ranz and Marshall, 1952):

$$\dot{m}_f = 2\pi\bar{\rho}_{air}\bar{D}_{air}R_d B_M \mathrm{Sh},$$

where Sh is calculated from Equation (2.2.1.2.24), $\mathrm{Sc} = \dfrac{\mu_{air}(T_{ref})}{\rho_{air}D_{air}}$, $\bar{\rho}_{air}$ and $\bar{D}_{air}$ are average air density and binary diffusion coefficient of the fuel's vapour in air. An empirical correlation suggested in Amsden et al (1985) was used in KIVA2:

$$\bar{\rho}_{air}\bar{D}_{air} = D_1 T_{ref}^{D_2}, \qquad (7.2.2.1$$

D_2 = 0.6, D_1 is a constant based on the fuel type.

KIVA2 code computes an evaporation, and subcycle the evaporation calculation a number of times. The choice for the evaporation timestep is based on the idea that the heat transfer to a particle in one timestep should not exceed half of the energy available for transfer.

7.2.3 Droplet break-up model

The spray atomization in KIVA2 is based on the TAB model (O'Rourke, 1987). This model is based on the Taylor's analogy between the oscillating and distorting drop and a spring-mass system. The external force corresponds to the aerodynamic force acting on the drop; the spring reaction is analogous to the liquid surface tension; finally the damping forces correspond to the liquid viscosity force (O'Rourke, 1987).

Therefore:

$$m\ddot{x} = F - kx - d\dot{x} \qquad (7.2.3.1)$$

where x is the displacement of the drop equator from its equilibrium position. In the Equation (7.2.3.1),

$$\frac{F}{m} = C_F\frac{\rho_g(U_d - U_g)^2}{\rho_l R_d},\quad \frac{k}{m} = C_K\frac{\sigma_l}{\rho_l R_d^3},\quad \frac{d}{m} = C_D\frac{\mu_l}{\rho_l R_d^2}$$

It is assumed that the drop break-up occurs if $x > C_b R_d$, where C_b is a dimensionless constant equal ½. Letting $y = x/(C_b R_d)$, Equation (7.2.3.1) can be rewritten as:

$$\ddot{y} = \frac{C_F}{C_b}\frac{\rho_g (U_d - U_g)^2}{\rho_l R_d^2} - \frac{C_K \sigma_l}{\rho_l R_d^3} y - \frac{C_D \mu_l}{\rho_l R_d^2}\dot{y} \qquad (7.2.3.2)$$

with break-up occurring if and only if $y > 1$.

For constant $(U_d - U_g)$ the solution of Equation (7.2.3.2) can be written as (O'Rourke, 1987):

$$y(t) = \frac{C_F}{C_K C_b} We + e^{-t/t_d}\left[\left(y(0) - \frac{C_F}{C_K C_b} We\right)\cos \omega t + \frac{1}{\omega}\left(\dot{y}(0) + \frac{y(0) - \frac{C_F}{C_K C_b} We}{t_d}\right)\sin \omega t\right] \qquad (7.2.3.3)$$

where $\frac{1}{t_d} = C_D \frac{\mu_l}{2\rho_l R_d^2}$, $\omega^2 = C_K \frac{\sigma_l}{\rho_l R_d^3} - \frac{1}{t_d^2}$ is the square of the oscillation frequency.

For each particle, first We, t_d and ω^2 are calculated. If $\omega^2 \le 0$ the droplets distortions and oscillations are negligible, which occurs only for very small droplets. The amplitude A of the undamped oscillation is calculated (O'Rourke, 1987):

$$A^2 = \left(y^n - \frac{C_F}{C_K C_b} We\right)^2 + \left(\frac{\dot{y}^n}{\omega}\right)^2 \qquad (7.2.3.4)$$

where superscript n refers to timestep.

If $\frac{C_F}{C_K C_b} We + A \le 1$, then according to Equation (7.2.3.3), the value of y will never exceed unity and break–up will not occur. If $\frac{C_F}{C_K C_b} We + A > 1$ the updated values of y and $\dot{y}$ are obtained for the next time step using Equation (7.2.3.3). In the latter case, the break-up is possible on the current timestep and the break-up time t_{bu} is calculated as the smallest root greater than t^n of the equation:

$$\frac{C_F}{C_K C_b} We + A\cos[\omega(t - t^n) + \phi] = 1, \qquad (7.2.3.5)$$

where $\cos\phi = \left(y^n - \frac{C_F}{C_K C_b} We \right) / A$ and $\sin\phi = -\dot{y}^n /(A\omega)$.

If time t^{n+1} is less than t_{bu} then no break-up occurs on the current time step, and y and $\dot{y}$ are obtained for the next time step using Equation (7.2.3.3).

The dimensionless terms C_F, C_K and C_D are the model constants that have to be adjusted to reproduce the experimental data. O'Rouke (1987) suggested C_F = 1/3, C_K =8 and C_D = 5. These values have been obtained using shock tube experimental data. As follows from these data, the critical Weber number is about 6 and it is matching to the fundamental oscillation mode. In this study I took C_F = 1/3, C_K = 3 and C_D = 5 (Beatrice et al, 1995).

7.3 Implementation of the ETC model into KIVA2

The droplet heating and evaporation processes are modeled in EVAP subroutine. The droplet's temperature was calculated based on the Spalding model (Equation (7.2.1.1)). The main modification of the KIVA2 CFD code was made in the EVAP subroutine where the Spalding heating model was replaced by the ETC model described in Chapters 4-6. This leads to replacing the numerical solution of Equation (7.2.1.1) by the analytical solution of heat conduction Equation (4.2.1) for constant h using the formula (4.3.1.19). The terms Q_n, T_{av} and P_n were calculated based on the analytical formulae in Appendix 5.

The droplet surface tension, the latent heat of vaporization and the vapour pressure were calculated based on droplet surface temperature while the liquid heat capacity at constant pressure and droplet viscosity were calculated based on droplet average temperature. T_{ref} was calculated based on the droplet surface temperature. The correlations for Nu, Pr, Re and Sh were used as described in Sections 7.2.1 and 7.2.2. The air thermal conductivity and viscosity were used as described in Equation (7.2.1.2). The liquid thermal conductivity was calculated for diesel fuel and tetradecane as a function of droplet average temperature, as described in Appendix 7, using LIQTC subroutine.

The effect of internal circulation inside fuel droplets was taken into account based on the so called effective conductivity model, where the actual thermal conductivity is replaced by the effective thermal conductivity $k_{eff} = \chi k_l$ where χ is defined by Equation (2.2.1.1.1). Thermal swelling effect was neglected. This approximation was applied by

Bertoli and Migliaccio (1999), where it was found that the thermal swelling is important for isolated single droplet computations while it does not modify significantly numerical results under high temperature and high turbulence conditions such as those in the combustion chamber of a DI diesel engine.

The new algorithm requires calculations of the eigenvalues λ_n based on Equation (4.3.1.9). They were calculated in LAMBDAN subroutine (Press, 1989). This subroutine is called by EVAP subroutine in KIVA2 code as shown in Figure (7.2).

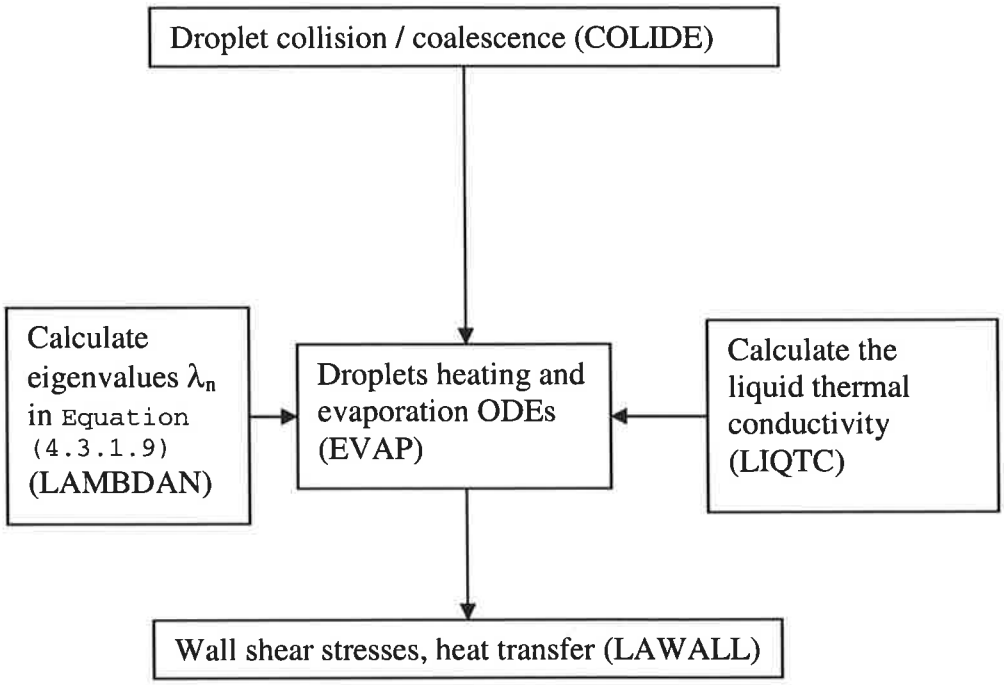

Fig. 7.2 Block diagram for the modified part of the KIVA2 CFD code.

Break-up and coalescence phenomena were simulated by standard KIVA subroutines after taking into account the temperature gradient inside the droplets. The liquid viscosity for the break-up model was calculated based on droplet average temperature, while surface tension was calculated based on droplet surface temperature.

The description of coalescence process was changed in such a way that the new droplet, which results from coalescence, has a uniform temperature equal to a mean value for the two coalescence droplets. The liquid droplet was assumed to consist of layers. The equivalent temperature for a layer "*i*" in the new droplet is calculated based on the conservation of enthalpy of the equivalent layers in the main droplets as:

$$m_{i1}c_{li1}T_{i1} + m_{i2}c_{li2}T_{i2} = m_{in}c_{lin}T_{in}, \tag{7.3.1.1}$$

where subscripts 1, 2 and n refer to the droplets and subscript i refer to the layer number. This approach agrees with the one used by Bertoli and Migliaccio (1999).

Sauter mean diameter (SMD) is calculated to compare the effect of the ETC model on the droplets mean diameter. SMD is defined as (Lefebvre, 1989):

$$\text{SMD} = \frac{\sum N_i d_i^3}{\sum N_i d_i^2} \tag{7.3.1}$$

where d_i represents the diameter of the droplet in parcel i while N_i represents the number of droplets in the same parcel.

7.4 Results and discussions

In order to evaluate the influence of taking into account temperature gradient inside droplets (the ETC model) on the spray behaviour, a preliminary analysis without considering combustion is discussed first in Section 7.4.1. After that the influence of the ETC model on combustion and exhaust emissions is discussed in Section 7.4.2. The numerical results from KIVA2 CFD code were validated using the experimental data from Beatrice et al (1995) and Belardini et al (1996). The effects of thermal radiation are neglected.

7.4.1 The effects of the temperature gradient inside droplets on the spray behaviour without combustion

Numerical calculations for several test cases were validated against experimental data for a combustion chamber of a realistic single cylinder, direct injection, naturally aspirated, diesel engine whose characteristics are reported in Table (7.1) (Beatrice et al, 1995).

The engine was equipped with a pressure transducer to measure the in-cylinder pressure. The engine cylinder head was also equipped with optical accesses to mount two water cooled endoscopes and perform high speed cinematography of the spray injection development. To transmit the image from the endoscope to the high speed camera an optical linkage was used. The frames acquisition speed is up to 32000 frames/sec. To obtain the tip penetration data the films were processed by Hithachi movie analyser. The film speed was set at 8000 frames/sec, obtaining a crank angle resolution of about 1 CA at 1250 rpm. To obtain reliable tip penetration measurements

with the same test condition different shots were performed and processed: the resulting variation coefficient was about 5% (Beatrice et al, 1995).

Numerical results in terms of typical spray characteristics are presented in Figures (7.3) - (7.6). Figure (7.3) represents the predicted amount of fuel vapour mass in the combustion chamber versus crank angle based on the ETC model and the original Spalding model in KIVA2 CFD code. As expected, it is shown that the predicted evaporation rate obtained by the ETC model is higher than that predicted by the Spalding model. The increase in the prediction amount of fuel vapour mass for the ETC model reaches 5% at 3 CA BTDC.

Compression ratio	18
Bore	100 mm
Stroke	95 mm
Connecting rod length	178 mm
Combustion chamber	Toroidal
Speed	1250 rpm
injector	4 holes D_n = 0.28 mm
Angle between two sprays	160°
Injection velocity	210 m/s
Fuel injected mass	0.02 g/cycle
Injection start	7.4 CA BTDC
Injection duration	7 CA
fuel	Diesel fuel
Computational Mesh	20×20×21

Table 7.1 The engine characteristics for the case without combustion.

This can be related to a higher surface temperature that leads to higher evaporation rate. Also there is a rather strong dependence of the surface tension coefficient on the droplet surface temperature, which is translated into more rapid decrease of the droplet diameter due to enhanced evaporation and break-up. Since the ETC model predicts more rapid initial increase in the droplet surface temperature compared with the Spalding model, it is expected that the break-up process, as predicted by the ETC model, will result in a wider range of droplet radii. As a consequence the evaporation of droplets, as predicted

by the ETC model, is expected to be more rapid when compared with the prediction of the Spalding model. This is consistent with the results in Chapter 6.

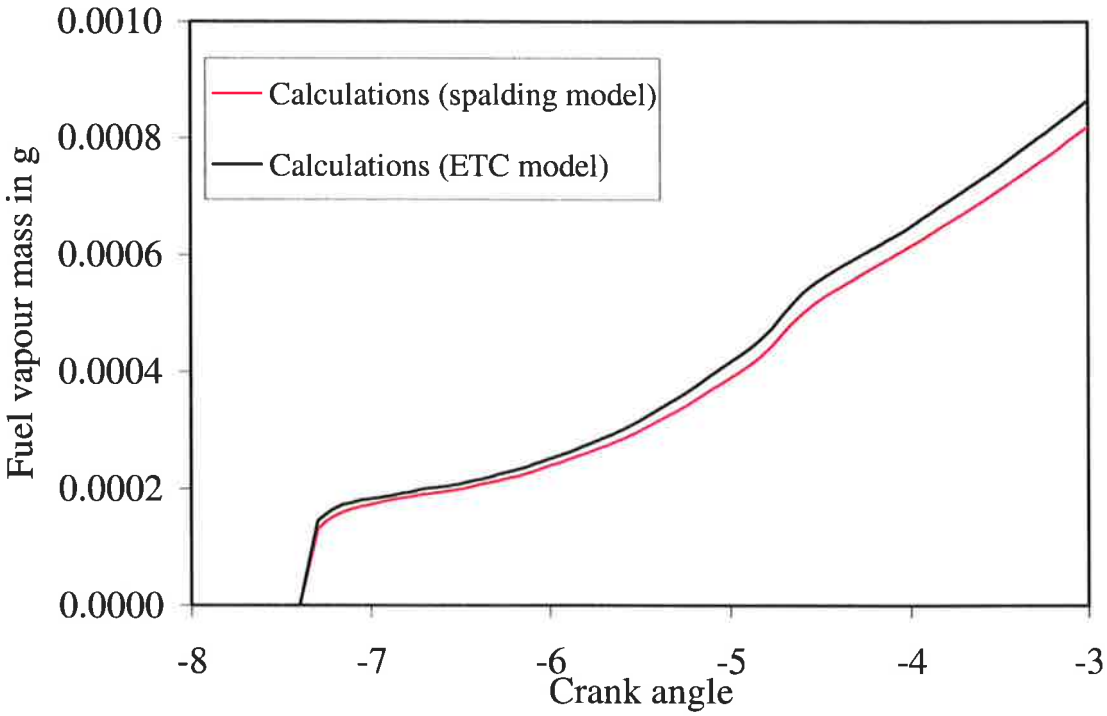

Fig. 7.3 The values of fuel vapour mass versus crank angle for diesel fuel calculated by KIVA2 CFD code without combustion based on the Spalding and the ETC models.

In Figure (7.4) the plots of SMD versus crank angle are presented based on the ETC model and the Spalding model. It can be noticed that the droplet size distribution in terms of SMD as predicted by the ETC model, is marginally lower than that predicted by the original Spalding model. This can be related to the higher predicted evaporation rate obtained by the ETC model compared with that predicted by the Spalding model as explained in Figure (7.3). Some oscillation of the results as seen in Figure (7.4) can be related to the coalescence process and continuing fuel injection, from 7.4 CA BTDC to 0.4 CA BTDC. The average SMD drops to about 8 μm almost immediately after the start of injection at 7.4 CA BTDC, staying at approximately this value until 3 CA BTDC.

The liquid spray tip penetration versus crank angle based on the ETC model and the Spalding model is presented in Figure (7.5). Experimental data, obtained from an in-cylinder high speed cinematography technique (Beatrice et al, 1995) were used for comparison with the numerical results.

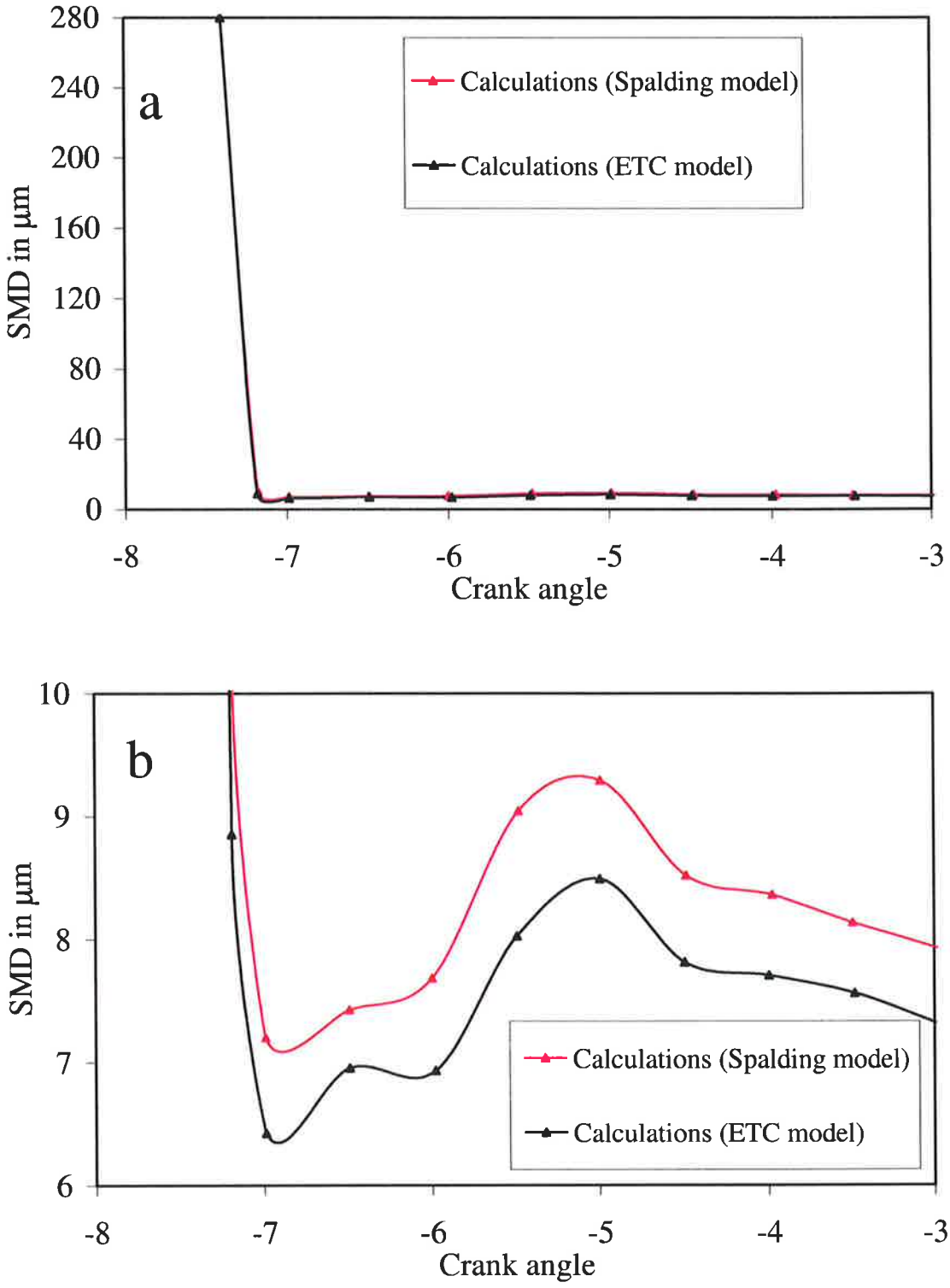

Fig. 7.4 The values of Sauter mean diameter (SMD) versus crank angle for diesel fuel calculated by KIVA2 CFD code without combustion based on the Spalding and the ETC models. The initial part of Figure (a) is magnified in Figure (b) for SMD upto 10 µm.

The calculations of the liquid tip penetration stopped at 4 CA BTDC to avoid impingement on the piston surface. It is observed that the penetration predicted by the ETC model was slightly lower than that predicted by the Spalding model and a better fits with the experimental results. This can be related to the fact that application of a temperature gradient inside droplets increases the predicted evaporation rate (see Figure (7.3)) and as a result droplet diameters are reduced (see Figure (7.4)). The latter leads to a reduction of the droplet momentum and finally the liquid spray tip penetration is reduced.

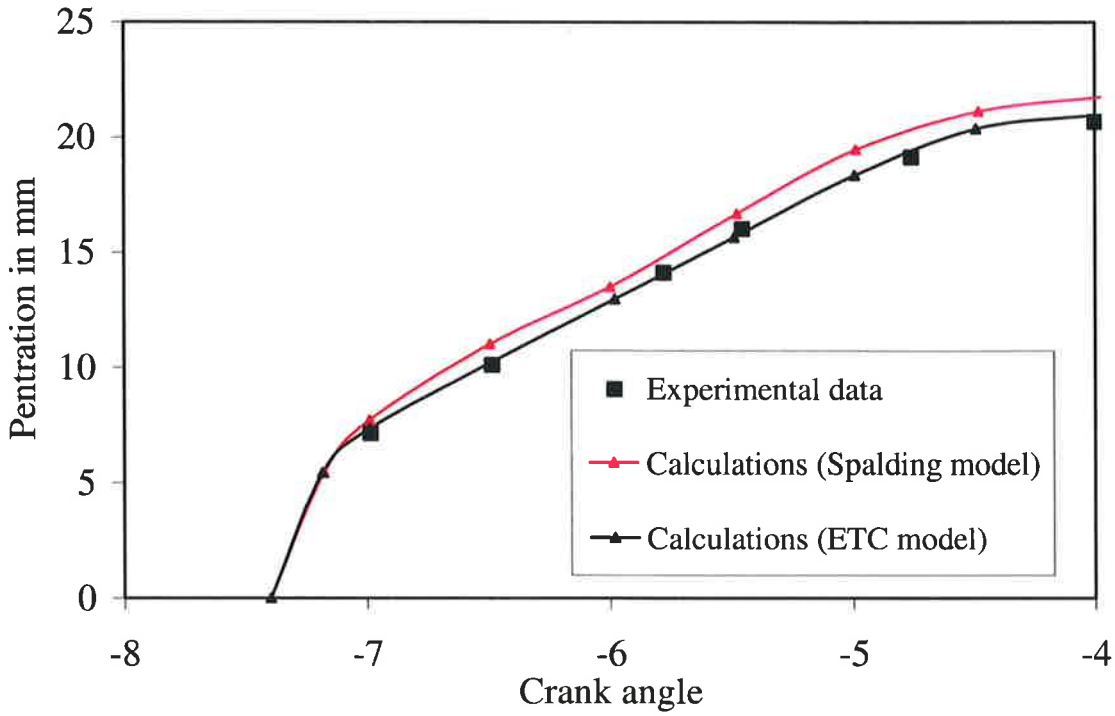

Fig. 7.5 The values of the liquid spray tip penetration versus crank angle for diesel fuel as measured by Beatrice et al (1995) and the results of calculations obtained by KIVA2 CFD code without combustion based on the Spalding and the ETC models.

Figure (7.6) shows the fuel distribution in the combustion chamber using the ETC model and the Spalding model. It confirms the tendency of the ETC model to predict more fuel vapour.

From the above investigation it is observed that the influence of the temperature gradient inside the fuel droplets on the break-up process is translated into an increase in the fuel evaporation rate and a decrease of the droplet SMD compared with the case when the gradient was neglected. As a consequence the liquid tip penetration is reduced for the case applying the temperature gradient model.

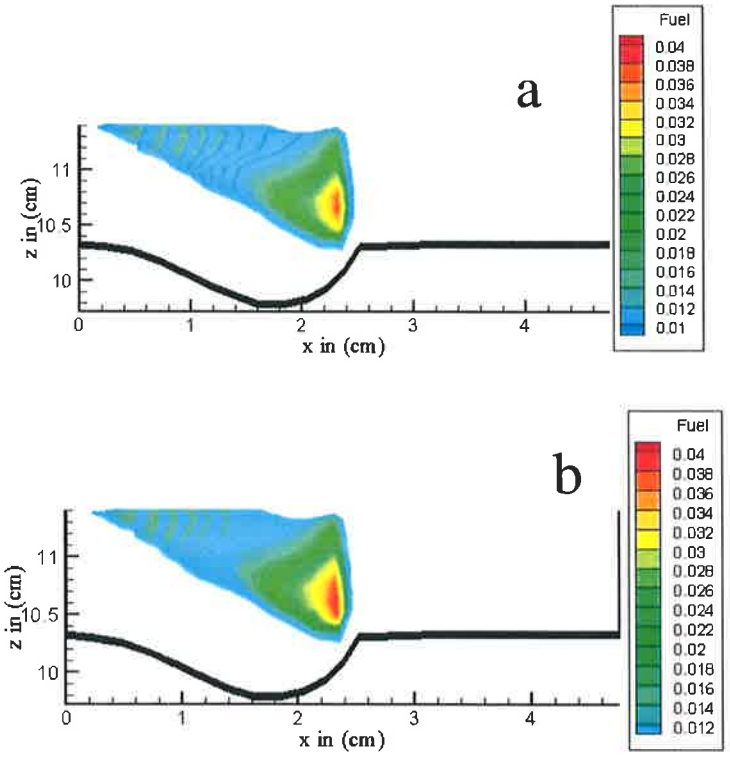

Fig. 7.6 Fuel vapour distribution for the Spalding model (a) and the ETC model (b) for diesel fuel without combustion. Meridional section (plane j = 4).

7.4.2 The effects of the temperature gradient inside droplets on combustion performance and exhaust emissions

To analyse the influence of the temperature gradient inside droplets on combustion process and exhaust emissions, a further number of numerical test cases were validated against experimental data obtained from a single cylinder DI (Direct Injection) diesel engine. The characteristics of this engine are reported in Table (7.2) (Belardini et al, 1996; Bertoli and Migliaccio, 1999).

The engine was equipped with cylinder and line pressure transducers as well as a Hall current needle lift transducer. The injection system comprised a Bosch P-type in-line pump and a four holes injector, with a cone angle between the sprays of 160°. The injection pump permitted variation of the injection timing during the engine runs. With a proper choice of plunger diameter and injection pipe bore to length ratio, a very stable operation at low-test speed allowed control of the cyclic variation of the injection with errors below 1%. The electronic control system of the valve was able to open the needle

for about 5-7 CA degrees at 1250 rpm engine speed for each engine cycle (Bertoli and Migliaccio, 1999).

Compression ratio	18
Bore	100 mm
Stroke	95 mm
Connecting rod length	178 mm
Combustion chamber	Toroidal
Speed	1250 rpm
Injector	4 holes $D_n = 0.28$ mm
Angle between two sprays	160°
Injection velocity	140 m/s
Fuel injected mass	0.02 g/cycle
Injection start	3.6 CA BTDC
Injection duration	7 CA
Fuel	Tetradecane
Computational Mesh	20×20×21

Table 7.2 The engine characteristics for the case with combustion.

In Figure (7.7) the computed in-cylinder pressures based on the ETC and the Spalding models are presented. Experimental data, obtained by Beatrice et al (1995) was used as a reference for the numerical data. It can be noted that, in the case of the ETC model, the higher quantity of fuel vapour in the combustion chamber resulted in a higher heat release rate and hence higher pressure. It is clear that the results obtained by using the ETC model fit the experimental results better than those obtained by using the Spalding model. The higher fuel vapour quantity predicted by the ETC model as compared to the Spalding model, is related to the enhancement of the break-up process, compared with the prediction of the Spalding model.

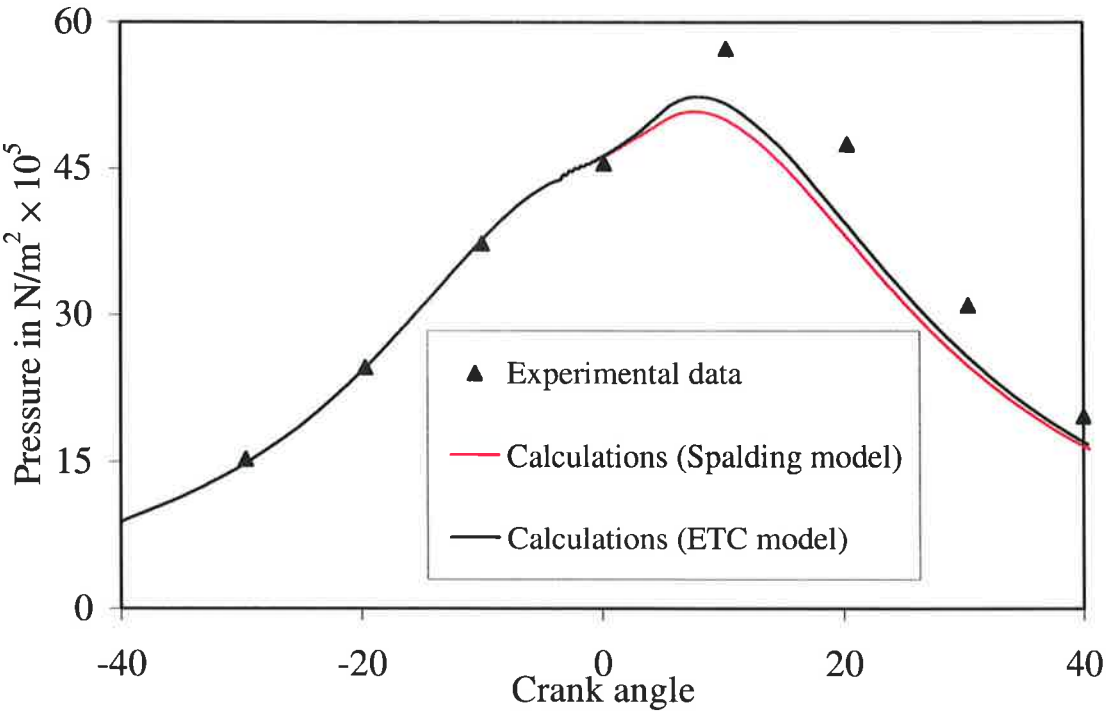

Fig. 7.7 Plots of the in-cylinder pressure versus crank angle for tetradecane fuel as measured by Belardini et al (1996) and the calculations obtained by KIVA2 CFD code based on the Spalding and the ETC models.

It is important to analyse the influence of the temperature gradient inside droplets on the chemical composition of in-cylinder mixture. Figures (7.8 - 7.12) show the results of calculation of: fuel vapour, O_2, CO_2, CO and NO masses versus crank angle based on the ETC model and the Spalding model. Figure (7.8) confirms that taking into account the temperature gradient inside droplets predicts higher evaporation rate. Also it can be noticed from Figure (7.8) that the reduction of the fuel vapour mass due to combustion as predicted by the ETC model is higher than that predicted by the Spalding model. This can explain the higher pressure peak values for the ETC model in Figure (7.7). Figure (7.9) shows the higher consumption of oxygen as predicted by the ETC model compared with that predicted by the Spalding model. The oxygen mass predicted by the ETC model is 3.3% less than that predicted by the Spalding model at 40 CA ATDC. This can be related to high combustion rate predicted by the ETC model. The latter can be related to two factors: firstly, the predicted high evaporation rate by the ETC model (see Figure (7.8)); secondly, the increase in the droplets surface temperature. As a result, the convectional heat transfer from the surrounding hot gas to the droplets is reduced. The latter leads to an increase in the gas temperature when using the ETC model. The combustion rate increases with increasing gas temperature (Heywood, 1988). As a consequence of the higher combustion rate for the ETC model, Figure (7-10) shows that

the predicted formation of CO_2 by using the ETC model is higher than that obtained by the Spalding model. This increase reaches 4.7% at 40 CA ATDC.

Figures (7-11) and (7-12) show the effects of taking into account the temperature gradient inside the fuel droplets on the predicted formation of CO and NO. From these figures, the amount of CO and NO predicted by the ETC model are 64.8 % and 29 % respectively higher than those predicted by the Spalding model at 40 CA ATDC. Again this is a consequence of modelling the temperature gradient inside droplets. This effect is transferred to the formation process of CO, which is mainly formed during the dissociation processes. The dissociation processes are sensitive to the gas temperature (Heywood, 1988). Also NO formation increases with increasing gas temperature (Heywood, 1988).

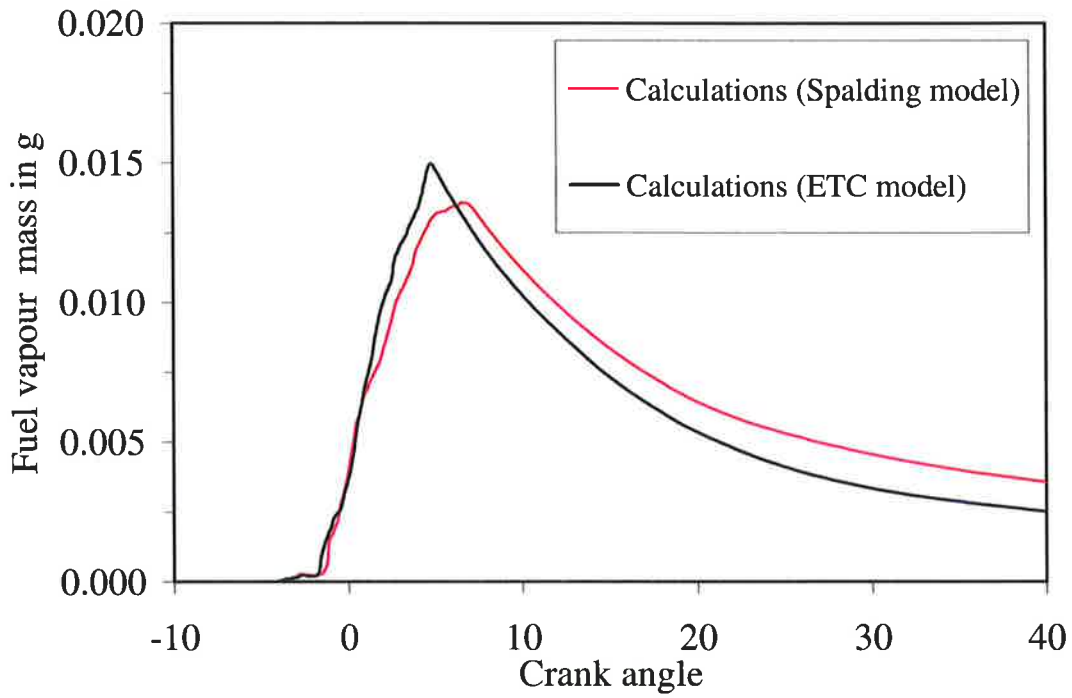

Fig. 7.8 The values of fuel vapour mass versus crank angle for tetradecane fuel calculated by KIVA2 CFD code based on the Spalding and the ETC models (both with combustion).

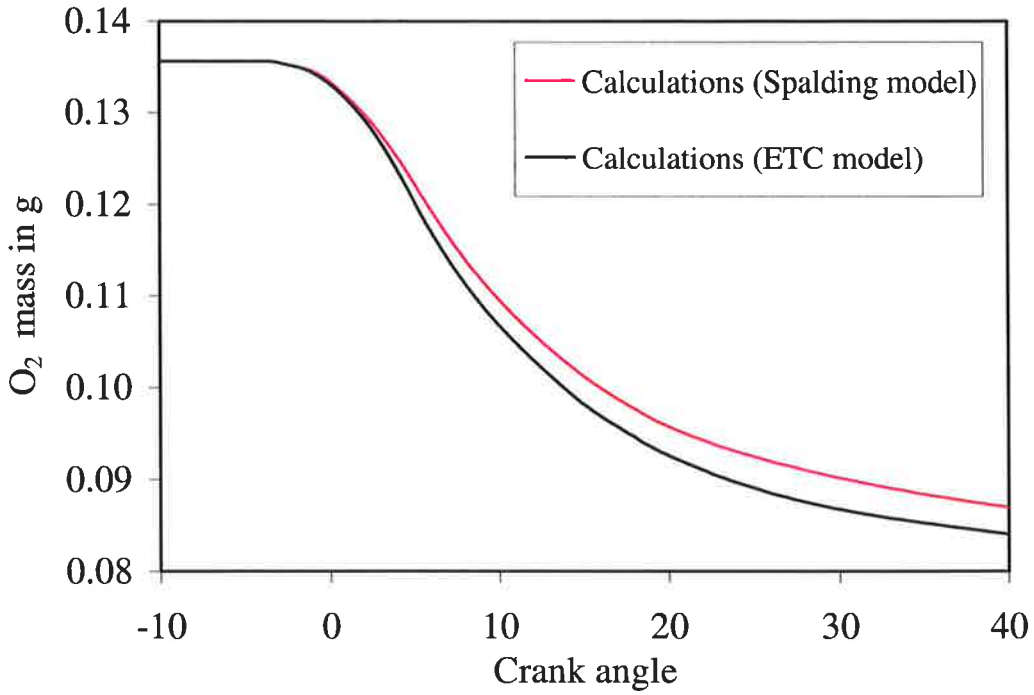

Fig. 7.9 The values of O_2 mass versus crank angle for tetradecane fuel calculated by KIVA2 CFD code based on the Spalding and the ETC models (both with combustion).

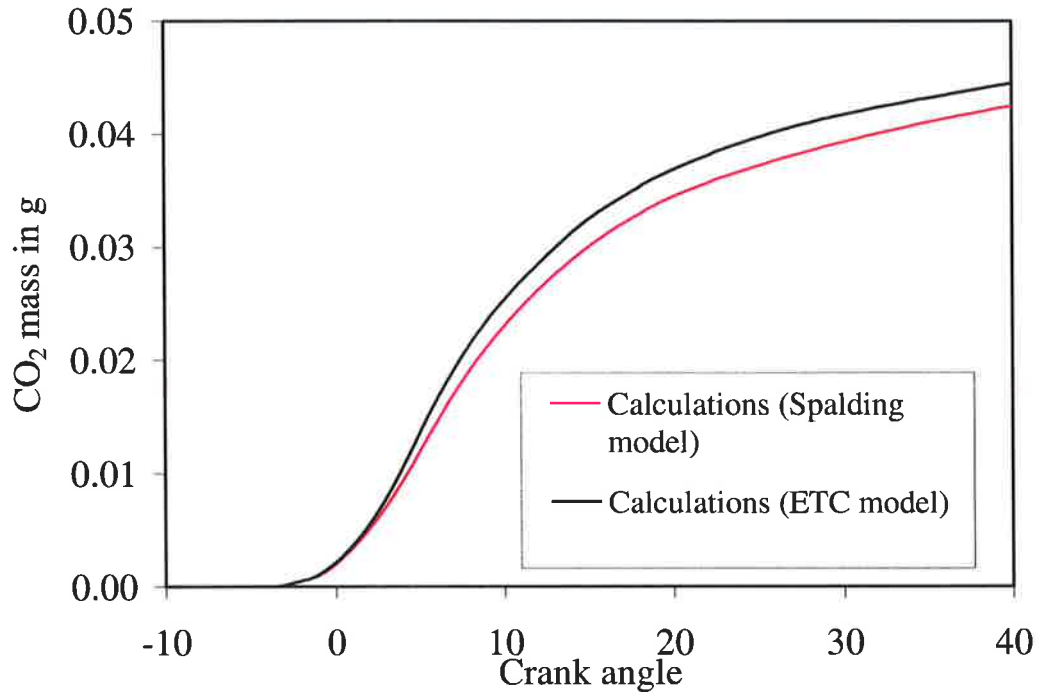

Fig. 7.10 The values of CO_2 mass versus crank angle for tetradecane fuel calculated by KIVA2 CFD code based on the Spalding and the ETC models (both with combustion).

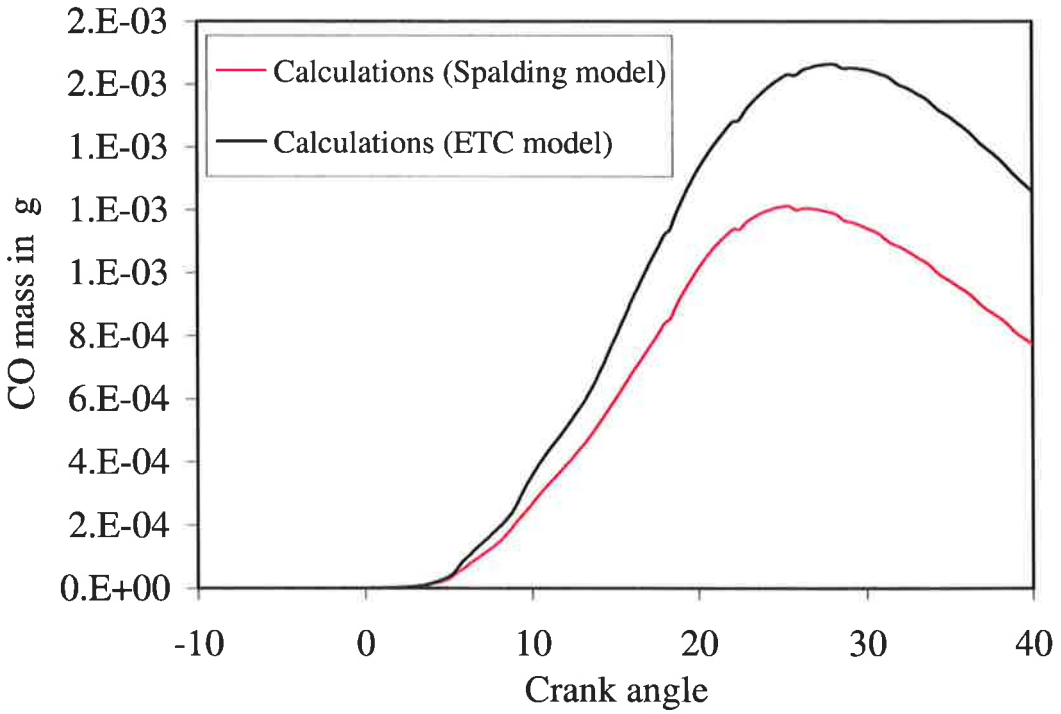

Fig. 7.11 The values of CO mass versus crank angle for tetradecane fuel calculated by KIVA2 CFD code based on the Spalding and the ETC models (both with combustion).

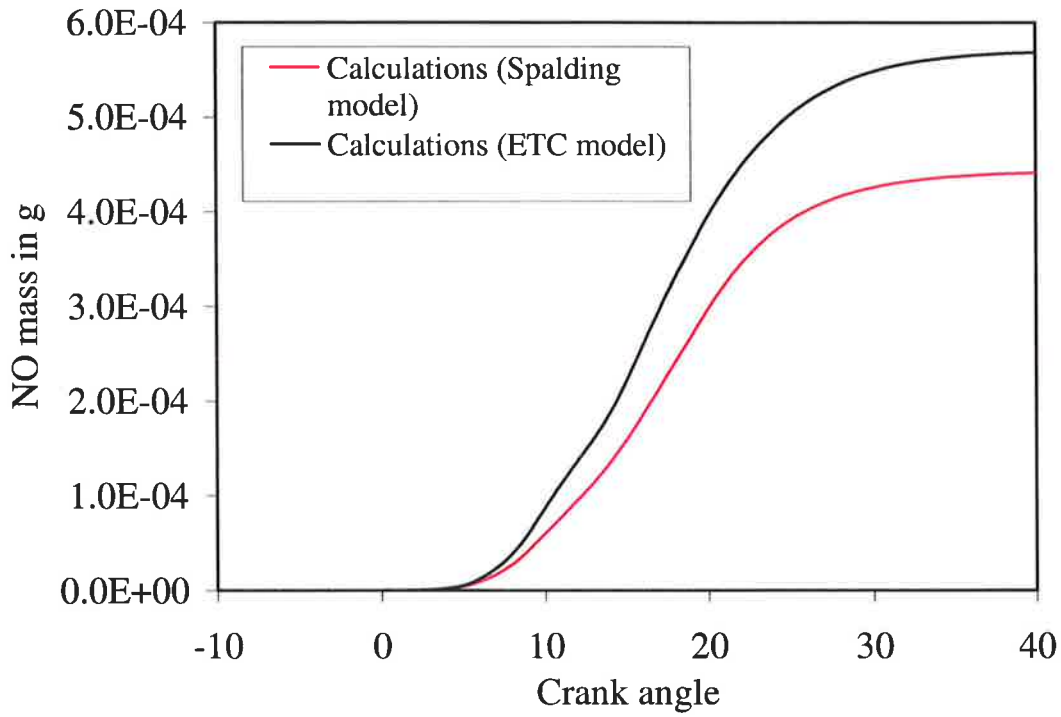

Fig. 7.12 The values of NO mass versus crank angle for tetradecane fuel calculated by KIVA2 CFD code based on the Spalding and the ETC models (both with combustion).

Figure (7-13) shows the temperature distribution at TDC inside the combustion chamber as predicted by both models. It can be noticed that the location of the maximum temperature of 2200 K, as predicted by the ETC model, covers a wider area than that predicted by the Spalding model. This can be related to the higher combustion rate predicted by the ETC model.

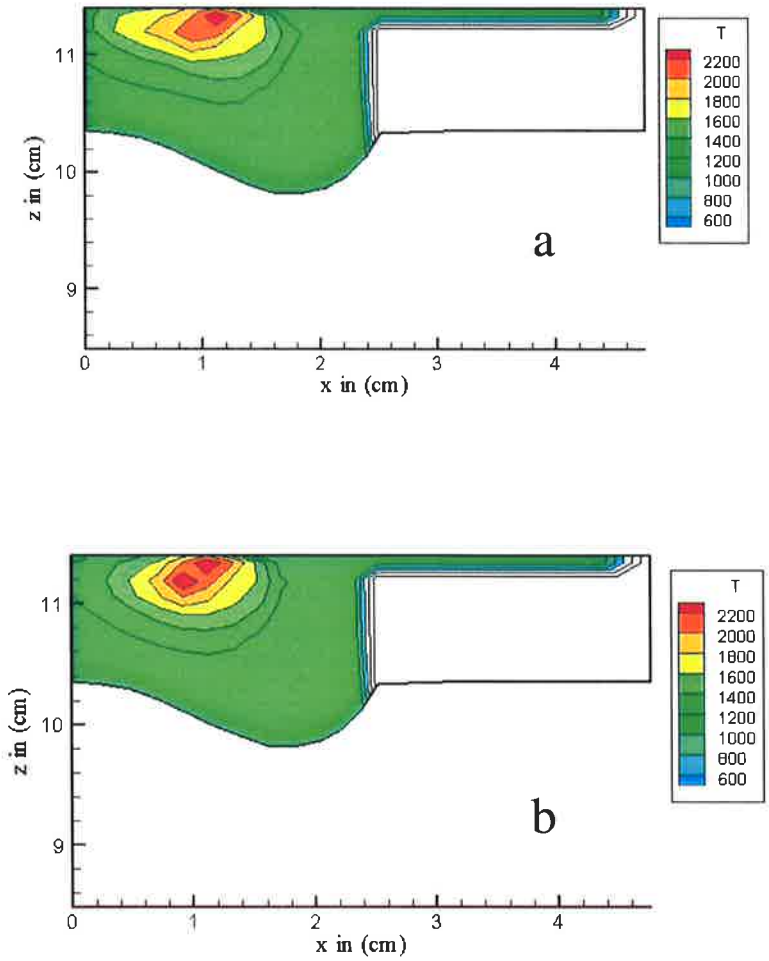

Fig. 7.13 Temperature distribution at TDC inside the combustion chamber for the Spalding model (a) and the ETC model (b) for tetradecane fuel with combustion. Meridional section (plane $j = 4$).

From the above investigation it can be observed that taking into account temperature gradient inside droplets has a significant effect on the prediction of the combustion species.

7.5 Conclusions of Chapter 7

A ETC model which takes into account the temperature gradient inside droplets, based on the analytical solution of the heat conduction equation for constant heat transfer coefficient, has been implemented into the KIVA2 CFD code. The influence of the temperature gradient inside droplets can lead to an increase in the fuel evaporation rate and consequently a decrease of the SMD. This is attributed to the fact that the effect of temperature gradient inside droplets leads to a substantial increase in the droplet surface temperature at the initial stages of its heating. This increase leads to the decrease of droplet surface tension and the threshold radii of the unstable droplets. This influence of temperature gradient inside droplets can lead to increased evaporation rate, and hence the amount of the fuel vapour in the combustion chamber. It can also lead to an increase in the formation of CO_2, CO and NO, and the consumption of O_2. This is attributed to the fact that increasing the droplet surface temperature leads to the decrease of convection heat transfer to the droplets, which in turn increases the gas temperature. The latter increases the combustion, the dissociation rates and the rate of formation of NO.

8. CONCLUSIONS

1) Results of the measurements of the index of absorption of four types of diesel fuel in the range of wavelengths 0.2 μm – 6 μm are presented.
2) The applicability of the approximation of the average absorption coefficient of droplets by the function aR_d^b, where R_d is the droplet radius, and a and b are polynomial functions of external temperature, is investigated for four types of diesel fuel in the range of external temperature and droplet radii 500 K - 3000 K and 2 μm – 200 μm, respectively. The accuracy of this approximation is shown to be reasonably good for droplet radii in the range 2-50 μm, but can be worse for droplet radii in the range 5-200 μm.
3) In agreement with the previously reported results, it is shown that the effect of thermal radiation on heating and evaporation of semi-transparent diesel fuel droplets is considerably smaller when compared with the case when droplets are approximated as black opaque spheres. The effect of thermal radiation increases with increasing droplet radii and external temperature and decreases with increasing the gas temperature in the vicinity of droplet.
4) New analytical solutions of the heat conduction equation inside a spherical droplet have been suggested and investigated in the limit of slow evaporation. The droplet has been assumed to be heated by convection and radiation from the surrounding hot gas. Three approximations for the convection heat transfer coefficient have been considered. Firstly, this coefficient has been assumed constant and an explicit formula for the time dependent distribution of temperature inside droplets has been derived and investigated. Secondly, the general case of time dependent convection heat transfer coefficient has been considered. In this case the solution of the original differential equation has been reduced to the solution of an integral equation. A numerical scheme for the solution of this equation has been suggested and tested. Thirdly, in the case of almost constant convection heat transfer coefficient the problem has been solved using the perturbation theory. A set of solutions corresponding to ascending approximations have been obtained and tested.
5) The solution based on the assumption of constant convective heat transfer coefficient is shown to be the most efficient for implementation into numerical codes when compared with the solutions based on arbitrary or almost constant h. Initially, this solution is applied to the first time step, using the initial distribution

of temperature inside the droplet. The results of the analytical solution over this time step are used as the initial condition for second time step etc.

6) The algorithm based on the analytical solution for constant h has been shown to be more effective (from the points of view of accuracy and CPU time requirement) than the approach based on the direct numerical solution of the heat conduction equation inside the droplet, and more accurate than the solution based on the parabolic temperature profile model.
7) Relatively small contribution of thermal radiation to droplet heating and evaporation allowed the use of a simplified model. This model takes into account droplet semi-transparency, but does not consider the spatial variations of radiation absorption inside droplets.
8) A zero dimensional code considering the temperature gradient inside droplets, the coupling between liquid and gas phases and describing the autoignition process based on the autoignition Shell model was developed. This code was used to study the effects of temperature gradient inside fuel droplets on droplet evaporation, break-up and the ignition of fuel vapour / air mixture. The predictions of the code were validated against available experimental data.
9) In the absence of break-up, the influence of temperature gradient on droplet evaporation in realistic diesel engine conditions is generally small (1 – 3%). In the presence of the break-up process, however, the temperature gradient inside droplets can lead to a decrease in the evaporation time by several times at the same conditions. Even in the absence of break-up the effect of temperature gradient inside droplets leads to a noticeable (up to about 20 %) decrease of the total ignition delay time (comprising the physical and chemical ignition delays). In the presence of break-up this effect is enhanced substantially, leading to more than halving of the total ignition delay.
10) The ETC model which considers temperature gradient inside droplets based on the analytical solution of the heat conduction equation for constant heat transfer coefficient has been implemented into KIVA2 CFD code. The results predicted by this code have been compared with the observed liquid tip penetration and in-cylinder pressure. The results predicted by the ETC model have been shown to fit the experimental data better than the Spalding model which ignores temperature gradient inside droplets. Preliminary results of modelling of combustion of diesel fuel spray, using the ETC model, but ignoring the effects of radiation, have been

reported. It is recommended that the effects of temperature gradient inside droplets are taken into account in computational fluid dynamics (CFD) codes used for modelling of fluid dynamics, heat transfer and combustion processes in diesel engines.

Recommendations for further work

The solution of the heat conduction equation inside droplets is obtained based on the assumption that the changes in droplet surface area are negligibly small. This assumption is justified when the time interval is small, while the latent heat of evaporation is large. It is suggested that the solution of this equation for the general case, with the moving droplet boundary, when the changes in droplet surface area are not neglected need to be developed. Further work in this direction would be beneficial.

KIVA2 CFD code does not have the Shell autoignition model to predict the ignition delay times. Also it does not have a proper mesh generator to create a realistic mesh for diesel engines environments including ports for 2-stroke engines or valves for 4-stroke engines. It is suggested that implementation of the autoignition Shell model into KIVA 3V REL2 will lead to a more accurate investigation of the effects of temperature gradient inside droplets on ignition delay time in realistic diesel engine conditions.

The effects of temperature gradient inside droplets on realistic diesel engine conditions were studied based on TAB break-up model, which is originally implemented into KIVA2 CFD code. It is suggested that implementing bag and stripping break-up model into KIVA CFD code and comparing the results obtained based on it with the results obtained based on TAB break-up model will lead to deeper understanding of the effect of temperature gradient inside droplet on the spray and combustion processes in realistic diesel engine conditions.

The thermal radiation effect was not taken in KIVA2 CFD code. It is suggested that implementing P-1 model into KIVA CFD code will allow us to investigate the effects of thermal radiation.

It is suggested that the additional work on simulation of exhaust emissions will lead to a better understanding of the effect of temperature gradient inside droplets and thermal radiation effects on the emissions of diesel engine.

APPENDIX 1. ESTIMATE OF $G(t, r)$ AT $t \to 0$

Series (4.3.2.6) converges absolutely and uniformly to the continuous function for $(t, r) \in [\delta, \infty] \times [0,1]$ for any small $\delta > 0$ since:

$$\exp[-K\lambda_n^2 t] < \exp[-Kn^2 t] \le \exp[-Kn^2 \delta] \tag{A1.1}$$

(recall that $\lambda_n^2 > n^2$ for $n^2 > 1$ according to inequalities (4.3.1.20). Now we prove the estimate (4.3.2.7) $t > 0$. Inequality (A1.1) allows us to write:

$$|G(t,r)| \le c_0 K\left\{1 + \sum_{n=2}^{\infty} \exp[-Kn^2 t]\right\} \equiv \tilde{G}(t) \tag{A1.2}$$

where c_0 is a constant for which the condition $\|v_n\|^2 \le c_0$ is satisfied. For example, if $h_0 \ge 0$ we can take $c_0 = 2$ since $\|v_n\|^2 \ge 1/2$.

The sum $\sum_{n=2}^{\infty} \exp[-Kn^2 t]$ can be considered as a sum of areas of polygons of unit width placed under the curve $\exp[-Ky^2 t]$. This sum is less than the area under this curve. Hence,

$$\sum_{n=2}^{\infty} -[Kn^2 t] < \int_1^{\infty} \exp[-Ky^2 t]dy < \int_0^{\infty} \exp[-Ky^2 t]dy = \frac{1}{\sqrt{Kt}} \int_0^{\infty} \exp[-z^2]dz$$

$$= \frac{\sqrt{\pi}}{2\sqrt{Kt}} \tag{A1.3}$$

Having substituted (A1.3) into (A1.2) we obtain:

$$|G(t,r)| \le \tilde{G}(t) < c_0 K\left[1 + \frac{\sqrt{\pi}}{2\sqrt{Kt}}\right] < \frac{\tilde{c}}{\sqrt{t}}, \qquad t \in [0, t_0] \tag{A1.4}$$

for any fixed $t_0 > 0$. The new constant $\tilde{c}$ depends on t_0. Inequality (A1.4) is equivalent to Inequality (4.3.2.7). It holds uniformly for $r \in [0,1]$.

APPENDIX 2. NUMERICAL SOLUTION OF EQUATION (4.3.2.9)

In what follows the numerical solution suggested in Section (4.3.2) will be described. Let $\psi(t) \equiv u(1,t)$ and rewrite Equation (4.3.2.9) as:

$$\psi(t) = U(1,t) - \int_0^t [M(\tau) - h_1(\tau)\psi(\tau)]G(t-\tau,1)d\tau \qquad \text{(A2.1)}$$

We look for the solution of Equation (A2.1) for $t \in [0, t^*]$, where t^* is a constant. Let $\Delta t = t^*/N$ and $t_n = n\Delta t$, where N is the total number of time step, $n = 0, 1 \ldots N$ is the number of the current time step. Note that $t_0 = 0$ and $t_N = t^*$. Discretisation of Equation (A2.1) gives:

$$\psi(t_n) = U(1,t_n) - \sum_{j=1}^{n} \int_{t_{j-1}}^{t_j} [M(\tau) - h_1(\tau)\psi(\tau)]G(t_n - \tau,1)d\tau, \qquad \text{(A2.2)}$$

where $n = 1,\ldots\ldots N$. Note that $\psi(\tau_0) = \psi(0) = U(1,0) = \tilde{T}_0(1)$ is a known constant.

The first (n-1) integrals in this sum can be approximated as:

$$\begin{aligned} &\int_{t_{j-1}}^{t_j} [M(\tau) - h_1(\tau)\psi(\tau)]G(t_n - \tau)d\tau \\ &\approx \{M(\tau_j) - h_1(\tau_j)[\psi(t_j) + \psi(t_{j-1})]/2\}G(t_n - \tau_j,1)\Delta t, \end{aligned} \qquad \text{(A2.3)}$$

where $j = 1, 2, \ldots\ldots, n$-1, $\tau_j = t_j - \Delta t/2$. Approximation (A2.3) is valid since all functions in the integrand are continuous, and we look for the solution in the class of continuous functions. The known functions are taken at $\tau = \tau_j$ (middle of the range $[t_{j-1}, t_j]$, while the unknown functions are taken as the average of the values at the end points t_{j-1} and t_j.

The last term in the sum in Equation (A2.2) requires special investigation since the kernel $G(t_n - \tau, 1)$ in the integrand becomes singular when $\tau \to t_n - 0$ (see estimate (A1.4)). All other functions in this integrand, including the unknown function $u(t)$ are assumed continuous. Hence, we can write:

$$\int_{t_{n-1}}^{t_n} [M(\tau) - h_1(\tau)\psi(\tau)]G(t_n - \tau,1)d\tau \approx \left\{ M(\tau_n) - h_1(\tau_n)\frac{\psi(t_n) + \psi(t_{n-1})}{2} \right\} \int_{t_{n-1}}^{t_n} G(t_n - \tau,1)d\tau. \qquad \text{(A2.4)}$$

Let us consider an auxiliary integral: $I(\bar{t}) = \int_{t_{n-1}}^{t_n} G(t_n - \tau,1)d\tau$, where $\bar{t} \in [t_{n-1}, t_n]$. In the range $[t_{n-1}, \bar{t}]$ series (4.3.2.10) converges uniformly and absolutely as proven in

Appendix 1. Also, all terms of this series are continuous. Hence the order of summation and integration can be changed and using formula (4.3.2.10), we can write:

$$I(\bar{t}) = -2K\sum_{m=1}^{\infty}\frac{\lambda_m^2}{h_0^2+h_0+\lambda_m^2}\int_{t_{n-1}}^{\bar{t}}\exp[-K\lambda_m^2(t_n-\tau)]d\tau$$

$$= -\sum_{m=1}^{\infty}\frac{2}{h_0^2+h_0+\lambda_m^2}\{\exp[-K\lambda_m^2(t_n-\bar{t})]-\exp[-K\lambda_m^2\Delta t]\}. \qquad \text{(A2.5)}$$

The denominator in series (A2.5) is always positive since $\|\upsilon_n\|^2 > 0$.

Remembering estimate (4.3.1.20), the series in (A2.5) converges absolutely and uniformly for $\bar{t} \in [t_{n-1}, t_n]$. Since all terms in series (A2.5) are continuous, the series is the continuous function as well. This allows us to consider the limit $\bar{t} \to t_n - 0$ in both formula (A2.5) to obtain

$$\int_{t_{n-1}}^{t_n} G(t_n-\tau,1)d\tau = \lim_{\bar{t}\to t_n-0} I(\bar{t}) = -\sum_{m=1}^{\infty}\frac{2}{h_0^2+h_0+\lambda_m^2}\left\{\lim_{\bar{t}\to t_n-0}\exp[-K\lambda_m^2(t_n-\bar{t})]-\exp[-K\lambda_m^2\Delta t]\right\}$$

$$= -2\sum_{m=1}^{\infty}\frac{1}{h_0^2+h_0+\lambda_m^2}\left(1-\exp[-K\lambda_m^2\Delta t]\right) \equiv g. \qquad \text{(A2.6)}$$

If $h_0 = 0$ then $\lambda_m = \pi(m-1/2)$. The combination of formulae (A2.3), (A2.4) and (A2.6) allows us to present Equation (A2.2) in the following form:

$$\psi(t_n) = U(1,t_n) - \{M(\tau_n) - h_1(\tau)[\psi(t_n)+\psi(t_{n-1})]/2\}g$$
$$-\sum_{j=1}^{n-1}\{M(\tau_j) - h_1(\tau_j)[\psi(t_j)+\psi(t_{j-1})]/2\}G(t_n-\tau_j,1)\Delta t, \qquad \text{(A2.7)}$$

where $n = 1,2,\ldots, N$ and g is given by series (A2.6).

Equation (A2.7) can be rearranged to the form particularly convenient for numerical analysis:

$$\psi(t_n) = \frac{1}{1-0.5h_1(\tau_n)g}\{U(1,t_n) - \left[M(\tau_n) - \frac{h_1(\tau_n)\psi(t_{n-1})}{2}\right]g$$
$$-\sum_{j=1}^{n-1}\{M(\tau_j) - h_1(\tau_j)[\psi(t_j)+\psi(t_{j-1})]/2\}G(t_n-\tau_j,1)\Delta t\} \qquad \text{(A2.8)}$$

For $n = 1$ the sum in formula (A2.8) is equal to zero and $\psi(t_0)$ is a known constant (see above). This allows us to calculate $\psi(t_1)$ explicitly from formula (A2.8). Once $\psi(t_1)$ has been calculated we can use formula (A2.8) for calculation of $\psi(t_2)$ etc. At the nth step, formula (A2.8) is used for calculation of $\psi(t_n)$ using the values of $\psi(t_0)$, $\psi(t_1)$, ..., $\psi(t_{n-1})$ calculated at the previous steps. At this step all terms in the sum $\sum_{j=1}^{n-1}$ are

already known. Once we have obtained the solution of Equation (4.3.2.9) we can find the value of $u(r,t^*)$ from a discretised form of Equation (4.3.2.5):

$$u(r,t^*) = U(r,t^*) - \sum_{j=1}^{N} \int_{t_{j-1}}^{t_j} \mu_{g0}(\tau) G(t-\tau,r)\, d\tau$$

$$= U(r,t^*) - \sum_{j=1}^{N-1} \frac{\mu_{g0}(t_{j-1}) + \mu_{g0}(t_j)}{2} G(t^* - \tau_j, r)\, \Delta t$$

$$- \frac{\mu_{g0}(t_{N-1}) + \mu_{g0}(t_N)}{2} \int_{t_{N-1}}^{t_N} G(t_N - \tau, r)\, d\tau, \qquad \text{(A2.9)}$$

where $t^* = t_N$. From estimate (4.3.2.7) it follows that the last integral is improper and needs to be calculated separately. Remembering Equation (4.3.2.6), we can write

$$\int_{t_{N-1}}^{t_N} G(t_N - \tau, r)\, d\tau = -K \sum_{n=1}^{\infty} \frac{\sin \lambda_n}{\|v_n\|^2} \sin \lambda_n r \int_{t_{N-1}}^{t_N} \exp[-K\lambda_n^2 (t_N - \tau)]\, d\tau$$

$$= -\sum_{n=1}^{\infty} \frac{\sin \lambda_n}{\|v_n\|^2} \frac{\sin \lambda_n r}{\lambda_n^2} [1 - \exp(-K\lambda_n^2 \Delta t)]$$

$$= -2 \sum_{n=1}^{\infty} \frac{h_0^2 + \lambda_n^2}{h_0^2 + h_0 + \lambda_n^2} \frac{\sin \lambda_n \sin \lambda_n r}{\lambda_n^2} [1 - \exp(-K\lambda_n^2 \Delta t)]. \qquad \text{(A2.10)}$$

when deriving this equation we took into account the expression for $\|v_n\|^2$ introduced in Equation (4.3.1.12). This derivation is similar to the one given above (see Equation (A2.6)). Having substituted Equation (A2.9) into (A2.8) we obtain the required value of $u(r,t^*)$. Note that $\mu_{g0}(t_j) = M(t_j) - h_1(t_j) u(1,t_j)$, where $u(1, t_j)$ is the solution of Equation (A2.8).

APPENDIX 3. INVESTIGATION OF THE CONVERGENCE OF SERIES (4.3.3.1)

Let t_0 be an arbitrary fixed positive number and introduce the norm of the continuous function $F(t)$ for $t \in [0,t_0]$:

$$\|F\|_0 = \max|F(t)| \qquad 0 \le t \le t_0 \tag{A3.1}$$

Let us rewrite integral in the last equation in the system (4.3.3.5) as:

$$\nu_j(t) = \int_0^t \eta(t-\tau)\nu_{j-1}(t-\tau)G(\tau,1)d\tau, \tag{A3.2}$$

where $t \in [0,t_0]$. Hence, we can estimate the terms in series (4.3.3.1) as:

$$\begin{aligned} &|\nu_j(t)| \le \int_0^t |\eta(t-\tau)||\nu_{j-1}(t-\tau)||G(\tau,1)|d\tau \le \|\eta\|_0 \|\nu_{j-1}\|_0 \int_0^t |G(\tau,1)|\,d\tau \\ &\le \|\eta\|_0 \|\nu_{j-1}\|_0 \int_0^t \frac{\tilde{c}}{\sqrt{\tau}} d\tau = 2\tilde{c}\sqrt{t}\|\eta\|_0 \|\nu_{j-1}\|_0 \end{aligned} \tag{A3.3}$$

where $t \in [0, t_0]$. When deriving this estimate we took into account inequality (A1.4) for $r = 1$.

Inequality (A3.3) can be applied for ν_{j-1}, ν_{j-2} etc. This leads to the new estimate:

$$|\nu_j(t)| \le \left(2\tilde{c}\sqrt{t}\|\eta\|_0\right)^2 \|\nu_{j-2}\|_0 \le \ldots\ldots\ldots\ldots \le \left(2\tilde{c}\sqrt{t}\|\eta\|_0\right)^j \|\nu_0\|_0, \tag{A3.4}$$

where ν_0 is given by formula (4.3.3.3) and $t \in [0,t_0]$. Inequality (A3.4) allows us to estimate series (4.3.3.1) as:

$$\sum_{j=0}^{\infty} \varepsilon^j |\nu_j(t)| \le \sum_{j=0}^{\infty} \left(2\tilde{c}\,\varepsilon\sqrt{t}\|\eta\|_0\right)^j \|\nu_0\|_0 \le \sum_{j=0}^{\infty} \left(2\tilde{c}\,\varepsilon\sqrt{t_0}\|\eta\|_0\right)^j \|\nu_0\|_0, \tag{A3.5}$$

The series on the right hand side of (A3.5) is the geometrical progression which converges when $2\tilde{c}\,\varepsilon\sqrt{t_0}\|\eta\|_0 < 1$, i.e. when

$$\varepsilon\sqrt{t_0} < 1/(2\tilde{c}\|\eta\|_0), \tag{A3.6}$$

where the constant $\tilde{c}$ is determined by inequality (A1.4). Based on the Weirschtrass criterion about uniform convergence of functional series, series (4.3.3.1) converges absolutely and uniformly for $t \in [0,t_0]$ if estimate (A3.6) is valid. If t_0 is fixed then the criterion (A3.6) can be rewritten as:

$$\varepsilon < 1/\left(2\tilde{c}\sqrt{t_0}\|\eta\|_0\right) \tag{A3.7}$$

Note that series (4.3.3.1) converges not only for small ε but also for arbitrary fixed ε when t_0 is small enough. In this case criterion (A3.7) needs to be replaced by the criterion:

$$t_0 < \left[1/\left(2\tilde{c}\sqrt{t_0}\|\eta\|_0\right)\right]^2 \tag{A3.8}$$

Let us now estimate the remainder of series (4.3.3.1) using inequality (A3.4):

$$\left|\sum_{j=N+1}^{\infty}\varepsilon^j v_j(t)\right| \le \|v_0\|_0 \sum_{j=N+1}^{\infty}(2\tilde{c}\,\varepsilon\sqrt{t_0}\|\eta\|_0)^j = \|v_0\|_0 \frac{\left(2\tilde{c}\,\varepsilon\sqrt{t_0}\|\eta\|_0\right)^{N+1}}{1-2\tilde{c}\,\varepsilon\sqrt{t_0}\|\eta\|_0}$$

$$= O\left(\left(\varepsilon\sqrt{t_0}\right)^{N+1}\right) \tag{A3.9}$$

Hence, it follows from series (4.3.3.1) that

$$v(t) = \sum_{j=0}^{N}\varepsilon^j v_j(t) + O\left(\left(\varepsilon\sqrt{t_0}\right)^{N+1}\right) \tag{A3.10}$$

where $t \in [0, t_0]$ and estimate (A3.6) is assumed to be valid.

APPENDIX 4. NUMERICAL SOLUTION OF THE DISCRETISED HEAT CONDUCTION EQUATION

The one-dimensional unsteady heat conduction equation in Cartesian coordinates (4.2.5) can be solved numerically as follows (Versteeg and Malalasekera, 1995):

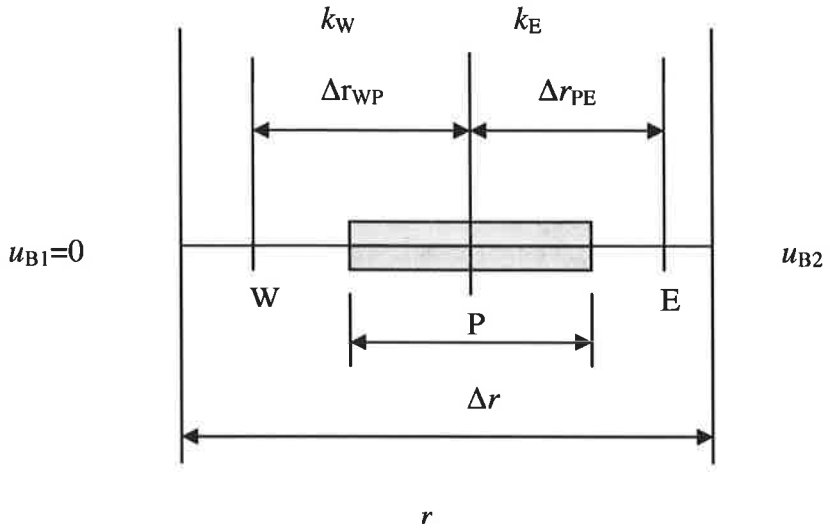

Fig. A4.1 The grid used for NSDE

Consider the one-dimensional control volume shown in Figure (4.1). Integration of Equation (4.2.5) over the control volume and over a time interval from t to $t + \Delta t$ gives:

$$\int_t^{t+\Delta t}\int_{CV}\frac{\partial u}{\partial t}dVdt = \int_t^{t+\Delta t}\int_{CV}\frac{\partial}{\partial r}\left(k\frac{\partial u}{\partial r}\right)dVdt + \int_t^{t+\Delta t}\int_{CV} S\,dVdt \qquad \text{(A4.1)}$$

This may be written as:

$$A\int_w^e\left[\int_t^{t+\Delta t}\frac{\partial u}{\partial t}dt\right]dr = \int_t^{t+\Delta t}\left[\left(kA\frac{\partial u}{\partial r}\right)_e - \left(kA\frac{\partial u}{\partial r}\right)_w\right]dt + \int_t^{t+\Delta t}\bar{S}\Delta V dt \qquad \text{(A4.2)}$$

In Equation (A4.2), A is the face area of the control volume; ΔV is its volume and $\bar{S}$ is the average source strength. The left hand side can be written as:

$$A\int_w^e\left[\int_t^{t+\Delta t}\frac{\partial u}{\partial t}dt\right]dr = (u_P - u_P^0)\Delta V \qquad \text{(A4.3)}$$

where ΔV is equal to $A\Delta r$ where Δr is the width of the control volume, superscript '0' refers to u at time t; u at the level $t + \Delta t$ are not superscripted. If the central differencing to the diffusion term on the right hand side is applied, Equation (A4.2) can be written as:

$$(u_P - u_P^0)\Delta V = \int_t^{t+\Delta t}\left[\left(k_e A\frac{u_E - u_P}{\Delta r_{PE}}\right) - \left(k_w A\frac{u_P - u_W}{\Delta r_{WP}}\right)\right]dt + \int_t^{t+\Delta t}\bar{S}\Delta V dt \qquad \text{(A4.4)}$$

To evaluate the right hand side of this equation we need to make an assumption about the moments of time when the values of u_P, u_E and u_W are taken. We introduce a weighting parameter θ between 0 and 1 and write the integral I_T of u_P with respect to time as:

$$I_T = \int_t^{t+\Delta t} u_P dt = [\theta u_P + (1-\theta)u_P^0]\Delta t \qquad \text{(A4.5)}$$

Using formula (A4.5) for u_W and u_E in Equation (A4.4), and dividing by $A\Delta t$ throughout, we have

$$\left(\frac{u_P - u_P^0}{\Delta t}\right)\Delta r = \theta\left[\frac{k_e(u_E - u_P)}{\Delta r_{PE}} - \frac{k_w(u_P - u_W)}{\Delta r_{WP}}\right] + (1-\theta)\left[\frac{k_e(u_E^0 - u_P^0)}{\Delta r_{PE}} - \frac{k_w(u_P^0 - u_W^0)}{\Delta r_{WP}}\right] + \bar{S}\Delta r \qquad \text{(A4.6)}$$

Assuming that $k_e = k_w = k$ and $\Delta r_{PE} = \Delta r_{Wp} = \Delta r$, Equation (A4.6) can be rearranged to:

$$[\frac{\Delta r}{\Delta t} + \frac{2\theta k}{\Delta r}]u_P = \frac{k}{\Delta r}[\theta u_E + (1-\theta)u_E^0] + \frac{k}{\Delta r}[\theta u_W + (1-\theta)u_W^0] + [\frac{\Delta r}{\Delta t} - 2(1-\theta)\frac{2\theta k}{\Delta r}]u_P^0 + \bar{S}\Delta r \qquad \text{(A4.7)}$$

We divided the domain into n control volumes. Equation (A4.7) is the discretised equation for the value of u_P at the centre of a control volume. The control volumes 1 and n have to be modified to take into account the boundary conditions. The discretised equation for the control volume 1 can be written as:

$$\left(\frac{u_P - u_P^0}{\Delta t}\right)\Delta r = \theta\left[\frac{k(u_E - u_P)}{\Delta r} - \frac{2k(u_P - u_{B1})}{\Delta r}\right] + (1-\theta)\left[\frac{k(u_E^0 - u_P^0)}{\Delta r} - \frac{2k(u_P^0 - u_{B1})}{\Delta r}\right] + \bar{S}\Delta r \qquad \text{(A4.8)}$$

where u_{B1}= 0. Equation (A4.8) can be re-arranged as:

$$\left[\frac{\Delta r}{\Delta t} + \frac{3\theta k}{\Delta r}\right]u_P = \frac{k}{\Delta r}[\theta u_E + (1-\theta)u_E^0] + \left[\frac{\Delta r}{\Delta t} - 3(1-\theta)\frac{2\theta k}{\Delta r}\right]u_P^0 + \bar{S}\Delta r \qquad \text{(A4.9)}$$

The discretised Equation for the control volume n can be modified as:

$$\left(\frac{u_P - u_P^0}{\Delta t}\right)\Delta r = \theta\left[\frac{2k(u_{B2} - u_P)}{\Delta r} - \frac{k(u_P - u_W)}{\Delta r}\right] + (1-\theta)\left[\frac{2k(u_{B2} - u_P^0)}{\Delta r} - \frac{k(u_P^0 - u_W^0)}{\Delta r}\right] \bar{S}\Delta r \qquad \text{(A4.10)}$$

where the value of u_{B2} can be obtained from the boundary condition in Equation (4.2.6) as:

$$u_{B2} = \frac{M(t) + \frac{2}{\Delta r} u_P}{H(t) + \frac{2}{\Delta r}} \tag{A4.11}$$

Substituting Equation (A4.11) into Equation (A4.10) we obtain:

$$\left[\frac{\Delta r}{\Delta t} + \frac{3\theta k}{\Delta r} - \frac{4k}{\Delta r^2 \left(H(t) + \frac{2}{\Delta r} \right)} \right] u_P = \frac{\theta k}{\Delta r} u_W + \frac{(1-\theta)k}{\Delta r} u_W^0 + \left(\frac{\Delta r}{\Delta t} - \frac{3(1-\theta)k}{\Delta r} \right) u_P^0 + \frac{2kM(t)}{\Delta r \left(H(t) + \frac{2}{\Delta r} \right)} + \bar{S} \Delta r \tag{A4.12}$$

The exact form of the final discretised equations depends on the value of θ. When θ is zero, we use u_P^0, u_W^0 and u_E^0 at the previous time level t on the right hand side of the Equations (A4.7), (A4.9) and (A4.12) to evaluate u_P at the new time level. The resulting algorithm is called explicit. When $0 < \theta < 1$ u at the new time level are used on both sides of the equation. The resulting algorithm is called implicit. The algorithm based on the assumption $\theta = 1$ is called fully implicit and the algorithm corresponding to $\theta = 1/2$ is called the Crank-Nicolson algorithm (Versteeg and Malalasekera, 1995). For implicit algorithm the solution of the discretization equation was obtained by Thomas algorithm or the TDMA (TriDiagonal-Matrix Algorithm) (Patankar, 1980).

APPENDIX 5. CALCULATION OF $\overline{T}$, q_n AND p_n

Let us present Equation (4.3.1.19) in the form:

$$T(r,t)=\frac{1}{r}\sum_{n'=1}^{\infty}\gamma_{n'(p)}\sin(\lambda_{n'(p)}r)\sin(\lambda_n r)+T_{eff}(t_n) \tag{A5.1}$$

where

$$\gamma_n=\frac{p_n}{K\lambda_n^2}+\exp\left[-K\lambda_n^2 t\right]\left(q_n-\frac{p_n}{K\lambda_n^2}\right)-\frac{\sin\lambda_n}{\|\upsilon_n\|^2\lambda_n^2}\mu_0(0)\exp\left[-K\lambda_n^2 t\right]-$$

$$\frac{\sin\lambda_n}{\|\upsilon_n\|^2\lambda_n^2}\int_0^t\frac{d\mu_0(\tau)}{d\tau}\exp\left[-K\lambda_n^2(t-\tau)\right]d\tau,$$

all parameters in Equation (A5.1) are taken at the previous time step t_{n-1} (indicated by the additional subscript (p).

Having substituted equation (A5.1) into Equation (5.3.2) we obtain:

$$\overline{T}(t_n)=3\sum_{n'=1}^{\infty}\gamma_{n'(p)}\int_0^1 r\sin(\lambda_{n'(p)}r)dr+3T_{eff}(t_n)\int_0^1 r^2dr$$

$$=3(1+h_0)\sum_{n'=1}^{\infty}\frac{\gamma_{n'(p)}\sin\lambda_{n'(p)}}{\lambda_{n'(p)}^2}+T_{eff}(t_n) \tag{A5.2}$$

Similarly, having substituted Equation (A5.1) into the definition of q_n we obtain:

$$q_n(t_n)=\frac{1}{\|\upsilon_n\|^2}\sum_{n'(p)}^{\infty}\gamma_{n'p}\int_0^1\sin(\lambda_{n'p}r)\sin(\lambda_{nc}r)dr+\frac{T_{eff}(t_n)}{\|\upsilon_n\|^2}\int_0^1 r\sin(\lambda_n r)dr$$

$$=\varphi_n+\frac{T_{eff}(t_n)(1+h_0)\sin\lambda_n}{\|\upsilon_n\|^2\lambda_n^2} \tag{A5.3}$$

where $\varphi_n=\begin{cases}\gamma_n & \text{when } \lambda_{n(p)}\neq\lambda_n\\ \dfrac{1}{2\|\upsilon_n\|^2}\displaystyle\sum_{n'=1}^{\infty}\gamma_{n'p}\left[\frac{\sin(\lambda_{n'(p)}-\lambda_n)}{(\lambda_{n'(p)}-\lambda_n)}-\frac{\sin(\lambda_{n'(p)}+\lambda_n)}{(\lambda_{n'(p)}+\lambda_n)}\right] & \text{when } \lambda_{n(p)}\neq\lambda_n\end{cases}$

Assuming that $\theta_R=T_{ext}$ and ignoring the contribution of $\overline{T}$, substitution of $P_1(R)$, defined by Equation (5.6.1) into the expression for p_n gives:

$$p_n=\frac{1}{\|\upsilon_n\|^2}\int_0^1 3\times10^6 a\sigma R_{d(\mu m)}^{b-1}T_{ext}^4 r\sin(\lambda_n r)dr=\frac{\beta_n}{\lambda_n^2}(1+h_0)\sin\lambda_n, \tag{A5.4}$$

where $$\beta_n=\frac{3\times10^6 a\sigma R_{d(\mu m)}^{b-1}T_{ext}^4}{\|\upsilon_n\|^2}$$

APPENDIX 6. THE SHELL AUTOIGNITION MODEL

In the Shell model the autoignition chemistry is reduced to eight-step chain branching reaction scheme incorporated into four processes (Halstead et al, 1977):

Initiation:

$$RH + O_2 \rightarrow 2R^* \qquad \text{Rate coefficient } k_q \qquad \text{(A6.1)}$$

Propagation:

$$R^* \rightarrow R^* + P \qquad \text{Rate coefficient } k_p \qquad \text{(A6.2)}$$

$$R^* \rightarrow R^* + B \qquad \text{Rate coefficient } f_1\, k_p \qquad \text{(A6.3)}$$

$$R^* \rightarrow R^* + Q \qquad \text{Rate coefficient } f_4\, k_p \qquad \text{(A6.4)}$$

$$R^* + Q \rightarrow R^* + B \qquad \text{Rate coefficient } f_2\, k_p \qquad \text{(A6.5)}$$

Branching:

$$B \rightarrow 2R^* \qquad \text{Rate coefficient } k_b \qquad \text{(A6.6)}$$

Termination:

$$R^* \rightarrow out \qquad \text{Rate coefficient } f_3\, k_p \qquad \text{(A6.7)}$$

$$2R^* \rightarrow out \qquad \text{Rate coefficient } k_t \qquad \text{(A6.8)}$$

where RH represents hydrocarbon fuel (C_nH_{2m}), R^* is the radical, B is the branching agent, Q is the intermediate agent and P is the product, consisting of H_2O, CO_2 and CO. The intermediate species can be generally related to aldehydes (RCHO) while the branching agent is related to hydroperoxide (RO_2H) at low temperatures and to hydrogen peroxide (H_2O_2) at high temperatures (Benson, 1981) The main assumption of the Shell autignition model is that the radicals R^* entering into the scheme are treated as one type of radical using the steady-state hypothesis.

The time variation of species concentrations are described by (Halstead et al, 1977):

$$\frac{d[R^*]}{dt} = 2(k_q[RH][O_2] + k_b[B] - k_t[R^*]^2) - f_3 k_p[R^*] \qquad \text{(A6.9)}$$

$$\frac{d[B]}{dt} = f_1 k_p[R^*] + f_2 k_p[Q][R^*] - k_b[B] \qquad \text{(A6.10)}$$

$$\frac{d[Q]}{dt} = f_4 k_p[R^*] - f_2 k_p[Q][R^*] \qquad \text{(A6.11)}$$

$$\frac{d[O_2]}{dt} = -pk_p[R^*] \qquad \text{(A6.12)}$$

$$[RH] = \frac{[O_2] - [O_2](t=0)}{pm} + [RH](t=0) \qquad \text{(A6.13)}$$

where $[M]$ is the molar concentration of the various species M. The parameter p is obtained from the overall product path (Schäpertöns and Lee, 1985):

$$C_{n/m}H_2 + pO_2 \rightarrow qP \tag{A6.14}$$

where

$$P = [(n/m)(\gamma CO + (1-\gamma)CO_2) + H_2O]/q$$

$$p = (n(2-\gamma)+m)/2m,$$

$$q = \frac{n}{m} + 1$$

The coefficient γ determines the burned products mixture via $[CO]/[CO_2] = \gamma/(1-\gamma)$.

The rate constants in Equations (A6.9)-(A6.13) are defined by the following expression (Halstead et al, 1977; Schäpertöns and Lee, 1985):

$$f_1 = A_{f1}\exp(-E_{f1}/RT)[O_2]^{x1}[RH]^{y1} \tag{A6.15}$$

$$f_2 = A_{f2}\exp(-E_{f2}/RT) \tag{A6.16}$$

$$f_3 = A_{f3}\exp(-E_{f3}/RT)[O_2]^{x3}[RH]^{y3} \tag{A6.17}$$

$$f_4 = A_{f4}\exp(-E_{f4}/RT)[O_2]^{x4}[RH]^{y4} \tag{A6.18}$$

$$k_i = A_i\exp(-E_i/RT) \tag{A6.19}$$

where i stands for $p1$, $p2$, $p3$, q, B and t, $k_p = \left[\frac{1}{k_{p1}[O_2]} + \frac{1}{k_{p2}} + \frac{1}{k_{p3}[RH]}\right]^{-1}$, R is the universal gas constant and A_f, E_f, x and y are the kinetic rate parameters fitted for each particular fuel.

The Shell autoignition model uses the following equation for the temperature (Halstead et al, 1977):

$$\frac{dT}{dt} = \frac{1}{C_v n_{tot}}\left(Q_K - Q_L - \frac{n_{tot}RT}{V}\frac{dV}{dt}\right) \tag{A6.20}$$

where C_v is the heat specific capacity for constant volume, n_{tot} is the total number of moles in the volume V, Q_K is the chemical heat release defined as:

$$Q_K = k_p qV[R^*] \tag{A6.21}$$

q is the exothermicity per cycle, Q_L is the heat loss through the boundary walls defined as:

$$Q_L = \phi V(T - T_w) \tag{A6.22}$$

where $\phi = hS/V$, S/V is the surface to volume ratio.

The last term on the right hand side of Equation (A6.20) accounts for the work due to the piston motion. This term, as well as the term Q_L, is accounted for by the enthalpy transport equation in CFD codes. In this case, the change in temperature must be based only on the contribution of the chemical reaction. Equation (A6.20) is simplified to (Sazhin et al, 1999):

$$\frac{dT}{dt} = \frac{1}{C_v n_{tot}} k_p q V [R^*] \tag{A6.23}$$

The development of the Shell model followed two main directions. The first one is focused on modifications of the coefficients without changing the overall structure by adjusting the kinetic rates to fit experimental data (Schäpertöns and Lee, 1985; Theobald, 1986). The second direction is focused on modifying the equations to better reflect the underlying chemistry and this leads to changes in the overall structure of the model. For example, Cox and Cole (1985) increase the number of generic reactions from 6 to 15.

Schäpertöns and Lee (1985) made the first attempt to modify the Shell model to ensure the required mass conservation by increasing the depletion of fuel and Oxygen to account for the formation of the generic species B and Q. They described the propagation path as:

$$R^* + (l+1)(C_{n/m}H_2 + pO_2) \rightarrow qP + f_1 B + f_4 Q + R^* \tag{A6.24}$$

where

$$l = (f_1 M_B + f_4 M_Q)/(M_{RH}/m + pM_{O_2}),$$

$$P = [(n/m)(\gamma CO + (1-\gamma)CO_2) + H_2O]/q$$

$$p = (n(2-\gamma)+m)/2m$$

$$q = \frac{n}{m} + 1$$

The increase (l times) of consumption of reactants accounted for the newly emerging masses of B and Q species. Radicals are converted to inert species in the termination reactions:

$$R^* \rightarrow (M_R / M_{N2})N_2 \tag{A6.25}$$

$$2R^* \rightarrow (2M_R / M_{N2})N_2 \tag{A6.26}$$

The main shortcoming of the Schäpertöns and Lee (1985) scheme is that it does not describe the increase in mass of radicals R^*. The change of their mass with time is not

compensated by respective change in mass of other species, as the reactions of the original Shell model are not balanced.

Sazhin et al (1999) has suggested a new mathematical formulation for the Shell model. This is particularly important for the implementation in CFD codes. The authors replaced the time as an independent variable by the fuel depletion, which is the difference between the initial fuel concentration and the current one. This has allowed reducing the original system of equations used in the model to only two coupled first-order ordinary differential equations for the concentration of radicals and branching agent. Then these two equations were reduced to one second-order differential equation for the concentration of radicals:

$$d_R[R^*][R^*]'' + d_R([R^*]')^2 + (-(d'_R - d_R f_B)[R^*] - d_R b_R - 2d_R c_R[R^*])[R^*]' = (d_R b'_R - b_R(d'_R - d_R f_B))[R^*] + (d_R c'_R - c_R(d'_R - d_R f_B))[R^*]^2 + d_B a'_R + d_R^2 g_B - a_R(d'_R - d_R f_B) \quad \text{(A6.27)}$$

where:

$$a_R = 2m\frac{k_q([RH]_0 - \xi)([O_2]_0 - pm\xi)}{k_p},\ b_R = -mf_3,\ c_R = -2m\frac{k_t}{k_p}$$

$$d_R = 2m\frac{k_B}{k_p},\ f_B = \frac{mk_B}{k_p[R^*]},$$

$$g_B = mA_{f1}\exp\left[-\frac{E_{f1}}{R(T_0 + \frac{mq}{C_v[N]}\xi}\right]([O_2]_0 - pm\xi)^{x1}([RH]_0 - \xi)^{y1} +$$

$$mA_{f2}\exp\left[-\frac{E_{f2}}{R(T_0 + \frac{mq}{C_v[N]}\xi}\right][Q]$$

Once the concentration of radicals is obtained, the concentration of the intermediate agent, temperature and time can be obtained from:

$$[Q] = e^{-F}\int_0^{\xi} g_Q e^F d\xi \quad \text{(A6.28)}$$

$$T = T_0 + \frac{mq}{C_v[N]}\xi \quad \text{(A6.29)}$$

$$t = t_0 + \sqrt{\frac{m\xi_1}{k_p k_q [RH]_0 [O_2]_0}} + \int_{\xi_1}^{\xi} \frac{d\xi}{\frac{k_p}{m}[R^*]}, \qquad \text{(A6.30)}$$

where $\xi = [RH]_0 - [RH], [RH]_0 = [RH](t = 0)$, $F = \int_0^{\xi} f_Q d\xi$, $T_0 = T\ (t = 0)$ and the value of ξ_1 is based on the accuracy of computations of the integral in Equation (A6.30).

This reformulation of the Shell model saves CPU time by about 40-60 % per step for a typical problem (Sazhin et al, 1999).

Sazhina et al (1999, 2000) considered the application of the Shell model to the autoignition of diesel fuel sprays, which takes place at a wide range of equivalence ratios, pressures and temperatures, in contrast to autoignition in premixed gasoline fuel. It was necessary to impose flammability limits to restrict the range of equivalence ratios for which the autoignition model is active. They suggested flammability limits in the range of equivalence ratios from 0.5 to 3.2 as a starting point and this limit increases linearly with increasing pressure. The Shell autoignition model does not predict autoignition for end of compression temperature lower than 570 K and is inhibited if the temperature increases higher than 1100 K or a very sharp temperature rise (> 10^7) K/s occurs. The authors showed that the autoignition chemical delay for diesel fuel (approximated by n-heptane and n-dodecane) is much less than the physical delay due to droplet transit time, atomization, heating, evaporation and mixing for typical droplet radii. This justifies the application of less accurate than DKM (detailed kinetic mechanism) , but more computer efficient Shell model for diesel fuel autoignition. The values of the coefficient A_{f4} in the Shell model for n-heptane were taken equal 3×10^6 and 6×10^6.

Sazhina et al (2000) followed the Schäpertöns and Lee (1985) idea that the increase in mass of R^*, B and Q originates in fuel and oxygen consumption. They suggested calculating the total change in mass of R^*, B and Q over a time step as:

$$\delta m_{RBQ} = \delta m_R + \delta m_B + \delta m_Q \qquad \text{(A6.31)}$$

where δm_R, δm_B and δm_Q are changes in mass of R^*, B and Q respectively in a given cell over a time step of integration. δm_{RBQ} is shared stoichiometrically between the reactants, $C_n H_{2m}$ and O_2, so that decrement of fuel mass is estimated as $\delta m_{RBQ}/(1+S)$ where S is the stoichiometric oxygen-fuel ratio by mass in the main propagation path:

$$1_{kg} C_n H_{2m} + S_{kg} O_2 \rightarrow (1+S)_{kg} P \qquad \text{(A6.32)}$$

In this case the O_2 consumption will increase by $\delta m_{RBQ} S/(1+S)$ and the termination reactions convert the R^* radicals into fuel and oxygen. In Sazhina et al (2000) a polydisperse spray ignition under condition close to those in the medium duty truck diesel engine is modelled using the Shell model implemented into VECTIS CFD code. Neither internal circulation nor the temperature gradient inside the droplets was taken into account and the effects of thermal radiation were neglected. The results showed that the gas temperature initially decreases due to droplet evaporation before it rapidly increases due to the development of autoignition process. The results also show that there is an initial increase in the fuel vapour mass fraction due to droplet evaporation. Then the concentration of oxygen and fuel vapour remained practically constant due to a very slow combustion process. The ignition process is accompanied by a rapid decrease of the concentration of fuel and oxygen and an increase in the concentration of the product. The ignition of the spray has started as expected at the periphery where the ignition delay for droplets is less than in its core.

In this work we used the Shell autoignition model (Sazhin et al, 1999; Sazhina et al, 1999; Sazhina et al, 2000) to predict the autoignition delay time for diesel fuel in typical conditions of Diesel engine. Both temperature gradient and circulations inside droplets were taken into account. Thermal radiation was taken into account with neglecting thermal radiation distribution inside droplets.

APPENDIX 7. PHYSICAL PROPERTIES OF FUELS

A7.1 Physical properties of tetradecane

Using data presented in Maxwell (1950), the latent heat of evaporation in J/kg was approximated as:

$$L = 4.7999679442\times10^{5} - 447.99679239T + 1.0772809826T^{2} - 8.4415064357\times10^{-3}T^{3} + 2.907585478\times10^{-5}T^{4} - 4.3509615486\times10^{-8}T^{5} + 2.1527777826\times10^{-11}T^{6}$$

when $T < T_{cr} = 693$ K (critical temperature) (Poling et al, 2000), and zero otherwise.

Using data presented in Maxwell (1950), the specific heat capacity of liquid in J/(kg K) is approximated as:

$$c_{l} = 1453.5010887\times\exp(0.001412293301 77T)$$

The specific heat capacity of vapour at constant pressure is approximated as (Poling et al, 2000):

$$c_{v} = -1.7787319 + 6.4564177T - 3.2454867\times10^{-3}T^{2} + 4.5752023\times10^{-7}T^{3} + 8.510382\times10^{-11}T^{4}$$

The saturated vapour pressure is assumed to be equal to:

$$p_{s} = 10^{5}\times10^{4.1379-1740.88/(T-105.43)} \quad \text{N/m}^{2}$$

when $T < T_{cr}$ and zero otherwise (Poling et al, 2000).

Using data presented in Maxwell (1950), the density of liquid is approximated as:

$$\rho_{l} = 915.017 - 0.366493T - 4.68132\times10^{-4}T^{2},$$

and the thermal conductivity of liquid in W/(m K) is approximated as:

$$k_{l} = 0.16243019148 + 1.1551271437\times10^{-4}T - 7.6492882118\times10^{-7}T^{2} + 5.9731934732\times10^{-10}T^{3}$$

when $T < T_{cr}$, and zero otherwise (Maxwell, 1950).

A7.2 Physical properties of n-heptane

Latent heat of evaporation in J/kg is approximated as (Chin and Lefebvre, 1985):

$$L = 317.8\times10^{3}\left(\frac{T_{cr}-T}{T_{cr}-T_{b}}\right)^{0.38},$$

where T_{cr} = 540.17 K and T_{b}= 371.4 K (Poling et al, 2000), when $T < T_{cr}$, and zero otherwise.

Using data presented in Maxwell (1950), the specific heat capacity of liquid in J/kg. K is approximated as:

$$c_l = 13058.45044066 - 126.5095282565T + 0.5279613848638T^2$$
$$- 0.0009457386295687T^3 + 6.369853422618\times10^{-7}T^4.$$

The specific heat capacity of vapour at constant pressure is approximated as (Poling et al, 2000):

$$c_v = 799.3401062 + 0.3448263942T + 0.0128554864T^2 - 1664.890863\times10^{-8}T^3$$
$$+ 644.6826474\times10^{-11}T^4.$$

The saturated vapour pressure is assumed to be equal to

$$p_s = 10^5 \times 10^{4.02677 - 1258.34/(T-53.85)} \quad \text{N/m}^2$$

when $T < T_{cr}$, and zero otherwise (Poling et al, 2000).

Using data presented in Maxwell (1950), the density of liquid is approximated as:

$$\rho_l = -941.03 + 19.96181T - 0.08612051T^2 + 1.579494\times10^{-4}T^3 - 1.089345\times10^{-7}T^4$$

when $T \leq 538$ K, and

$$\rho_l = 4.195281\times10^7 - 2.360524\times10^5 T + 442.7316T^2 - 0.2767921T^3$$

when $T > 538$ K.

Using data presented in Maxwell (1950), the thermal conductivity of liquid in W/(m. K) is approximated as:

$$k_l = 0.2584489011 - 4.5549450549\times10^{-4}T$$

when $T < T_{cr}$, and zero otherwise.

A7.3 Physical properties of n-dodecane

Latent heat of evaporation in J/kg (Borman and Johnson, 1962)

$$L = 329037.62 + 1883.02T - 10.99644T^2 + 0.021056T^3 - 1.44737\times10^{-5}T^4$$

when $T < T_{cr} = 659$ K (Poling et al, 2000) and zero otherwise

Using data presented in Maxwell (1950), the specific heat capacity of liquid in J/kg. K is approximated as:

$$c_l = 803.42 + 5.076T - 0.00221T^2 + 1.673\times10^{-6}T^3$$

The specific heat capacity of vapour at constant pressure is approximated as (Durret et al, 1987):

$$c_v = 380.63 + 4.1372T + 2.004\times10^{-4}T^2 - 1.8009\times10^{-8}T^3$$
$$+ 7.7875\times10^{-10}T^4 - 1.0152\times10^{-13}T^5$$

The saturated vapour pressure is assumed to be equal to:

$$p_s = 6894.757 \times \exp[12.12767 - 3743.84/(T - 93.022)] \ \text{N/m}^2$$

when $T < T_{cr}$, and zero otherwise (Chin and Lefebvre, 1985).

The density of liquid is approximated as (Handbook of aviation fuel properties, 1984):

$$\rho_l = 1104.98 - 1.9277T + 0.003411T^2 - 3.2851 \times 10^{-6} T^3$$

The thermal conductivity of liquid n-dodecane and liquid diesel fuel in W / (m.K) was used as a look-up table (see Table (A7.1)) (Reid et al, 1987)

The surface tension is approximated as (Durret et al, 1987):

$$\sigma_s = 0.0528\left(1 - \frac{T}{T_{cr}}\right)^{0.121}$$

A7.4 Physical properties of diesel fuel

In this section a compilation of physical properties of a 'typical' diesel fuel is given. These are expected to differ slightly from any particular diesel fuel.

Latent heat of evaporation in J/kg (Chin an Lefebvre, 1985):

$$L = 254 \times 10^3 \left(\frac{T_{cr} - T}{T_{cr} - T_b}\right)^{0.38},$$

when T_{cr}= 725.9 K and T_b = 536.4 K, when $T < T_{cr}$, and zero otherwise.

The specific heat capacity of liquid in J / (kg K) is approximated as (Durret et al, 1987):

$$c_l = 264 + 6.33T - 0.00296T^2$$

The specific heat capacity of vapour at constant pressure is approximated as equal to that of n-dodecane (Durret et al, 1987).

The saturated vapour pressure is assumed to be equal to (Chin an Lefebvre, 1985):

$$p_s = \begin{cases} 1000 \times \exp[8.5872101 - 2591.5232/(T - 43)] & \text{when} \quad T < 380\,\text{K} \\ 1000 \times \exp[14.060729 - 4436.099/(T - 43)] & \text{when} \quad 380 \le T < 500\,\text{K} \\ 1000 \times \exp[12.93692 - 3922.5184/(T - 43)] & \text{when} \quad 500 \le T < 620\,\text{K} \\ 1000 \times \exp[16.209535 - 5810.817/(T - 43)] & \text{when} \quad 620 \le T < T_{cr}\,\text{K} \\ 0 & \text{when} \quad T \ge T_{cr}\,\text{K} \end{cases}$$

The density of liquid is approximated as (Handbook of aviation fuel properties, 1984):

$$\rho_l = 840/[1 + 0.00067(T - 288)]$$

The thermal conductivity of liquid is presented in Table (A7.1).) (Reid et al, 1987).

The surface tension is approximated as (Durret et al, 1987):

$$\sigma_s = 0.059\left(1 - \frac{T}{T_{cr}}\right)^{0.121}$$

T (K)	k_l	(W/(m. K)
	Diesel fuel	*n*-dodecane
250	0.156	0.150
260	0.153	0.148
270	0.151	0.146
280	0.149	0.143
290	0.147	0.141
300	0.145	0.139
310	0.143	0.136
320	0.141	0.134
330	0.139	0.132
340	0.137	0.130
350	0.135	0.128
360	0.133	0.126
370	0.131	0.123
380	0.129	0.121
390	0.127	0.119
400	0.125	0.117
410	0.123	0.115
420	0.121	0.112
430	0.119	0.110
440	0.117	0.108
450	0.115	0.106
460	0.113	0.103
470	0.111	0.101
480	0.109	0.098
490	0.107	0.096
500	0.104	0.093
510	0.102	0.091
520	0.100	0.088
530	0.098	0.086
540	0.096	0.083
550	0.094	0.080
560	0.091	0.077
570	0.089	0.073
580	0.086	0.070
590	0.084	0.066
600	0.081	0.062
610	0.078	0.058
620	0.076	0.053
630	0.073	0.047
640	0.069	0.040
650	0.066	0.030
660	0.062	0
670	0.059	0
680	0.054	0
690	0.049	0
700	0.043	0
710	0.036	0
720	0.025	0
730	0	0

Table A7.1 Thermal conductivity of *n*-dodecane and diesel fuel.

REFERENCES

Abdelghaffar, W A, Osman, M M, Saeed, M N and Abdelfattah, A I (2002) Effects of coolant temperature on the performance and emissions of a diesel engine. *ASME*, **38**, 2002-ICE-464, 2002 ICE Spring Technical Conference.

Abdelghaffar, W A, Sazhin, S S, Sazhina, E M and Heikal, M R (2005) Advanced gas-droplets heat transfer models and their applications. *International Symposium on Heat and Mass Transfer in Spray Systems* 5-10 June 2005, (Turkey).

Abraham, J and Magi, V (1997) Modelling radiation heat loss characteristics in a diesel engine. *SAE*, Paper No. 970888.

Abramzon, B and Sazhin, S S (2005) Droplet vaporization model in the presence of thermal radiation. *International Journal of Heat Mass Transfer*, **48**, 1868 - 1873.

Abramzon, B and Sirignano, W A (1989) Droplet vaporization model for spray combustion calculations. *International Journal of Heat Mass Transfer*, **32**, 1605-1618.

Aggrawal, S K (1998) A review of spray ignition phenomena: present status and future research. *Prog. Energy and Combustion Science*, **24**, 565-600.

Ahrenkiel, R K (1971) Modified Kramers-Krönig analysis of optical spectra. *J of the Optical Society of America*, **61**, 1651-1655.

Alkidas, A C (1987) Heat release studies in divided-chamber Diesel engine. *Transactions of the ASME, Journal of Engineering for Gas Turbines and Power* - April, **109**, 193-199.

Alloca, L, Corcione, F E, Fusco, A, Papettl, F and Succi, S (1994) Modelling of diesel spray dynamics and comparison with experiments. *SAE Paper No* 941895.

Amsden, A A (1993) KIVA-3: a KIVA program with block-structured mesh for complex geometries, *Los Alamous Scientific Laboratory Report LA-12503-MS.*

Amsden, A A (1999) KIVA-3V, release2, improvements to KIVA-3V, *Los Alamous Scientific Laboratory Report LA-13608-MS.*

Amsden, A A, Ramshaw, J D, O'Rourke, P J and Dukowicz, J K (1985) KIVA: A computer program for two and three-dimensional fluid flows with chemical reaction and fuel sprays. *Los Alamous Scientific Laboratory Report LA-10245-MS.*

Amsden, A A, Butler, T D and O'Rourke, P J (1987) The KIVA-II computer program for transient multidimensional chemically reactive flows with sprays. *SAE*, Paper No 872072.

Amsden, A A, O'Rourke, P J and Butler, T D (1989) KIVA2: A computer program for chemically reactive flows with sprays. *Los Alamos National Laboratory report*, LA-11560-MS.

Amsden, A A, O'Rourke, P J, Butler, T D, Meintijes, K and Fansler, T D (1992) Comparisons of computed and measured three-dimensional velocity fields in a motored two-stroke engine. *SAE*, Paper No 920418.

Annand, W J D and Ma, H T (1972) Instantaneous heat transfer to the cylinder head surface of a small compression ignition engines. *Proc. Inst. Mech. Engrs.*, **185**, 976-987.

Assanis, D N and Heywood, J B (1986) Development and use of a computer simulation of the turbo compounded Diesel system for engine performance and component heat transfer studies. *SAE*, Paper No 860329.

Assanis, D N and Badillo, E (1989) On heat transfer measurements in diesel engines using coaxial thermocouples. *Transactions of the ASME, Journal of Engineering for gas turbines and power*, **111**, 458-465.

Axesson, O (1994) Iterative solution methods. *Cambridge University Press*, U.K.

Ayoub, N S and Reitz, R D (1997) Multidimensional modelling of fuel effects and split injection on diesel engine cold-starting. *Journal of Propulsion and Power*, **13**, 123-130.

Bai, C and Gosman, A D (1995) Development of methodology for spray impingement simulation, *SAE*, Paper No 950283.

Baker, D M and Assanis, D N (1994) A methodology for coupled thermodynamic and heat transfer analysis of a diesel engine. *Applied Mathematical Modelling*, **18** (11), 590-601.

Basevich, V Y, Beleyaev, A A, Branshtater, V, Neigauz, M G, Tashl, R and Frolov, S M (1994) Modelling of iso-octane and *n*-heptane autoignition with reference to IC engines. *Physics of combustion and explosion*, **30**, 15-24. (in Russian)

Basevich, V Y and Frolov, S M (1994) A reduced kinetic scheme for autoignition modelling of iso-octane and *n*-heptane / air mixtures during the induction period for internal combustion engines. *Chem. Phys*, **13**,146-156 (in Russian)

Bazari, Z (1992) A DI diesel combustion and emission predictive capability for use in cycle simulation. *SAE*, Paper No 920462.

Beatrice, C, Belardini, P, Bertoli, C, Cameretti, M C and Cirillo, N C (1995) Fuel jet models for multidimensional diesel combustion calculation: an update. *SAE*, Paper No 950086.

Belardini, C, Bertoli, C, Lazzaro, M and Massoli, P (1992) Single droplet evaporation rate: experimental and numerical investigations. *Proceedings of the Second International Conference on Fluid-mechanics, Combustion Emissions and Reliability in Reciprocating Engines*, Capri, Italy, 265-270.

Belardini, P, Bertoli, C and Giacomo, N D (1996) A simple auto-ignition model for three dimensional diesel combustion computations. *IMechE transaction*, **1**, C499/047, London, 305-315.

Bellan, J (2000) Supercritical (and subcritical) fluid behaviour and modelling: drops, steams, shear and mixing layers, jets and sprays. *Prog. Energy Combustion Science*, **26**, 329-366.

Benson, S W (1981) The kinetics and thermochemistry of chemical oxidation with application to combustion and flames. *Prog. Energy Combust. Sci.*, **7**, 125-134.

Berlad, A and Hibberd, R (1952) Effect of radiant energy on vaporization and combustion of liquid fuels. *NACA RME*-52109.

Bertoli, S L (2000) Radiation and convective heat transfer on pneumatic transport of particles: an analytical study, *International Journal of Heat and Mass Transfer*, **43**, 2345-2363.

Bertoli, C and Migliaccio, M (1999) A finite conductivity model for diesel spray evaporation computations, *International Journal of Heat and Fluid Flow*, **20**, 552-561.

Bird, R B, Stewart, W A and Lightfoot, E N (2002) Transport phenomena. *John Wiley & Sons.*

Borman, G L, Johnson, J H (1962) Unsteady vaporization histories and trajectories of fuel drops injected into swirling air. *SAE*, Paper No 620271.

Borman, G L and Nishiwaki, K (1987) Internal combustion engine heat transfer. *Progress in Energy Combustion Science*, **13**, 1-46.

Borman, G L and Ragland, K W (1998) Combustion engineering. *McGraw-Hill*, New York, *USA*.

Brady, R N (1996) Modern diesel technology. *Prentice-Hall*, New Jersey.

Bradley, D, Merdjani, S, Sheppard, C G W and Yeo, J (1996a) A computational model of autoignition in spark ignition engines. *Joint Meeting of Portugese, British, Spanish and Swedish sections of the Combustion Institute*, **17.3**, 1-4.

Bradley, D, Kalghatgi, G T, Golombok, M and Yeo, J (1996b) Heat release rates due to autoignition and their relationship to knock intensity in spark ignition engines. *Symposium (International) on Combustion*, 2653-2660.

Bradley, D and Morley, C (1997) Autoignition in spark-ignition engines. *Low Temperature Combustion and Autoigntion*, **35,** 661-760.

Bradley, D, Morley, C, Gu, X and Emerson, D R (2002) Amplified pressure waves during autoignition: relevance to CAI engines. *SAE*, Special Papers SP-1718, 191-202.

Bykov, V, Goldfarb, I, Gol'dshtein, V and Greenberg, J B (2002) Thermal explosion in a hot gas mixture with fuel droplets: a two reactant model. *Comb. Theory and Modelling*, **6**, 339-359.

Caldas, M and Semiao, V (1999) Modelling of scattering and absorption coefficients for a polydispersion. *International Journal of Heat and Mass Transfer*, **42,** 4535-4548.

Carslaw, H S and Jaeger, J C (1986) Conduction of heat in solids. *Clarendon Press,* Oxford.

Castanet, G, Lavieille, P, Lemoine, F, Lebouché, M, Atthasit, A, Biscos, Y and Lavergne, G (2002) Energetic budget on an evaporating monodisperse droplet stream using combined optical methods: evaluation of the convective heat transfer. *International Journal of Heat and Mass Transfer*, **45**, 5053-5067.

Castanet, G, Lavieille, P, Lebouché, M, Lemoine, F (2003) Measurements of the temperature distribution within monodisperse combusting droplets in linear streams using two-color laser- induced fluorescence. *Experiments in Fluids*, **35**, 563-571.

Chang, K C and Shieh, J S (1995) Theoretical investigation of transient droplet combustion by considering flame radiation. *International Journal of Heat and Mass Transfer*, **14**, 2611-2621.

Chang, S L and Rhee, K T (1983) Computation of radiation heat transfer in diesel combustion. *SAE*, Paper No 831332.

Chapman, M, Friedman, M C and Aghan, A (1983) A time-dependent spatial model for radiation heat transfer in diesel engines. *SAE*, Paper No 831725.

Chehroudi, B and Bracco, F V (1988) Structure of a transient hollow cone spray. *SAE*, Report No 880522.

Cheung, C S, Leung, C W and Leung,T P (1994) Modelling spatial radiative heat flux distribution in a direct injection diesel engine. *Proc Inst Mech Enging.*, **208**, 275-283.

Chiang, C H, Raju, M S and Sirignano, W A (1992) Numerical analysis of convecting, vaporizing fuel droplet with variable properties. *Int. Journal Heat Mass Transfer*, **35**, 1307-1324.

Chin, J S and Lefebvre, A H (1983) Steady-state evaporation characteristics of hydrocarbon fuel droplet. *AIAA Journal*, **21**, No. 10.

Chin, J S and Lefebvre, A H (1985) The role of the heat-up period in fuel drop evaporation. *International Journal of Turbo and Jet Engines*, **2**, 315-325.

Clift, R, Grace, J R and Weber, M E (1978) Bubbles, drops and particles. *Academic Press*, New York.

Comer, M A, Bowen, C J, Sapsford, S M and Johns, R J R (1999) Transient 3D analysis of a DI gasoline engine injector spray. *Atomization And Sprays*, **9**, 467-482.

Cox, R A and Cole, J A (1985) Chemical aspects of the autoignition of hydrocarbon - air mixtures. *Combustion and Flame*, **60**, 109-123.

Crespo, A and Liñan, A (1975) Unsteady effects in droplet evaporation and combustion, *Combustion Science and Technology*, **11**, 9-18.

Crook, R F and Ju-Ger, J S (1985) Design of radiators for low flow cooling systems. *SAE*, Paper No 851472.

Crua, C, Kennaird, D A, Sazhin, S S, Heikal, M R and Gold, M R (2004) Diesel autoignition at elevated in-cylinder pressures. *International Journal of Engine Research*, **5** (4), 565 – 374.

Dombrovsky, L A (1996a) Approximation methods for calculating radiation heat transfer in dispersed systems. *Thermal Engineering*, **43** (3), 235-243.

Dombrovsky, L A (1996b) Radiation heat transfer in disperse systems. *Begell House*, inc., Publishers, New York, Wallingford (UK)

Dombrovsky, L A (1996c) Evaluation of the error of the P_1 approximation in calculations of thermal radiation transfer in optically inhomogeneous media. *High Temperature*. **35** (4), 676-679.

Dombrovsky, L A (2000) Thermal radiation from nonisothermal spherical particles of a semitransparent material. *International journal of Heat and Mass Transfer*, **43**, 1661-1672.

Dombrovsky, L A (2002a) A modified differential approximation for thermal radiation of semitransparent nonisothermal particles: application to optical diagnostics of plasma spraying. *Journal of Quantitative Spectroscopy& Radiative Transfer*, **73**, 433-441.

Dombrovsky, L A (2002b) Spectral model of absorption and scattering of thermal radiation by diesel fuel droplets. *High Temperature*, **40**, 242-248.

Dombrovsky, L A and Zaichik, L I (2001) Conditions of thermal explosion in a radiating gas with polydisperse liquid fuel. *High Temperature*, **39**, 604-611.

Dombrovsky, L A, Sazhin, S S, Sazhina, E M, Feng, G, Heikal, M R, Bardsley, M E A and Mikhalovsky, S V (2001) Heating and evaporation of semi-transparent diesel fuel droplets in the presence of thermal radiation. *Fuel*, **80**(11), 1535-1544.

Dombrovsky, L A, Sazhin, S S and Heikal, M R (2002) A model for computation of radiative characteristics of diesel fuel droplets. *Proceeding of 3rd Russian National Heat and Mass Transfer Conference*, **6**, 262-265 (in Russian)

Dombrovsky, L A and Sazhin, S S (2003a) A parabolic model for convective heating of droplets. *ASME Journal of Heat Transfer*, **125**, 535-537.

Dombrovsky, L A and Sazhin, S S (2003b) Absorption of thermal radiation in a semi-transparent spherical droplet: a simplified model. *International Journal of Heat and Fluid Flow Transfer*, **24**, 919-927.

Dombrovsky, L A and Sazhin, S S (2003c) Absorption of thermal radiation inside a fuel droplet. In: Lybaert, P, Feldheim, V, Lemonnier, D, Selcuk, N (Eds), *Proceeding Of Eurotherm Seminar "Computational Thermal Radiation in Paricipating Media"*, 15-17 April, Mons, Begium. Elsevier, 249-258.

Dombrovsky, L A and Sazhin, S S (2004) Absorption of external thermal radiation in asymmetrically illuminated droplets. *Journal of Quantitative Spectroscopy & Radiative Transfer*, **87**, 119-135

Dombrovsky, L A, Sazhin, S S, Mikhalovsky, S V, Wood, R and Heikal, M R (2003) Spectral properties of diesel fuel droplets. *Fuel*, **82** (1), 15-22.

Douglas, J F, Gasiorek, J M and Swaffield J A (1995) Fluid mechanics. *Longman*, London.

Dukowicz, J K (1980) A particle-fluid numerical model for liquid sprays. *Journal of Computational Physics*, 35, 229–253.

Durret, R P, Oren, D C and Ferguson, C R (1987) A multidimensional data set for diesel combustion model validation: initial conditions, pressure history and spray shapes. *SAE* Paper No 872087.

El Wakil, M M, Uyehara, O A and Myers, P O (1954) A theoretical investigation of the heating-up period of injected fuel droplets. *NACA TN 3179*.

Faeth, G M (1977) Current status of droplet and liquid combustion. *Prog. Energy and Combustion science*, **3**, 191-224.

Faeth, G M (1983) Evaporation and combustion of sprays. *Progress in Energy and Combustion Science*, **9**, 1-76

Feng, Z G and Michaelides, E E (1996) Unsteady heat transfer from a sphere at small Peclet numbers. *Journal of Fluid Engineering*, **118**, 96-102.

FIRE 5.1 User guide (1993), 2nd Edn, *AVL*.

Flynn, P F, Mizusawa, M, Uyehara, O A and Myers, P S (1972) An experimental determination of the instantaneous potential radiant heat transfer within an operating diesel engine. *SAE*, Paper No 720022.

Flynn, P F, Durrett, R P, Hunter, G L, ZurLoye, A O, Akinyemi, O C, Dec, J E and Wetbrook, C K (1999) Diesel combustion: an integrated view combining laser diagnostics, chemical kinetics, and empirical validation. *SAE*, Report No 1999-01-0509.

Friedman, M H and Churchill, S W (1965) The absorption of thermal radiation by fuel droplets. *Chemical Engineering Progress Symposium*, **61**, 1-4.

Furmanski, P, Banaszek, J, Wisniewski, T S, and Rebow, M (1997) Influence of thermal radiation from the burned zone on heat transfer in the piston of diesel engine. *Progress in Engineering heat transfer*, 11-18.

Givler, S D and Abraham, J (1996) Supercritical droplet vaporization and combustion studies. *Prog. Energy and Combustion Science*, **22**, 1-28.

Gogos, G, Soh, S, Pope, D N (2003) Effects of gravity and ambient pressure on liquid fuel droplet evaporation. *International Journal of Heat and Mass Transfer*, **46**, 283-296.

Goldrafb, I, Gol'dshtein, V, Kuzmenko, G and Sazhin, S S (1999) Thermal radiation effect on thermal explosion in gas containing droplets. *Combustion Theary and Modelling*, **3**, 769-787.

Golub, G and Van Loan, C (1983) Matrix computations. *The Johns Hopkins University Press,* Baltimore. U.S.A.

Gorelov, G N, Sobolev, V A and Schepakina, E A (1999) Singularly perturbed combustion models. *Samara State University Publishing House*, (in Russian).

Gorokhovski, M (2001) The stochastic lagrangian model of drop break-up in the computation of liquid sprays. *Atomization and Sprays*, **11**, 505-519.

Griffiths, J F (1995) Reduced kinetic models and their application to practical combustion systems. *Prog. Energy Combust. Sci.*, **21**, 25-107

Griffiths, J F and Barnard, J A (1995) Flame and combustion. *Blackie Academic & Professional.*

Halstead, M, Kirsh, L and Quinn, C P (1977) The autoignition of hydrocarbon fuels at high temperatures and pressures: fitting of a mathematical model. *Combustion and Flame*, **30**, 45-60.

Hamosfakidis, V and Reitz, R D (2003) Optimization of a hydrocarbon fuel ignition model for two single component surrogates of diesel fuel. *Combustion and Flame*, **132**, 433-450.

Han, Z and Reitz, R (1997) A temperature wall function formulation for variable-density turbulent flows with application to engine convective heat transfer modelling. *International Journal of Heat and Mass Transfer.* **40** (3), 613-625.

Handbook of Aviation Fuel Properties (1984). *SAE CRC*, Report No 530.

Harpole, G M (1980) Radiative absorption by evaporating droplets. *International Journal of Heat and Mass Transfer*, **23**, 17-26.

Haywood, R J and Renksizbulut, M (1986) On variable property, blowing and transient effects in convective droplet evaporation with internal circulation. *In proceedings of the Eighth International Heat Transfer Conference*, Hemishere: New York, 1861-1866.

Haywood, R J, Nafziger, R and Renksizbulut, M (1989) A detailed examination of gas and liquid phase transient processes in convective droplet evaporation. *Journal of Heat Transfer*, **111**, 495-502.

Heywood, J B (1976) Pollutant formation and control in spark-ignition engines. *Prog. Energy Combust. Sci.*, **1**, 135-164.

Heywood, J B (1988) Internal Combustion Engine Fundamentals. *McGraw-Hill*, New York.

Hinze, J O (1948) *Appl. Sci. Research*, **1**, 263, 273.

Hiroyasu, H, Kadota, T and Arai, M (1980) Supplementary comments: fuel spray characteristics in diesel engines. *In: Combustion Modelling in Reciprocating engines*. Plenum Press, New York, 369-405.

Hirsch, C (1994) Numerical of internal and external flows. *John Wiley & Sons,* Chichester.

Hirschfelder, J O, Curtiss, C F and Bird, R B (1954) Molecular theory of gases and liquids. *John Willey and Sons*, New York.

Hirt, C W, Amsden, A A and Cook, J L (1974) An arbitrary Lagrangian-Eulerian computing method for all flow speeds. *Journal of Computational Physics*, **14**, 227 – 253.

Hohmann, S and Renz, U (2003) Numerical simulation of fuel sprays at high ambient pressure: the influence of real gas effects and gas solubility on droplet vaporization. *International Journal of Heat and Mass Transfer*, **46**, 3017-3028.

Holman, J P (1990) Heat transfer. *McGraw-Hill*, New York.

Hottel, H C, Wiliams, G C and Simpson, H C (1955) Combustion of droplet of heavy liquid fuels. *Fifth Symposium (International) on Combustion*, Reinhold, New York, 101.

Hottel, H C and Sarofim, A F (1967) Radiative transfer. *McGraw-Hill*, New York, 256-288.

Hubbard, G L, Denny, V E and Mills, A F (1975) Droplet evaporation: effects of transient and variable properties. *Int. Journal of Heat Mass Transfer*, **18**, 1003-1008.

Ikegami, M, Nakatani, K T, Tanaka, K and Yamane, K (1997) Fuel injection rate shaping and its effects on exhaust emissions in a direct-injection diesel engine using spool acceleration type injection system. *SAE*, Paper No 970347.

Incropera, F P and DeWitt, D P (2002) Introduction to heat transfer. *John Wiley& Sons*, New York.

Jin, J D and Borman, G L (1985) A model for multicomponent droplet vaporization at high ambient pressures. *SAE*, Paper No 850264.

Johns, R J R (1990) Progress in the development of a detailed model for diesel combustion. *International Symposium COMODIA*, **90**, 577-586.

Kartashov, E M (2001) Analytical methods in the heat transfer theory in solids. *Vysshaya shkola*, Moscow (in Russian)

Kavtaradze, R Z (2001) Local heat transfer in reciprocating engines. *Moscow State Technical Bauman University Publishing House* (in Russian).

Kim, H and Sung, N (2003) The effect of ambient pressure on the evaporation of a single droplet and a spray. *Combustion and Flame*, **135,** 261-270.

Kong, S C, Han, Z and Reitz, R D (1996) The development and application of a diesel ignition and combustion model for multidimensional engine simulation. *SAE*, Paper No 950278.

Kryukov, A P, Lavashov, V Yu and Sazhin, S S (2004) Evaporation of diesel fuel droplets: kinetic versus hydrodynamic models. *International Journal of Heat and Mass Transfer*, **47** (12-13), 2541-2549.

Kunitomo,T, Matsuoka, K and Oguri, T (1975) Predication of radiative heat flux in a diesel engine. *SAE*, Paper No 750786.

Kuo, K K (1986) Principles of combustion. *John Wiley & Sons.*

Labuntsov, D V and Kryukov, A P (1989) Analysis of intensive evaporation and condensation. *International Journal of Heat and Mass Transfer*, **22**, 989-1002.

Lage, P L C and Rangel, R H (1993a) Single droplet vaporization including thermal radiation absorption. *Journal of Thermodynamics and Heat Transfer*, **7,** 502-508.

Lage, P L and Rangel, R H (1993b) Total thermal radiation absorption by a single spherical droplet. *Journal of Thermodynamics and Heat Transfer*, **7** (1), 101-109.

Launder, B E and Spalding, D B (1972) Mathematical models of turbulence. *Academic Press*, New York.

Lavieille, P, Lemoine, F, Lavergne, G, Virepinte, J F and Lebouche, M (2000) Temperature measurements on droplets in monodisperse stream using laser-induced fluorescence. *Experiments in Fluids*, **29**, 429-437.

Lavieille, P, Lemoine, F, Lavergne, G and Lebouche (2001) Evaporating and combusting droplet temperature measurements using two-colour laser-induced fluorescence. *Experiments in Fluids*, **31**, 45-55

Laveille, P, Lemoine, F and Lebouché, M (2002) Measurement of the temperature distribution over a combusting droplet in monodisperse stream using two-colour laser-induced fluorescence. *Proceedings of the 12th International Heat Transfer Conference*, **2**, 917, Elsevier (available on CD).

Lefebvre, A H (1989) Atomization and sprays. *Taylor& Francis.*

Levich, V G (1962) Physicochemical hydrodynamics. *Prentice-Hall Inc*, N.J.

Lichty, L C (1967) Combustion engine processes. *McGraw-Hill*, New York.

Lingen, C, Fanming, Z, Fengrui, S and Chih, W (1996) Heat-transfer effects on network and/or power as functions of efficiency for air-standard diesel cycles. *Energy*, **21** (12), 1201-1205.

Liu, A B and Reitz, R D (1993) Mechanisms of air-assited liquid atomization. *Atomization and Spray*, **3**, 55-75.

Liu, L H, Tan, H P and Tong, T W (2002) Transient coupled radiation-conduction in semitransparent spherical particle. *Journal of Thermophysics and Heat transfer*, **16**, No. 1.

Lorenzo, C, Aggarwal, S K and Murad, S (2003) A molecular dynamics simulation of droplet evaporation. *International Journal of Heat and Mass Transfer*, **46**, 3179-3188.

Loth, E (2000) Numerical approaches for motion of dispersed particles, droplets and bubbles. *Prog. Energy of Combustion Science*, **26**, 161-223.

Luikov, A V (1968) Analytical heat diffusion theory. *Academic Press*, New York and London.

Marchese, A J and Dryer, F L (1997) The effect of non-luminous thermal radiation in microgravity droplet combustion. *Combustion Science and Technology*, **124**, 371-402.

Marshak, R E (1947) Note on the spherical harmonic method as applied to the Milne problem for a sphere. *Phys Rev*, **71** (7), 443-446.

Matlosz, R L, Leipziger, S and Torda, T P (1972) Investigation of liquid drop evaporation in a high-temperature and high-pressure environment. *International Journal of Heat and Mass Transfer*, **15**, 831-852.

Maxwell, J B (1950) Data book on hydrocarbons: Applocation to process engineering. *D. van Nostrand Company, INC.*, New York.

Megaridis, C M (1993) Comparizon between experimental measurements and numerical predictions of internal temperature distribution of a droplet vaprorizing under high-temeparture convective conditions. *Combustion and Flame*, **93**, 287-302.

Meintjes, K and Morgan, A P (1987) Element variables and the solution of complex chemical equilibrium problems. *General Motors Research Publication*, GMR-5827.

Mengüc, M P, Viskanta, R and Ferguson, C R (1985) Multidimensional modelling of radiative heat transfer in diesel engine. *SAE*, Paper No 850503.

Miliauskas, G (2003) Interaction of the transfer processes in semitransparent liquid droplets. *International Journal of Heat and Mass Transfer*, **46**, 4119 – 4138.

Modest, M F (1993) Radiative heat transfer. *McGraw-Hill*, New York.

Moriue, O, Schnubelt, S, Eigenbrod, C and Rath, H J (2003) Numerical simulation of the ignition of a single fuel droplet in an air with finite volume. *9th International Conference on Liquid atomization and Spray Systems*, Sorrento, Italy.

Morsi, S A and Alexander, A J (1972) An investigation of particle trajectories in two-phase flow systems. *Journal of Fluid Mech*, **55**(2), 193-208.

Mukhopadhyay, A and Sanyal, D (2001) A spherical cell model for multi – component droplet combustion in a dilute spray. *International Journal of Energy Research*, **25**, 1275 – 1294.

Mukhopadhyay, A and Sanyal, D (2005) A semi-analytical model for evaporating fuel droplets. *Journal of Heat Transfer*, 127, 199 – 203.

Müller, U C, Peters, N and Liňan, A (1992) Global kinetics for n-heptane ignition at high pressures. *Twenty-Fourth Symposium (Intrnational) on Combustion*, The Combustion Institute, 777-784.

Nishida, K and Hiroyasu, H (1989) Simplified three dimensional modelling of mixture formation and combustion in a DI diesel engines. *SAE*, Paper No 890269.

Nomura, H, Ujiie, Y, Rath, H J, Sato, J and Kono, M (1996) Experimental study on high-pressure droplet evaporation using microgravity conditions. *26 th Symposium(International) on Combustion, The combustion Institute*, 1267-1273.

Nomura, H, Rath, H, Sato, J and Kono, M (1997) Effects of ambient pressure and natural convection on fuel droplet evaporation. *4th Asian-Pacific International Symposium on Combustion and energy Utilization*, 266-271.

Orme, M (1997) Experiments on droplet collisions, bounce, coalescence and disruption. *Prog. Energy of Combustion Science*, **23**, 65-79.

O'Rourke, P J (1981) Collective drop effects in vaporizing liquid sprays. *Ph.D. thesis 1532*, Princeton University.

O'Rourke, P J (1987) Statistical properties and numerical implementation of a model for droplet dispersion in a turbulent gas. *Los Alamos National Laboratory report*, LA UR 87 2376, accepted by J. Comput. Phys.

O'Rourke, P J and Amsden, A A (1987) The TAB method for numerical calculation of spray droplet break up. *SAE*, Paper No 872089.

Paál, G (1992) Transient characteristics of diesel engine sprays. *Ph.D. thesis*, Imperial College of Science, Technology and Medicine, University of London, U.K.

Pagel, S, Stiesch, G and Maker, G P (2002) Modelling the evaporation of a multicomponent fuel. *Twelfth International Heat Transfer Conference.*

Panton, R L (1996) Incompressible flow. *Wiley*, London.

Papageorgakis, G and Assanis, D N (1996) A spray break-up model for low injection pressures, *Int. Comm. Heat Mass Transfer*, **23**, No. 1, 1-10.

Pascal, L, Fabrice, L and Mickel, L (2002) Measurement of the temperature distribution over a combusting droplet in monodisperse stream using two colors laser-induced fluorescence. *Proceeding of the Twelfth International Heat Transfer Conference*, Grenoble

Patankar, S V (1980) Numerical heat transfer and fluid flow. *McGraw-Hill*, New York

Patterson, M A and Reitz, R D (1998) Modelling the effects of fuel spray characteristics on diesel engine combustion and emission. *SAE*, Paper No 980131.

Picher, G, Wigley, G and Saffman, M (1990) Velocity and drop size measurements in fuel sprays in a direct injection diesel engine. *Particle and Particle systems Charact*, **7**, 160-168.

Poling, B E, Prausnitz, J M and O'Connell, J (2000) The properties of gases and liquids. *McGraw-Hill*, New York.

Poppe, C, Schereiber, M and Griffiths, J F (1993) Modelling of *n*-heptane autoignition and validation of the results. *In Proceeding of joint meeting of British and German Societies*, 360-363.

Pracht, W E (1975) Calculating three-dimensional fluid flows at all speeds with an Eulerian-Lagrangian computing mesh. *Journal of Computational Physics*, **17**, 132 - 159.

Press, W H, Flannery, B P, Teukovsky, S A and Vetterling W T (1989) Numerical recipes: the art of scientific computing. *Cambridge University Press.*

Putnam, A (1961) Integrable form of droplet drag coefficient. *J. Am. Rocket Soc.*, **31**, 1467-1468.

Ramshaw, J D (1980) Partial chemical equilibrium in fluid dynamics. *Phys. Fluids,* **23**, 675.

Ramshaw, J D and Amsden, A A (1985) Improved iteration scheme for partial equilibrium flow. *J. compu. Phys.*, **59** (3), 484.

Ranz, W E and Marshall, W R (1952) Evaporation from drops. *Chem. Eng. Prog.*, **48**, Part I, 141-146, Part II, 173-180.

Reichelt, L, Meingast, U and Renz, U (2002) Calculating transient wall heat flux from measurements of surface temperature. *International Journal of Heat and Mass Transfer,* **45**, 579-584.

Reid, R C, Prausnitz, J M and Poling , B E (1987) The properties of gases and liquids. *McGraw-Hill Book*, New York.

Reitz, R D (1987) Modelling atomization process in high pressure vaporizing spray. *Atomization Spray Technol.*, **3**, 309.

Reitz, R D and Diwakar, R (1987) Structure of high pressure fuel spray. *SAE*, Paper No 870598.

Reitz, R D and Rutland, C J (1995) Development and testing of diesel engine CFD models. *Prog. Energy Combust. Sci.*, **21**, 173-196.

Renksizbulut, M and Haywood, R J (1988) Transient droplet evaporation with variable properties and internal circulation at intermediate Reynolds Numbers. *Int. of Multiphase Flow*, **14**, 1730-1742.

Reynolds, W C (1981) Modelling of fluid motions in engines- An introductory overview. *in Combusion Modelling in Reciprocating Engines Eds. J. N. Mattavi and C. A. Amann* (plenum Press, New York).

Ricardo, H R (1930) Combustion in diesel engines. *Proc. IAE.*

Ristau, R, Nagel, U, Iglseder, H, Konig, J, Rath, H J, Nomura, H, Kono, M, Tanabe, M and Sato, J (1993) Theoretical and experimental investigations on droplet evaporation and droplet ignition at high pressure. *Microgravity Sci. Technol.* **VI/4**, 223-2228.

Robertson, J, A and Crowe, C, T (1997) Engineering fluid mechanics. 6th ed, *Wiley*, New York, 834.

Saeed, M N (1989) Experimental investigations on the cooling system of an idled spark- engine. *Alexandria Engineering Journal*, Alexandria University- July, **28** (3), 363- 382.

Saitoh, T, Yamazaki, K and Viskanta, R (1993) Effect of thermal radiation on transient combustion of a fuel droplet. *Journal of Thermophysicals and Heat Transfe,* **7** (1), 94.

Sakakibara, J and Adrian, R J (1999) Whole field measurement of temperature in water using two-colour laser-induced fluorescence. *Experiments in Fluids*, **26**, 7-15.

Sazhin, S S, Wild, P, Leys, C, Toebaert, D and Sazhina, E (1993) The three temperature model for the fast-axial-flow CO_2 laser. *Journal of Physics*, **26**, 1872-1883.

Sazhin, S S, Sazhina, E M, Faltsi-Saravelou, O and Wild, P (1996) The P-1 model for thermal radiation transfer: advantages and limitations. *Fuel*, **75** (3), 289-294.

Sazhin, S S, Sazhina, E M, Heikal, M R, Maroony, C and Mikhalovsky, S V (1999) The Shell autoignition model: a new mathematical formulation. *Combustion and Flame*, **117** (3), 529-540.

Sazhin, S S, Sazhina, E M and Heikal, M R (2000) Modelling of the gas to fuel droplets radiative exchange. *Fuel*, **79,** 1843-1852.

Sazhin, S S, Gol'dshtein, V A and Heikal, M R (2001a) A transient formulation of Newton's cooling law for spherical bodies. *ASME J of Heat Transfer*, **123** (1), 63-64.

Sazhin, S S, Goldshtein, V, Heikal, M R, Goldfarb, I, Gol'dshtein, V and Kuzmenko, G (2001b) Thermal ignition analysis of a monodisperse spray with radiation. *Combustion and Flame,* **124** (4), 684-701.

Sazhin, S S, Feng G, Heikal, M R, Goldfarb, I, Goldshtein, V and Kuzmenko, G (2001c) Thermal ignition analysis of a monodisperse spray with radiation, *Combustion and Flame*, **124**(4), 684-701.

Sazhin, S S, Dombrovsky, L A, Krutitskii, P, Sazhina, E M and Heikal, M R (2002) Analytical and numerical modelling of convective and radiative heating of fuel droplets in diesel engines. *Proceeding of the Twelfth International Heat Transfer Conference*, Grenoble (August 18-23, 2002) Editions scientifique et medicale, Elsevier SAS, **1**, 699-704.

Sazhin, S S and Krutitskii, P A (2003) A conduction model for transient heating of fuel droplets. *Proceedings of the 3d International ISAAC (International Society for Analysis, Applications and Computations)* Congress (August 20 - 25, 2001, Berlin). Eds. H.G.W. Begehre, R.P.Gilbert, M.W.Wong. World Scientific, Singapore, **2**, 1231–1239.

Sazhin, S S, Crua, C, Kennaird, D and Heikal, M R (2003) The initial stage of fuel spray penetration. *Fuel*, **82**, 875-885.

Sazhin, S S, Abdelghaffar, W A, Sazhina, E M, Mikhalovsky, S V, Meikle, S T and Bai, C (2004a) Radiative heating of semi-transparent diesel fuel droplets. *ASME Journal of Heat Transfer,* **126**, 105-109. Erratum (2004), **126**, 490-491.

Sazhin, S S, Krutitskii, P A, Abdelghaffar, W A, Mikhalovsky, S V, Meikle, S and Heikal, M R (2004b) Transient heating of diesel fuel droplets. *International Journal of Heat and Mass Transfer*, **47**, 3327-3340.

Sazhin, S S, Abdelghaffar, W A, Krutitskii, P A, Sazhina, E M and Heikal, M R (2004c) Numerical modelling of droplet transient heating and evaporation. *5th Minsk International Heat and Mass Transfer Forum*, Minsk, 24-28 May.(Belarus) (available on CD).

Sazhin, S S, Abdelghaffar, W A, Krutitskii, P A, Sazhina, E M and Heikal, M R (2005a) New approaches to numerical modelling of droplet transient heating and evaporation. *International Journal of Heat and Mass Transfer.* (in press)

Sazhin, S S, Abdelghaffar, W A, Sazhina, E M and Heikal, M R (2005b) Models for droplet transient heating: effects on droplet evaporation, ignition, and break up. *International Journal of Thermal Science*, **44**, 610-622.

Sazhina, E M (1999) Numerical analysis of autoignition and thermal radiation processes in diesel engines. *Ph. D. Thesis*, Brighton University.

Sazhina, E M, Sazhin, S S, Heikal, M R and Marooney, C (1999) The Shell autoignition model: application to gasoline and diesel fuels. *Fuel*, **78**(4), 389-401.

Sazhina, E M, Sazhin, S S, Heikal, M R, Babushok, V I and Johns, R J R (2000a) A detailed modelling of the spray ignition process in diesel engines. *Combustion of Science and Technology*, **160**, 317-344.

Sazhina, E M, Sazhin, S S, Heikal, M R and Bardsley M E A (2000b) The P-1 model for thermal radiation transfer: application to numerical modelling of combustion processes in diesel engine. *Proceeding of the 16th IMACS World Congress 2000 on Scientific Computation, applied Mathematics and Simulation.* (Available on CD, paper 125-10).

Schnaubelt, S, Moriue, O, Coordes, T, Eigenbord, C and Rath, H, J (2000) Detailed numerical simulations of the multiscale self-ignition processes of *n*-heptane isolated droplets and their verification by comparison with microgravity experiments. *Proceedings of the Combustion Institute*, **28**, 953-960.

Schäpertöns, H and Lee, W (1985) Multidimensional modelling of knocking combustion in SI engines. *SAE*, Paper No 850502.

Schrage, R W (1953) A theoretical study of interphase mass transfer. *Columbia University Press,* New York.

Shayler, P J and May, S A (1993) The determination of heat transfer from the combustion of SI engines. *SAE*, Paper No 931131.

Siegel, R and Howell, J R (1992) Thermal radiation heat transfer. *Hemishere Publishing Corporation*, Washington DC.

Sirignano,W A (1999) Fluid dynamics and transport of droplets and sprays. *Cambridge University Press.*

Spalding, D B (1953) The combustion of liquid fuels. *Fourth Symposium (International) on Combustion, Williams & Wilkins,* Baltimora, 847-864.

Spalding, D B (1963) Convective mass transfer. *Edward Arnold Ltd.*

Tanabe, M, Kono, M, Sato, J, Koenig, J, Eigenbrod, C, Dinkelacker, F and Rath, H J (1995) Two stage ignition of *n*-heptane isolated droplets. *Combustion Science and Technology*, **108**, 103-119.

Tanner, F X (2004) Development and validation of a cascade atomization and droplet break-up model for high-velocity dense spray. *Atomization and Spray*, **14**, 211-242.

Taylor, C F (1979) The internal combustion engine in theory and practice. *MIT Press*, Cambridge, Massachusetts.

Taylor, G I (1963) The instability of liquid surfaces when accelerated in a direction perpendicular to their planes. *The scientific papers of G. I. Taylor, ed. G. K. Batchelor*, **III**, University Press, Cambridge.

Theobald, M A (1986) Numerical simulation of diesel autoignition. *PhD Thesis*, MIT.

Todes, O M (1966) Quasi-stationary regimes of mass and heat transfer between a spherical body and ambient medium. *Proceedings of the Sixths Conference on Evaporation, Combustion and Gas Dynamics of Disperse Systems*, Odessa University Publishing House, Odessa, USSR, 151-159 (in Russian).

Torres, D J, O'Rourke, A A and Amsden, A A (2003) Efficient multicomponent fuel algorithm. *Combustion Theory and Modelling*, **7**, 67 – 86.

Uchimi, T, Taya, K, Hagihara, Y, Kimura, S and Enomoto, Y (2000) Heat loss to combustion chamber wall in a D.I. diesel engine: First report: Tendency of heat loss to piston surface. *JSAE*, **21**, 133-141.

Utyuzhnikov, S V (2002) Numerical modelling of combustion of fuel-droplet-vapour releases in the atmosphere. *Flow, Turbulence and Combustion*, **68**, 137-152.

Vargaftik, N B (1983) Handbook of physical properties of liquids and gases. *Hemisphere Publishing. Corp.*

Versteeg, H K and Malalasekera, W (1995) An introduction to computational fluid dynamics: the Finite Volume method. *Longman Group,* Harlow.

Viskanta, R and Mengüc, M P (1987) Radiation heat transfer in combustion systems. *Prog Energy Comb Science*, **13**, 97-160.

Wahiduzzaman, S, Moral, T, Timar, J and DeWitt, D P (1987) Experimental and analytical study of heat radiation in diesel engine. *SAE,* Paper No 870571.

Wallis, G B (1969) One dimensional two-phase flows. *McGraw-Hill*, New York.

White, F, M (1999) Fluid mechanics. 4th ed, *McGraw-Hill*, New York, 457.

Woschni, G (1967) A universally applicable equation for the instantaneous heat transfer coefficient in the internal combustion engine. *SAE*, Paper No 670931.

Woschni, G and Spindler, W (1988) Heat transfer with insulated combustion chamber walls and its influence on the performance of diesel engines. *Transactions of the ASME, Journal of Engineering for Gas Turbines and Power -July*, **110**, 482-502.

Wong, S C and Lin, A C (1992) Microexplosion mechanisms of aluminium /carbon slurry droplets. *Combustion and Flame,* **89** (1), 64-76.

Xu, Z, Johnson, J H and Chiang, E C (1984) A simulation study of a computer controlled cooling system for a Diesel powered truck. *SAE*, Paper No 841711.

Yamada, Y, Emi, M, Ishii, H, Suzuki, Y, Kimura, S and Enomoto, Y (2002) Heat loss to the combustion chamber wall with deposit in D.I. diesel engine: Variation of instantaneous heat flux on piston surface with deposit. *JSAE*, Paper No 20024661.

Yamane, K and Shimamoto, Y (1999) Prediction of NO and soot from diesel engines with fuel injection rate shaping using multidimensional engine simulation. *Proceedings of the 15th International Internal Combustion Engine Symposium*, Seoul, Korea.

Yang, J R and Wong, S C (2001) On the discrepancies between theoretical and experimental results for microgravity droplet evaporation. *International Journal of Heat and Mass Transfer*, **44**, 4433-4443.

Yang, J R and Wong, S C (2003) On the suppression of negative temperature coefficient (NTC) in autoignition of n-heptane droplets. *Combustion and Flame*, **132**, 471 – 491.

Yao, G F, Abdel-Khalik, S I and Ghiaasiaan, S M (2003) An investigation of simple evaporation models used in spray simulations. *Journal of Heat Transfer*, **125**, 179-182.

Yong, L and Reitz, R D (1998) Modelling of heat conduction within chamber walls for multidimensional internal combustion engine simulations. *International Journal of Heat and Mass Transfer*, **41** (6-7), 859-869.

Zeng, Y and Lee, C – F (2002) A preferential vaporization model for multicomponent droplet and sprays. *Atomization and Sprays*, **12**, 163 – 186.

Papers published by the author

Journal papers

Sazhin, S S, Abdelghaffar, W A, Krutitskii, P A, Sazhina, E M and Heikal, M R (2005a) New approaches to numerical modelling of droplet transient heating and evaporation. *International Journal of Heat and Mass Transfer.* (in press)

Sazhin, S S, Abdelghaffar, W A, Sazhina, E M and Heikal, M R (2005b) Models for droplet transient heating: effects on droplet evaporation, ignition, and break up. *International Journal of Thermal Science*, **44**, 610-622.

Sazhin, S S, Abdelghaffar, W A, Sazhina, E M, Mikhalovsky, S V, Meikle, S T and Bai, C (2004a) Radiative heating of semi-transparent diesel fuel droplets. *ASME Journal of Heat Transfer,* **126**, 105-109. Erratum (2004), **126**, 490-491.

Sazhin, S S, Krutitskii, P A, Abdelghaffar, W A, Mikhalovsky, S V, Meikle, S and Heikal, M R (2004b) Transient heating of diesel fuel droplets. *International Journal of Heat and Mass Transfer*, **47**, 3327-3340.

Conference proceedings

Abdelghaffar, W A, Sazhin, S S, Sazhina, E M and Heikal, M R (2005a) Models for droplet transient heating: a comparative analysis, *4th International Conference on Heat Transfer, Fluid Mechanics and Thermodynamics*, Cairo, 18-22 September (Egypt) (in press)

Abdelghaffar, W A, Sazhin, S S, Sazhina, E M and Heikal, M R (2005) Advanced gas-droplets heat transfer models and their applications. *International Symposium on Heat and Mass Transfer in Spray Systems* 5-10 June 2005, (Turkey).

Sazhin, S S, Abdelghaffar, W A, Martynov, S B, Sazhina, E M, Heikal, M R and Krutitskii, P A (2005c) Transient heating and evaporation of fuel droplets: recent results and unsolved problems. *Proceeding of the 5th International Symposium on Multiphase Flow, Heat Mass Transfer and Energy Conversion*, Xi'an, China 3-6 July (in press).

Sazhin, S S, Krutitskii, P A, Abdelghaffar, W A, Sazhina, E M and Heikal, M R (2004) Transient heating of droplets. *Proceeding of '3rd International Symposium on Two-Phase Flow Modelling and Experimentation'*, Pisa, 22-24 September (available on CD).

Sazhin, S S, Abdelghaffar, W A, Krutitskii, P A, Sazhina, E M and Heikal, M R (2004c) Numerical modelling of droplet transient heating and evaporation. *5th Minsk*

International Heat and Mass Transfer Forum, Minsk, 24-28 May, (Belarus) (available on CD).

Abdelghaffar, W A (2004) Numerical modelling of heating and evaporation of